

PL-TR-96-2307

**PATH CALIBRATION, SOURCE ESTIMATION AND REGIONAL
DISCRIMINATION FOR THE MIDDLE EAST AND WESTERN
MEDITERRANEAN**

**C.K. Saikia
H.K. Thio
B.B. Woods
X. Song
L. Zhu
D.V. Helmberger**

**Woodward-Clyde Federal Services
566 El Dorado Street, Suite 100
Pasadena CA 91101-2560**

1 July 1996

Scientific Report No. 2

Approved for public release; distribution unlimited

**19970421
056**



**PHILLIPS LABORATORY
Directorate of Geophysics
AIR FORCE MATERIEL COMMAND
HANSCOM AIR FORCE BASE MA 01731-3010**

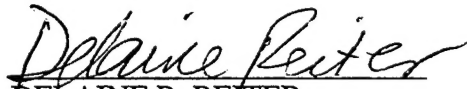
DTIC QUALITY INSPECTED 3

SPONSORED BY
Advanced Research Projects Agency (DoD)
Nuclear Monitoring Research Office
ARPA ORDER No. C-325

MONITORED BY
Phillips Laboratory
CONTRACT No. F19628-95-C-0093

The views and conclusions contained in this document are those of the authors and should not be interpreted as representing the official policies, either express or implied, of the Air Force or U.S. Government.

This technical report has been reviewed and is approved for publication.



DELAINE R. REITER
Contract Manager
Earth Sciences Division



JAMES F. LEWKOWICZ
Director
Earth Sciences Division

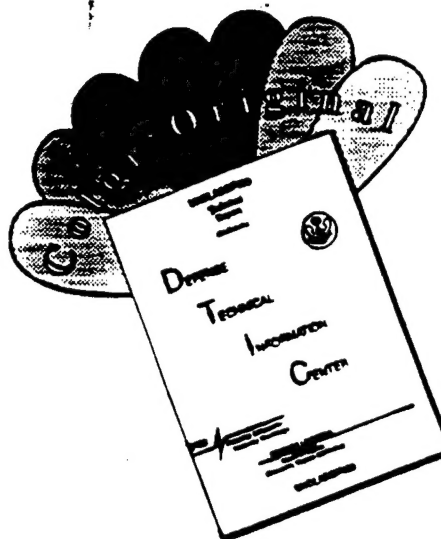
This report has been reviewed by the ESD Public Affairs Office (PA) and is releasable to the National Technical Information Service (NTIS).

Qualified requestors may obtain copies from the Defense Technical Information Center.
All others should apply to the National Technical Information Service.

If your address has changed, or you wish to be removed from the mailing list, or if the addressee is no longer employed by your organization, please notify PL/IM, 29 Randolph Road, Hanscom AFB, MA 01731-3010. This will assist us in maintaining a current mailing list.

Do not return copies of this report unless contractual obligations or notices on a specific document requires that it be returned.

DISCLAIMER NOTICE



**THIS DOCUMENT IS BEST
QUALITY AVAILABLE. THE COPY
FURNISHED TO DTIC CONTAINED
A SIGNIFICANT NUMBER OF
COLOR PAGES WHICH DO NOT
REPRODUCE LEGIBLY ON BLACK
AND WHITE MICROFICHE.**

REPORT DOCUMENTATION PAGE

Form Approved
OMB No. 0704-0188

Public reporting burden for this collection of information is estimated to average 1 hour per response, including the time for reviewing instructions, searching existing data sources, gathering and maintaining the data needed, and completing and reviewing the collection of information. Send comments regarding this burden estimate or any other aspect of this collection of information, including suggestions for reducing this burden, to Washington Headquarters Services, Directorate for Information Operations and Reports, 1215 Jefferson Davis Highway, Suite 1204, Arlington, VA 22202-4302, and to the Office of Management and Budget, Paperwork Reduction Project (0704-0188), Washington, DC 20503.

1. AGENCY USE ONLY (Leave blank)			2. REPORT DATE 1 July 96		3. REPORT TYPE AND DATES COVERED Scientific Report #2	
4. TITLE AND SUBTITLE Path Calibration, Source Estimation and Regional Discrimination for the Middle East and Western Mediterranean			5. FUNDING NUMBERS Contract No: F19628-95-C-0093 PE62301E			
6. AUTHOR(S) C.K. Saikia, H.K. Thio, B.B. Woods X. Song*, L. Zhu* and D.V. Helmberger*			7. PERFORMING ORGANIZATION NAME(S) AND ADDRESS(ES) Woodward-Clyde Federal Services 566 El Dorado Street, Suite 100 Pasadena CA 91101-2560			
8. PERFORMING ORGANIZATION REPORT NUMBER WCFS-R-96-02			9. SPONSORING/MONITORING AGENCY NAME(S) AND ADDRESS(ES) Phillips Laboratory 29 Randolph Road Hanscom AFB MA 01731-3010			
10. SPONSORING/MONITORING AGENCY REPORT NUMBER PL-TR-96-2307			11. SUPPLEMENTARY NOTES *California Institute of Technology Seismological Laboratory 252-21 Pasadena CA 91125			
12a. DISTRIBUTION/AVAILABILITY STATEMENT Approved for public release; distribution unlimited.				12b. DISTRIBUTION CODE		
13. ABSTRACT (Maximum 200 words) In our efforts to calibrate regional crustal paths and upper-mantle teleseismic effects for the Middle East and North Africa we have extended the coverage to include the Western Mediterranean and North Africa, a region of sharp lateral variations in the crustal waveguide. Such calibration is for use in regional magnitude corrections and path attenuation relations. We have established a regionalized zonation of surface wave paths at longer periods ($T > 15$ secs) and presently have a first-order working model for PnI propagation across old oceanic paths. In the area previously calibrated -- centered about the Pamir-Hindu Kush region, and covered by the IMS β -stations NIL and AAK, we have analyzed the performance of our source location and characterization methods to smaller ($4 > M_L > 3$) earthquakes using data from co-located or nearby temporary arrays. We establish from this analysis that two broadband three-component stations can provide useful location and depth estimates for small regional events with few (1 or 2), if any, teleseismic observations. A serendipitous result of this work is a depth estimator based on a signal's S-wave complexity. This technique is also complimentary to the short-period:long-period ($E_{sp-Pz}:E_{lp-3}$) discriminant. In regions with deep seismicity, mantle earthquakes have						
14. SUBJECT TERMS Waveform Modeling Master Events 1-D Crustal Structure Seismic Monitoring Relocation Seismology Western Mediterranean Path Calibration Discrimination					15. NUMBER OF PAGES 214	
16. PRICE CODE						
17. SECURITY CLASSIFICATION OF REPORT Unclassified	18. SECURITY CLASSIFICATION OF THIS PAGE Unclassified	19. SECURITY CLASSIFICATION OF ABSTRACT Unclassified	20. LIMITATION OF ABSTRACT SAR			

Unclassified

SECURITY CLASSIFICATION OF THIS PAGE

CLASSIFIED BY:

DECLASSIFY ON:

13. Abstract (Continued)

$E_{sp-Pz}:E_{lp-3}$ ratios characteristic of explosions (whereas crustal earthquakes have lower energy ratio values). Thus, a technique to differentiate the two is of considerable importance. The calibration and performance analysis of the $E_{sp-Pz}:E_{lp-3}$ discriminant itself has been extended to the Western Mediterranean/North Africa region too, as well as to the IMS β -station ABKT in Turkmenistan. Because of short-period body-wave scattering across oceanic paths in the Mediterranean, events are depleted in energy in this phase relative to surface waves. Consequently the regional measuring threshold for Pnl or turning P-waves is higher than for surface waves, and the $E_{sp-Pz}:E_{lp-3}$ ratio vs. distance curves are depressed relative to the other regions.

SECURITY CLASSIFICATION OF THIS PAGE

Unclassified

TABLE OF CONTENTS

1. Introduction	1
2. Pamir-Hindu Kush Region	3
2.1 Review of Regional Modeling (Master Events)	8
a) Method and regional velocity model	8
b) Focal depths and source mechanisms	9
c) Event relocation	16
d) Lateral variation of shallow structure	17
e) Results from two stations	21
3. Event Trigger Algorithm and Source Location	23
3.1 Estimation of P and S Travel Times Using Detection Algorithm	24
3.2 Approximate Epicentral Distance and Regional Magnitudes	28
3.3 “Waveform Complexity” as a Depth Estimator	34
3.4 Relocation of Events Using Two Stations	40
4. $E_{sp-Pz}:E_{lp-3}$ Ratio Discriminant for the Middle East - Further Analysis	48
4.1 Work in Progress Relating to the $E_{sp-Pz}:E_{lp-3}$ Ratio:	62
5. The Western Mediterranean	63
5.1 Regional Tectonics	63
5.2 Historic Seismicity	65
5.3 Seismic Structure from Previous Work	66
5.4 Data and Surface Wave Analysis	67
5.5 Preliminary Structure	78
5.6 Regionalization	78
5.7 Moment Tensor Solutions	82
5.8 P_{nl} Propagation	91
5.9 Source Estimation Using Whole Waveforms	96
5.10 $E_{sp-Pz}:E_{lp-3}$ Ratio Discriminant Results for the Western Mediterranean	99
5.11 Discussion and Future Work	107
6. Conclusions and Recommendations	107
References	111
Appendix	117

1. Introduction

To monitor the Comprehensive Test Ban Treaty (CTBT) at the kiloton level requires locating and identifying seismic events down to magnitude 4. Since events at this magnitude generally can only be detected at a few teleseismic arrays, the basic IMS must incorporate regional data into its source location and characterization procedures. This data displays strong local characteristics with its own magnitude scale M_L , and needs to be calibrated with respect to teleseismic measurements before it can be used routinely by the IMS. Monitoring still smaller events appropriate for possible evasion scenarios becomes exclusively a local seismic situation (Murphy *et al.*, 1995). Thus, the relationship between M_L , M_S , m_b , have a strong regional dependence which needs to be addressed on a global scale. We will discuss these issues in our study area of the extended Middle-East, ranging from the western Mediterranean to India. The region forms the boundary between several plates which have had a complex tectonic history. This situation produces a richness in earthquake depths and styles, and distinguishing them from explosions often proves difficult.

One of the most successful and proven methods to discriminate seismic events is the classical m_b : M_S comparison for which explosions have a significantly smaller surface-wave magnitude (M_S , measured from the peak long-period surface wave amplitude) than an earthquake with the same body-wave magnitude (m_b , measured from the peak short-period P-wave amplitude). The physical explanation of this effect is that the source spectrum of an earthquake is richer in long-period energy than that of an explosion. This effect is attributable, in part, to the difference in characteristic source dimensions. An earthquake ruptures over a plane which is large in size relative to the cavity that an underground explosion creates. One can also think of this source difference in terms of the source time function which tends to be long for earthquakes and short and impulsive for explosions. Stevens and Day (1985) found that other factors relating to these differences in spectral content involve source mechanism and material source properties.

Although these conclusions were reached by studying teleseismic data, they become particularly obvious when viewing modern broadband seismograms as in Figure 1a for regional recordings of the JVE Kearsarge ($M_L = 5.6$) and the Little Skull Mountain earthquake ($M_L = 5.7$). For each event, the broadband signals (top trace) are convolved with classical analog instruments operated at Caltech since the beginning of NTS testing. To the right of each trace is given the peak amplitude. All instruments have a gain equal to 1. Records from the many NTS events were used extensively in

Woods and Harkrider (1995) and Woods *et al.* (1993) in establishing the relationships between magnitude scales for moderate-size and small explosions. The peak WASP amplitudes are used to calculate M_L . One obtains a ratio of long-period surface wave amplitude (vertical component) to short-period body-wave amplitude of about 3 for Kearsarge and about 20 for the earthquake; in short, an order of magnitude larger surface waves for the earthquake as compared to the explosion relative to short-period amplitudes.

As discussed in Woods *et al.* (1993) this difference between earthquakes and explosions persists as far down in magnitude as $M_L = 4$ where it becomes difficult to see surface waves from explosions. Note that it is often possible to see surface waves for earthquakes smaller than this especially if they are shallow. Song and Helmberger (1996), reporting on Northridge aftershocks as recorded on the TERRAscope network, find that shallow events have relatively low-stress drops and strong surface waves compared to deep earthquakes of the M_L . Thus, the ratio of short-period to long-period energy at regional distances appears quite useful in discrimination, especially in tectonic regions where earthquakes are plentiful.

A number of research projects at the 18th seismic research symposium on monitoring a CTBT (1996) have used this physical distinction to develop global monitoring tools. For example, Stevens and McLaughlin (1996) display encouraging results of m_b (NEIC) and m_b (IDC) *vs.* moments derived from regionalization to this end. The weakest link in this approach is in obtaining good estimates of short-period magnitudes for events less than about $m_b = 4.2$ depending on region where variability in earth structure makes m_b ($\Delta < 30^\circ$) difficult. This problem has been discussed at length by Denny *et al.* (1987), Taylor *et al.* (1989), and many others.

Extensive regionalization of surface wave data appears to be possible as discussed by Levshin *et al.* (1996) and others. However, to use this information at small magnitudes still requires some assumption about the source, see Patton and Walters (1993). Woods and Helmberger (1996) circumvent this problem by simply plotting the direct short-period energy in the extended P-wave window (P_{nl}) against the accumulated surface wave energy ($E_{sp-Pz} \cdot E_{lp-3}$) summed over three components, or the ratio of (1Hz) P-wave to (.14 to .05 Hz) surface wave energy. This measure is close to the teleseismic m_b *vs.* M_s empirical approach used so successfully for many years by AFTAC and confirmed by other research studies.

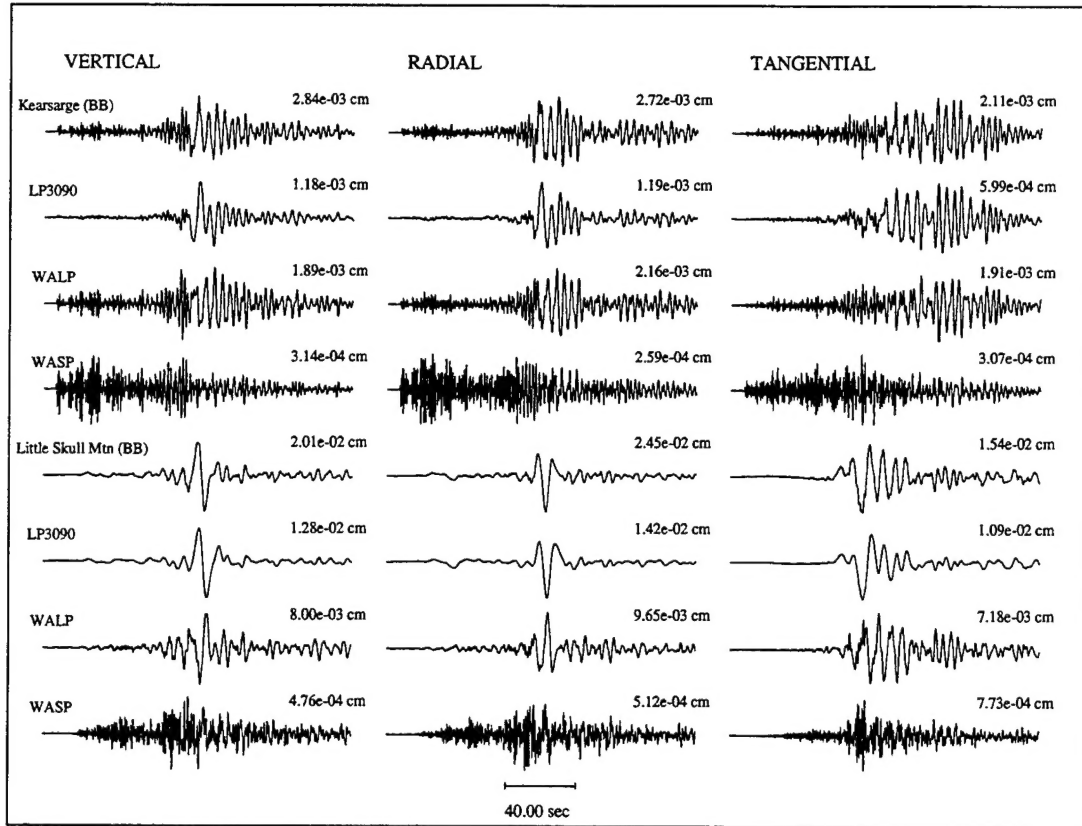
Figure 1b (Woods and Helmberger, 1996) displays a plot of this ratio for a population of NTS explosions and earthquakes from the southwestern U.S. where the ratio has been multiplied by a measure of short-period magnitude, M_L in this case, as a normalizing scale factor. This feature helps separate the two populations by providing a rough correction for expected earthquake-size scaling.

One problem with this particular discriminant is that deep earthquakes generally have high energy ratios relative to shallower earthquakes as discussed in our previous scientific report #1 (Saikia *et al.*, 1996) regarding Hindu-Kush events. This feature is obviously caused by the lack of fundamental-mode surface waves for deep earthquakes as is well-known for the $m_b \cdot M_S$ discriminant (Marshall and Basham, 1972). Thus, establishing methods to constrain relatively deep events ($h > 33$ km), becomes a key part of this discrimination process, as well as for the more general problem. The magnitude of this problem can be seen in Figure 2 which displays seismicity for the Middle-East. Note that there are numerous pockets of deep seismicity scattered throughout the region. Unfortunately, most of these events are small so that they can only be seen regionally and calibration of path effects become essential in analyzing waveforms for such events.

To address these issues of source location and discrimination we have broken the study into several sections. Section 3 deals with refining the calibrations in the Hindu-Kush region in terms of locating events down to relatively small magnitudes. We introduce methods for locating and estimating the source parameters of moderate-sized events using sparse data from two stations. The usefulness of the $E_{sp-Pz} : E_{lp-3}$ discriminant for treating events in this region is discussed in Section 4. Section 5 deals with the calibration of paths in the western Mediterranean covering the regions of Spain, Morocco and northern Algeria and the effectiveness of the energy ratio discriminant there.

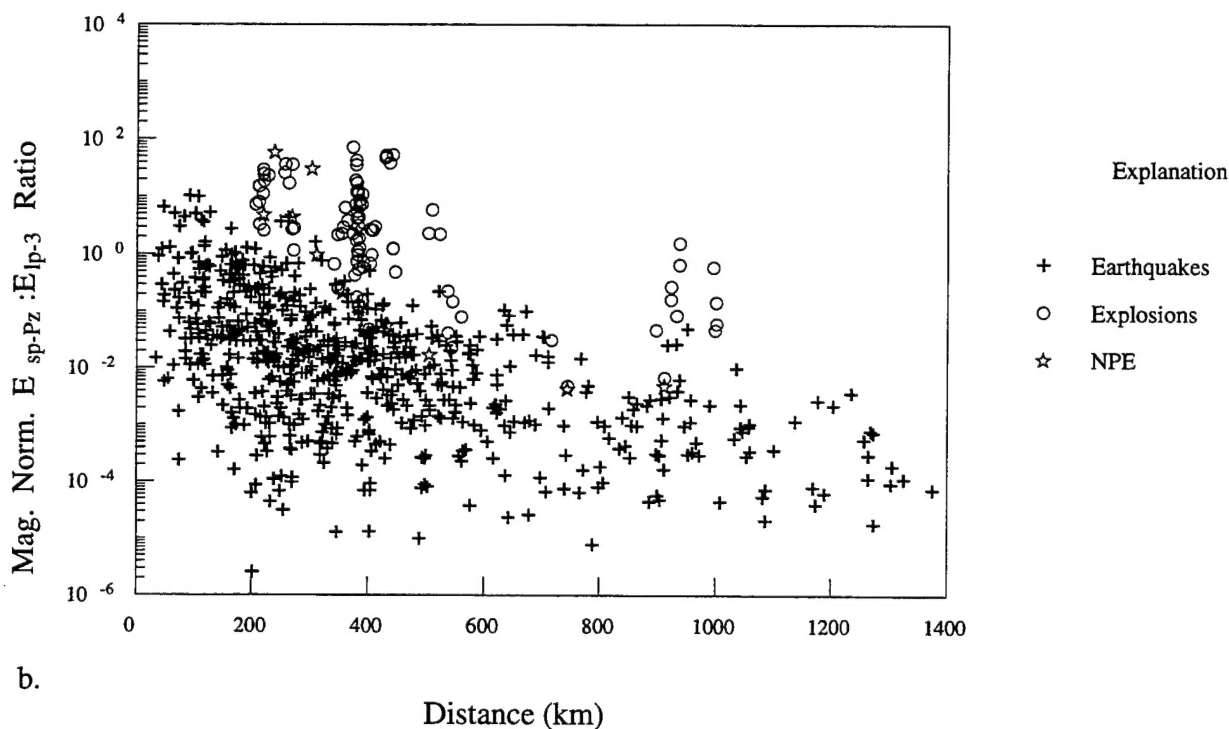
2. Pamir-Hindu Kush Region

Most intermediate-depth and deep earthquakes occur inside subducting slabs which are cold and apparently strong enough to accumulate the stress necessary for brittle failure. There are only a few places in the world where intermediate-depth seismicity is not directly related to recent subduction, several of these zones are located along an alignment from Spain to Tibet. One of these is the Pamir-Hindu Kush region where the subduction of oceanic lithosphere is believed to have



a.

Mag. Norm. $E_{sp-Pz} : E_{lp-3}$ Ratio vs. Distance



b.

Distance (km)

Figure 1. a) Comparison of PAS records for the Kearsarge explosion (top 4 traces) and the Little Skull Mtn. earthquake (bottom 4 traces). The top row of traces in each event suite is the broadband displacement, below which are some records convolved with three historical instruments. The instrument ID is given to the far left of the traces.
b) Magnitude-normalized $E_{sp-Pz} : E_{lp-3}$ Ratio vs. distance for TERRAscope data.

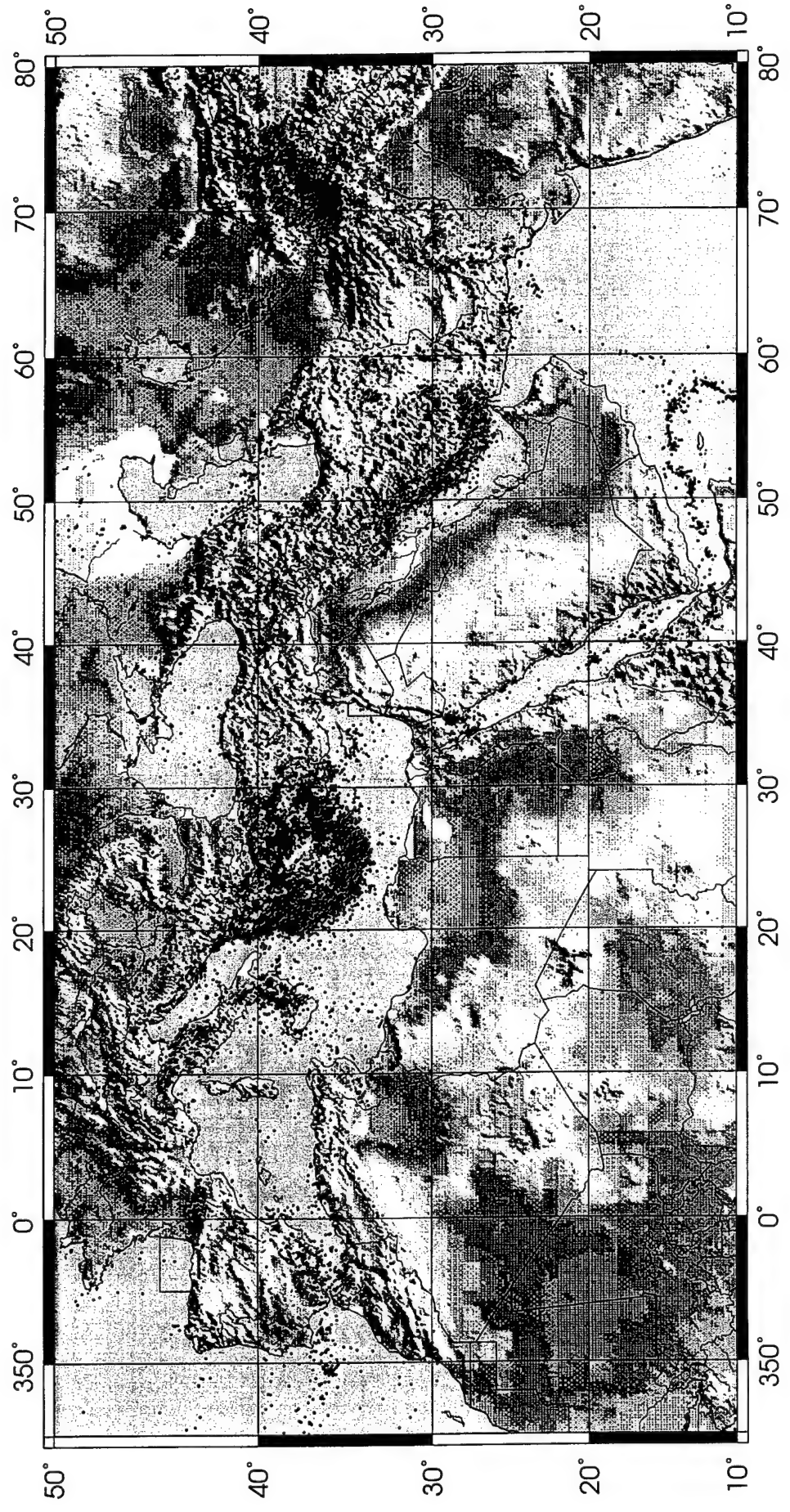


Figure 2. Seismicity map of the Middle-East and North Africa, showing epicenters from the ISC catalog. The events are color-coded according to their depth. Red (0-33 km), green (33-100 km), blue (100-500 km) and black (> 500 km).

ended about 40 Ma ago (Molnar and Tapponnier, 1975), but intensive intermediate-depth seismic activity is nonetheless an outstanding feature in the seismicity of the region.

Several detailed studies have shown that the SW-NE Pamir-Hindu Kush intermediate-depth seismic zone is composed of two separate segments (Figure 3): an eastern segment beneath the Pamir and a western segment striking EW beneath the northern end of Hindu Kush where the seismicity is more intense and extends deeper (Billington *et al.*, 1977; Roecker *et al.*, 1980; Chatelain *et al.*, 1980). Correspondingly, two narrow Wadati-Benioff zones were defined, with the one under the Hindu Kush dipping to the north and the other, under the Pamir, dipping to the southeast. These studies suggest dual interpretations of either a single contorted slab (Billington *et al.*, 1977) or two distinct slabs with opposing subduction directions (Burtman and Molnar, 1993; Fan *et al.*, 1994).

Since most direct evidence of subducting slabs comes from the earthquake distribution, accurate hypocenter locations are crucial to resolving the shapes of the slabs and their relation to surficial geology. Focal mechanisms can provide additional information about the stress regime near the source. Unfortunately, the quality of earthquake locations in this remote area using global network has not been satisfactory, largely due to the incomplete station azimuth coverage. Although earthquakes occur frequently in the Pamir-Hindu Kush region, most of them are small to moderate in size and therefore are not recorded well at teleseismic distances, if at all.

One aim of the installation of the new broadband global network is to monitor local seismicity. In this study we establish the ability of two permanent IRIS stations, NIL in Pakistan and AAK in Kyrgyzstan, to locate and determine source characteristics of events in the Pamir-Hindu Kush region. AAK is one of the stations of Kyrgyzstan Regional Network (KNET). In the winter of 1992 a temporary PASSCAL array (PAKN, see Sandvol *et al.*, 1994) was deployed in northern Pakistan which is very close to NIL. To address this data, we have divided this topic into two parts. Section 2.1 reviews the work done on the master events and presents a procedure for estimating the source parameters for future events ($M_w > 3.8$). Section 3 discusses a procedure for estimating the location and depths for small events ($M_w < 3.8$ or only observable at short-periods) using the arrays in combination with a single 3-component station.

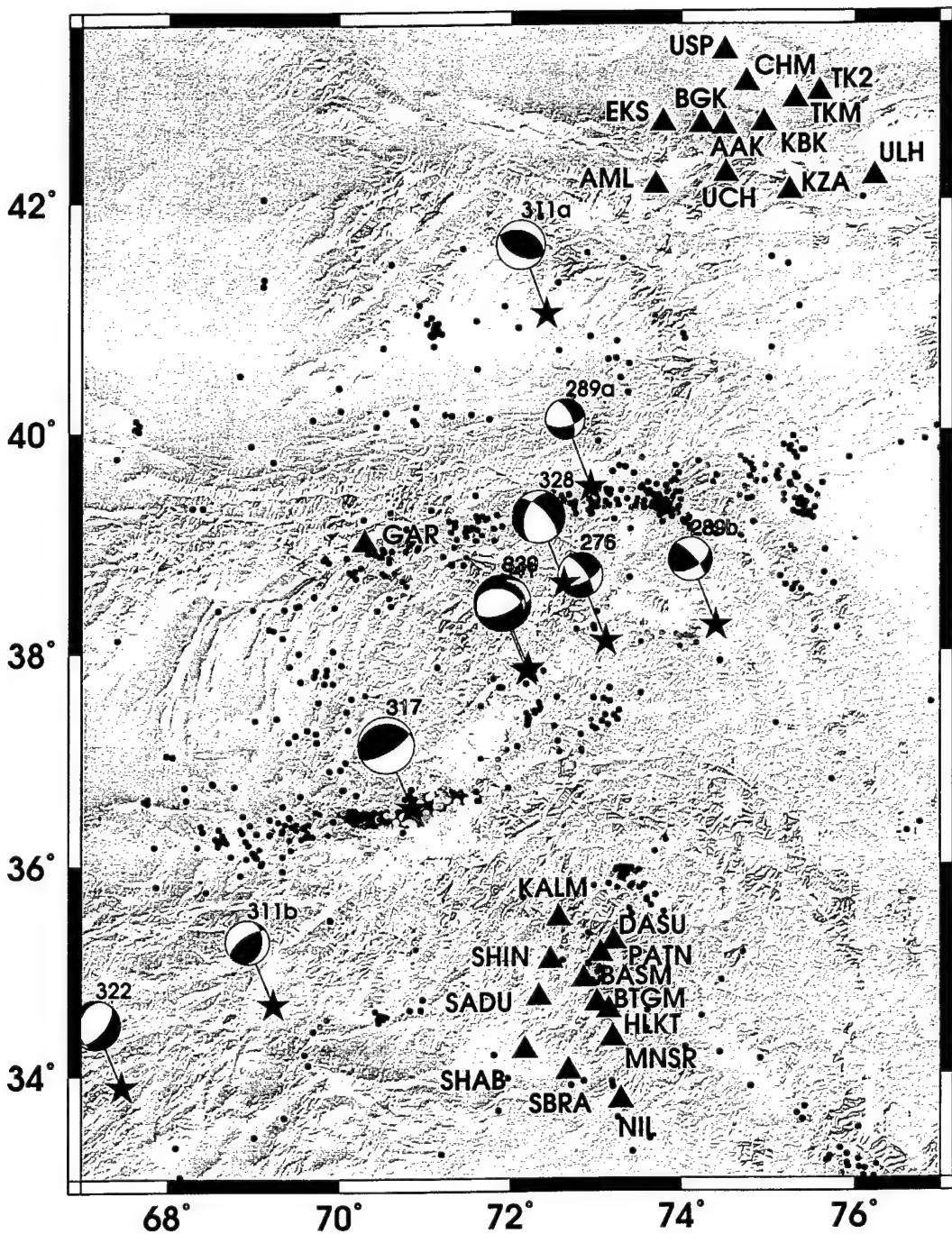


Figure 3. Map of the Pamir Hindu-Kush region showing the stations of the KNET and PAKN arrays and the 10 events studied in this section (stars). Events reported by the ISC between 1964 and 1986 are plotted with colors varying from blue (300 km deep) to red (0 km). These events all have more than 30 stations reporting and the location errors are less than 10 km as listed in the ISC catalog. The focal spheres are from the waveform inversions in this study, red ones for crustal events and blue for mantle events.

2.1 Review of Regional Modeling (Master Events)

To calibrate the paths of events to AAK and NIL, we selected 10 moderate magnitude events (m_b 4-5.5, see Table 1) which occurred in the time window of the PAKN deployment, determined the fault parameter of the 10 events, and relocated them using the two arrays. Then we repeated the same process using only two stations. Since NIL was not installed in this time period, a nearby station from the PAKN array, SBRA, was used as a surrogate together with AAK when performing the two-station analysis. We found that they gave results compatible to those using the two arrays. Thus, future events in the Pamir-Hindu Kush region can be processed routinely using stations AAK and NIL.

a) Method and regional velocity model

Zhao and Helmberger (1994) developed a "cut and paste" (CAP) source estimation technique using broadband regional waveforms. The method breaks the whole waveform into P_{nl} and surface wave segments and inverts them independently. It allows time shifts between the seismogram and synthetics. This relaxation of timing proves quite helpful when only imperfect velocity models and inaccurate event locations are available at the start. Recently we improved the method by redefining the waveform misfit error to preserve amplitude information in the inversion so the focal depth and source mechanisms can be better constrained (Zhu and Helmberger, 1996b).

The velocity model used for the study area is listed in Table 2. This simple 1-D velocity model was developed from teleseismic receiver functions in the adjacent Tibet plateau (Zhu *et al.*, 1993; Zhu and Helmberger, 1994). We believe that, to the first order, the Pamir and Tibet have similar crustal structures. Both are young plateaus produced by India-Eurasia collision and have experienced similar tectonic processes. Seismic refraction data indicate a thick crust of up to 75 km under the Pamir (Lukk *et al.*, 1983), which is close to the average crustal thickness of the Tibet plateau.

The vertical displacements of the 3 fundamental faults at different depths are displayed in Figure 4. The corresponding tangential components are quite simple and have been presented in Zhu and Helmberger (1996a). For crustal events, the amplitudes of Rayleigh waves are very large for shallow events and so the amplitude ratio between them and P_{nl} or Love waves is quite diagnostic in determining focal depth. As the source moves into the mantle, the high-frequency signals trapped

by the crustal wave-guide disappear. The waveforms become increasingly simple as the focal depth increases, essentially reducing to just a P-wave and SV-wave, as shown in the figure. However, there is still important information about polarity and relative strengths of the phases. We will discuss this in detail in the next section.

b) Focal depths and source mechanisms

The velocity records of the 10 events at the two arrays were integrated into displacement and band-passed between 5 to 100 secs. These waveforms were then inverted for source mechanisms and depths using the CAP method. The results are listed in Table 3 along with the Harvard CMT solutions for the 5 largest events. These events were discussed at length in our last report, Saikia *et al.* (1996). Our focal mechanisms agree with the Harvard ones quite well. The lower-hemisphere projections of the corresponding focal spheres are plotted in Figure 3.

One of the best recorded shallow events is the magnitude 5.1 earthquake (event 328) which occurred at about an equal distance between the two arrays. Figure 5 is a comparison of the observed and synthetic waveforms. The overall fit is excellent, in both shapes and amplitudes. Note that the surface waves (Love and Rayleigh) are about equal amplitude, indicating a mixed mechanism. The relative strengths of the two types of surface waves and the P_{nl} waves play a key role in determining the focal depth.

Figure 6 is a plot of the waveform misfit as function of source depth, and shows a well-defined minimum at 15 to 20 km for this event. Although the focal mechanism is very similar to the Harvard CMT, see Table 3, the focal depth is distinctly shallower than the Harvard depth of 43 km. For all crustal events our solutions prefer shallower depths than the ISC depths or Harvard solutions when the latter are available for comparison.

For intermediate-depth earthquakes, the waveforms become simpler with sharp P arrivals and an absence of surface waves. Figure 7 shows an example of waveform fits for one of the mantle events (event 341). An easily recognizable phase is the large amplitude long-period phase before the direct S arrival. It is actually produced by the S-to-P conversion at the free surface and then reflected to the receiver by Moho (sPmP), as discussed at length in our first report (Saikia *et al.*, 1996). After the reflection reaches critical angle, part of this P-wave travels along the Moho as a

Table 1. Locations of the events from ISC catalog

Event	Date	Origin time	Location °N/°E	Depth (km)	m_b
276	10-02-92	14 ^h 38 ^m 46.4	38.08/73.12	139	4.6
289a	10-15-92	02 ^h 42 ^m 06.7	39.24/72.80	16	4.5
289b	10-15-92	19 ^h 42 ^m 13.8	38.20/74.44	157	4.4
311a	11-06-92	07 ^h 21 ^m 56.0	41.09/72.50	21	5.1
311b	11-06-92	17 ^h 58 ^m 39.0	34.87/69.15	25	4.5
317	11-12-92	20 ^h 41 ^m 05.2	36.45/70.87	204	5.5
322	11-17-92	02 ^h 38 ^m 50.7	33.83/67.53	35	5.1
328	11-23-92	23 ^h 11 ^m 06.9	38.57/72.65	43	5.6
339	12-04-92	11 ^h 36 ^m 35.5	37.79/72.21	114	5.8
341	12-06-92	03 ^h 44 ^m 29.3	37.79/72.19	122	5.5

Table 2. 1-D velocity model of the Tibetan Plateau

Layer	Th. (Km)	V_p (km/s)	V_s (km/s)
1	4	4.70	2.70
2	60	6.20	3.50
3	-	8.14	4.70

Table 3. Focal mechanisms and relocation results.

Event	strike/dip/rake	M_w	h (km)	Δt_0 (sec)	Δr (km)	Azimuth
276	325/70/-30	4.4	150	-0.41	2	0
	330/80/-25	4.5	150	-0.62	7	89
289a	335/65/-30	3.9	5	0.25	31	22
	145/85/0	4.0	5	-0.12	30	30
289b	60/55/20	4.2	160	0.36	5	321
	60/55/35	4.2	150	0.00	2	0
311a	290/40/85	4.7	15	1.75	9	225
	290/45/80	4.8	15	1.12	11	180
	322/25/110	4.3	19			
311b	10/35/50	4.3	10	2.60	23	161
	350/40/35	4.3	10	4.51	26	172
317	60/70/80	5.5	190	0.57	11	350
	40/75/70	5.5	170	0.40	14	338
	33/77/71	4.9	188			
322	40/60/-75	4.7	10	4.35	8	320
	24/55/-94	4.7	10	4.16	9	337
	29/60/-75	4.4	33			
328	200/45/-35	5.1	15	3.16	6	345
	200/45/-40	5.1	10	3.05	89	321
	211/33/-49	4.9	44			
339	80/65/-75	5.5	110	-0.10	6	0
	50/75/-93	5.6	100	-0.17	8	57
	56/74/-85	5.1	131			
341	290/35/-55	4.8	110	0.45	4	0
	290/25/-45	4.9	100	0.20	6	14

For each event, the first line is the result using the two arrays and the second line is the result using two stations, SBRA and AAK. Harvard CMT solution, if available, is listed in the third line.

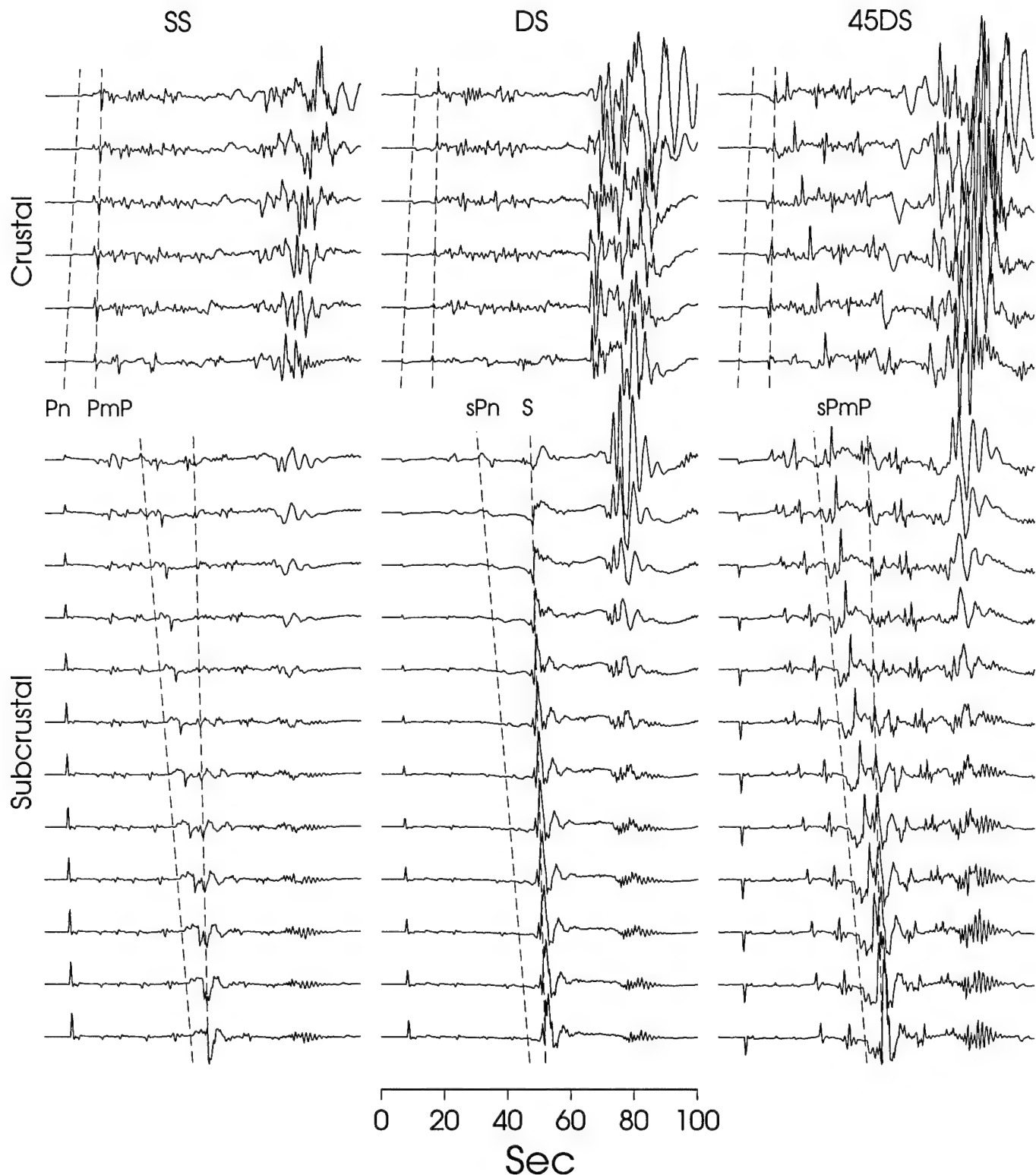


Figure 4. Vertical displacements of the 3 fundamental faults, vertical strike-slip (SS), vertical dip-slip (DS) and 45° dip-slip (45DS), at every 10 km of source depth starting at a depth of 10 km. The Moho is at a depth of 64 km for the Tibet velocity model. The amplitudes for mantle events have been multiplied by 2 to account for the velocity and density jumps across the Moho. Several phases that are discussed in the text are labeled

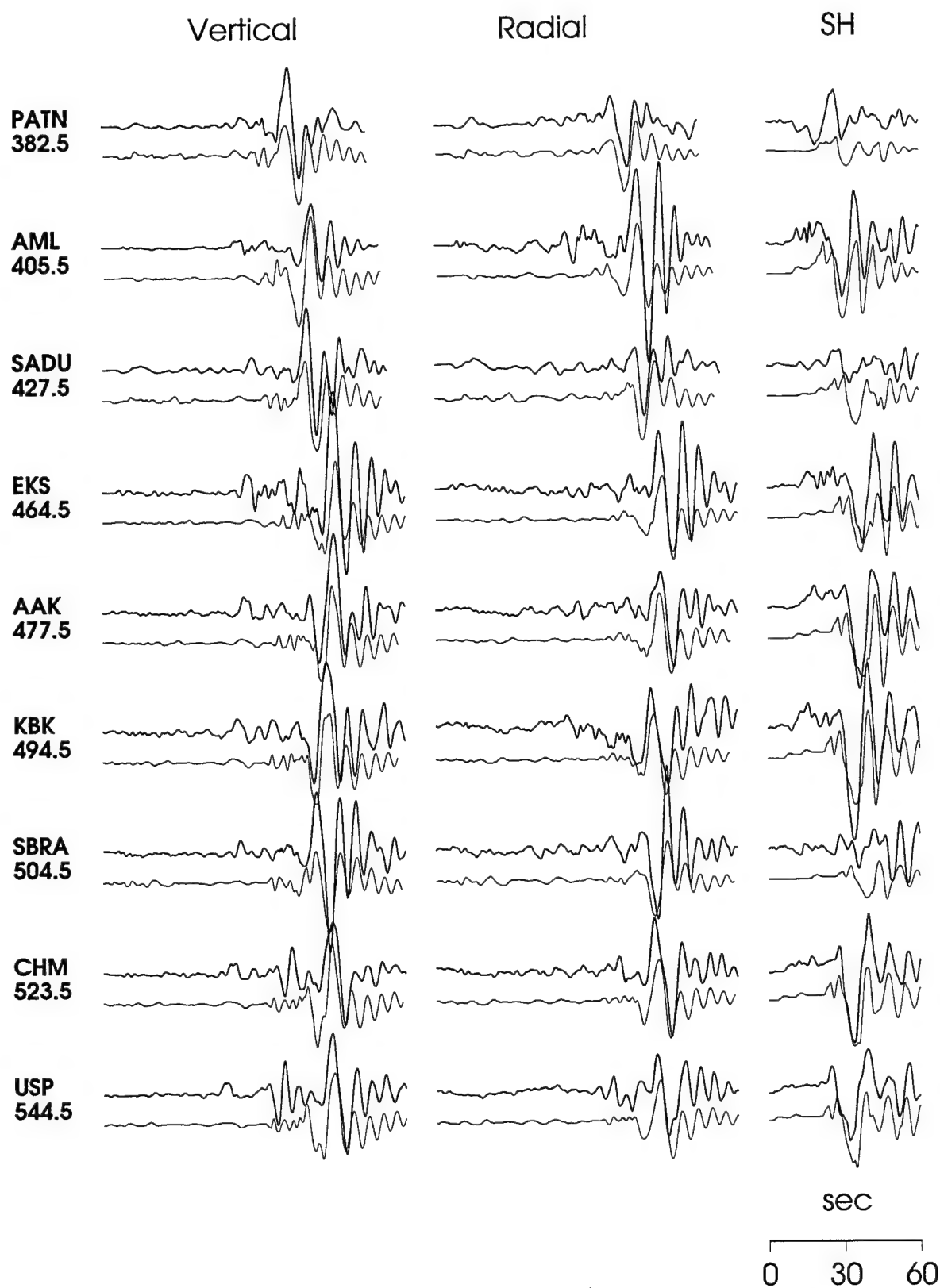


Figure 5. Waveform fits for event 328, thickened lines are the data, thin lines are synthetics using the source mechanism and depth determined from the two-array waveform inversion.

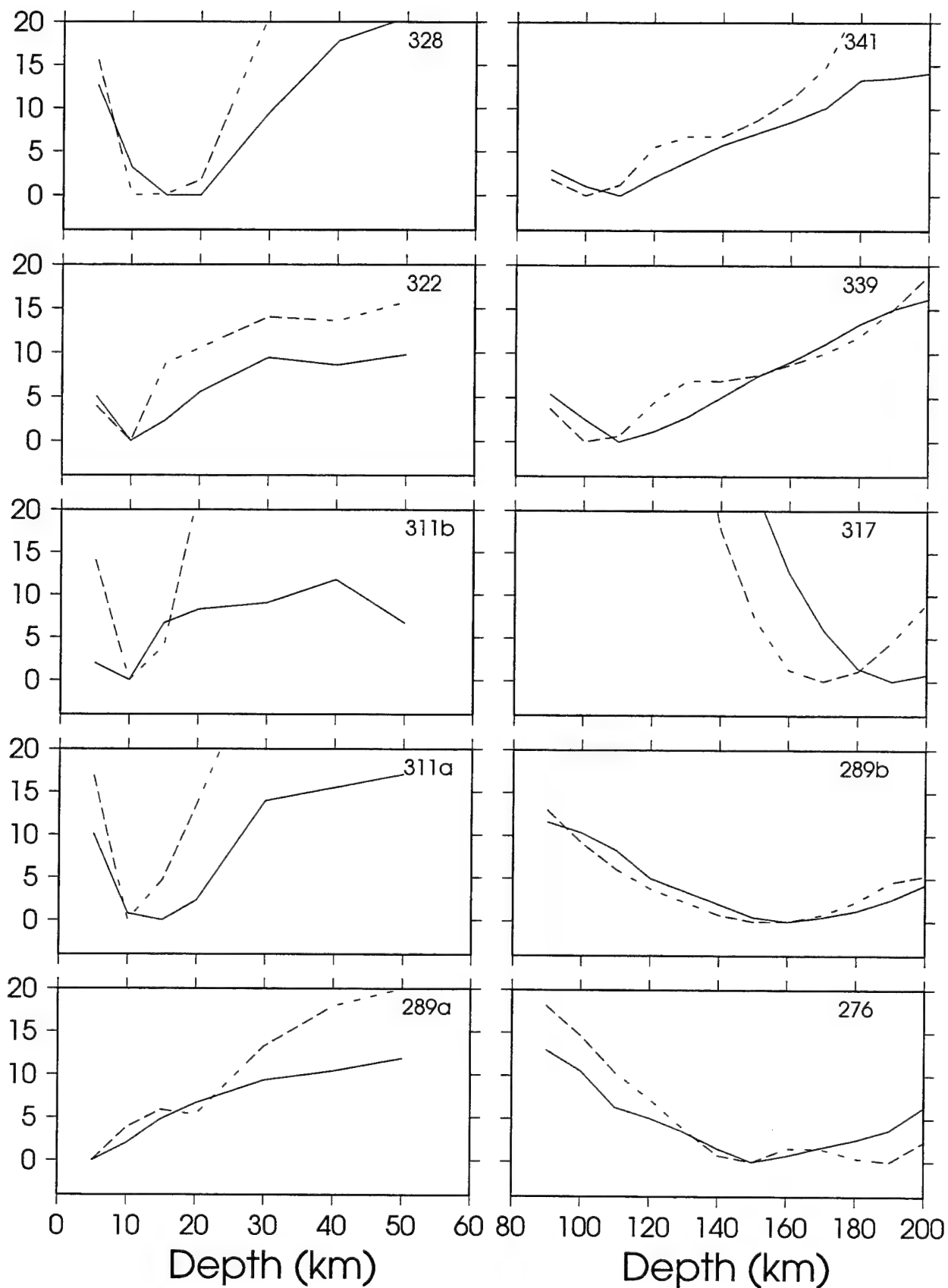


Figure 6. Waveform misfit error (vertical axes) as function of focal depth. Thick lines are from the two-array inversion and thin lines are from the two station inversion. The misfit errors for each event are normalized by the minimum value.

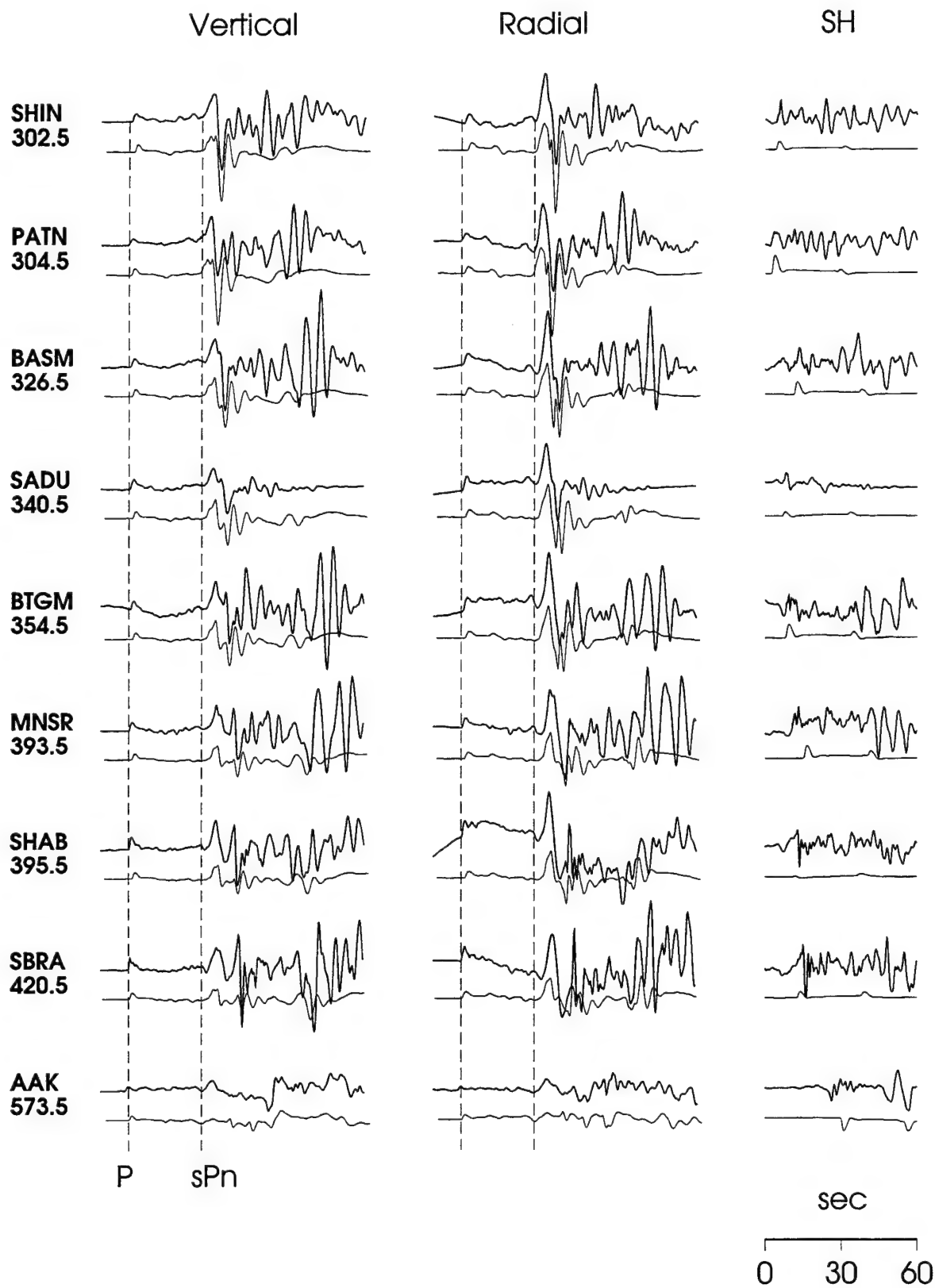


Figure 7. Waveform fits for mantle event 341, thickened lines are the data, thin lines are synthetics using the source mechanism and focal depth determined from the two-array waveform inversion. The two parallel dashed lines show the arrivals of direct P and sPn .

head wave (sP_n) which has similar apparent velocity to direct P. The shear-coupled P-waves at regional distances from intermediate-depth earthquakes for this region have been noted earlier by Zhao and Helmberger (1993). Recently they are reported in many places (Singh *et al.*, 1995; Zandt *et al.*, 1996). Our data show that they are commonly observed in the Pamir-Hindu Kush region. Because of the strong amplitude of this phase and small move-out with distance with respect to the direct P, the time separation between P and sP_n is ideal for controlling focal depth.

Because of the "cut and paste" nature of our source estimation technique, the time separation between P and SV waves is not employed to constrain depth. This causes no difficulty in inverting crustal events because their depths are mainly controlled by the relative amplitude of surface waves and P_n . But since the time separation between P and sP_n is so important for depth determination of mantle events, we perform the inversion in two steps. First the whole seismogram is broken down into P and SV segments and inverted for source mechanism and depth. Then we fix the mechanism and use the whole waveform to search for a more precise focal depth, controlled by the S-P separation. Note that this depth estimate becomes closely tied to the velocity model. The misfit errors as function of depth for the mantle events are also presented in Figure 6. Well-defined minima are observed for these deep events, although they are not quite as well defined as for the crustal events.

c) Event relocation

After the focal depths are established from waveform inversion, we can now relocate events horizontally using their first-arrival times. By fixing the source depth, the strong trade-off between depth and origin time can be avoided. The relocation is also done using a grid search method whereby we minimize the object function defined by

$$\Phi(x,y) = \sqrt{\frac{1}{N} \sum_{i=1}^N (\delta T_i - \bar{\delta T})^2 + \lambda \Delta r}, \quad (1)$$

where δT_i is the travel time residual of first-arrival at station i. The average residual over all stations, $\bar{\delta T}$, is subtracted to remove the uncertainty of origin time. Δr is the distance between the new location and the original location. The weighting constant, λ , can be chosen in a range of 0 to 0.01 sec/km.

For each event, an area of 1° by 1° centered at its ISC location is grid-searched. The relocation results are listed in Table 3. It can be seen that for all deep events and large shallow events ($m_b \geq 5$) the differences between the ISC locations and the new locations are less than 10 km. However, small shallow events can move significantly in their locations. In this study, there is up to 30 km movement of relocations for small shallow events (see events 289a and 311b). This is not surprising because deep events and larger shallow events usually have sharp onsets at teleseismic distances which can be easily picked, see Figure 8. The Chiang Mai array in Thailand is located at the regional-teleseismic cross-over distance near 30° . Since the upper-mantle path is mainly shield (Zhao and Helmberger, 1993), we can expect to see a late arriving upper-mantle phase arriving about 15 secs back for shallow events, see LeFevre and Helmberger (1989). The shallow events indicate such a phase but they are complicated by the depth phases pP, and sP, see our previous scientific report (Saikia *et al.*, 1996). While the first arrival is easily identified for the top trace (deep event) and larger crustal events, they become obscure as the M_w decreases. Thus, small shallow events often show emergent onsets as indicated in the ISC bulletins and the time picking errors can be relatively large.

The largest relocation (31 km) occurs for event 289a which is the smallest ($M_w = 4$) among the 10 events. Before the relocation, it shows unanimously earlier P arrivals (δT of more than -4 sec) throughout the PAKN array and later P arrivals (δT of +3 sec) at KNET. Figure 9 shows the contour diagram of the object function. As a result of relocation, the event is moved beneath the northern slope of the Trans-Alai Range (Figure 10). The waveform inversion indicates that the event is very shallow (less than 5 km, see Figure 6) which suggests that there should be some relationship of this new location to surface faulting. In fact, there is clear evidence of Quaternary and Holocene faulting and folding along the northern margin of the Trans-Alai Range (Nikonov *et al.*, 1983; Burtman and Molnar, 1993). Numerous landslides, rockfalls and avalanches, as well as tension cracks are found in this area, which can be associated with preinstrumental earthquakes (Nikonov, 1988). Thus, the new epicenter appears quite acceptable at this new location.

d) Lateral variation of shallow structure

The paths of propagation from our master events to KNET and PAKN arrays traverse more than one major tectonic block. These complications did not disrupt our waveform modeling success using the CAP approach which allows some time shifting between surface waves and body waves.

WAVEFORM OF PAKISTANI EARTHQUAKES (1992)
 CHIANG MAI ARRAY, THAILAND
 Station: CM05 (Approx:30 Deg)

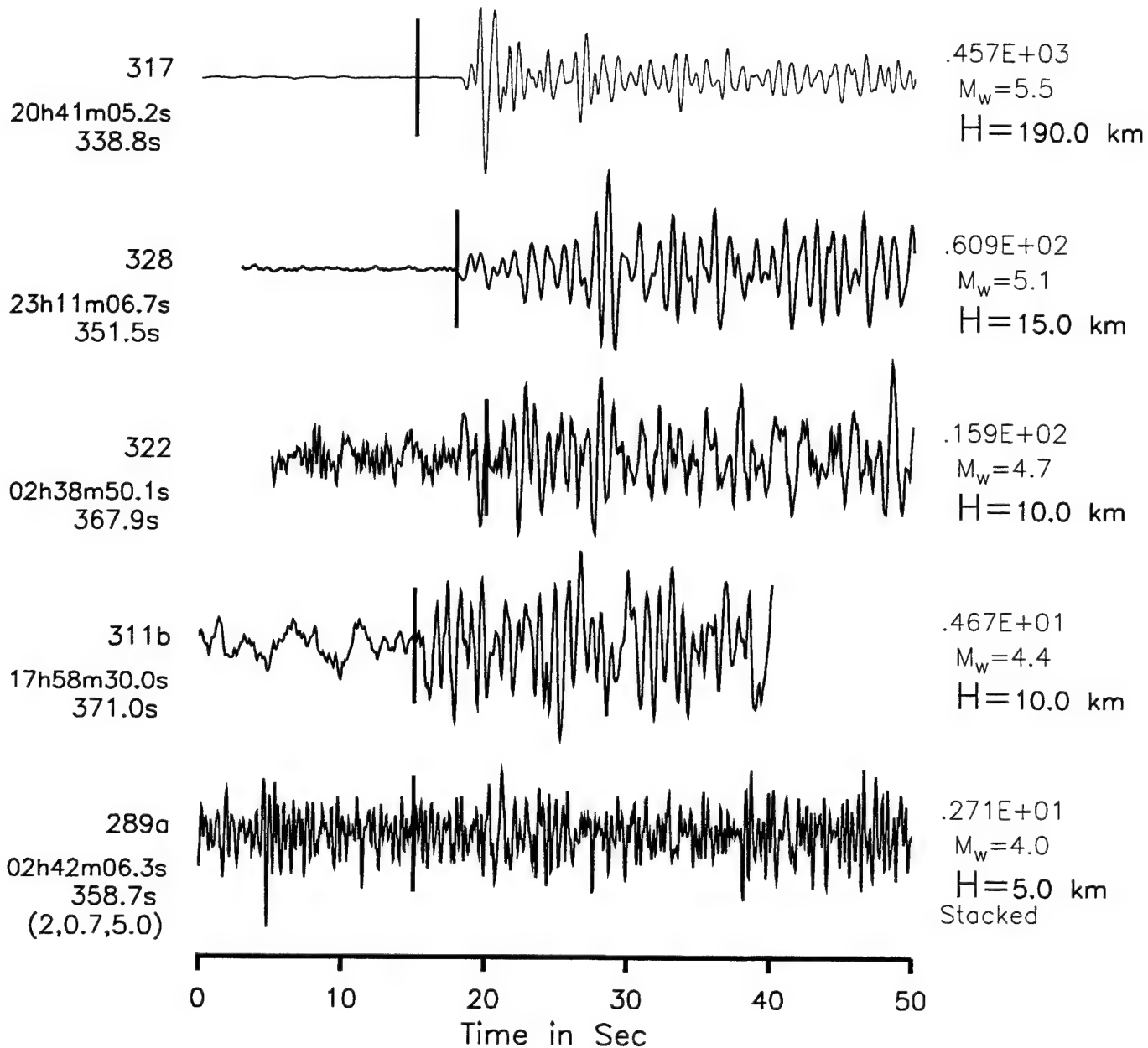


Figure 8. Seismograms recorded at the CM05 station of the CHG array from several Pakistani events. These waveforms are shown as a function of depth (H) and moment magnitude (M_w). The solid vertical lines are the arrivals of P waves according to the ISC bulletin.

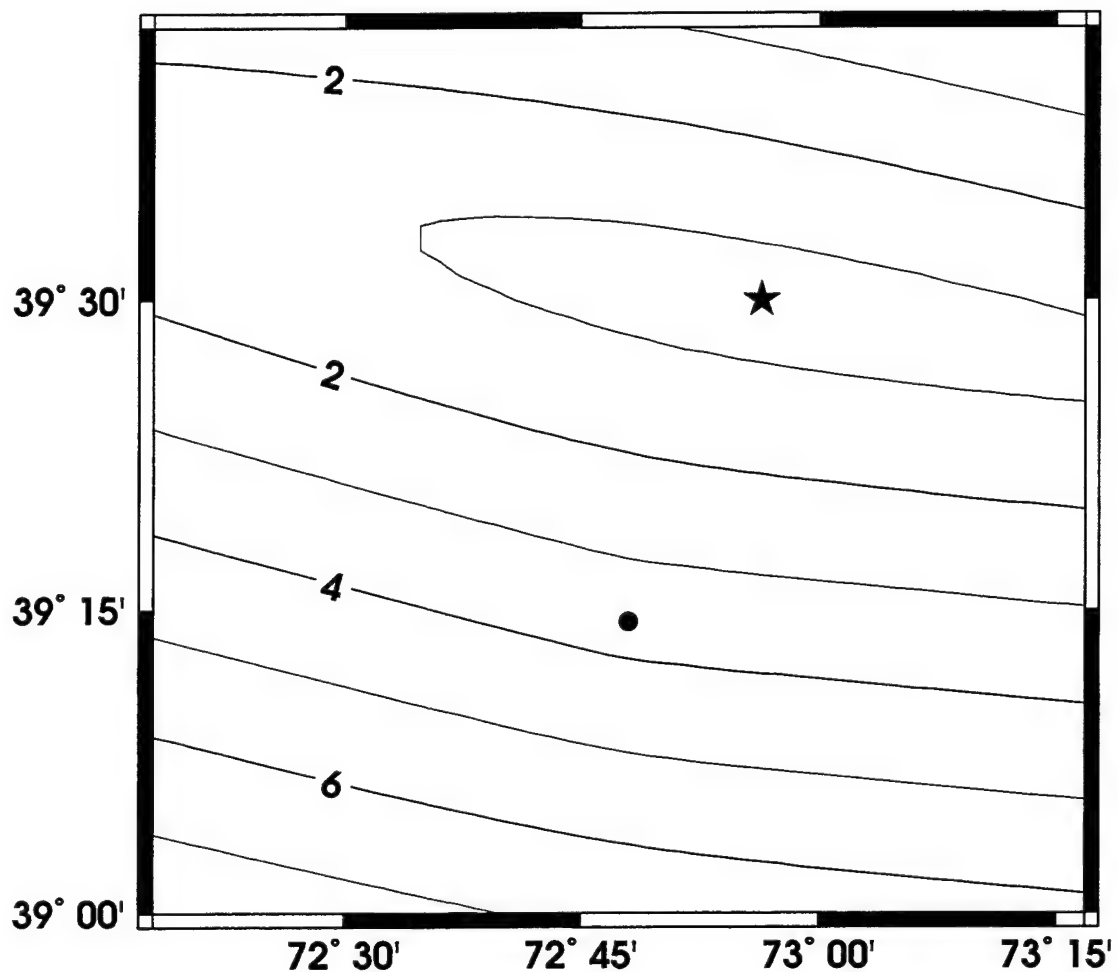


Figure 9. Contour diagram of the relocation objection function for event 289a.
The dot is the ISC location and the star is our new location.

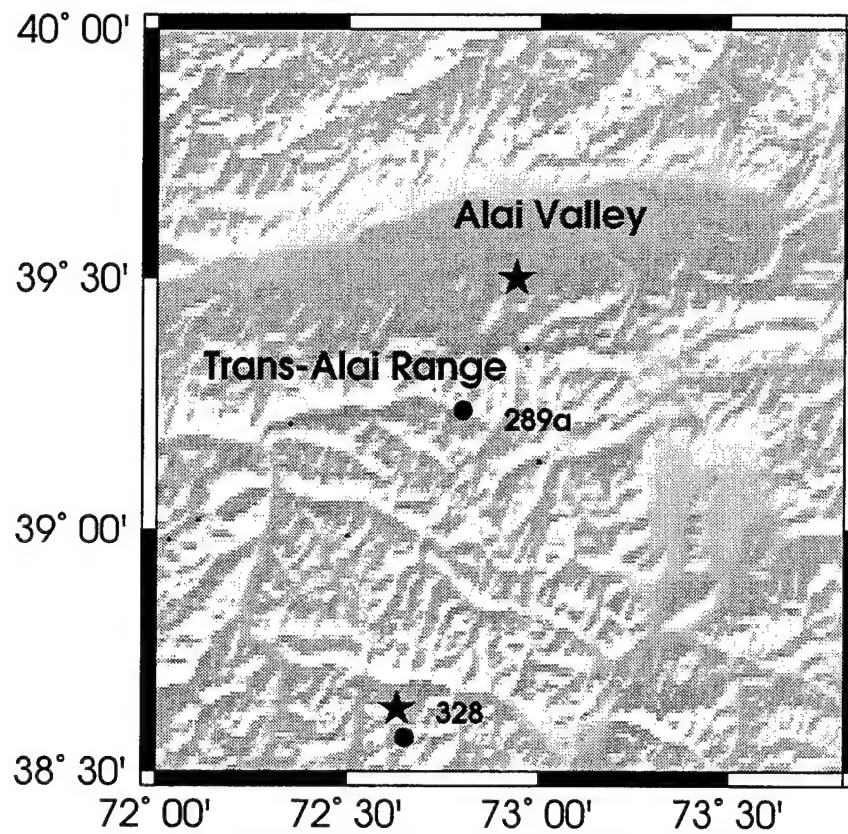


Figure 10. Comparison of geographic locations of the ISC epicenter (dot) and the relocation epicenter (star) for event 289a. The relocation moves the event from the southern slope of the Trans-Alai Range onto its northern margin where the Trans-Alai Range Thrust Fault runs through. The relocation result for event 328 is also shown for comparison.

Generally, P_{nl} is more stable than the surface waves which are easily affected by shallow structure. Figure 11 shows the velocity anomalies of Love waves as measured by the time shifts produced by the waveform inversion. Red and yellow paths indicate lower velocities than predicted by the 1-D model, and blue and green indicate faster paths. We can see that the Love waves are faster for paths within the Pamir, while paths associated with the Tien Shan or traversing the northern Pakistan basin are slower. There are also complications to this simple pattern. Paths from events 289a and 328 to KNET display contradictory anomalies which seems difficult to interpret. However, as we have shown before, event 289a is very shallow and located at the southern edge of the Alai Valley (Figure 11), so the Love waves going north are strongly influenced by the low velocity sedimentary valley. On the other hand, event 328 is deeper (15 to 20 km) under the mountainous Pamir and less affected by this shallow structure. These observations are consistent with numerical sensitivity result (Song *et al.*, 1996) which shows that the timings of surface waves are controlled mainly by the S velocity above the source.

e) Results from two stations

Both KNET and PAKN are small aperture, broadband, three-component arrays. The successful source retrieval and relocation from these two arrays suggests that it is also possible to accomplish the same results by using only two stations, one from each array. This is of great practical significance because although PAKN is a temporary experiment, a new IRIS station, NIL, was installed near station SBRA in 1993 (Figure 3). In addition, one of the KNET stations, AAK, is also a permanent IRIS station. If we can calibrate the propagation paths to station AAK and SBRA using our 10 events, we will be able to process events in this region routinely in the future, assuming that NIL will perform similarly to SBRA.

As a test, we repeat the same waveform inversion and relocation procedure applied above but using only stations AAK and SBRA. The results are summarized in Table 3. A comparison of depths determined by two-array and two-station can be found in Figure 8. Quite encouragingly, the two-station inversion gives very similar results as the two-array inversion.

A comparison of our results with the ISC catalog shows that the focal depths for the mantle events are compatible, but they can differ by as much as 30 km for the crustal events. This is not surprising because the ISC catalog relies heavily on the determination of depth phases (pP, etc) to

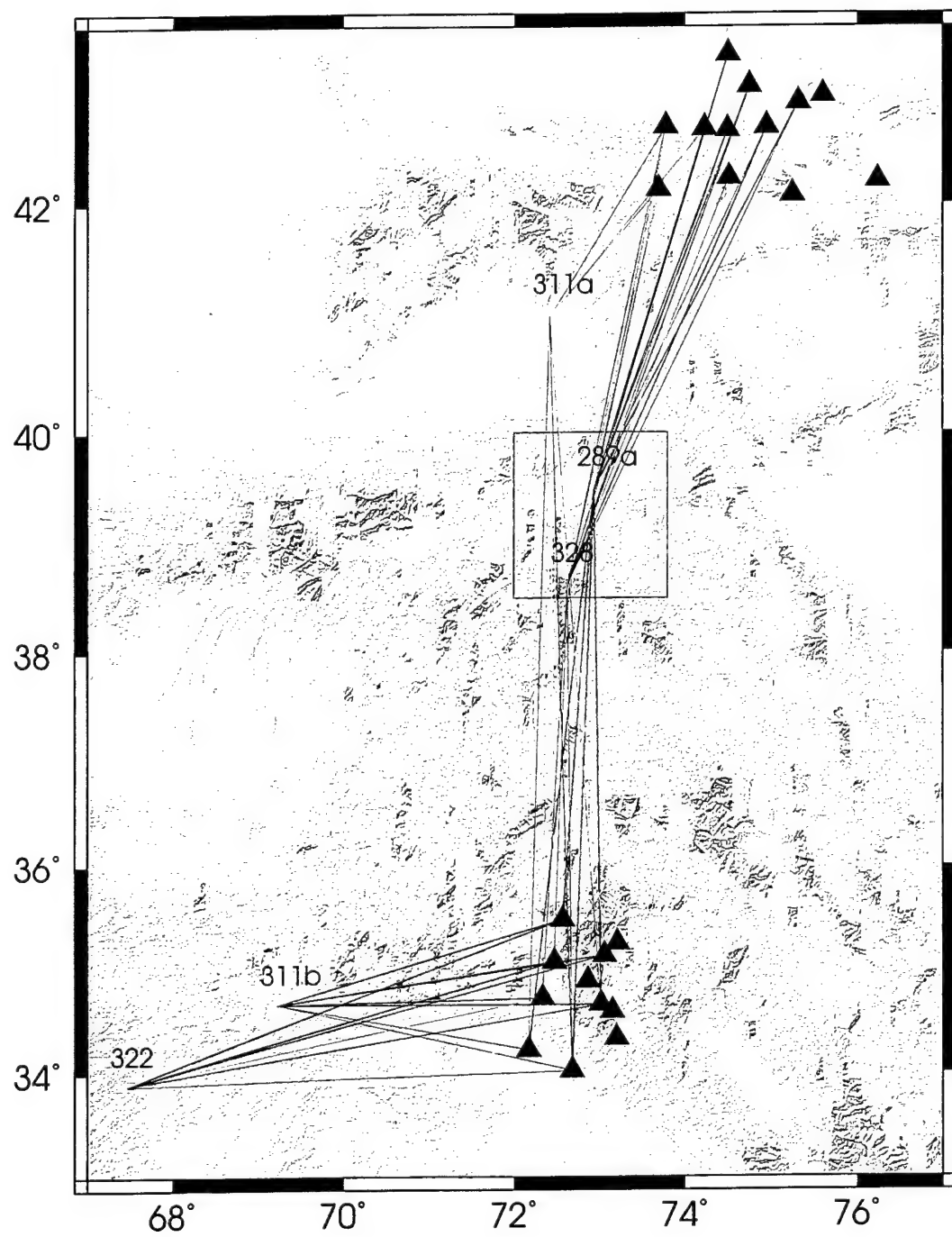


Figure 11. The Love wave phase velocity anomalies measured by the time-shifts of the waveform inversion. Red paths correspond to time shifts of +4 sec and larger (slow paths), and blue paths correspond to time shifts of -4 sec and smaller (fast paths). The insert box shows the location of Figure 10 which gives a close-up view of shallow structure variation near event 289a.

establish focal depth. However, identifying depth phases on short-period recordings can be very difficult, if not impossible, for crustal events. Without reliable depth phase constraints, a strong trade-off exists between the origin time and depth. Zhao and Helmberger (1991), using long period teleseismic body waveforms, found that throughout the Tibetan Plateau the PDE-reported crustal events are systematically located about 15 km deeper and occurred about 4 sec earlier than our estimates. An advantage of using regional broadband waveforms is that focal depths can be better constrained, either from the amplitude ratio of P_{nl} to surface waves for crustal events, or from the time separation between direct P and the depth phase sP_n for mantle events. In our study, we find that all crustal events are relocated shallower compared with their ISC depths or the Harvard CMT solutions.

As the magnitudes of shallow events drop below about 4.5, the number of useful teleseismic recordings becomes small and location becomes progressively more difficult. However, accurate locations of these shallow events are important for seismotectonic studies as well as for nuclear explosion monitoring. In this section, we have established a procedure of focal mechanism determination and relocation using as few as two broadband stations at regional distances. A real-time event locating program by a single 3-component station is under development which can provide preliminary location within minutes of an event's occurrence. Our procedure can then be employed to refine the location, independent of the PDE or ISC locations which usually come weeks or months later.

3. Event Trigger Algorithm and Source Location

In the previous section, we presented various methods useful for regional path calibration using broadband seismograms and for locations of seismic events with magnitude (M_w) larger than 4. But in regions with high natural seismicity, many events have magnitude less than 4 which cannot be detected at large teleseismic distances unless aided by focussing of seismic waves. Hence, for a meaningful seismic monitoring program, these events must be detected and their preliminary locations must be obtained to characterize their source type. Keeping this in mind, we describe a procedure designed for detection and location of small magnitude seismic events ($M_w \leq 4$) using regional seismograms recorded in areas where short-period arrays may or may not still be operational and the IMS (international monitoring system) station coverage of the region is sparse. Previous studies concerning the location of regional events were in the regions where short-period

array data were readily available (Bratt and Bache, 1988; Shlien and Toksöz, 1973). But in the context of the present monitoring program for regions where the operation of such arrays is hindered by both logistic and political issues, our focus is primarily on developing an algorithm to detect and find preliminary locations of seismic events by making use of data recorded by only a sparse network of three component broadband stations. To test the capability of our algorithm, which will be automated to accommodate large amount of data, we are presently using data recorded on the PAKN network as a test bed. This array consisted of 11 stations which operated near NIL (Nilore, Pakistan) for three months in 1992 and recorded a fairly large number of regional events in the M_L magnitude range between 3.0 and 4.5. To have a better control on the location parameters, the PAKN network data are augmented by additional data from the AAK station located in the middle of the KNET network in Kyrgyzstan (Figure 11).

The real-time detection and location of earthquakes are best accomplished with seismic array data and it is likely that the station NIL will co-locate events with the PAKR α array. Array data are useful to enhance the signal to noise ratio (SNR). By stacking or beam forming of array data, we can reduce the incoherent and diffuse noise coming from all directions and increase the strength of signals for the selected phase velocities. Any detection algorithm is expected to perform better for small magnitude events when such stacked time series are used for detecting P and S waves. The PAKN network data have shown that the region adjacent to PAKN's location is rich in natural seismicity and has recorded many events, at least 15 locateable small magnitude ($M_L < 4.0$) events per day. The majority of these events are located in between the stations NIL and AAK. By examining the quality of these events in the KNET network, we find that about one-third of them are also recorded by AAK. Thus, the station NIL, which is permanently located southeast of the PAKN network and became operational in March 1995, must be recording many small events every day and a dial-up capability to this station to access both continuous and segmented data can prove quite useful to characterize the seismic sources in the region. In addition, after the PAKR array becomes operational, the IMS will be able to detect small events and refine locations, and perform event characterization of seismic activity throughout the region.

3.1 Estimation of P and S Travel Times Using Detection Algorithm

The underlying basis for the event detection algorithm that we have developed is quite similar to the detection algorithm designed to use array data (Shlien and Toksöz, 1973). In their

algorithm, a time series is obtained by the beam forming of array data and confining the signal to a narrow band around a frequency, f , in which the signal-to-noise (SNR) is best observed. The beam is then passed through two integrators of different time durations computing a short-term average (*STA*) and a long-term average (*LTA*). The *LTA* is a measure the natural noise and is determined over an user specified time window and the *STA* is a measure the signal which is computed over a time window much shorter than the time window used for the *LTA* measurement. Both the *LTA* and *STA* are measured in the quantum unit (\approx millimicron) and when $20.\log_{10}(STA/LTA)$ is above 8db, a particular beam is declared to be in detection state.

Our detection algorithm is also based on the construction of two measurements, *LTA* and *STA*, and use of their ratios employing different preset detection thresholds for P and S waves. To detect and locate seismic events, we developed an algorithm which automatically picks both P and S waves and estimates approximate epicentral distance using the S-P travel time. Given a time series $f(t)$, we remove the mean and any undesirable noise and generate a characteristic function $g(t)$ which is defined as:

$$g(t) = f^2(t) + c^2 [df(t)/dt]^2 \quad , \quad (2)$$

where the weighting constant "c" varies the relative weight assigned to the first derivative and depends on the digital sample rate and noise characteristics of the station (Allen, 1978). Thus, the function $g(t)$ is one-sided as shown in Figure 12 and is more powerful than the characteristic functions used in other event detection algorithms (Ambuter and Solomon, 1974; Stevenson, 1976; Stewart, 1977). In the algorithms of Ambuter and Solomon (1974) and Stevenson (1976), it is the seismic trace rather than the characteristic function on which the averages are carried out. In Stewart's algorithm, a simple first difference of the in-coming signal is used.

To carry out the averages, we filter $g(t)$ to a short-period band to measure *STA* and to a long-period band to measure *LTA* as follows:

$$STA(t) = \int_t^{t_r+t} g(t) dt \quad LTA(t) = \int_t^{t_r+t} g(t) dt \quad , \quad (3)$$

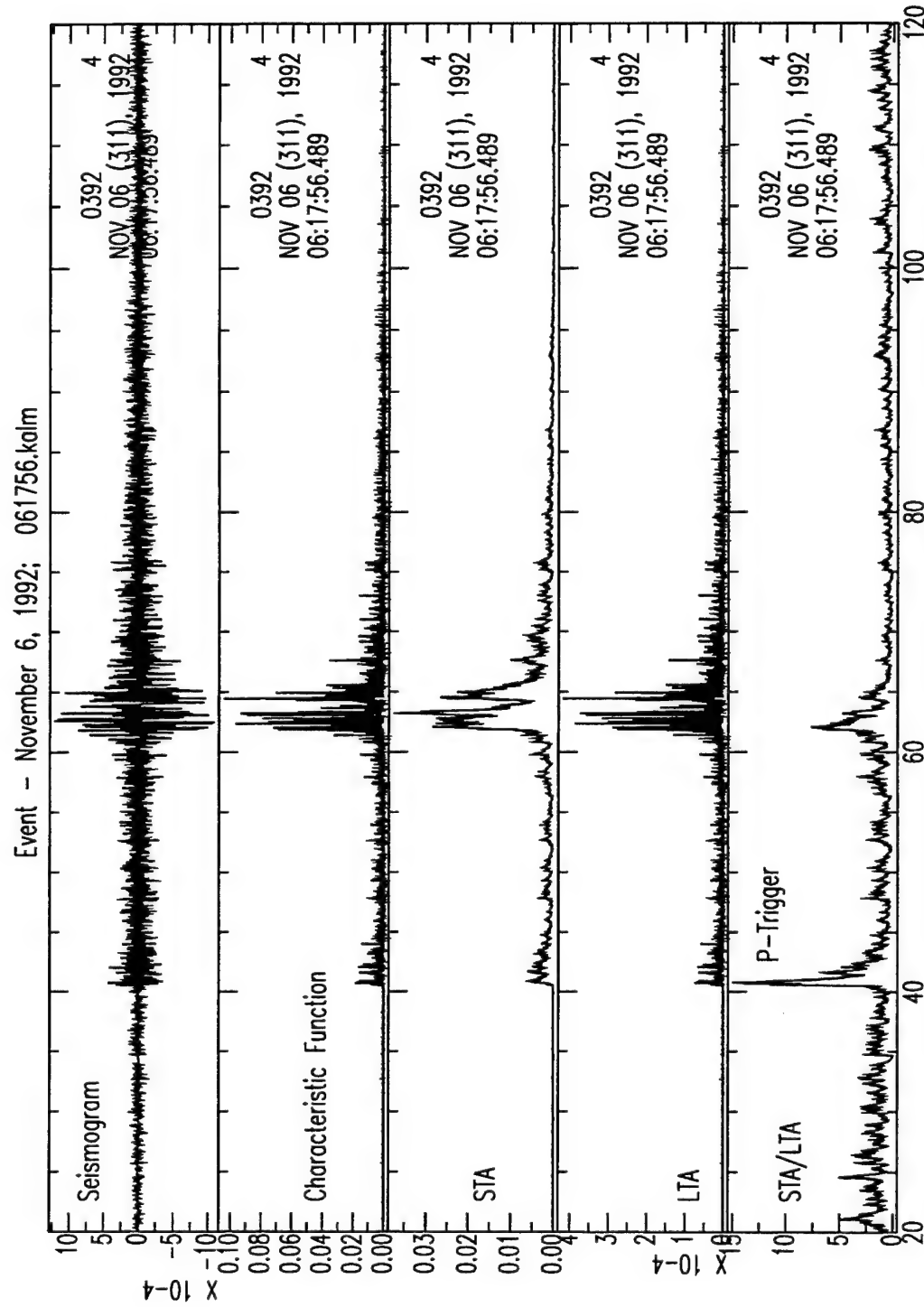


Figure 12. Figure illustrating the various steps used in the event-triggered algorithm. The top trace corresponds to the broad-band seismogram, and the second, third and fourth traces correspond to the characteristic function, short-term and long-term averages respectively. The bottom trace shows the temporal variation of the ratio of the STA to the LTA.

where t_r is the reference time, i.e., the time when the detection algorithm is set to start and the STA and LTA are measured at each transient point t by integrating the filtered $g(t)$ function from the reference time through time t . The window lengths t_s and t_L can be modified as needed to enhance the STA measurement relative to the LTA measurement. After we have computed STA and LTA , we use the following detection criterion

$$L(t) = \frac{STA(t_s)}{LTA(t_r)} \geq \epsilon \quad , \quad (4)$$

where ϵ is a preset detection threshold, to detect both P and S waves. The LTA is the long-term average of $g(t)$ and measures the background noise level at the time of detection. In most cases, the shape of $L(t)$ has an impulse-like onset for P-waves but can vary in shape for S waves depending upon whether it is a deep or a shallow event.

At present, we have implemented the algorithm to a data set consisting of segmented data in which each segment represents an occurrence of a single event and the P waves can occur anywhere after 20 seconds from the start of the signal. We use the vertical component seismograms for the P-wave detection and the transverse component seismograms for the S-wave detection. For the P-wave detection, the reference time for STA and LTA measurements is set at the start of the seismogram and both $STA(t)$ and $LTA(t)$ are computed progressively with time using the appropriate filter constants. The function $L(t)$ is constructed starting at 20 seconds and examined for whether its value has increased to a threshold value (≈ 5) which is set for the P wave detection. Once the P wave is triggered, we rotate horizontal components and estimate back azimuth by minimizing energy on the transverse component using a small window following the P onset. In most cases, we find that back azimuths are estimated within 20° of the true back azimuths obtained from the hypocentral location code (Lienert and Havskov, 1995) for the master events. To detect the S-waves, we use the transverse component processed using the back azimuth found from the minimization of transverse motion energy. Generally, the value of $L(t)$ becomes largest in both transverse and radial components at or in the neighborhood following the S arrival. In our algorithm, LTA is held fixed and is computed using a time window (≈ 20 seconds) starting at the P-wave trigger time. $STA(t)$ is calculated in the same way as before with its reference time being the P-wave trigger time. We compute $L(t)$ over the entire time series from the reference time and determine where it becomes the largest and start the S-triggering algorithm midway between P trigger time and the time when

$L(t)$ is the largest. In this way, we can even trigger the S_n phase (classical S head wave) on clean seismograms.

We have applied this triggering algorithm to pick P and S travel times of many small events ($M_L > 2.0$) recorded by the PAKN network and located 88 small events over a period of 10 days (see Table 4), in addition to 10 master events. Figure 13 shows the locations of these new events obtained by using P- and S-wave travel-time picks from event trigger algorithm using the PAKN network data. Since the azimuthal coverage of these events is limited (all stations of the PAKN network lie within a narrow azimuth range for these events), most of their depths are unconstrained. Many other events were also recorded by the PAKN network during these 10 days, but could not be located as they were recorded by fewer than three stations. For large events with good SNR, the raw seismograms can be fed directly into the event detection algorithm. However, for small events coming from several hundred kilometers away, the SNR can be poor, generally dominated by the long-period noise which must be reduced. We find that seismograms of small events when bandpass filtered between 1 and 8 Hz, are free of long-period noise and both P- and S-waves generally become observable. In order to check how well the P- and S-waves are detected by the algorithm, we filtered seismograms of 10 master events in this frequency band and applied the detection algorithm. The P- and S-wave arrival times detected by the detection algorithm were same as those travel times that were picked by displaying the seismograms on the computer screen and visually inspecting each of these phases.

3.2 Approximate Epicentral Distance and Regional Magnitudes

In addition to detecting the P- and S-waves, the event detection algorithm outlined in the previous section also computes the initial epicentral distance and regional magnitude, M_L , using three-component seismograms from a single station. Hence, our detection algorithm is complementary to the short-period P_z to long-period surface wave energy ratio ($E_{sp-Pz} : E_{lp-3}$) vs. distance discriminant as it requires the epicentral distance for the discriminant to be viewed, a parameter that comes out of the detection algorithm just from the three-component broadband seismograms of a single station. The M_L value can be used for the magnitude normalization as well. The epicentral distance, R , is obtained by using the separation time between the S and P waves which depends upon the crustal velocity model and the source depth. Assuming that all the crustal earthquakes occur at a depth of 20 km and that all the subcrustal earthquakes occur at a depth of 100

Table 4. Hypocentral Locations of Seismic Events Recorded by
PAKN Network (using only the PAKN network data)

Yr/Mo/Dy	h:m:s	Lat °N	Long °E	Depth (Km)
1992/10/02	00:10:02.6	36.729	71.224	260.0
1992/10/02	01:02:15.6	36.019	70.751	0.0
1992/10/02	01:38:24.9	36.458	71.085	123.6
1992/10/02	02:28:49.3	37.288	72.506	8.8
1992/10/02	04:10:30.7	37.835	64.335	20.0
1992/10/02	04:23:37.4	37.018	73.919	6.7
1992/10/02	12:36:25.3	35.487	70.154	20.0
1992/10/02	14:38:47.1	38.085	73.174	150.8
1992/10/02	15:01:39.4	36.200	69.866	20.0
1992/10/02	18:32:09.8	36.543	70.989	160.4
1992/10/02	18:37:58.4	36.094	70.559	116.6
1992/10/02	20:56:09.0	37.700	72.424	160.5
1992/10/02	21:25:55.9	36.465	70.861	186.4
1992/10/02	21:37:15.0	32.978	69.965	59.0
1992/10/02	22:12:23.3	33.983	72.898	19.9
1992/10/02	22:29:02.3	35.566	70.766	21.1
1992/10/02	22:38:43.0	36.564	70.765	192.6
1992/10/03	01:02:02.2	37.789	73.053	22.4
1992/10/03	02:57:54.5	37.902	74.553	9.1
1992/10/03	09:13:03.2	37.018	71.335	129.0
1992/10/03	19:15:56.9	36.706	73.592	0.0
1992/10/03	19:46:56.8	36.482	70.044	236.0
1992/10/03	20:46:29.9	36.641	71.221	10.0
1992/10/15	00:37:57.1	36.650	70.895	182.8
1992/10/15	02:09:34.5	36.068	70.853	0.0
1992/10/15	10:50:30.2	37.432	73.867	7.8
1992/10/15	12:23:41.0	36.438	71.139	113.8
1992/10/15	19:42:12.7	38.361	74.212	149.1
1992/10/15	20:43:42.5	36.902	72.334	20.3
1992/10/15	22:13:37.9	36.050	70.610	20.0
1992/10/15	22:38:34.6	36.025	70.478	22.3
1992/10/15	23:52:14.4	36.568	71.057	201.3
1992/11/07	01:27:55.6	36.029	70.981	48.3
1992/11/07	02:32:48.5	36.757	71.324	179.3
1992/11/07	02:51:30.2	36.407	70.623	24.0
1992/11/07	07:21:53.2	41.257	73.053	20.0

Table 4. (Continued) Hypocentral Locations of Seismic Events Recorded by PAKN Network (using only the PAKN network data)

Yr/Mo/Dy	h:m:s	Lat °N	Long °E	Depth (Km)
1992/11/07	09:05:13.8	36.440	71.511	10.0
1992/11/07	12:48:38.8	36.569	71.400	155.7
1992/11/07	17:58:28.9	34.810	68.516	20.0
1992/11/07	18:25:04.4	36.284	70.436	1.4
1992/11/07	18:37:40.5	34.645	69.040	0.0
1992/11/07	19:48:46.4	35.762	73.258	37.4
1992/11/07	21:00:53.4	37.649	72.704	184.1
1992/11/12	01:15:04.4	36.797	73.373	20.1
1992/11/12	01:36:59.8	35.176	73.584	20.0
1992/11/12	02:11:24.6	35.566	70.149	28.8
1992/11/12	05:02:10.1	36.985	73.845	8.2
1992/11/12	07:42:09.5	36.465	71.366	20.0
1992/11/12	09:09:35.3	36.011	70.029	12.4
1992/11/12	11:45:06.8	36.445	71.176	69.2
1992/11/12	13:54:33.1	35.891	70.574	31.8
1992/11/12	19:25:24.2	39.330	75.125	20.0
1992/11/12	19:59:53.0	35.894	70.714	53.0
1992/11/12	20:41:03.4	36.494	70.612	20.0
1992/11/12	22:45:12.3	32.431	80.771	20.0
1992/11/17	00:44:08.2	36.547	70.989	21.1
1992/11/17	02:38:26.2	32.301	65.919	20.0
1992/11/17	04:40:10.6	36.950	71.808	73.5
1992/11/17	05:42:22.6	36.713	71.250	218.9
1992/11/17	06:55:24.2	36.190	62.278	20.0
1992/11/17	08:51:30.9	36.594	70.931	201.9
1992/11/17	14:19:59.3	36.053	70.672	83.5
1992/11/17	14:35:53.8	37.018	73.929	20.0
1992/11/17	14:48:19.6	36.420	71.181	115.0
1992/11/17	15:43:19.1	37.629	70.783	188.1
1992/11/17	16:22:11.6	36.478	71.559	23.9
1992/11/17	16:36:14.3	36.561	71.272	124.9
1992/11/17	16:48:40.2	36.674	71.066	222.9
1992/11/17	18:59:38.0	36.947	71.405	20.0
1992/11/17	19:26:59.5	37.678	72.839	20.0
1992/11/17	22:03:41.9	36.320	70.627	20.0
1992/11/17	22:27:10.0	37.944	74.050	20.1

Table 4. (Continued) Hypocentral Locations of Seismic Events Recorded by PAKN Network (using only the PAKN network data)

Yr/Mo/Dy	h:m:s	Lat °N	Long °E	Depth (Km)
1992/11/23	01:35:22.5	36.470	70.482	20.0
1992/11/23	03:40:08.4	37.077	71.800	161.8
1992/11/23	07:11:17.1	36.864	70.946	27.7
1992/11/23	17:51:00.4	36.686	70.510	20.0
1992/11/23	18:31:57.3	36.976	71.521	32.8
1992/11/23	23:10:52.0	39.580	73.557	20.6
1992/12/04	00:58:26.2	32.992	70.055	44.0
1992/12/04	01:16:21.4	36.760	70.991	220.1
1992/12/04	03:28:19.2	37.802	72.614	135.8
1992/12/04	03:45:49.3	36.787	71.152	113.2
1992/12/04	05:12:37.4	33.928	73.954	20.0
1992/12/04	07:43:14.2	36.601	71.804	21.1
1992/12/04	09:21:36.6	37.128	72.281	40.7
1992/12/04	11:36:32.9	37.779	72.277	22.8
1992/12/04	13:55:16.9	37.562	72.413	14.9
1992/12/04	20:04:29.8	35.136	72.593	57.2
1992/12/04	22:06:27.0	37.759	72.377	45.5
1992/12/04	23:09:30.7	36.646	71.340	80.8
1992/12/06	00:56:35.5	35.350	72.498	57.1
1992/12/06	01:52:54.6	37.297	71.577	20.0
1992/12/06	03:44:27.3	37.714	72.262	26.6
1992/12/06	13:48:01.4	34.578	69.896	24.1
1992/12/06	15:47:49.9	36.620	71.924	10.0
1992/12/06	15:58:54.1	37.101	72.744	23.6
1992/12/06	16:16:16.7	32.434	77.036	20.0
1992/12/06	21:45:04.8	39.420	71.387	0.0

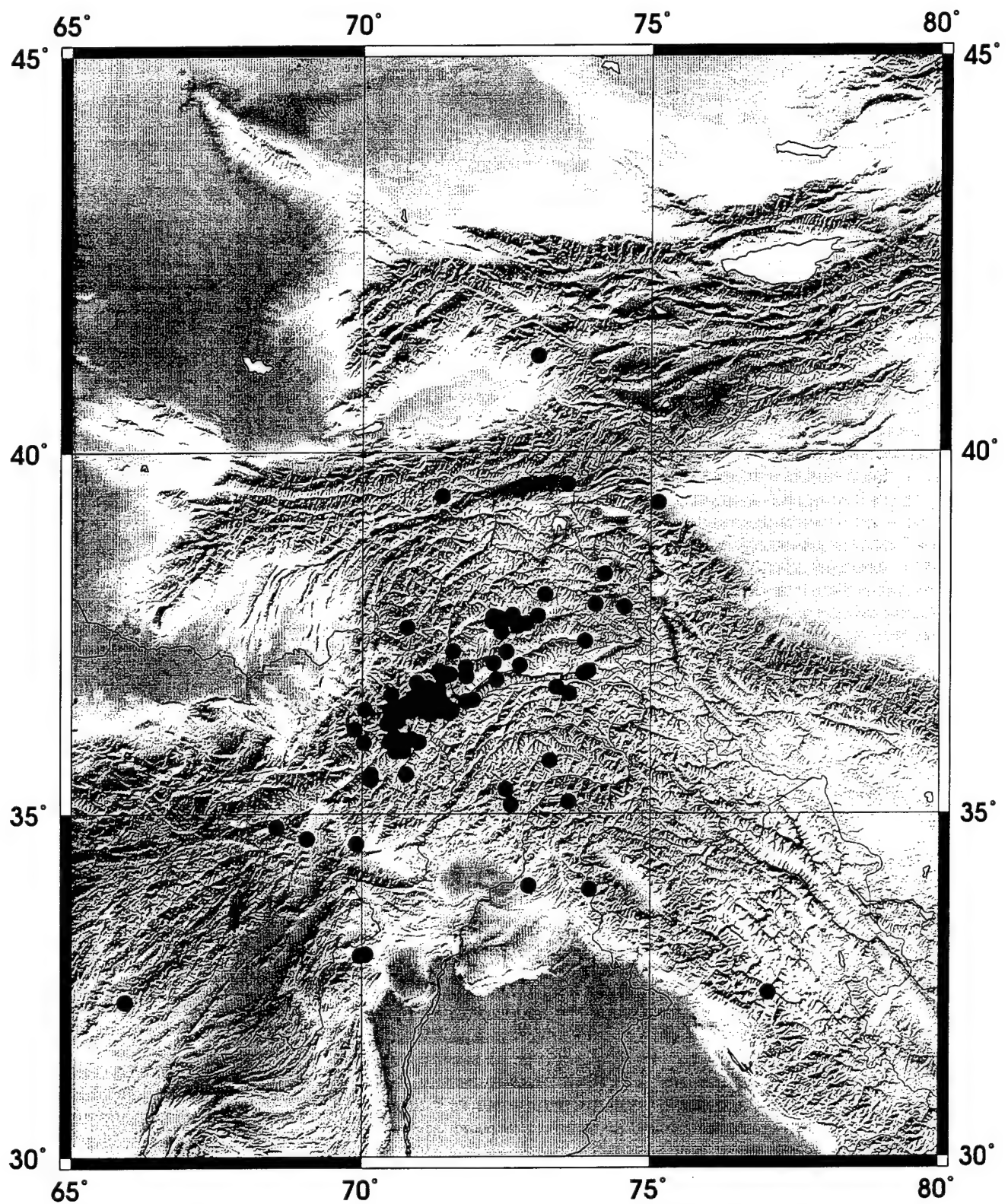


Figure 13. Map showing epicentral locations of events presented in Table 4. These epicenters were obtained using the P- and S-wave travel times picked by the event-triggered algorithm using the PAKN network seismograms.

km, it is possible to find two approximate epicentral distances for individual S-P travel time separation as follows:

$$R = \sum_{i=0}^{i=3} a_i (T_S - T_P)^i , \quad (5)$$

where T_S and T_P are the arrival times of P and S waves, respectively, and the a_i 's are the constants for the deep and shallow events derived separately from the Hindu-Kush crustal model. It should be noted that errors can creep into the distance estimation due to incorrectly identified seismic phases, especially for small magnitude crustal earthquakes. For example, the SmS wave can be misidentified as the S_n phase for the earliest arrival when the noise level is high. Thus, this algorithm warrants a careful scanning scheme for phase association to individual seismic arrivals.

We have also added an additional capability to the detection algorithm for estimating M_L . To do this, we first simulate Wood-Anderson seismograms from the broadband seismograms, and determine M_L from each of the three components, using the standard method described by Richter (1935), and average them. The local magnitude M_L (Richter, 1935) is simple and is just the base 10 logarithm of the maximum amplitude A on a seismogram (measured in mm) minus a correction factor $\log_{10}(A_o)$ which is an attenuation term that was initially derived for southern California and was given a mathematical form:

$$q(r) = cr^{-n} \exp(-kr), \quad r^2 = \Delta^2 + h^2 , \quad (6)$$

with $c = 0.49710$, $n = 1.2178$, $k = 0.0053 \text{ km}^{-1}$, and $h = 8 \text{ km}$ by Kanamori *et al.* (1993). Bakun and Joyner (1984) proposed a different attenuation form given by

$$-\log_{10} A_o = \log_{10}(r) + 0.00301r + 0.70, \quad h = 10 \text{ km.} \quad (7)$$

Both these attenuation forms produce the original attenuation for $-\log_{10}(A_o)$ given by Richter (1935) for southern California, but do not give attenuation correction factors, in a strict sense, appropriate for any other regions. To apply the M_L scale to the Hindu Kush earthquakes, we need to obtain new correction factors. Due to the lack of these new correction factors, we applied the southern California correction factors (Kanamori *et al.*, 1993) to the M_L calculation, but expect to make "corrections" to these corrections factors by applying a differential attenuation operator representing

the difference in attenuation between Pakistan and southern California. Figure 14a shows the M_L measurements made for the 10 master events. Both panels show M_L versus M_w , the latter being the moment magnitude estimated from the regional modeling (Saikia *et al.*, 1996). On the left panel are shown the magnitude estimates for the deep and shallow events; the shallow events are marked by the open symbols and the deep events by the filled symbols. On the right panel are shown the M_L estimates of individual stations using the same symbol convention for the deep and shallow events. Clearly, the distance dependence and large scatter in the M_L values in both these panels indicate that the attenuation correction factors used in defining the magnitude may not be adequate and M_L measurements by themselves may not be stable. In Figure 14b, variation of the average M_L magnitude obtained using the PAKN network data versus the M_w magnitude suggests that average M_L values for the shallow and deep earthquakes computed using the southern California attenuation may correlate with the network estimate of M_w , each with a different relation. However, it should be kept in mind that more analysis of additional events is necessary for a definite conclusion as this preliminary analysis consists only of a few data points. The right panel of Figure 14b shows a large amount of scatter in the M_L estimates for all the events when compared to the network estimate of M_w . Even though the data analyzed in this study are from the PAKN network and its aperture is large compared to the conventional arrays, the scatter in the magnitude values suggests that the M_L measurements may not be robust. To better understand the M_L scatter, the M_L scatter should be examined relative to the scatter observed in M_w measurements and determine how well the M_L and M_w measurements do correlate at individual stations, especially at SBRA (surrogate of NIL) and AAK stations.

3.3 "Waveform Complexity" as a Depth Estimator

In our recent study (Saikia *et al.*, 1996), we noted that the $E_{sp-P_z}:E_{lp-3}$ vs. R discriminant values for deep earthquakes in the Hindu-Kush region are large relative to the general shallow earthquake population and they fall into the zone of the expected explosion population. Following this observation, we have developed a new diagnostic tool to identify deep earthquakes in conjunction with the $E_{sp-P_z}:E_{lp-3}$ discriminant. Deep earthquakes produce large estimates of $E_{sp-P_z}:E_{lp-3}$ because of the deficiency in long-period fundamental mode surface waves relative to strong body waves. On the other hand, $E_{sp-P_z}:E_{lp-3}$ remains high for explosions because explosions are rich in P waves relative to the P waves excited by shallow earthquake sources. For the $E_{sp-P_z}:E_{lp-3}$ vs. R discriminant to be

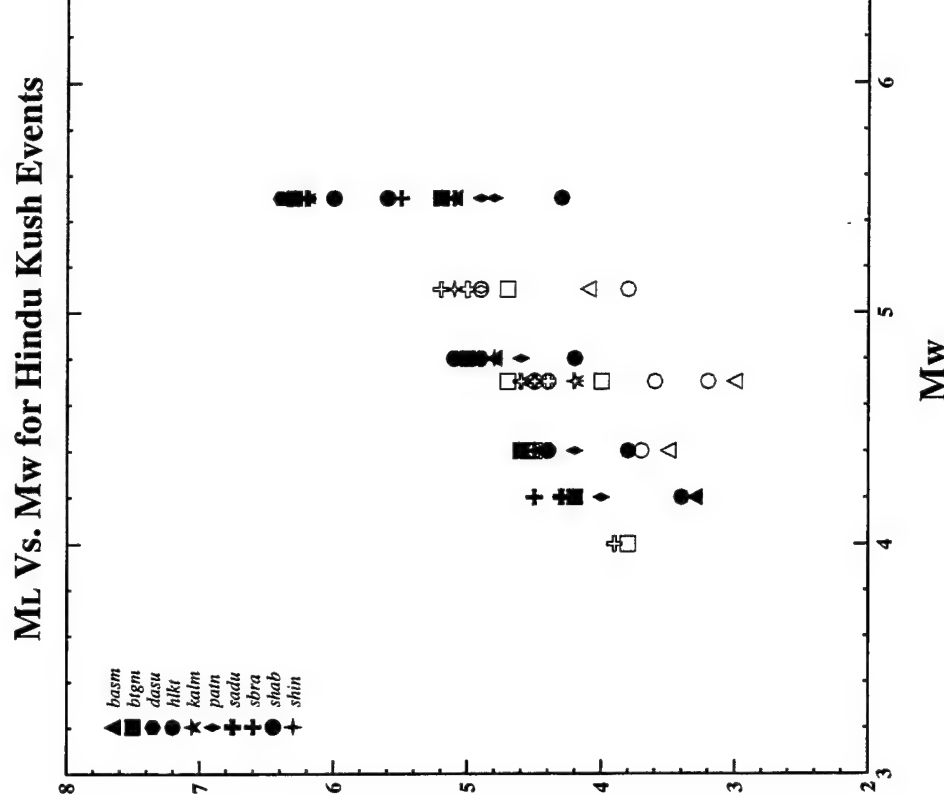
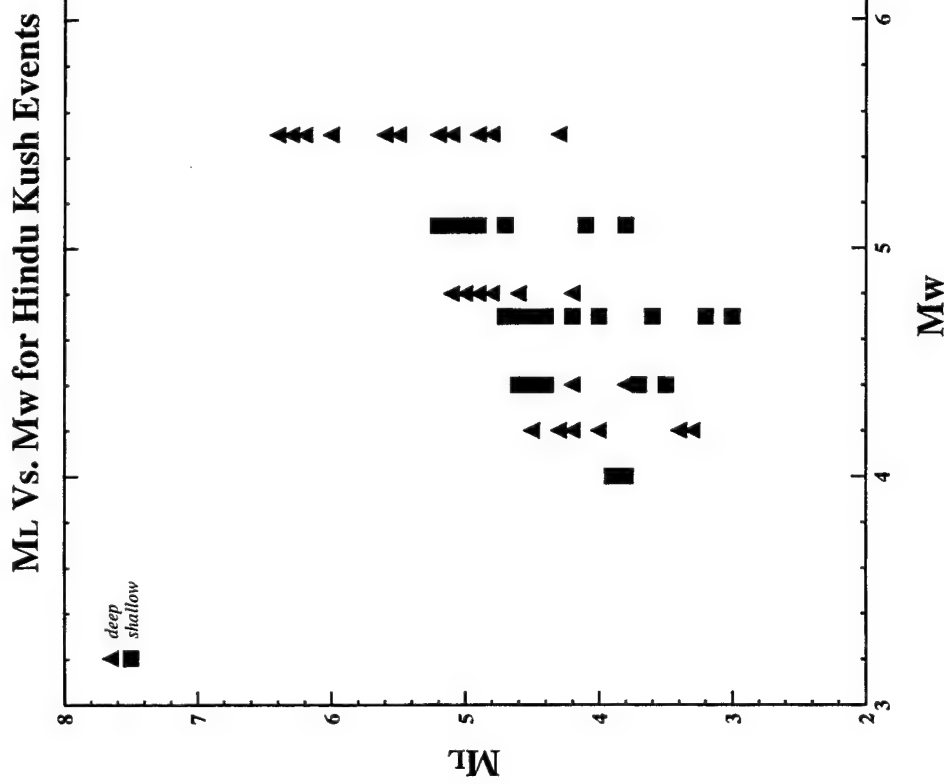


Figure 14a. Correlation of regional magnitudes, M_L vs. M_w , for the 10 master events. Each M_L value is an average over the three M_L values obtained from the simulated Wood-Anderson seismogram using the Southern California attenuation correction (Kanamori et al., 1993). Left panel: deep vs. shallow earthquakes; right panel: deep vs. shallow events stationwise, shallow events have open symbols and deep events have filled symbols.

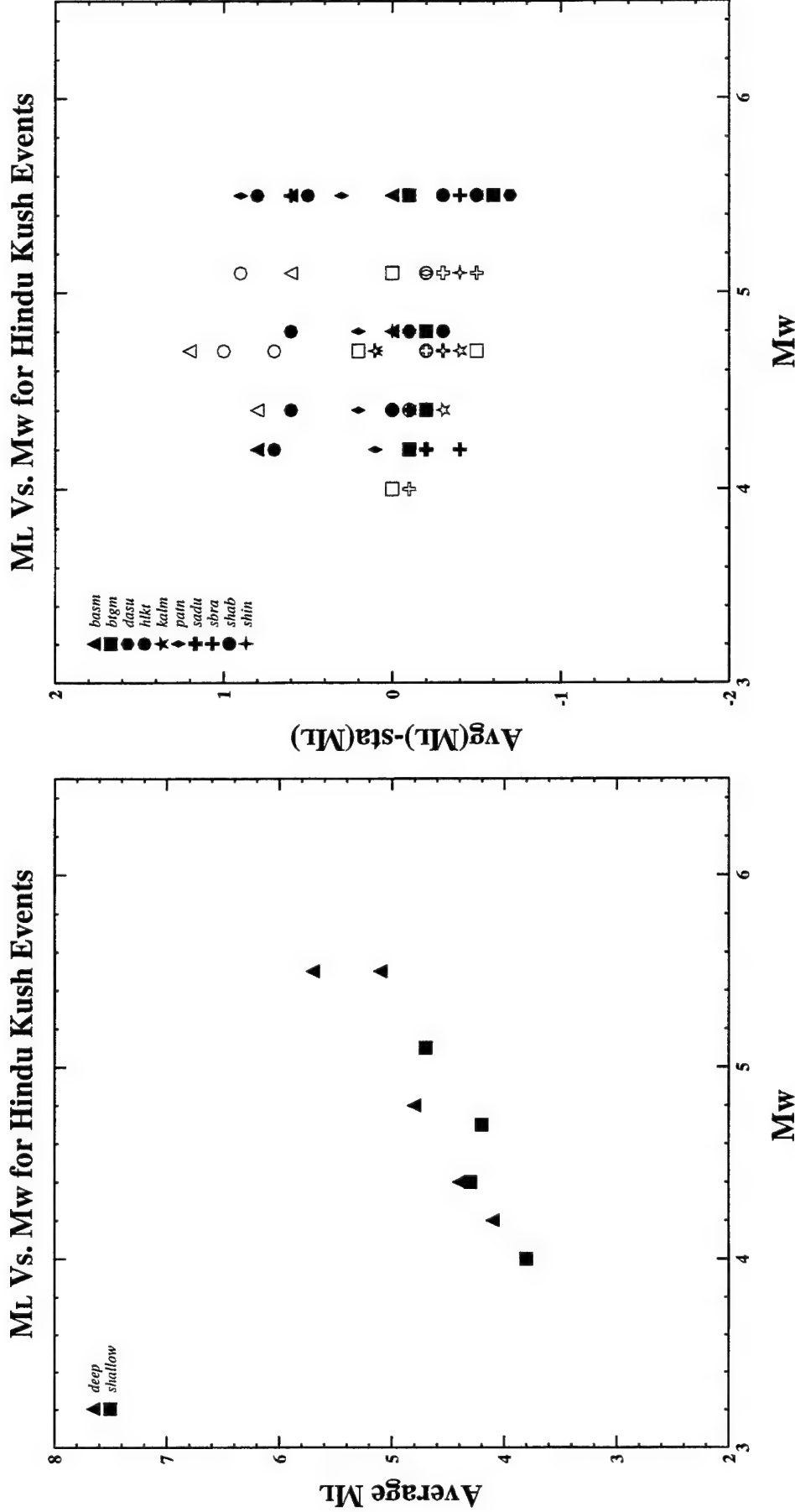


Figure 14b. Left: correlation of regional magnitudes, ML vs. M_w , for the 10 master events. In this figure, each ML value is obtained by averaging of ML values for the entire PAKN network. Right: scatter in values for each station vs. M_w , shallow events have open symbols and deep events have closed symbols.

effective in regions with deep seismicity, it is necessary to identify the depth of those events for which $E_{sp-Pz}:E_{lp-3}$ estimates are large. If an event with a large $E_{sp-Pz}:E_{lp-3}$ value is proven to be deep, then its source is characterized with respect to nuclear monitoring concerns, while others still need to be considered as outliers to the earthquake population and require further analysis.

In several recent studies (Saikia *et al.*, 1996), we have demonstrated that regional waveform modeling can be used to identify deep earthquakes, but the events have to be sufficiently large so that the regional seismograms have enough long-period signals to model. Generally, events with M_w greater than 4 meet this criterion and the entire process, which includes finding focal mechanism and source depth, can be completed within a reasonable time for analysis (≈ 10 minutes per event). This method, which has been robustly established for two stations (Saikia *et al.*, 1996), also performs well with single-station data, and its success depends primarily on the adequacy of path calibration and availability of Green's functions on disk ranging many distances and depths.

Following this approach, we find the function $g(t)$ (Section 3.1) has some interesting features which can be quantified to isolate the deep Hindu Kush earthquakes in the $E_{sp-Pz}:E_{lp-3}$ population. For the deep events, the duration of the S wave packet observed in $g(t)$ appears narrow compared to the duration of the S wave packet observed for the shallow events (Figure 15). Except for a few exceptions which are related to site complexity, we found this to be true for the five shallow and five deep master events in the region (see Appendix). Thus, by quantifying this observation it is possible to identify all the deep events in the $E_{sp-Pz}:E_{lp-3}$ population. Once the S wave is detected, we retrace 5 seconds and compute a time series $L(t)$ of the cumulative sum of the test function $g(t)$ over a time window of 2 minutes using both SV and SH seismograms separately. The SV and SH seismograms are obtained by rotating the horizontal seismograms using the back azimuth which minimized the energy in the P-wave window of the SH seismogram. The $L(t)$ time series are normalized to unity and using the normalized $L(t)$, we measure two durations where $L(t)$ attains 60% and 95% of the total values. The ratios of the two durations, DUR_{60} and DUR_{95} , equalized to the measured S-P times and divided by 100 seconds are formed and used to identify deep events from the shallow ones. This new depth estimator, which is actually a measure of waveform complexity, is defined as follows:

$$\{c_1[DUR_{60}/DUR_{95}]_{SH} + c_2[DUR_{60}/DUR_{95}]_{SV}\} * \frac{(T_s - T_p)}{100} \quad (8)$$

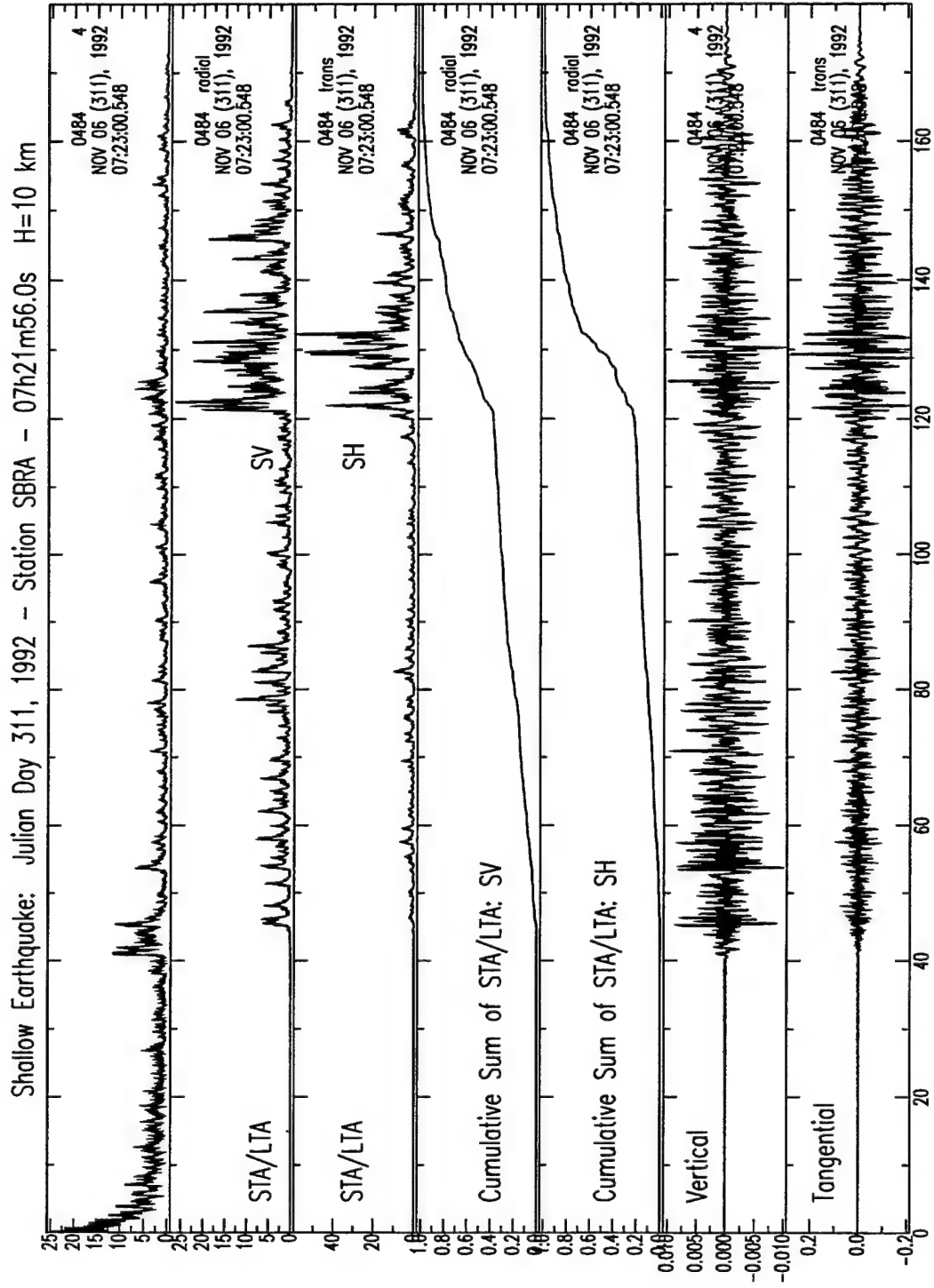


Figure 15a. Comparison of the waveform complexities for the SV and SH components for shallow vs. deep earthquakes, in various measurements, including the cumulative sum of STA/LTA as a function of time. Bottom two traces show the vertical and tangential seismograms; all these seismograms are highpass filtered with a corner frequency of 1 Hz. This figure shows various traces processed from broadband seismograms recorded at station SBRA from a shallow master earthquake which occurred on November 6, 1992.

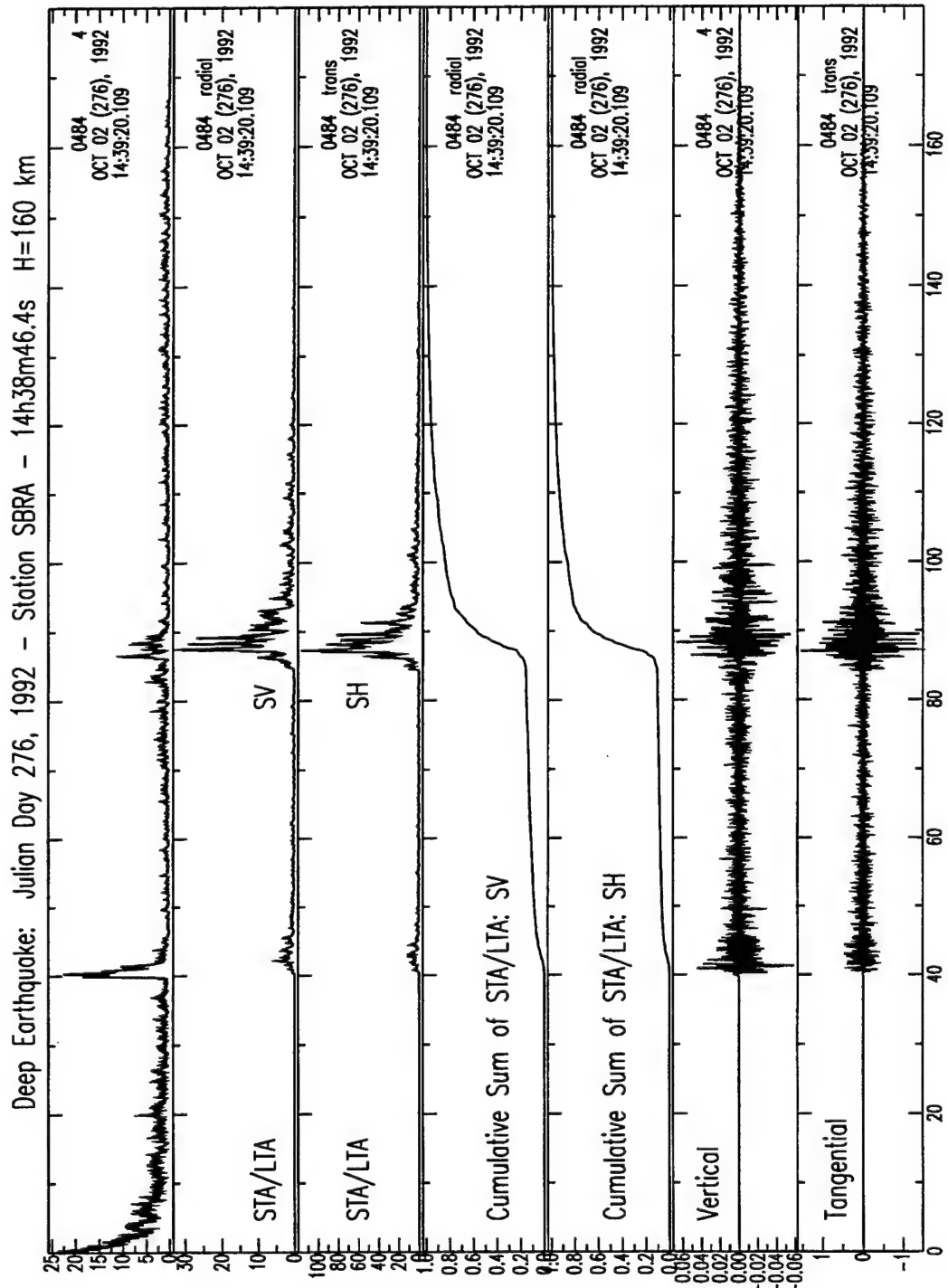


Figure 15b. Similar to Figure 15a but for a deep master event which occurred on October 2, 1992.

where $c_1=c_2=0.5$ when both SV and SH measures are used, $c_1=1$, $c_2=0$ when only the SH measure is available, and $c_1=0$, $c_2=1$ for case when only the SV measure is available. For deep events, the DUR_{60} estimate captures the dominant features of $g(t)$ and is much smaller relative to its DUR_{95} estimate. For shallow events, S waves in $g(t)$ extends dominantly for a long duration and its DUR_{60} value relative to the DUR_{95} value is large compared to that for deep events. Thus, the ratio of the two durations produce better separation between the two populations than do the DUR_{95} estimates alone.

We applied the above approach to the population of 10 master events and the result is shown in the left panel of Figure 16. Each station is assigned a symbol which is open for the shallow events and filled for the deep events. While the shallow events do indicate some scatter, the deep events are well behaved and have a pattern of systematically small values relative to shallow earthquakes. The dashed line shows the demarcation of the deep events from the shallow events as estimated by eye-ball. Notice that there are points corresponding to the shallow events below this line which could be related to the site or radiation condition of the S-waves. Whenever a shallow event falls below the separation line, it does not cause much concern as our objective is to isolate the deep events in the $E_{sp-Pz}:E_{lp-3}$ population. A few other points of deep events do fall within the population of shallow events. The observations for deep events are recorded at large epicentral distances, far beyond the critical distances of the S-waves which causes the S-waves to scatter over a longer time window and producing longer duration. It is clear that this depth estimator which is based on waveform complexity appears quite promising with the caveat that it is likely to be region-specific. Careful evaluation of the characteristic function $g(t)$ in a new area can produce insight for quantifying the waveform complexity to isolate deep events from the shallow events. The advantage of this complexity measure is that it is applicable at high frequencies (> 1 Hz) allowing a significant reduction in the magnitude threshold from $M_w 4.0$ to about 3.0 where regional waveform modeling becomes unsuitable as regional seismograms from small magnitude events generally lack long-period signals.

In the right panel of Figure 16, we show the duration measure for all new events shown in Figure 13 including the master events. The dotted line in this panel is the same line which separated the deep master events from the shallow master events. We have then selected two events (Figure 17), one shallow and one deep, at random using the duration criterion and identified by in this panel.

Shallow Vs. Deep Master Events Hindu-Kush Region

All Events of Hindu-Kush Region

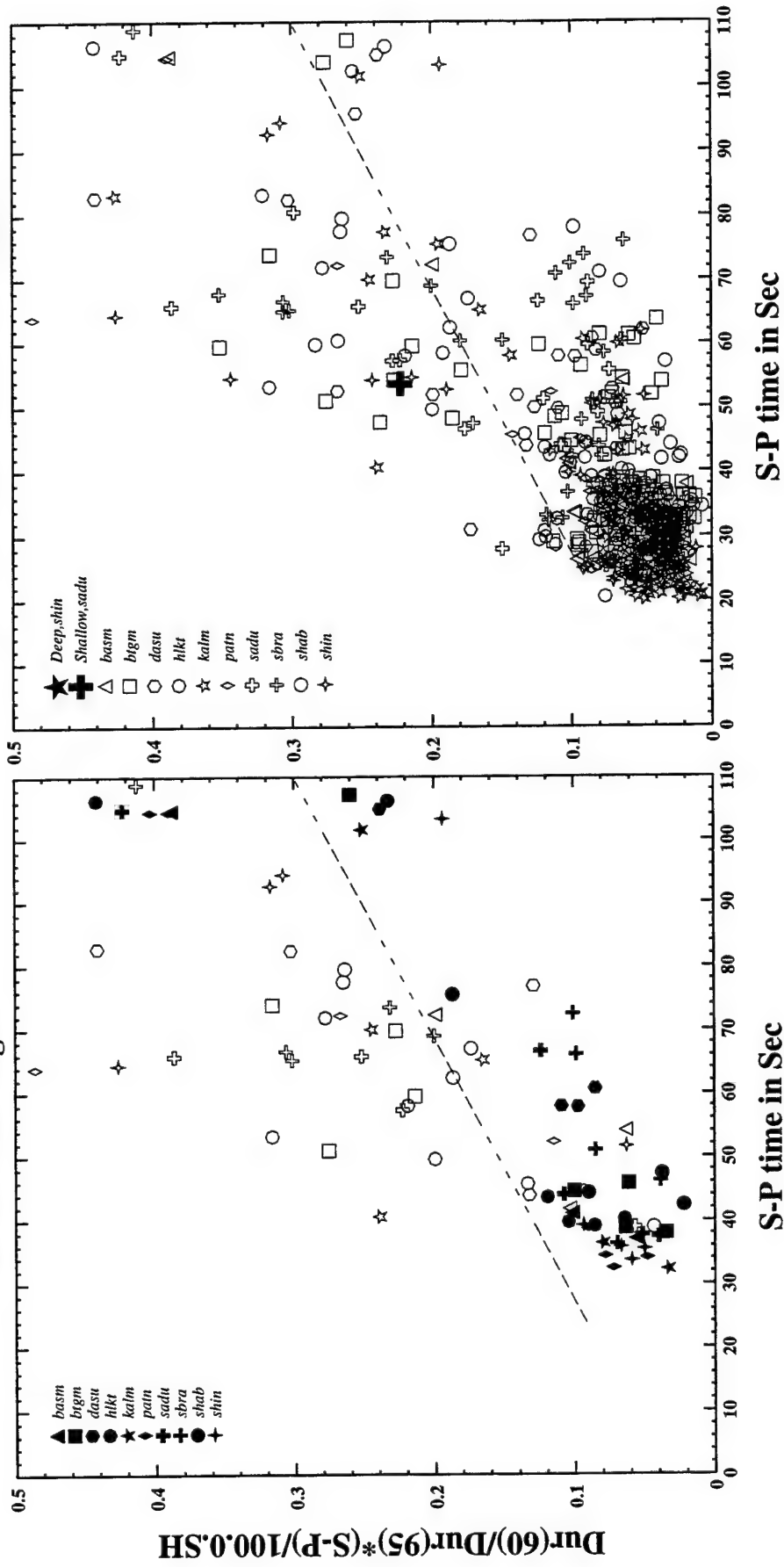


Figure 16. Left: duration measurements for various stations for shallow vs. deep master earthquakes. Solid filled symbols correspond to the deep earthquakes and the open to the shallow earthquakes. The deep earthquakes lie mainly below the dotted lines, except for those at large distances. Right: duration measurements for various stations for all ($ML > 3.0$) earthquakes recorded by the PAKN network. Also shown are two points, one for the shallow event (+) and a filled star for the deep earthquake which is masked by many events near the 30 to 40 sec window. Events were located using the P- and S-wave travel times picked by the event triggered algorithm.

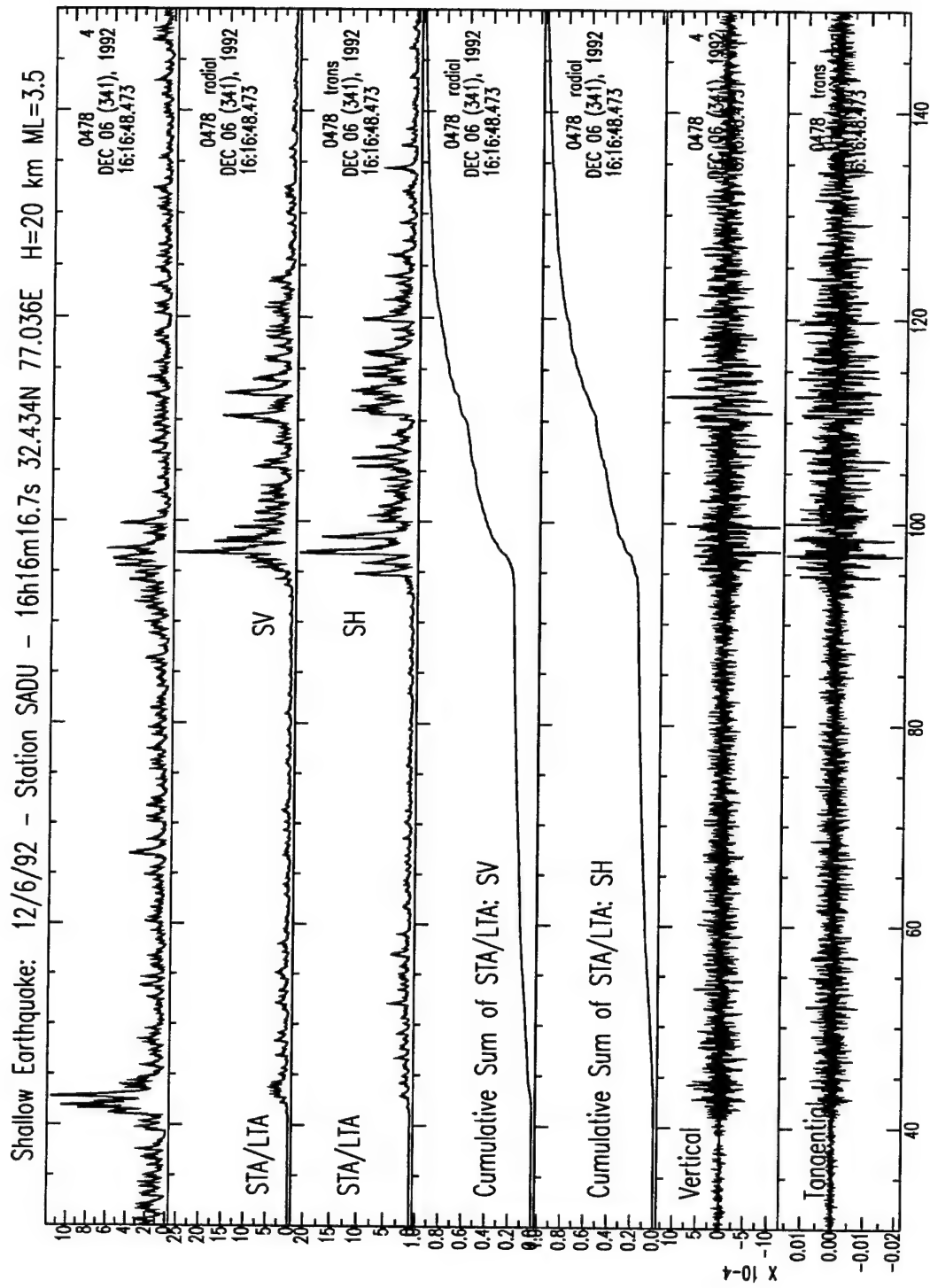


Figure 17a. Comparison of the waveform complexities for the SV and SH components for shallow vs. deep earthquakes, in various measurements, including the cumulative sum of STA/LTA as a function of time. The bottom two traces show the vertical and tangential seismograms; all these seismograms are highpass filtered with a corner frequency of 1 Hz. This figure shows the various traces processed from broadband seismograms recorded at station SADU from a shallow earthquake which occurred on December 6, 1992.

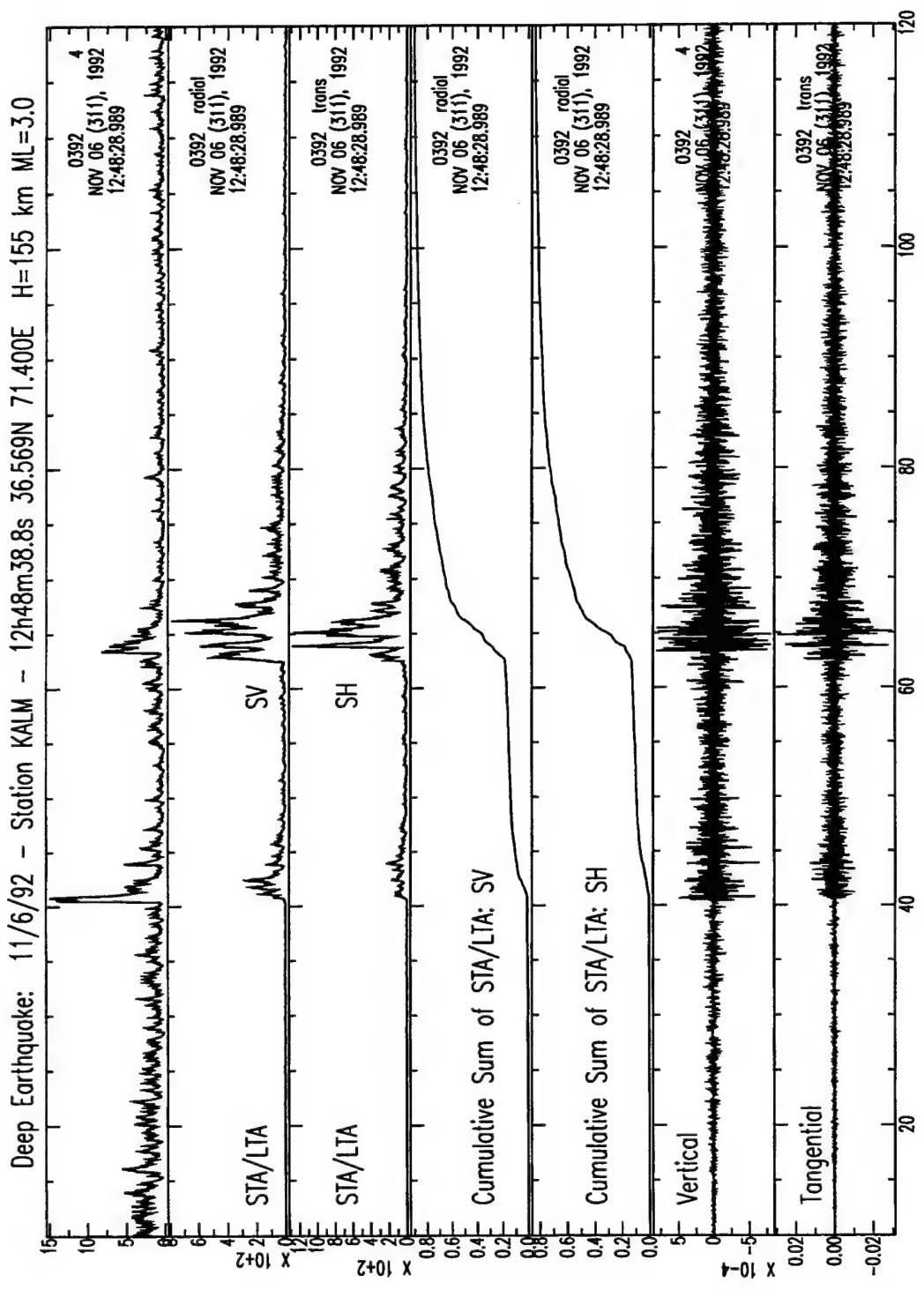


Figure 17b. Analogous to Figure 17a but for a deep event (December 6, 1992, 12:48:38.8) recorded at station KALM.

The filled cross symbol is for the shallow event which plots above the dashed line and the deep event (a filled star) plots in the population of deep events. Most of the deep events concentrate at the bottom on the left side and their epicenters lie in the zone of deep seismicity to the north of the PAKN network.

3.4 Relocation of Events Using Two Stations

Obtaining precise locations of seismic events is difficult when events are small in magnitude ($M_L < 4$) as in many cases they cannot be seen teleseismically. At many short-period teleseismic arrays their first arrivals may lie within the noise level and not be amenable even to the stacking process. For example, the Chiang Mai array which is located in the range of $29^\circ - 33^\circ$ away from the NIL station failed to record the October 15, 1992 event (Julian day 289, $M_w = 4$) above the noise level (Figure 8). In the Alice Spring and Warramunga arrays, which are located in Australia at 82° away, events of $M_w = 4.3$ could be seen only marginally above the noise level after stacking. These observations imply a serious problem for the detection and location of small magnitude seismic events in Pakistan. We are in the process of examining these events at other short-period arrays in Scandinavia. For small events, the P- and S-waves are distinct phases observed in regional seismograms when filtered to high frequencies and can provide travel time information with sufficient accuracy to find their preliminary locations. Our goal is to determine how the locations of the small events determined using the PAKN array data alone (Figure 13) are affected when travel time data from a station in the KNET array are added.

Of the events shown in Figure 13, we found that 23 events were also recorded at AAK or AML (KNET network stations) and the event triggered algorithm could detect both P- and S-waves in the frequency band between 1 and 8 Hz. We found evidence for more events recorded at AAK, but the algorithm failed to detect these additional events due to the poor SNR level as is shown in Figure 18. The top three seismograms are the three-component broadband seismograms recorded at AAK and are dominated by long-period noise. By filtering these broadband seismograms in different frequency bands, both P- and S-waves can be somewhat enhanced above the noise level as shown in the next six seismograms. We mark the P arrivals on the vertical component and S arrivals on the horizontal components. The first three seismograms were filtered in the 1.5-2.5 Hz frequency band and bottom three seismograms were filtered in the 1.0-8.0 Hz frequency band.

Event - 10/15/92 : 020700k

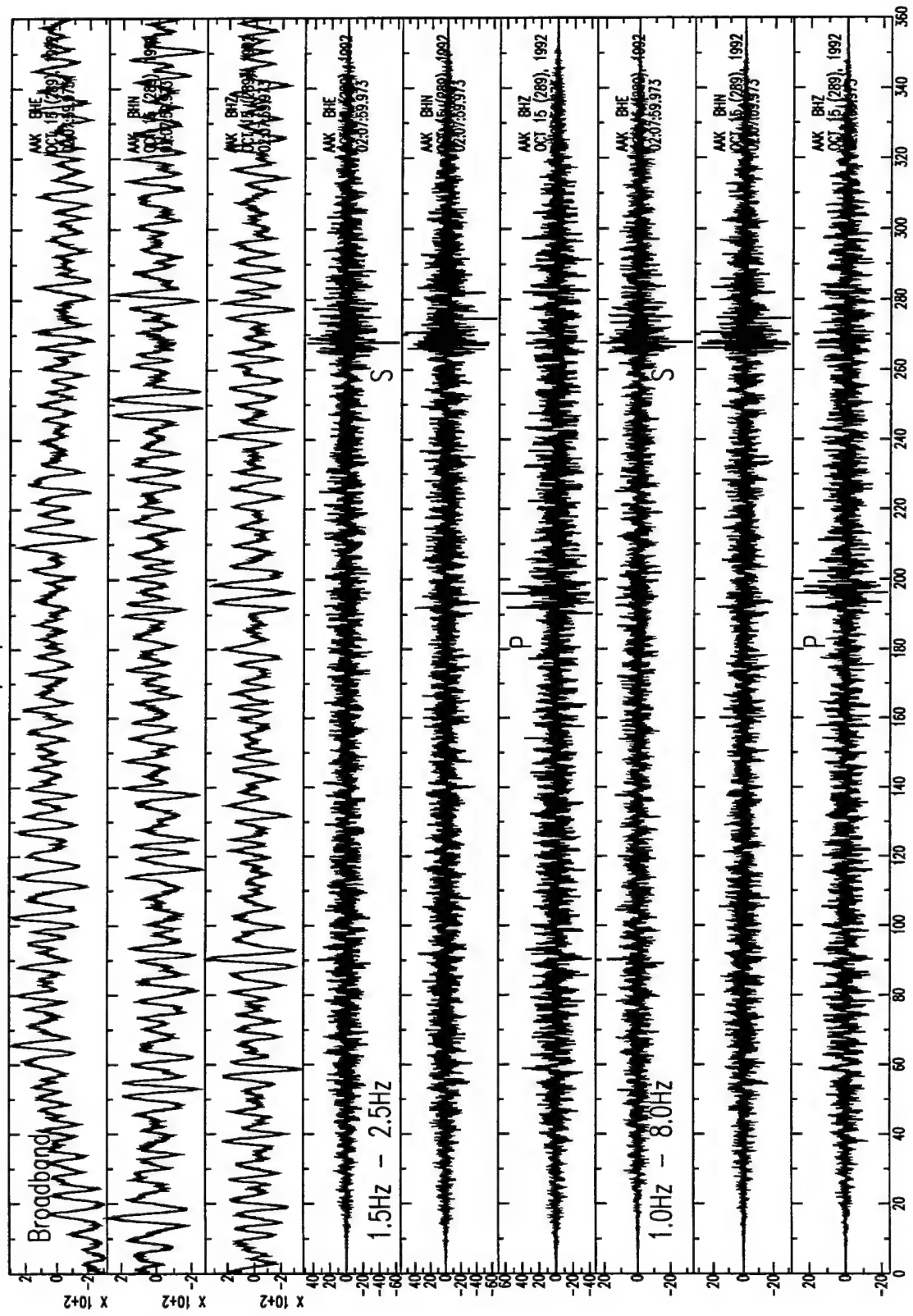


Figure 18. Examples of broadband seismograms from a small magnitude earthquake recorded at AAK. When filtered in different frequency bands, both P and S waves can be seen, but could not be detected by the event-triggered algorithm. About 50 such events were found in 10 days in the PAKN network database.

Although the signals are discernable from the noise in these high frequency bands, the characteristic function used in our event triggered algorithm could not sense these signals.

We have relocated these 23 earthquakes by augmenting the P- and S-wave travel time picks of the PAKN arrays with P- and S-wave travel time picks from AAK (or when not available, AML instead). Their new locations are shown in Figure 19. Epicenters shown in blue correspond to original locations of the events and the new locations are marked by red dots. The two locations for each event are connected by a blue line. Note that one event has shifted significantly from the original location. This event occurred close to AAK ($\approx 100\text{km}$) compared to more than 700 km away for the PAKN network. The event location begins with a starting solution closer to AAK when the travel-time information of this station are included.

The next step in our relocation effort is to determine the best locations for the events which produce minimum travel-time errors to the two broadband stations AAK and NIL, which are the existing GSETT-3 stations. This is done by improving upon the locations presented in Table 4 by using a grid search technique over a $1.5^\circ \times 1.5^\circ$ area with increments of 0.02° . Since NIL was not operating in 1992, we replace NIL by SBRA (PAKN) because it is the closest PAKN station to NIL, or by an another station from the network located close to SBRA when SBRA was not operational. This relocation algorithm follows the following mathematical formulation and requires station co-ordinates, initial locations and a one-dimensional layered velocity structure for the region.

Given the initial epicentral location for a seismic event, the code computes epicentral distances (R) to all the stations and finds ray parameters (p) for the direct P- and S-waves, and for the diving P and S rays from the Moho discontinuity appropriate for those distances at some selected source depths (in our case $h = 20\text{ km}$ and 100 km). Using these ray parameters and epicentral distances, travel times of individual rays are determined which are computed using the following relation:

$$T = pR + \sum_{j=1}^N h_j \eta_j , \quad (9)$$

where h_j and η_j are the thickness of a layer and vertical slowness of either the P or the S wave, respectively. To compute the reference time of the event, we compute the average of origin times

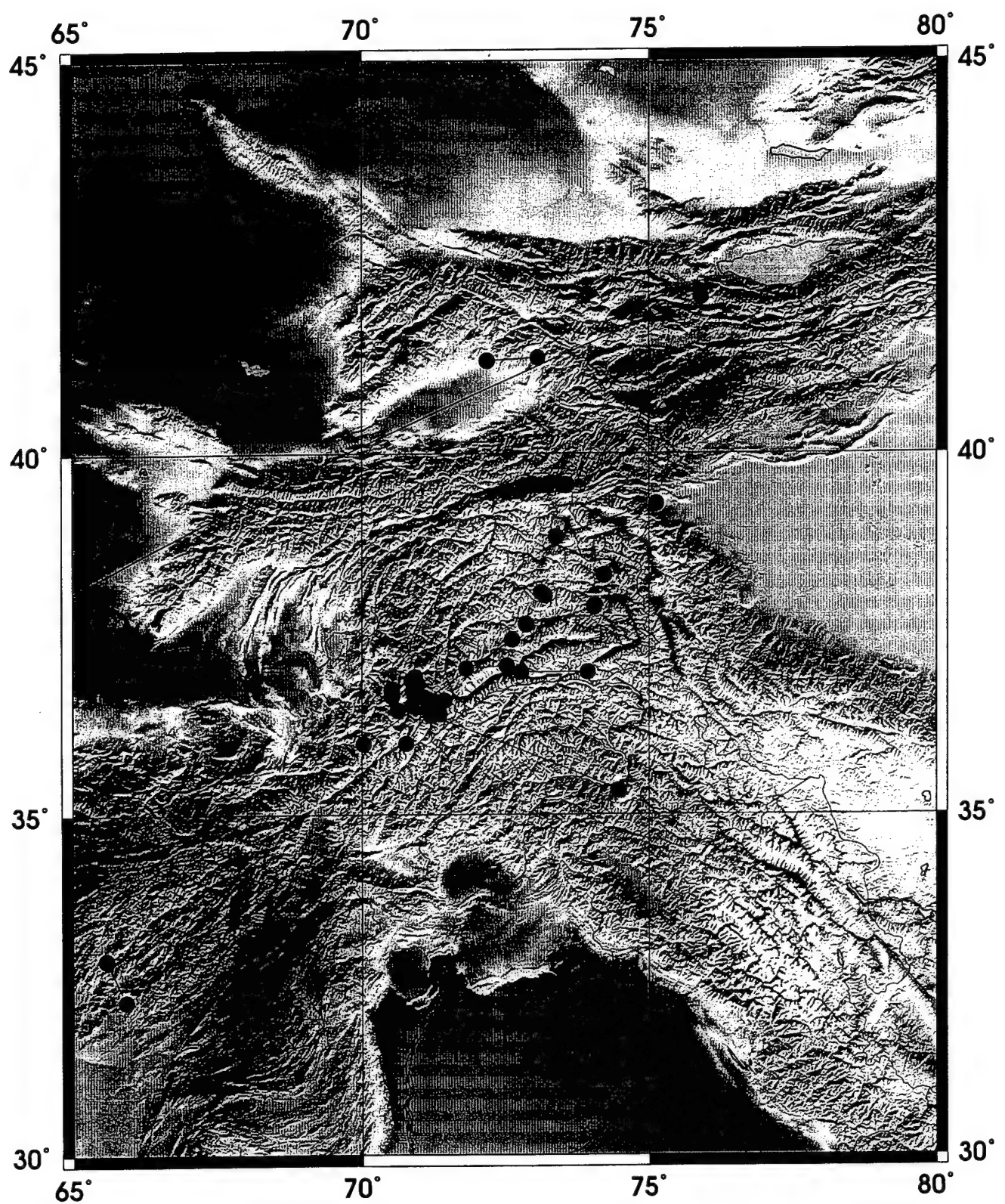


Figure 19. Map showing the shifts in epicentral locations of events presented in Table 5 relative to their locations presented in Table 4. These relocations are based on augmenting the PAKN travel-time data by adding the travel-time data from one KNET station, in most cases AAK.

calculated for the event from every station by subtracting travel times of the P- wave from the P arrival times for all stations. This reference time is used to minimize the travel time residual of the P- and S-waves to find the best location. This algorithm was tested on synthetic seismograms and solutions converged to the true solution for as few as two stations. However, when applying to data, it appears it may encounter difficulty in finding the depth based on two stations as more than one solution was identified for several events. This limitation comes from the deficiency in the crustal model and in the misidentification of the S phase. We have assumed that beyond the critical distance the S phase identified by the detection algorithm in high-frequency seismograms is the diving ray and the P-wave identified by the algorithm is the P_n wave. Figure 20 shows the comparison of these new locations determined using two stations with those obtained using all stations from the PAKN network and one station from the KNET network. These locations are also presented in Table 5. It is clear that new locations (shown by red circles) obtained using two stations, one from each network, have moved from the locations determined using the PAKN network and AAK data. These are our final locations relative to two broadband stations AAK and SBRA.

Thus, we have established a procedure for locating small events ($M_L > 3.5$) relative to two broadband stations when a temporary broadband array is emplaced in the same region. Such an array allows one to characterize small events in a region, and to calibrate two-station locations relative to those of a more extensive array. Location information of this type is crucial to identifying small events which may be observed only by two regional IMS stations or by one teleseismic array of the IMS.

4. $E_{sp-Pz}:E_{lp-3}$ Ratio Discriminant for the Middle East - Further Analysis

As part of the calibration procedure, we have extended the analysis of the $E_{sp-Pz}:E_{lp-3}$ discriminant from the region covered by the stations NIL (surrogate for the PAKO array and itself an IDC beta station) and AAK, west to the region covered by ABKT, site of the ABKO array. Figure 21 is a map of the greater area showing the stations and the events observed; events are color-coded with respect to the recording stations. The results for the stations AAK and NIL, and the PAKN array are in the previous technical report (Saikia *et al.*, 1996). We compiled additional broadband seismograms from fifty-eight events recorded by ABKT and analyzed them to calibrate the station with respect to the $E_{sp-Pz}:E_{lp-3}$ discriminant. Hypocentral parameters of these events are taken from the monthly PDE (preliminary determination of epicenters) bulletin and given in Table

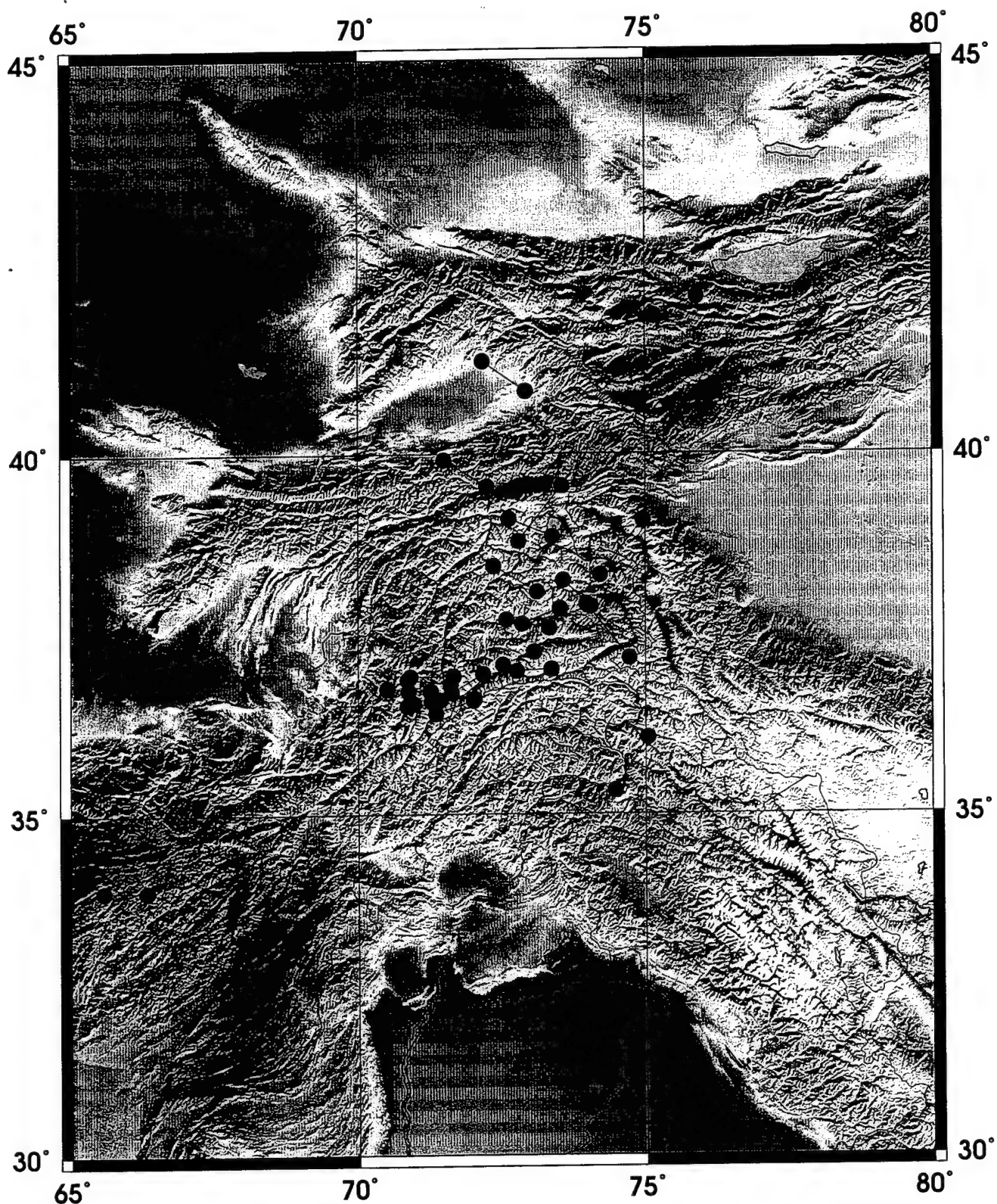


Figure 20. Map showing the refined epicentral locations of events relative to the locations presented in Table 5. This was done by a grid-search technique presented in Section 3.3. These relocations were made using travel-time data from SBRA (surrogate for station NIL) and station AAK.

Table 5. Relocations of Events using the PAKN network and
AAK station data

Yr/Mo/Dy	h:m:s	Lat °N	Long °E	Depth (Km)
1992/10/02	01:02:13.0	36.603	71.274	20.1
1992/10/02	04:10:34.5	42.032	75.908	44.7
1992/10/02	14:38:47.7	38.122	73.109	74.3
1992/10/15	02:42:02.3	39.929	71.484	20.0
1992/10/15	19:42:12.8	38.358	74.213	149.2
1992/11/06	07:21:53.9	41.220	72.167	20.0
1992/11/12	09:09:35.6	37.474	72.597	17.6
1992/11/12	11:45:06.4	36.436	71.343	43.3
1992/11/12	14:54:12.9	37.206	74.724	20.0
1992/11/12	19:25:36.2	38.880	73.376	32.0
1992/11/12	20:41:04.0	36.549	70.856	202.6
1992/11/17	00:44:03.7	36.758	70.873	20.0
1992/11/17	02:38:25.1	32.904	65.574	20.0
1992/11/17	14:35:53.8	37.023	72.757	0.0
1992/11/17	14:48:19.9	35.348	74.470	30.9
1992/11/17	16:36:12.8	36.628	71.427	20.0
1992/11/17	16:48:39.0	36.904	70.851	29.1
1992/11/17	19:26:59.3	37.684	72.842	20.0
1992/11/17	22:27:10.2	37.920	74.041	18.8
1992/11/23	03:40:08.6	37.110	72.510	10.0
1992/11/23	07:11:17.0	36.952	70.909	40.6
1992/11/23	17:50:59.3	36.780	70.505	20.0
1992/11/23	23:10:52.1	39.575	73.539	20.0

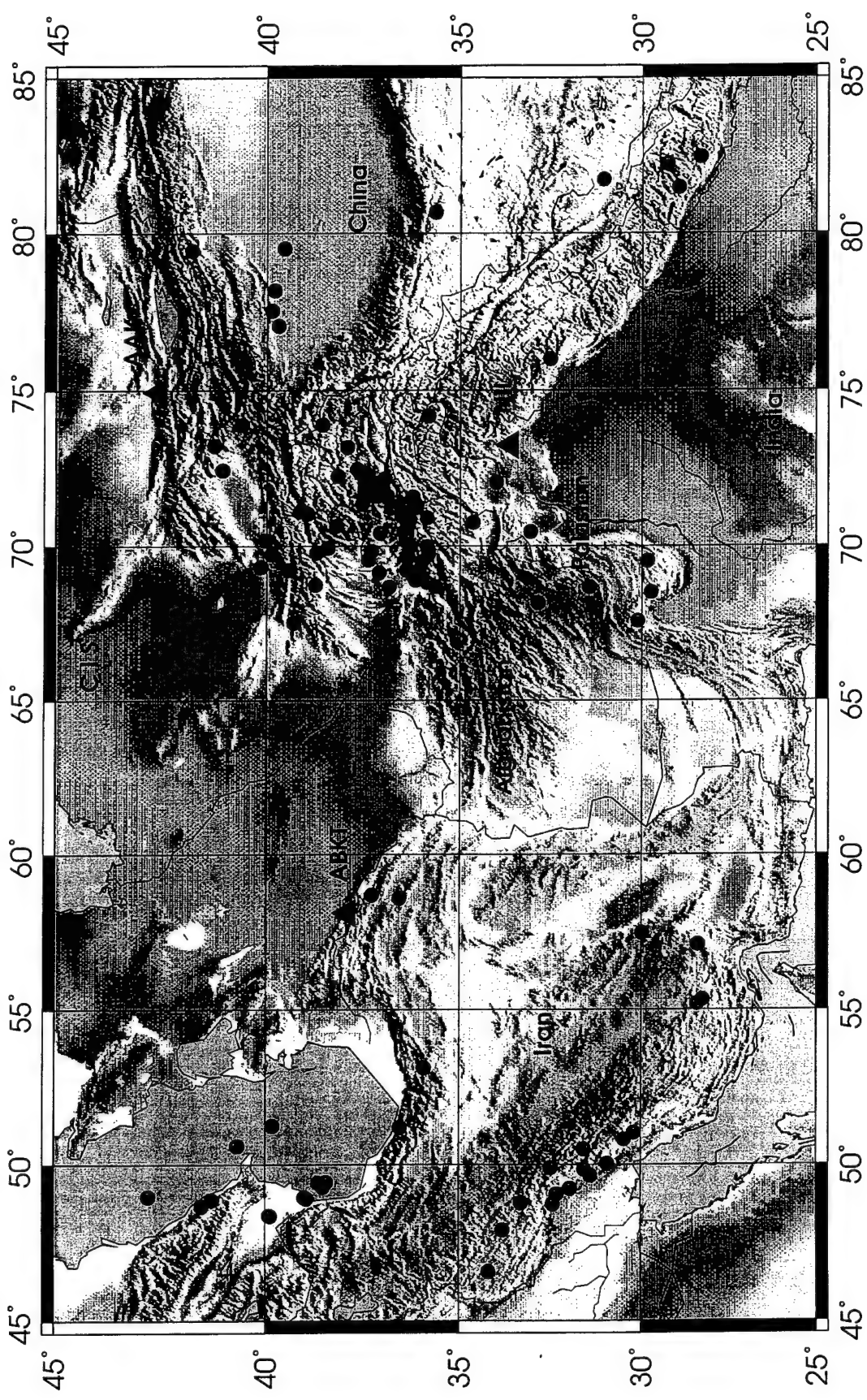


Figure 21. Map of that portion of the Middle-East for which calibration analysis of the $E_{sp-Pz}:E_{lp-3}$ ratio has been done. The IMS stations used are triangles. Events are color-coded with the station by which they were recorded.

6. Body-wave magnitudes of these events range between 3.8 and 4.9 and thirty-seven events have depth given as 33 km. Deep seismicity ($h > 100$ km) is limited to the Hindu-Kush region, with the exception of the Caspian Sea where there are a few deep events as well. Seismicity in Iran appears to extend down to a depth of 80 km. No known large explosions within this area are recorded by ABKT.

As had been discussed in the last scientific report (Saikia *et al.*, 1996), depth has a significant influence on the $E_{sp-Pz}:E_{lp-3}$ ratio, with deep earthquakes generating little or no long-period surface wave energy and thus appearing explosion-like by the discriminant's criterion. This is shown in Figure 22, which plots the $E_{sp-Pz}:E_{lp-3}$ ratio *vs.* distance for PAKN-recorded events; the deep events (circles) plot higher than other earthquakes at crustal (squares) or near-moho (triangles) depths. Thus, it is important when calibrating data, to analyze them in terms of source depth. Also as noted in the previous report, normalizing the energy ratios with respect to magnitude, helps to mitigate source-scaling effects on the discriminant parameter and improves the separation between explosions and crustal earthquakes.

In the previous analyses of AAK and NIL data, depth information was taken from the PDE catalog, however source depths were not available for all events. In order to fill-out the ground truth source depth data, we have incorporated IDC REB depth information, whenever available. It should be noted, however, that the PDE and REB depths did not always correlate well. Figure 23 plots the PDE *vs.* REB depth. For plotting purposes, PDE depths of 33 km were used as such and events without RED depths are given a depth of 5 km. Note that in some cases that crustal or sub-moho ($D < 80$) depth events for one catalog are considerably deeper according to the REB catalog. For consistency's sake we used the PDE depths whenever possible. These depth discrepancies are discussed further in other sections of this report.

The $E_{sp-Pz}:E_{lp-3}$ discriminant data for NIL and AAK are plotted in Figures 24 and 25, respectively. The energy ratios have been normalized with respect to magnitude and the events have been sorted by depth. At both stations the effect of source depth on the ratio is more apparent with the updated and more extensive depth listing. The deep events which plot low, within the shallower earthquake population are those with large long-period S-wave energy or which have considerable long-period noise in the surface-wave time window. Figure 24 also includes one data point for a Lop

Table 6. Catalog of events recorded by ABKT and used in
the short-period:long-period energy ratio study

Jdate	ID	Hr:Mn:Sec	Mag	Lat	Lon	Depth
9500301		23:32:44.0	4.3	38.761	68.735	33
9500401		00:57:51.6	4.5	41.285	48.874	33
9506301		21:36:14.9	4.1	36.236	69.031	314
9506401		08:14:52.7	3.9	35.837	69.871	200
9506701		06:27:26.1	4.1	35.832	69.747	150
9506703		07:38:08.5	4.2	34.223	46.563	21
9506702		07:58:01.9	4.3	31.614	50.493	33
9508101		00:44:46.9	4.3	36.433	70.223	230
9508102		06:28:36.8	4.8	30.209	51.040	79
9508201		08:07:51.5	3.8	32.889	68.143	85
9508401		11:23:27.9	4.6	33.834	47.905	33
9512101		05:31:50.6	4.4	33.331	48.771	33
9512501		02:40:28.4	4.5	35.880	68.824	33
9512502		03:06:53.5	4.4	36.017	69.508	160
9513301		07:20:43.2	4.8	40.678	50.592	53
9513401		04:47:00.1	4.8	39.883	69.728	34
9513501		00:16:52.5	4.8	38.468	49.435	119
9513502		00:21:54.7	4.5	38.540	49.290	33
9514501		09:05:02.0	4.4	40.017	70.190	43
9514701		08:34:38.3	4.6	30.488	50.817	51
9514702		21:21:31.9	4.8	39.028	48.944	33
9515401		20:08:33.1	4.0	35.927	53.124	33
9515402		23:17:21.7	4.2	28.420	55.193	33
9515801		10:04:06.3	4.3	31.989	49.234	33
9515802		23:09:47.0	4.6	32.461	48.737	21
9515901		07:32:15.9	4.4	28.275	55.332	33
9515902		20:21:09.5	4.4	32.360	49.050	33
9516401		15:55:00.8	4.5	36.419	69.654	33
9516501		05:42:33.3	4.5	36.585	58.598	33

Table 6. (Continued) Catalog of events recorded by ABKT
and used in the short-period:long-period energy ratio study

Jdate	ID	Hr:Mn:Sec	Mag	Lat	Lon	Depth
9516601		03:01:35.7	4.2	31.600	49.850	280
9516602		18:37:28.0	4.6	38.446	69.928	90
9516801		05:57:27.5	4.0	36.870	68.659	33
9517701		21:12:55.8	4.1	36.560	51.196	33
9517702		23:27:38.8	4.4	39.873	48.344	67
9517801		00:46:46.3	4.3	39.900	48.372	74
9518601		14:56:31.8	4.3	36.324	69.969	204
9518701		16:45:10.7	4.0	38.664	49.411	33
9519101		01:54:55.7	4.3	30.964	50.028	33
9519501		14:03:06.6	4.2	42.810	48.970	53
9520101		04:20:52.8	4.5	35.874	69.978	33
9520102		20:44:24.5	4.3	31.494	68.675	33
9520201		01:48:18.3	4.4	32.504	49.906	61
9520401		11:28:06.7	4.3	39.460	69.210	54
9521701		16:46:56.1	4.1	31.430	49.650	33
9522501		00:57:23.4	3.9	36.403	69.626	110
9522801		02:16:50.6	3.9	37.120	70.410	33
9522901		18:09:58.7	4.5	38.961	48.908	74
9523001		04:24:36.6	4.3	41.542	48.672	61
9523701		01:53:51.7	4.0	35.655	68.688	33
9523702		10:53:01.4	4.9	28.417	57.116	79
9524301		03:18:03.5	4.1	37.145	69.138	41
9524501		20:48:57.2	3.9	36.421	69.222	245
9524701		12:10:20.6	4.2	39.820	51.250	33
9524702		17:47:09.5	4.4	29.995	57.486	33
9525601		01:37:20.4	4.0	37.423	69.543	33
9526501		04:16:33.3	3.8	36.341	70.037	172
9526502		12:56:23.7	3.9	37.320	58.706	33

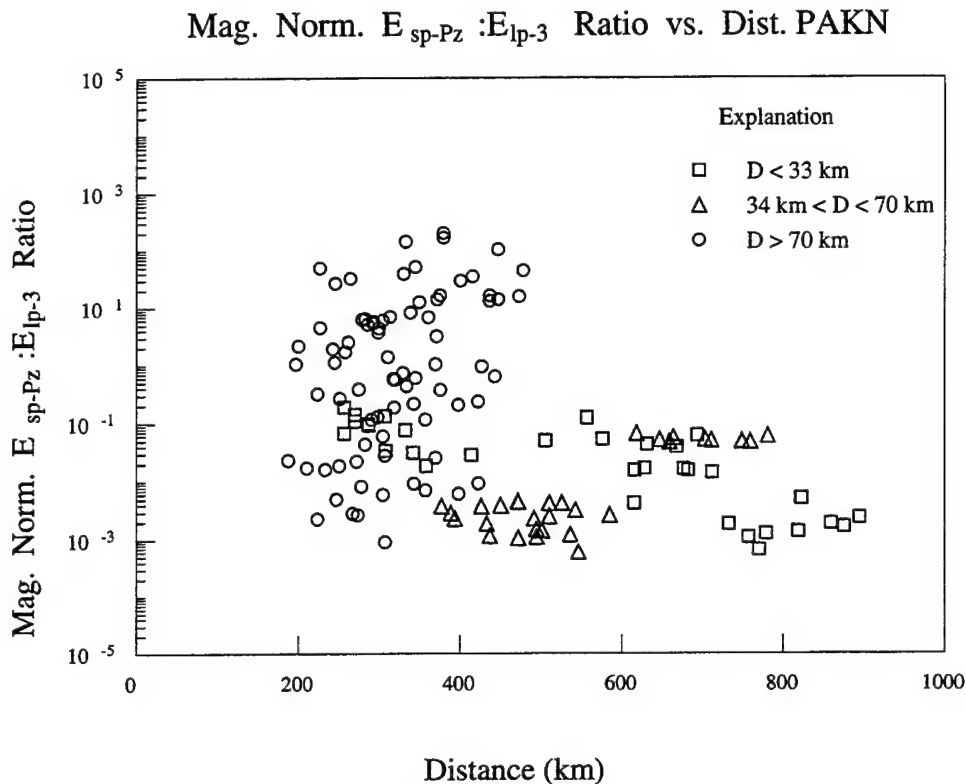
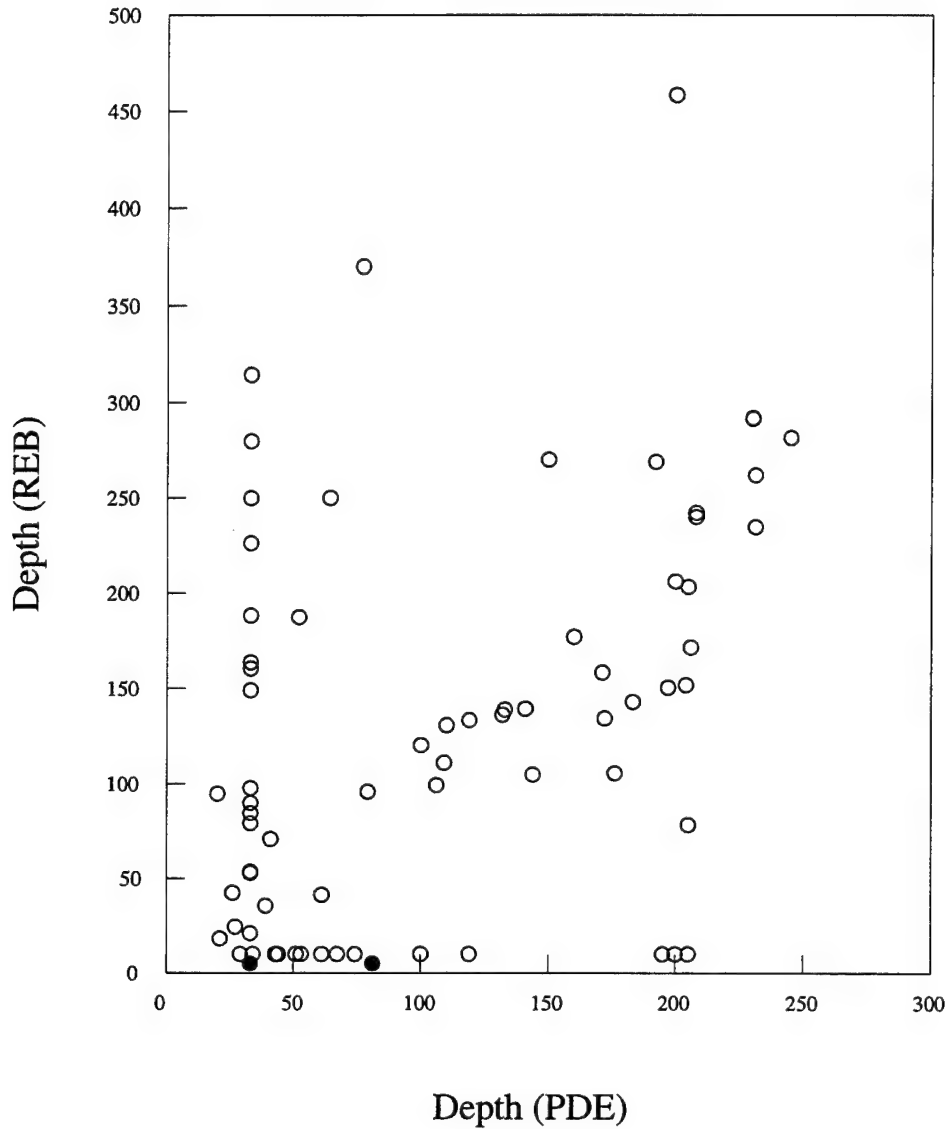


Figure 22. Magnitude-normalized $E_{sp-Pz} : E_{lp-3}$ ratio vs. distance for master event data recorded by the PAKN array and are sorted with respect to PDE source depth. Shallow earthquakes ($D \leq 33 \text{ km}$) are denoted by squares, intermediate-depth ones ($33 < D < 70 \text{ km}$) by triangles, and deep events ($D > 70 \text{ km}$) by circles.

PDE vs. REB Depth



Mag. Norm. $E_{sp-Pz} : E_{lp-3}$ Ratio vs. Dist. NIL

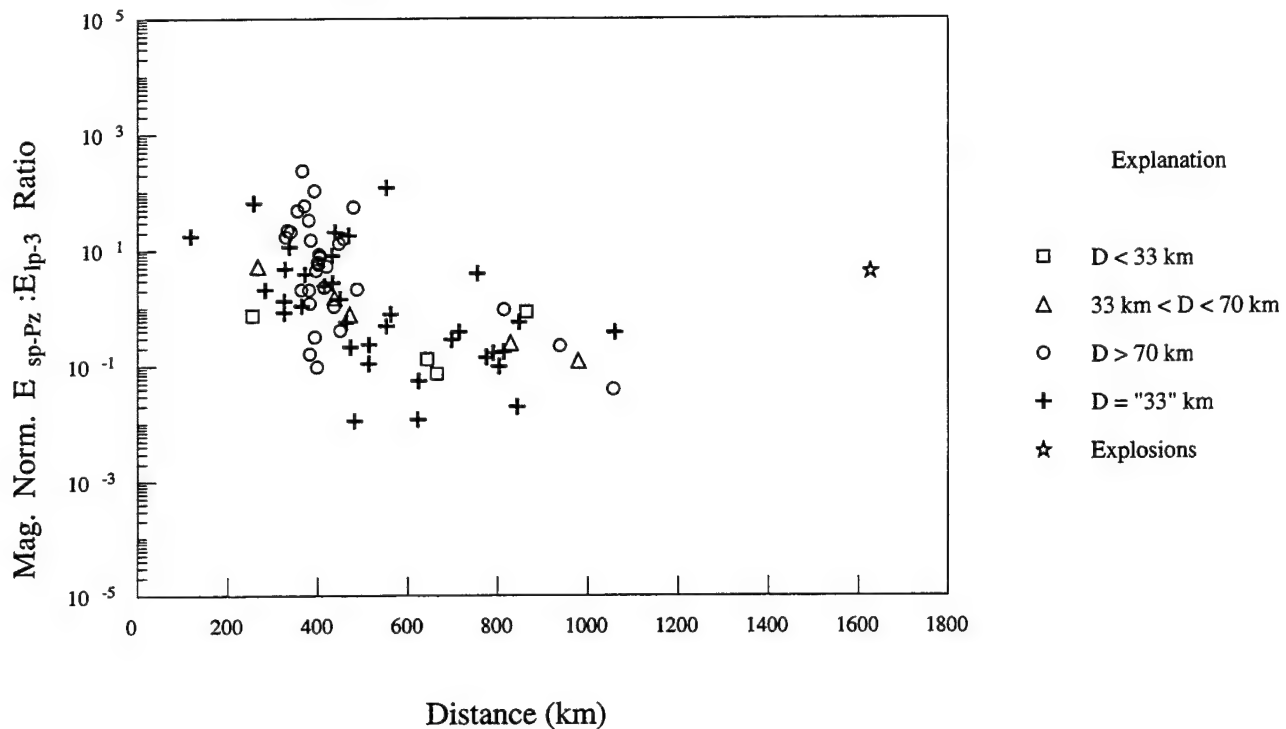


Figure 24. Magnitude-normalized $E_{sp-Pz} : E_{lp-3}$ ratio vs. distance of earthquakes and one Lop Nor explosion (star) recorded by NIL. Again, the earthquakes are sorted by depth. Shallow earthquakes ($D \leq 33$ km) are denoted by squares, intermediate-depth ones ($33 < D < 70$ km) by triangles, deep events ($D > 70$ km) by circles, and events with PDE depth "33 km" by crosses. When available, REB source depths were used to fill-out the data set.

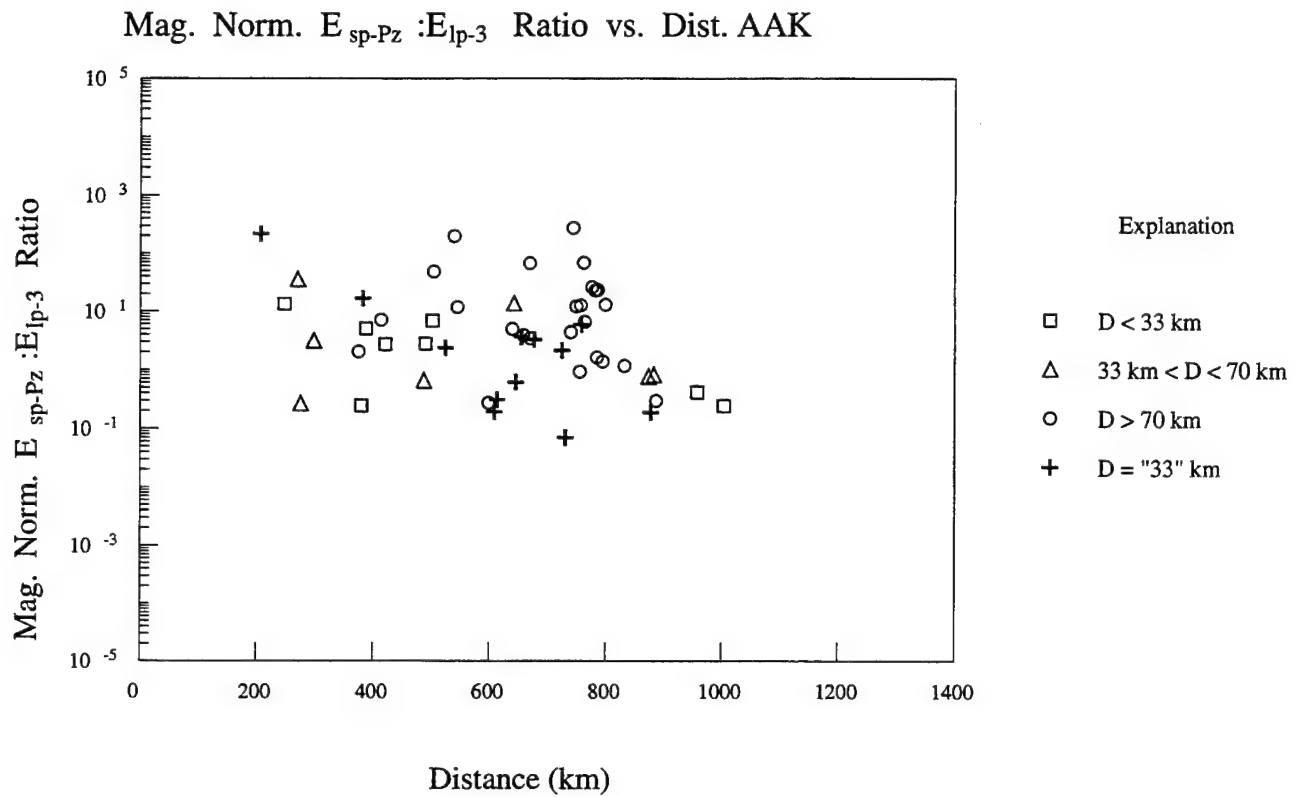


Figure 25. Magnitude-normalized $E_{sp-Pz} : E_{lp-3}$ ratio vs. distance for earthquakes recorded by AAK. Again, the earthquakes are sorted by depth. Shallow earthquakes ($D \leq 33$ km) are denoted by squares, intermediate-depth ones ($33 < D < 70$ km) by triangles, deep events ($D > 70$ km) by circles, and events with PDE depths of "33" km by crosses. When available, REB source depths were used to fill-out the data set.

Nor explosion recorded by NIL. It appears that this point should plot high with respect to the energy-ratio/distance curve for crustal and shallow mantle earthquakes, although it may well fall into the deep earthquake population. We are currently retrieving the data for all Lop Nor explosions (as well as moderate-sized earthquakes with hypocenters within several degrees of Lop Nor) recorded by these stations to make more conclusive analysis of this discriminant using a more comprehensive ground truth database. Moreover, events in Southern Pakistan below the 33° latitude are also being gathered for analysis in order to extend the calibration of NIL azimuthally.

Figure 26 is a plot of the magnitude-normalized $E_{sp-Pz}:E_{lp-3}$ ratio vs. distance for ABKT recorded events. In comparing them to Figure 24 for the AAK data, the ABKT energy ratios have lower values than those for the other station, implying that propagation effects differ between the two regions covered by the stations. Further, there are no events identified as having source depths less than 34 km for the ABKT data set, so it is not clear how upper-crustal earthquakes behave, although it is expected that they would have the lowest energy ratios of all the data. Re-analysis of the $E_{sp-Pz}:E_{lp-3}$ discriminant for these data in terms of depth effects should be done once a regional crustal model is developed for this station and accurate depth estimates can be obtained for all events analyzed.

In an effort to ascertain whether or not there is regional variations in energy ratio values, the data for ABKT were separated into two general regions, one being the Hindu-Kush area and other being all events to the west. Figure 27 is a modified version of Figure 26 with events to the far east of ABKT in Hindu-Kush shown as open symbol, while events west of there are filled. No obvious differences are seen between the two regions, implying that a single regional calibration for $E_{sp-Pz}:E_{lp-3}$ ratios will suffice for this station. However, a more extensive data set is required to make a conclusive statement to this effect.

A test set of small events ($M_L < 4$) was obtained from the PAKN array in order to ascertain the magnitude threshold limits on the energy ratio discriminant and source location procedure (Section 3 of this report). These events were too small to be listed by the PDE. It was found by examining the waveforms that the long-period SNR went below unity at about M_L of 3.8. Thus, the $E_{sp-Pz}:E_{lp-3}$ analysis for these events was not performed, as the ratios would only reflect minimum values.

Mag. Norm. $E_{sp-Pz} : E_{lp-3}$ Ratio vs. Dist. ABKT

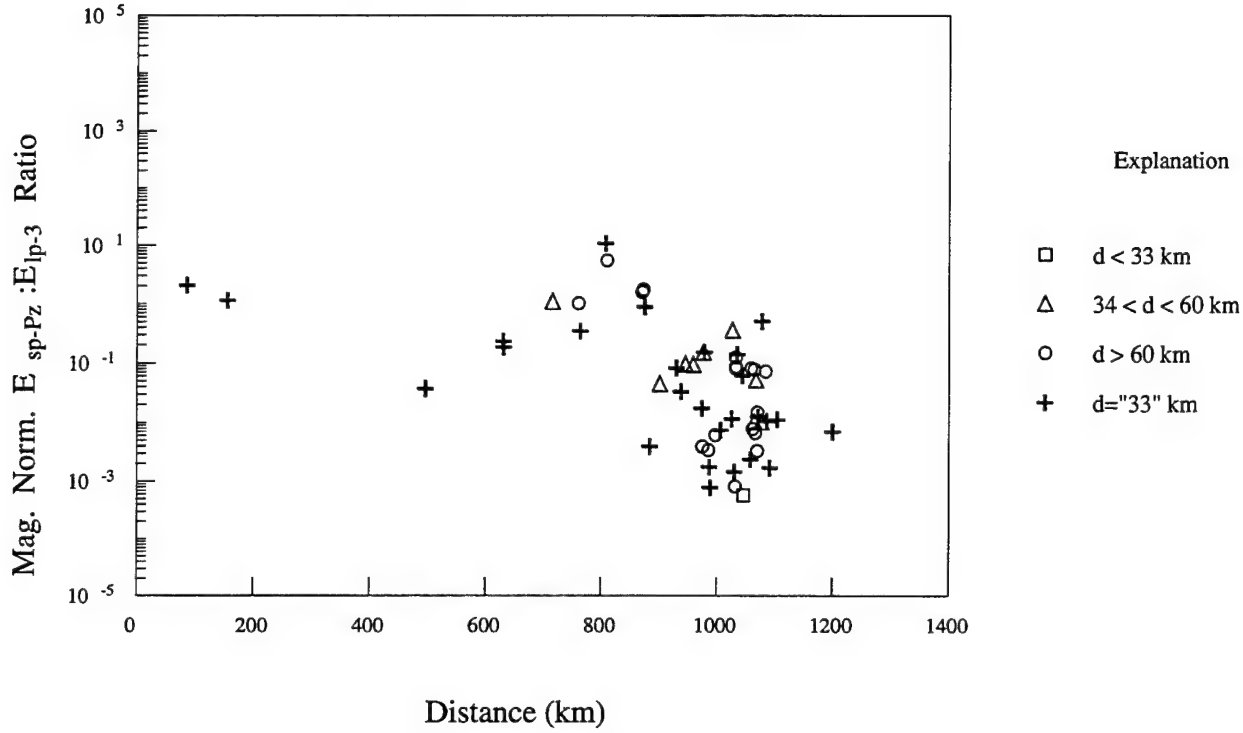


Figure 26. Magnitude-normalized $E_{sp-Pz} : E_{lp-3}$ ratio vs. distance for earthquakes recorded by ABKT. Again, the earthquakes are sorted by depth. Shallow earthquakes ($D \leq 33$ km) are denoted by squares, intermediate-depth ones ($33 < D < 70$ km) by triangles, deep events ($D > 70$ km) by circles, and events with PDE depths of "33" km by crosses. When available, REB source depths were used to fill-out the data set.

Mag. Norm. $E_{sp-Pz} : E_{lp-3}$ Ratio vs. Dist. ABKT

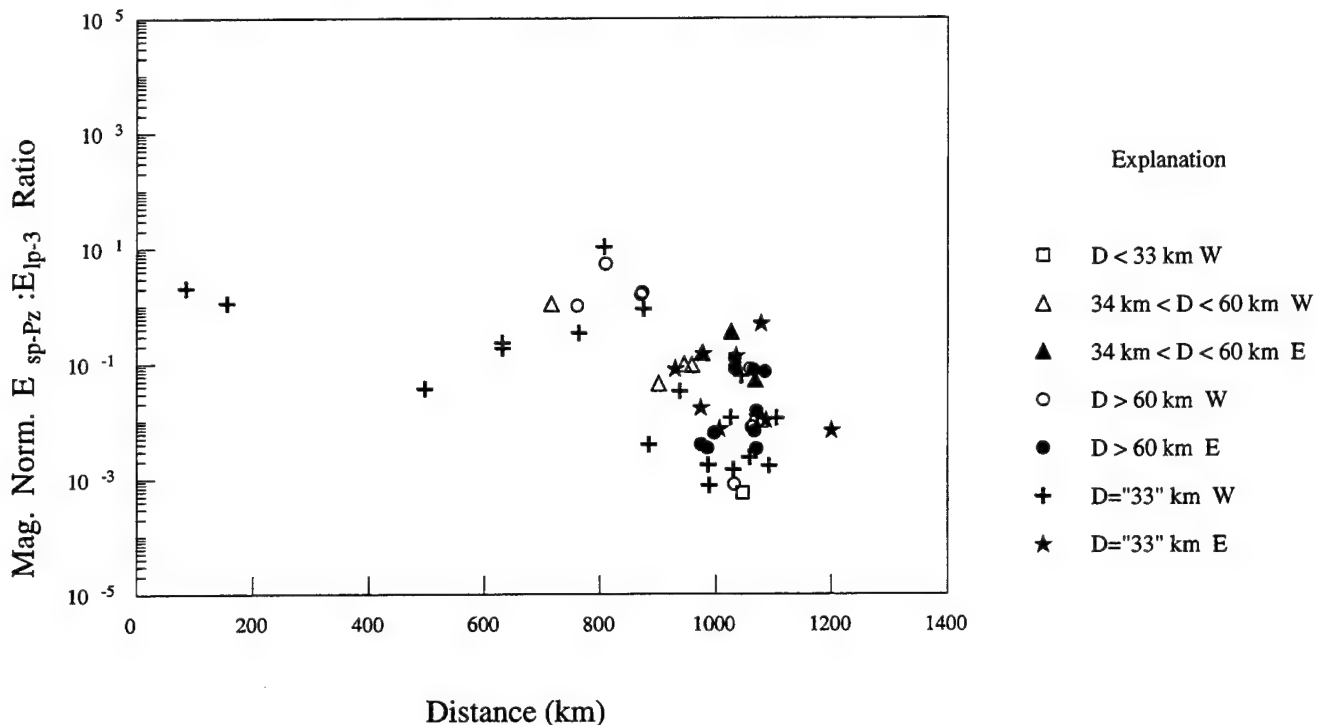


Figure 27. Magnitude-normalized $E_{sp-Pz} : E_{lp-3}$ ratio vs. distance for earthquakes recorded by ABKT. Again, the earthquakes are sorted by depth and geographic location. Shallow earthquakes ($D \leq 33 \text{ km}$) are denoted by squares, intermediate-depth ones ($33 < D < 70 \text{ km}$) by triangles, deep events ($D > 70 \text{ km}$) by circles. Symbols for earthquakes in the east in predominantly the Hindu-Kush region are filled; symbols for events to the west of ABKT are open. Western events with unknown source depths are denoted by crosses, while such events to the east are denoted by stars.

4.1 Work in Progress Relating to the $E_{sp-P_z}:E_{lp-3}$ Ratio:

In order to expand characterization of the performance of the $E_{sp-P_z}:E_{lp-3}$ ratio for this region of the world, we are extending event analysis to other azimuths and greater distances. In particular, we are now acquiring and processing data for events in Southern Pakistan and into India (Latitude < 33°), as well as to the Northeast towards the Lop Nor test site. This latter region will yield data at distances of between 1100 km and 1700 km for AAK and NIL, respectively, as well providing ground truth data regarding nuclear explosions to determine the performance of these stations with respect to the energy ratio discriminant.

In regard to the operational status of this discriminant for the IDC, we will be quality-checking the current processing practices. Currently, only approximately 10 to 15 percent of IMS identified events are being analyzed with respect to this discriminant; which is on par with the performance of the regional $m_b:M_s$ discriminant (Robert North, personal communication 1996). To that end we will evaluate the present IDC SNR criteria for the discriminant to determine whether or not the measurement can be extended to a larger percentage of the data. Further, we will quality-check the IDC energy ratio measurements to insure that proper time windows and signal to noise levels are being used in calculating the discriminant ratio.

As the IDC energy ratio measurement is being conducted globally, we will evaluate the discriminant for other regions throughout the world where other anomalous event (non-earthquake) data is available. In particular large mining blasts, collapses, and large chemical explosions, as well as natural seismicity in Europe shall be examined.

As part of the global monitoring mandate, it is necessary to be able to directly compare the behavior of any operational discriminant from region to region. To this end, we will develop empirical path corrections for the monitoring stations in our study area as well as for other stations throughout the world which have recorded anomalous events, (i.e. non-earthquakes).

5. The Western Mediterranean

Monitoring of a Comprehensive Test Ban Treaty (CTBT) in the Mediterranean region and North Africa is complicated because of the strongly varying geologic structure in the region, and sparse station distribution in North Africa. The purpose of this section is to familiarize the reader with the tectonic and geologic setting of the region, and to point to the specific problems that this region poses on seismic studies as well as to present our approach to solving these problems.

5.1 Regional Tectonics

The Western Mediterranean region, including Southern Spain and Northern Africa, consists of several contrasting geologic provinces. The tectonically most active areas are found along the coast of North-Africa, from the Gulf of Sirte to the east, to the Strait of Gibraltar to the west, along the southern coast of Spain and along the length of the Italian peninsula and through Sicily (Figure 28). The major tectonic provinces in the region are: the Betic, Rif and Tell mountains, the Alboran Sea, the Atlas mountains and the Saharan shield.

Subcrustal earthquakes occur in two zones, the Calabrian arc where a well-defined subduction zone exists and near and around the Alboran Sea, where earthquakes occur down to a depth of 150 km, except for a very small area near Granada, where earthquakes occur at a depth greater than 600 km.

The Betic Cordillera of Southern Spain on one end and the Rif Mountains of Morocco and the Tell Atlas of Northern Algeria on the other end are mirror images of each other and these mountain ranges form the opposing limbs of a very tight arcuate structure, the arc of Gibraltar. The mountains are regarded as part of the general Alpine system of Europe.

The western end of the Mediterranean sea between the Betic and Rif mountains, called the Alboran sea, is regarded as a tectonic entity separate from the rest of the Mediterranean and probably more related to the Betic/Rif regions. The Alboran sea is a very deep sedimentary basin containing Pliocene and quaternary sediments with thicknesses up to 3 km. The on-land Cheliff basin, located in and along the Tell Atlas mountains in Northern Algeria, is similar in content to the Alboran basin and reaches sediment thicknesses of up to 5 km.

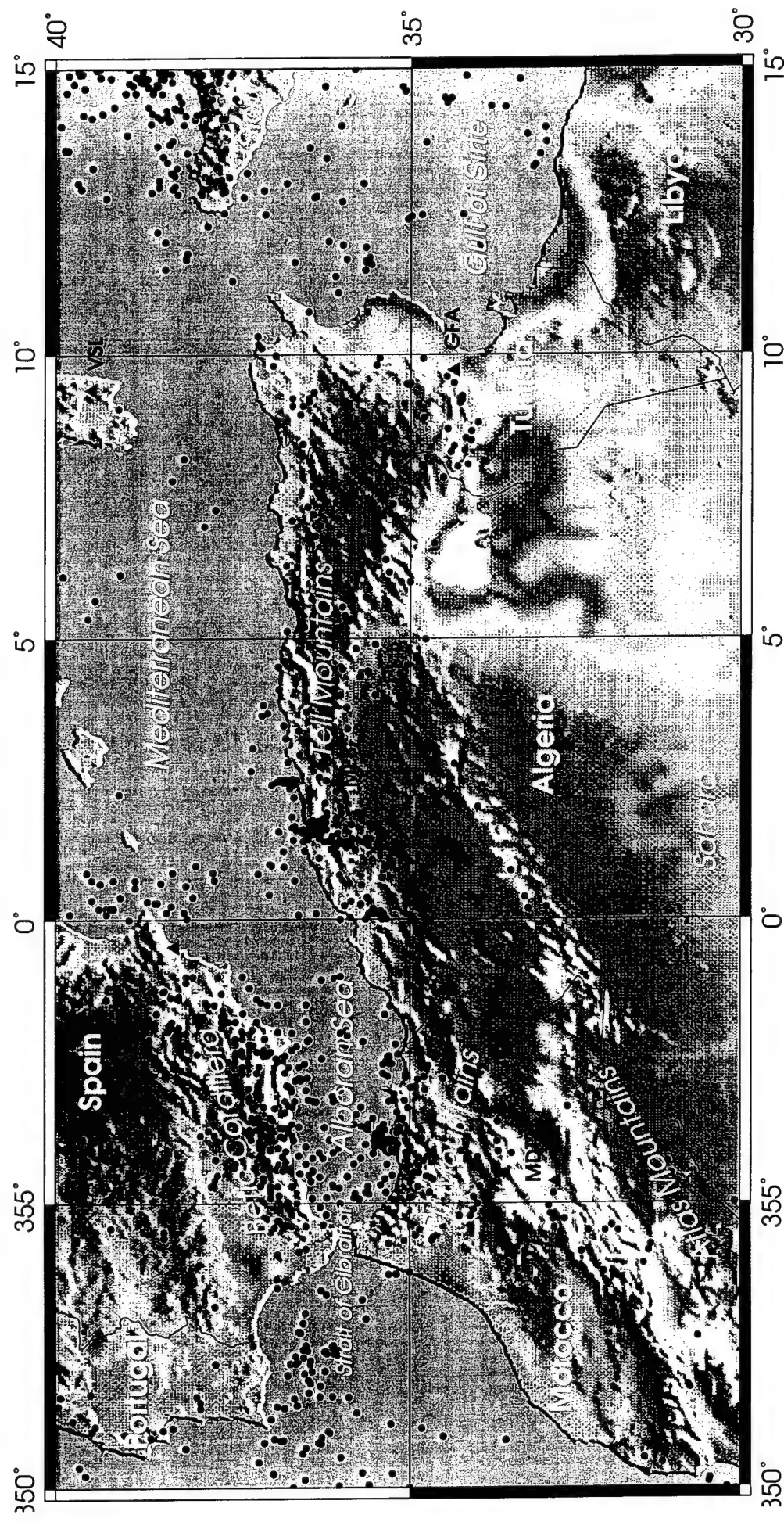


Figure 28. Seismicity map of the western Mediterranean area. Locations are from the ISC bulletin, red for crustal events ($z < 33$ km), green ($33 < z < 100$), blue ($100 < z < 500$) and grey ($z > 500$ km) for mantle events. Also indicated are the stations used in this study (black triangles).

Away from the Betic/Rif/Tell massifs we find the high plateaus, the Meseta in Spain, on which station TOL/PAB and the Sonseca array are located, and the Maghreb massif in Morocco and Algeria. These, and the main Atlas ranges are of pre-alpine age. However, there is considerable seismic activity along the High Atlas mountains. The 1960 Agadir earthquake, one of the most well-known earthquakes in the region, occurred at the Southwestern end of the Atlas mountains, on the border between the Atlas mountains and the Precambrian Sahara plateau to the south.

The Precambrian plateaus south of the Atlas mountains can be divided into two platforms, the West African shield, which has not seen any tectonic activity since the late Precambrian, and the Touareg shield which is part of the trans Saharan mobile belt, a Precambrian shield which has undergone major tectonic activity in the very late Precambrian. The Hoggar plateau in southern Algeria, near the location of station Tamanrasset (TAM) has also undergone major igneous activity in the late Precambrian, as well as tertiary to present day volcanic activity (Cahen & Snelling, 1984). Both the West African Shield as well as the Touareg shield are virtually free of any seismic activity. West of Gibraltar, the Azores-Gibraltar fracture zone delimits the boundary between the Eurasian and African plates.

5.2 Historic Seismicity

The historical seismicity of the Western Mediterranean region is well documented and we will present a short overview of the most significant events in the region. The largest event to have affected the region was the 1755 "Lisbon" ($M \approx 8.7$, Johnston, 1996) earthquake which probably occurred in the Atlantic ocean.

The 1980 Al Asnam ($M_s = 7.3$) earthquake has been studied extensively, and is the largest earthquake to have occurred in this region this century. Several other significant earthquakes have occurred in the same general area, the Cheliff Valley, including the 1954 Orleansville earthquake, the 1922 Cavaignac ($M_s = 5.9$) earthquake (Aoudia & Meghraoui, 1995), and an estimated $M_s = 6.5$ earthquake in 1858. Further east, there occurred a $M_s = 6.6$ earthquake in 1910 (Ambraseys *et al.*, 1991).

To the west, the seismicity decreases until beyond the Moroccan border where we find a band of seismicity around the Alboran Sea, the Rif mountains, and along the Atlas mountain ranges. The

1960 Agadir earthquake was located at the southwestern termination of the Atlas mountains. It occurred along a fault which separates the Atlas mountains from the West African shield.

Across the Straits of Gibraltar the only large recorded earthquake is the deep ($d = 600$ km) 1954 earthquake near Granada ($M = 7.0$). Although the background seismicity is fairly high in Southern Spain, no major shallow earthquakes have been recorded this century or are known to have occurred from historical records.

5.3 Seismic Structure from Previous Work

Seismic studies of the Western Mediterranean and North Africa consist of deep seismic sounding studies (Working Group for Deep Seismic Sounding in Spain, 1977; Research Group for Lithospheric Structure under Tunisia, 1992), surface-wave group velocity studies (e.g. Hadiouche & Jobert, 1988), and tomographic studies (Zielhuis, 1992).

In a tomographic study of Africa using surface waves, Hadiouche and Jobert (1988) found that the SV velocities show a sharp contrast in Northern Africa between fast velocities west of the Greenwich meridian and slow velocities east of the meridian. This corresponds roughly to the boundary between the West African craton and the Trans Saharan Mobile Belt. Snieder (1988) and Zielhuis (1992) found that the upper mantle below the Western Mediterranean is relatively slow. Corchete *et al.* (1995) studied lateral variations of the S velocity in the subcrustal lithosphere under the Iberian peninsula and concluded that a low velocity channel exists throughout most of Spain at a depth of around 40-50 km, with S velocities decreasing from between 4.5 to 4.65 km/sec to 4.3 to 4.5 km/sec. A similar low velocity zone was found under the Betic Cordillera from deep seismic sounding experiments (WGDSSS, 1977).

Seber *et al.* (1996) investigated teleseismic P-wave residuals recorded at stations in Morocco, and concluded that the Rif mountains, as well as the Alboran sea are underlain by fast upper mantle. This contradicts low P_n velocities found by Banda (1988). They reconcile these difference by assuming that the thickened lithosphere under the Rif mountains and the Alboran Sea has delaminated, so that the faster lithosphere is now overlain by hotter and slower astenospheric material.

5.4 Data and Surface Wave Analysis

We selected several earthquakes which were well-recorded at several stations in the region (Figure 29). Due to a two year lag in data availability from the MedNet network there is currently no overlap yet between the MedNet data and data available through the experimental IDC. We expect however that in the second year of this contract period there will be sufficient overlap so that we can perform direct comparisons and calibrations of the IMS stations.

Harvard and MedNet CMT solutions were available for some of these events (Table 5.1), and for one event, Al Hoceima (94146), there was sufficient high quality teleseismic body-wave data available to perform a teleseismic source inversion.

If we compare the observed seismograms (Figure 30) of the different stations for the Gafsa event (92164) it is clear that the seismic structure in the region is very heterogeneous. The stations MEB and VSL are at very similar distances (Figure 30a), yet their records are very different in character and the arrival times for the surface Rayleigh waves seem to be quite different. The same holds true for the station pair TAM and TOL (Figure 30b). Even at longer periods (Figure 31), there still exists a clear difference in group arrival times and surface waveforms between the different stations. Another striking observation is the difference in high-frequency content between the records. The recordings for paths that are located within North Africa (MEB and TAM) have a much higher frequency content than those with paths that cross the Mediterranean Sea (TOL and VSL). This suggests that the Mediterranean Sea is a very effective at blocking L_g waves and this effect becomes very obvious after applying a high-pass filter to the data (Figure 32). Whereas the stations MEB and TAM show distinct L_g arrivals, there are no L_g waves discernible on the records that have crossed the Mediterranean, i.e. at PAB and VSL. Therefore, seismic discriminants based on L_g observations are ineffective for waves crossing this part of the Mediterranean, and this probably holds true for the whole Mediterranean.

Another illustration of the effects of lateral heterogeneity can be seen from recordings from the NARS network in Spain (Nolet and Patton, 1991) for an event located in North Algeria (88305). Stations that are located close, near the coast in Spain, show considerable ringing in the surface waves (Figure 33) which diminishes as the waves propagate inland.

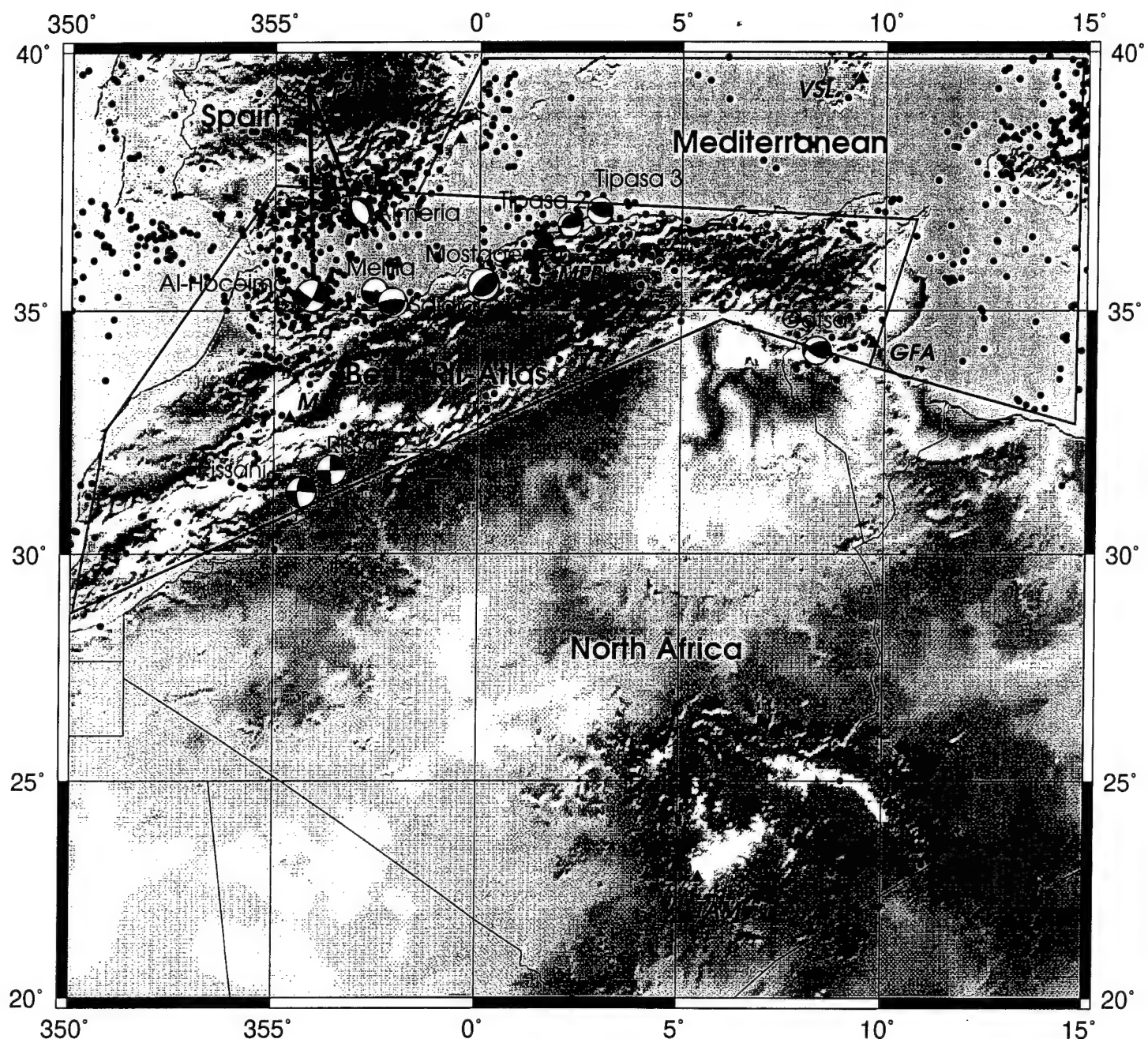


Figure 29. Regionalized model for the Western Mediterranean region. Also shown are the mechanisms and names for our master events, as well as the paths to station PAB referred to in Section 5.11. Station names are in italics.

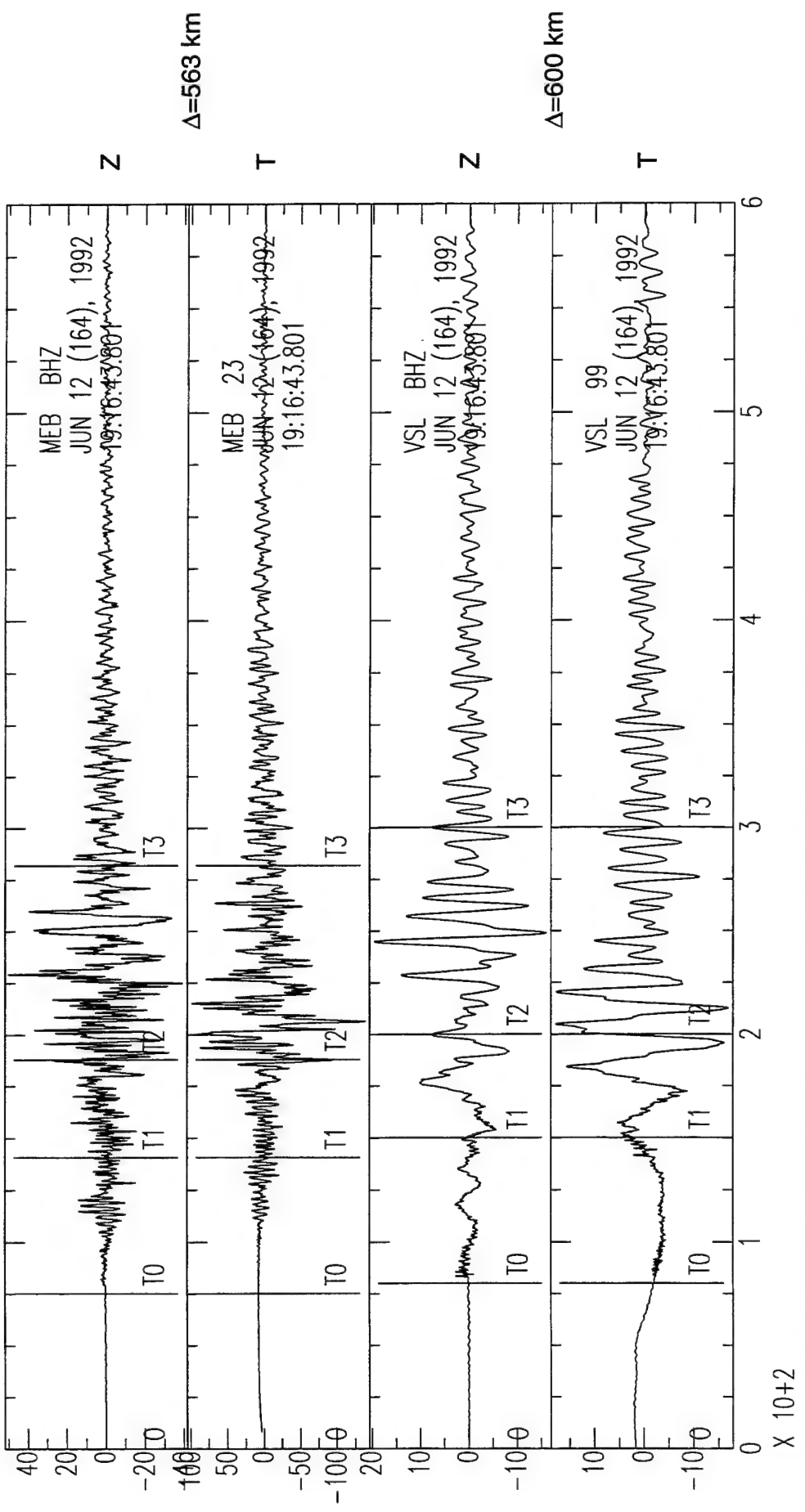


Figure 30a. Broad-band displacement seismograms for the Gafsa event recorded at stations MEB and VSL. Z - vertical traces, T - tangential traces. Amplitudes are in microns. T0 - arrival time corresponding to a group velocity of 7.5 km/sec, T1 - 4 km/sec, T2 - 3 km/sec and T3 - 2 km/sec.

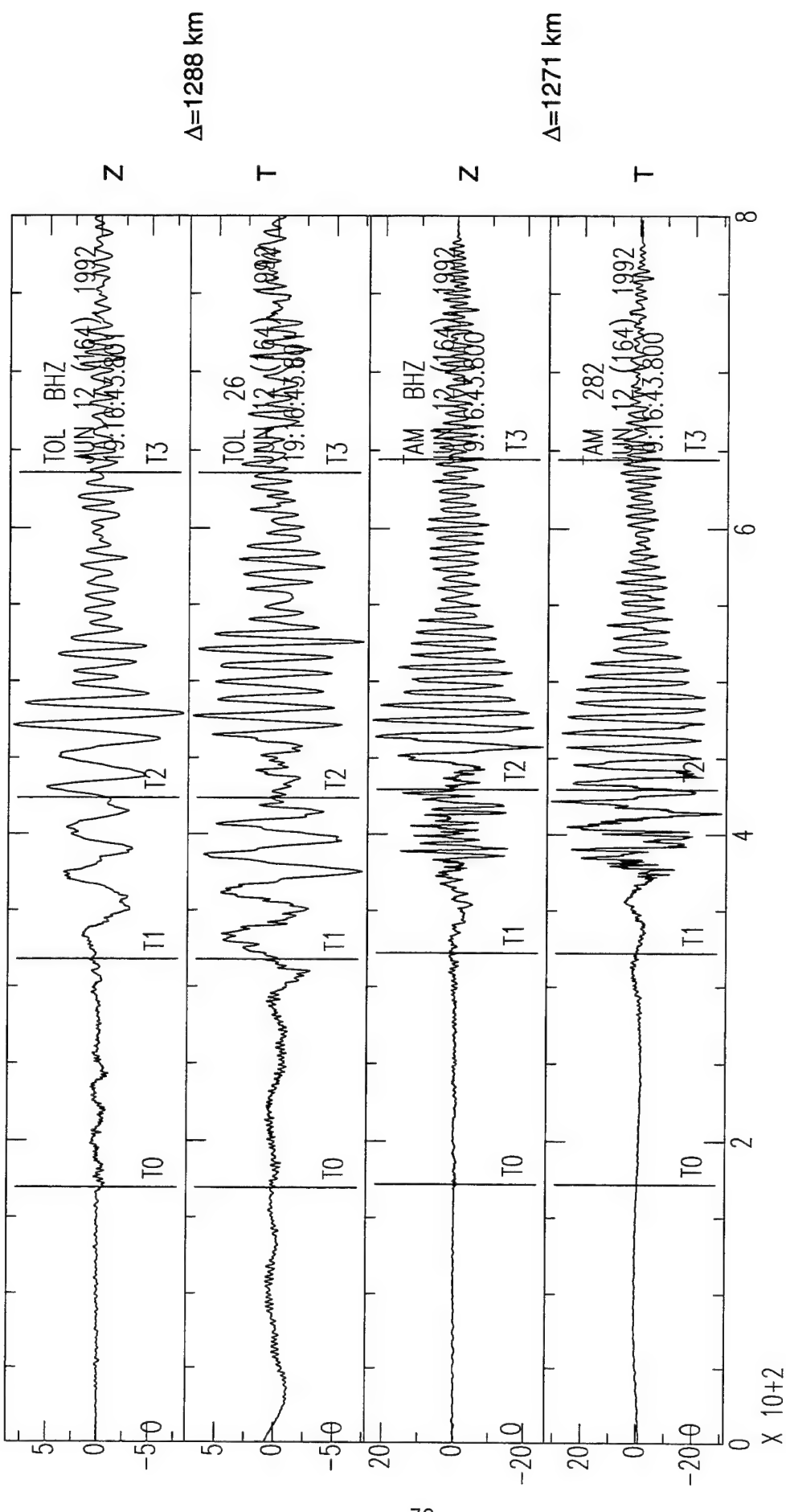


Figure 30b. Similar to Figure 30a for stations TOL and TAM

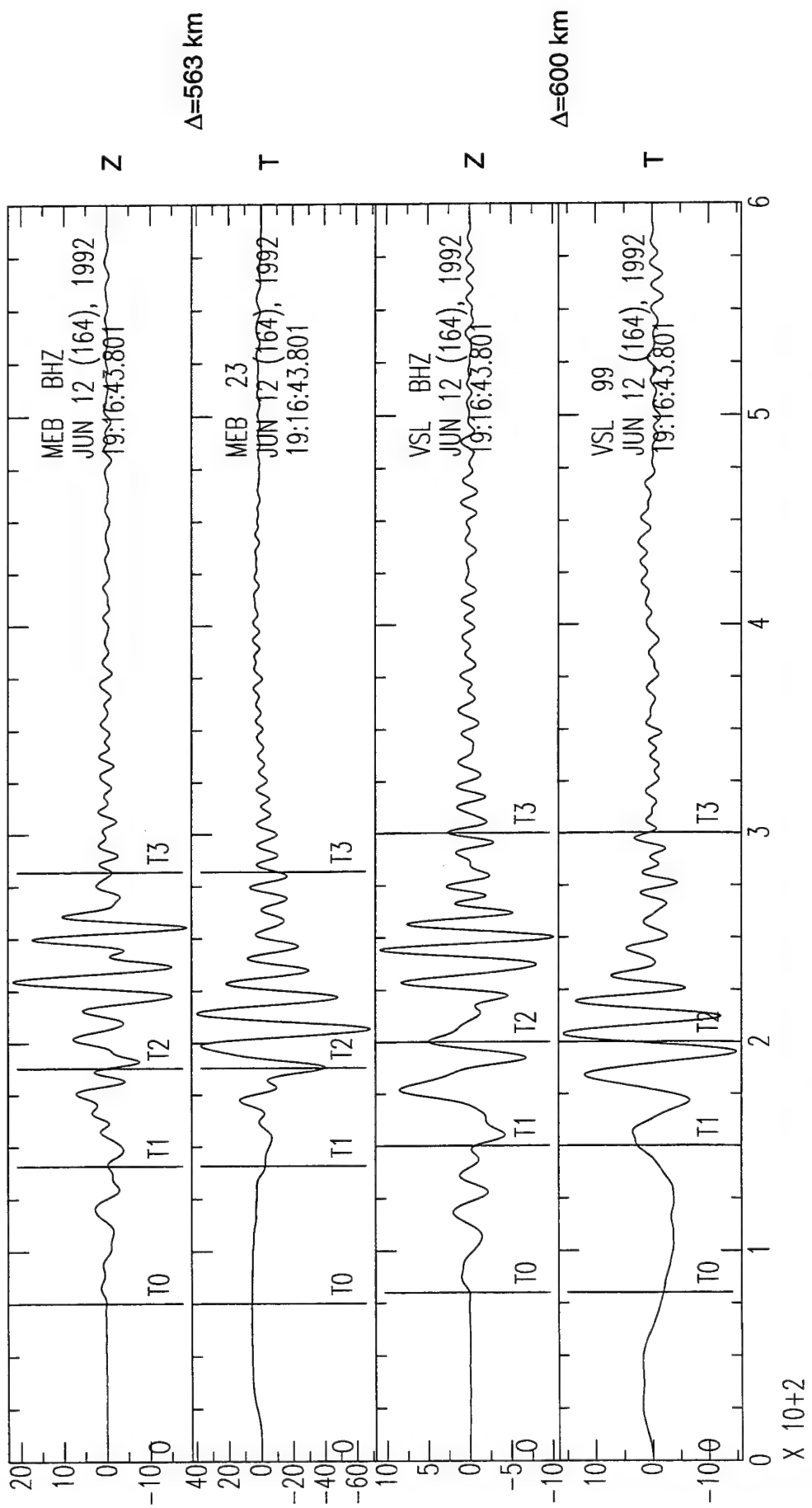


Figure 31a. Low passed ($T > 10 \text{ sec}$) displacement seismograms for the Gafsa event recorded at stations MEB and VSL. Z - vertical traces, T - tangential traces. Amplitudes are in microns. T_0 - arrival time corresponding to a group velocity of 7.5 km/sec, T_1 - 4 km/sec, T_2 - 3 km/sec and T_3 - 2 km/sec.

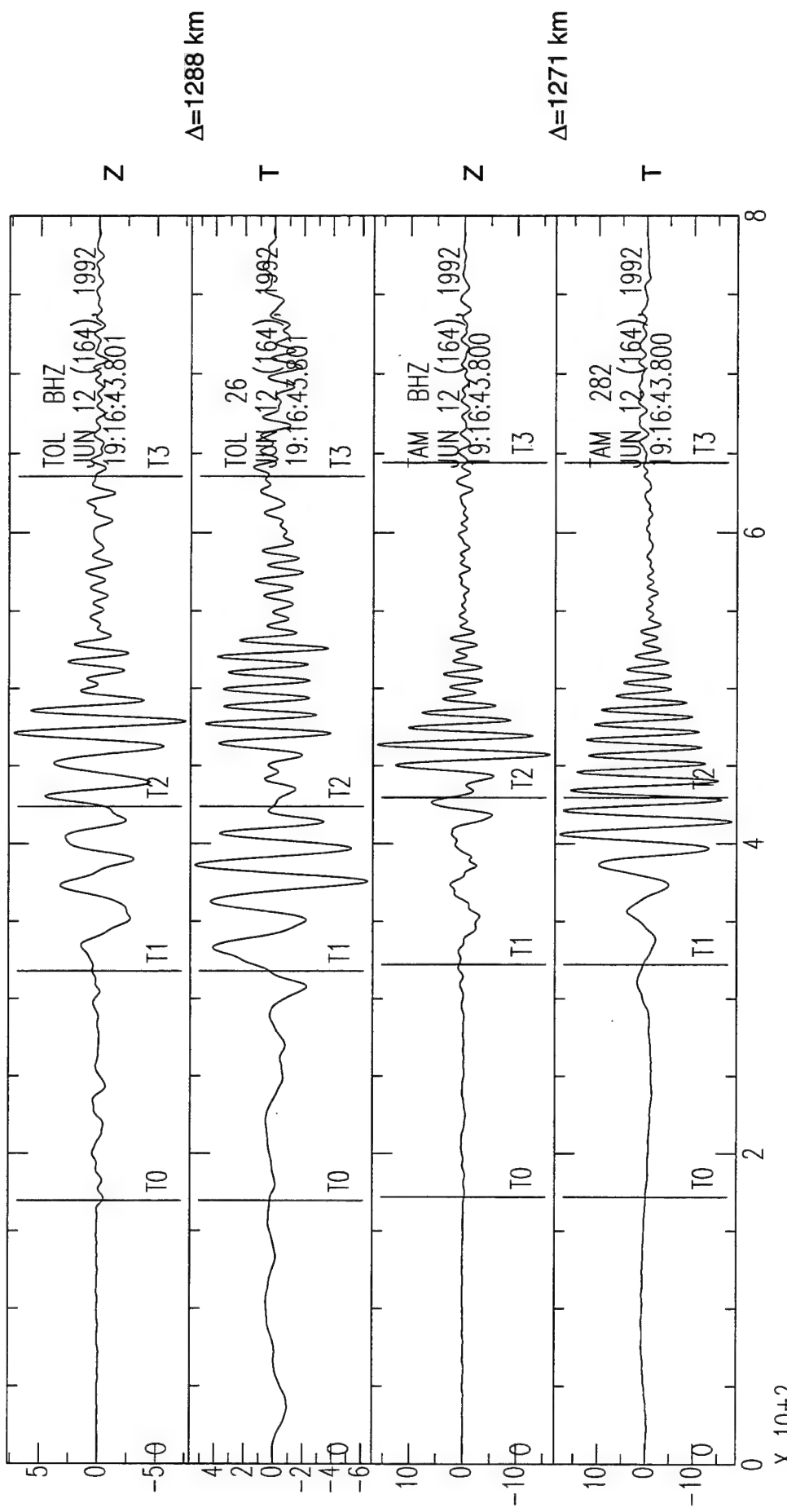


Figure 31b. Same as Figure 31a for stations TOL and TAM

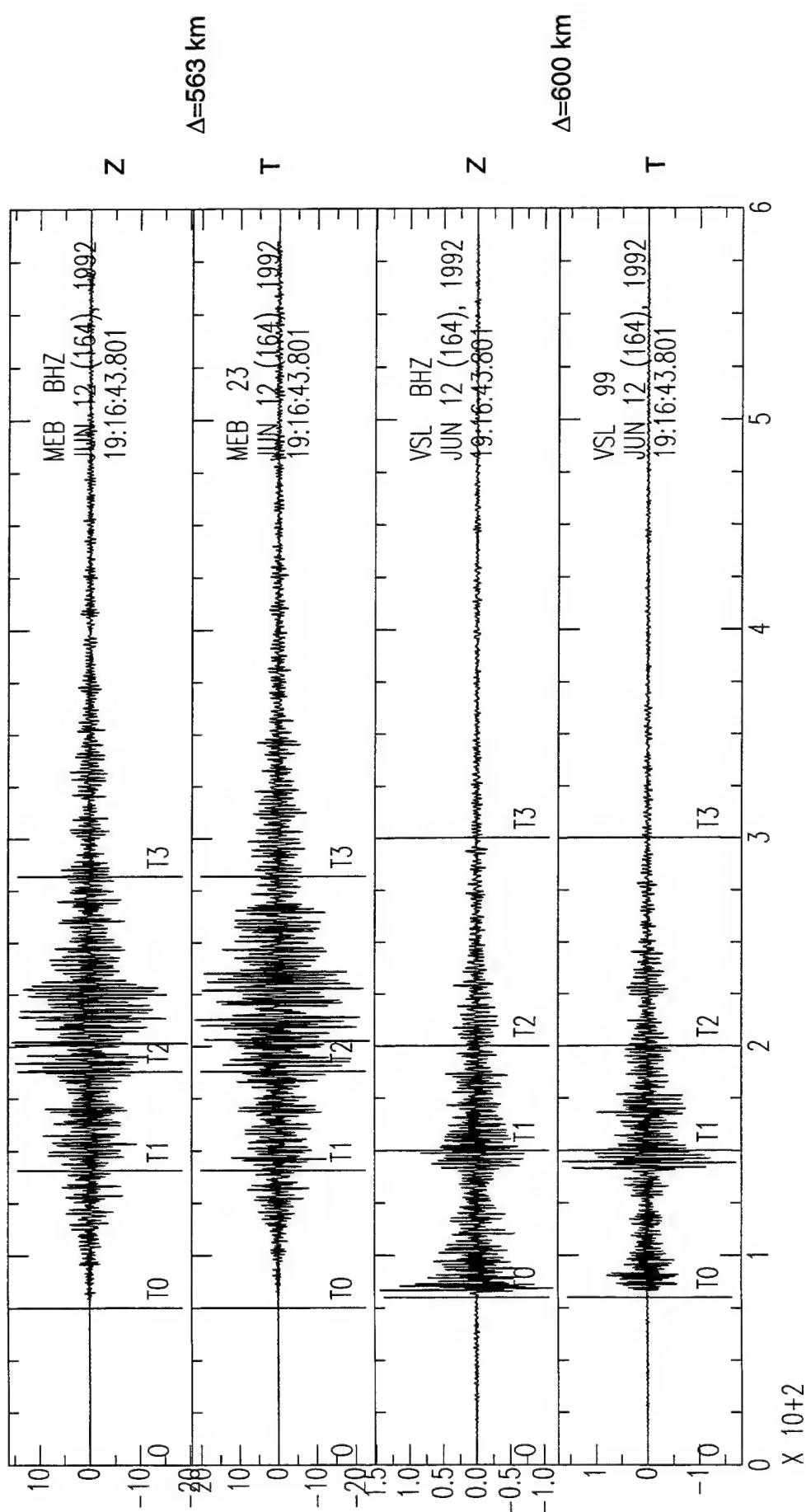


Figure 32a. High-passed ($T < 2$ sec) displacement seismograms for the Gafsa event recorded at stations MEB and VSL. Z - vertical traces, T - tangential traces. Amplitudes are in microns. T0 - arrival time corresponding to a group velocity of 7.5 km/sec, T1 - 4 km/sec, T2 - 3 km/sec and T3 - 2 km/sec.

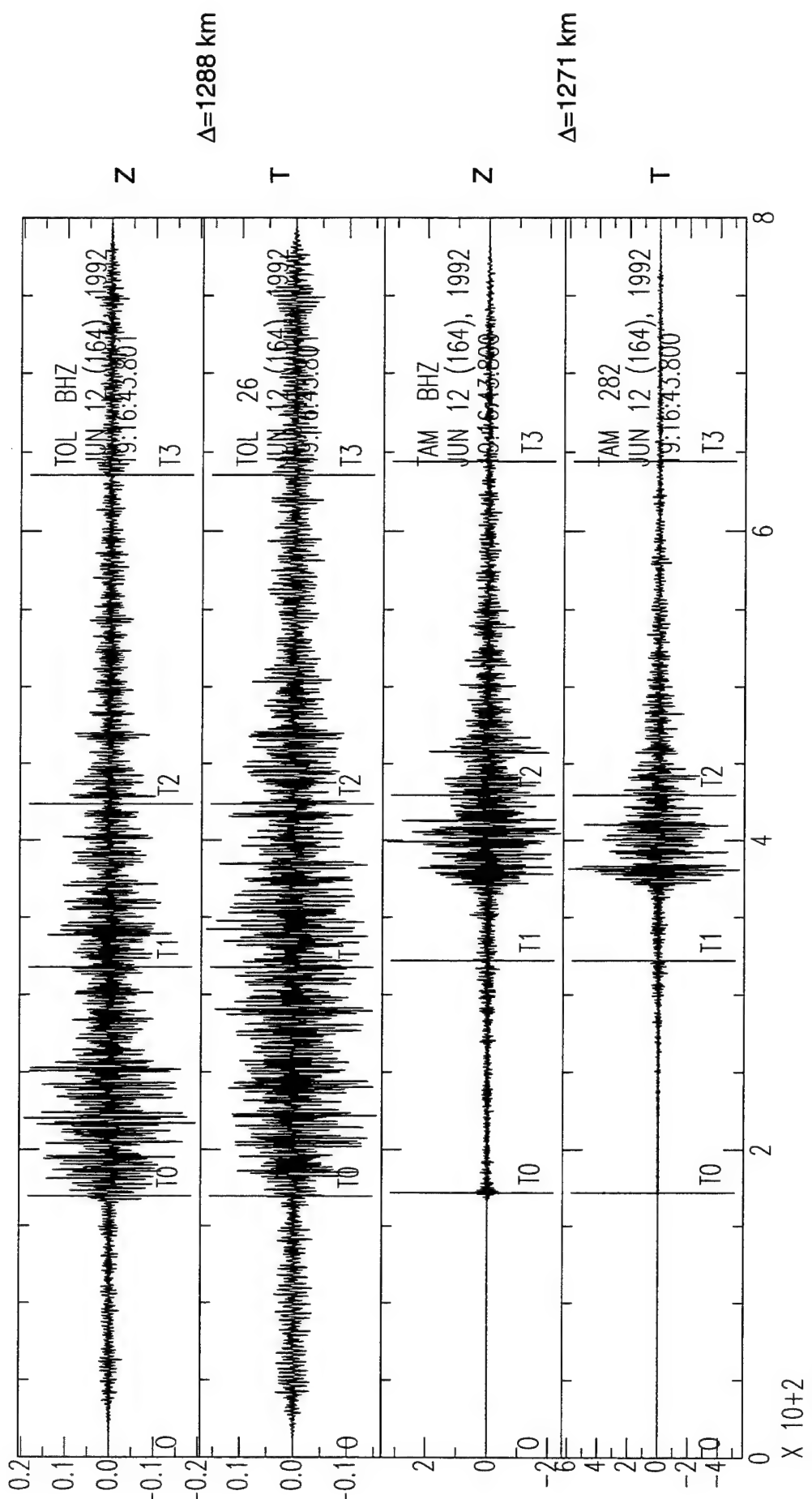


Figure 32b. Same as Figure 32a for stations TOL and TAM.

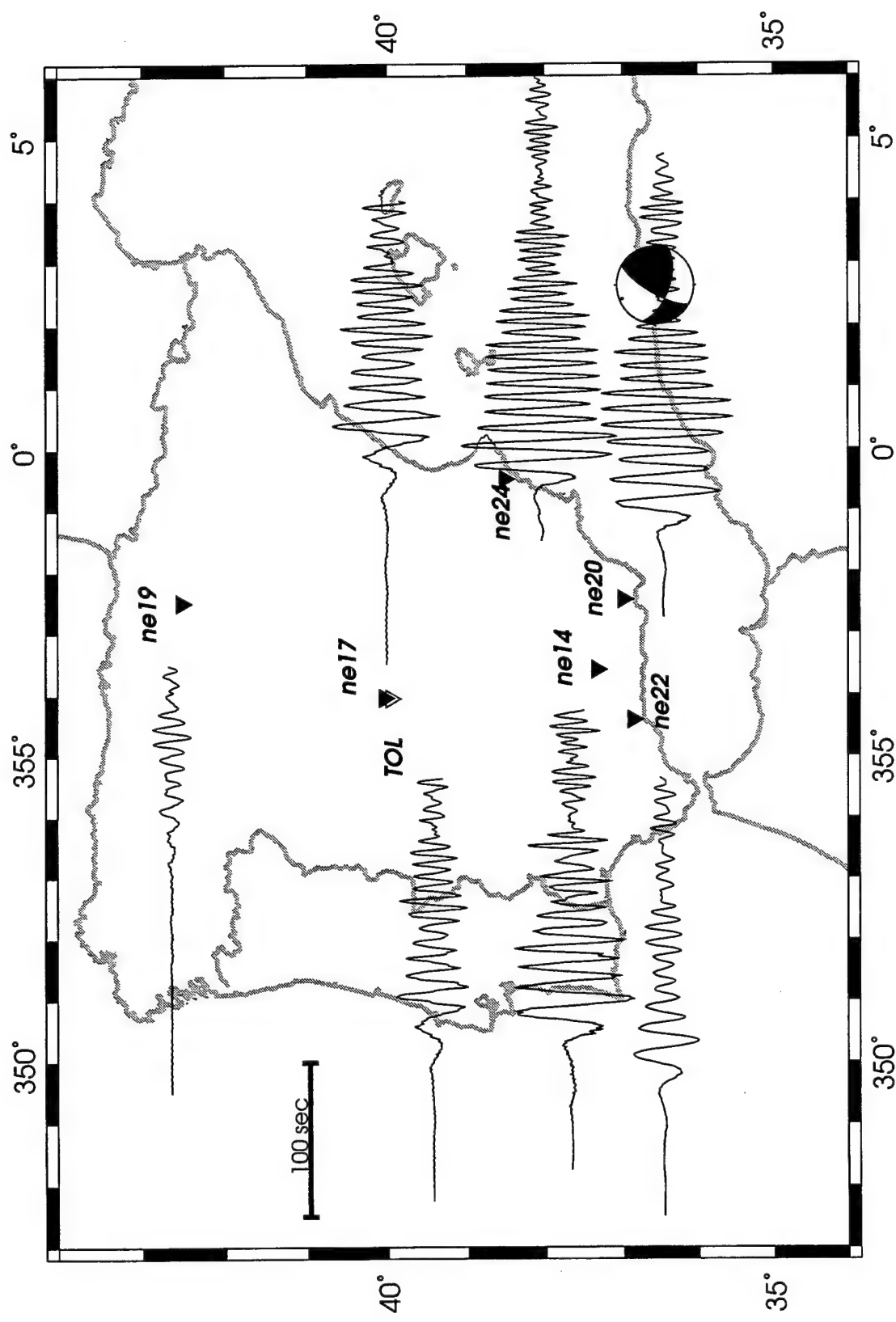


Figure 33. Tangential recordings for the North African event (88305) at the NARS stations.

In order to quantify the lateral heterogeneity, we first determined the group velocities so that we could get an estimate for the velocity structure in the region. These velocities were determined using a moving window analysis, similar to the method of Dziewonski *et al.*, (1969). We present the group velocity measurements for selected events arranged per station in Figure 34. It is clear that for most stations the group velocities vary significantly, except for paths to station Tamanrasset (TAM). This station is located well within the African craton and all events primarily traverse a pure continental path. Also plotted in Figure 34 are group velocities that we computed for our preliminary models.

Group velocities measured at station PAB (Figure 34a) show considerable variations, even at longer periods. Even though the path from the events in Southern Spain is relatively short, and therefore has poor resolution at longer periods (>50 sec), we can still conclude that the group velocities are substantially higher than those observed for paths from North Africa.

At VSL (Figure 34b), the group velocities are invariably low, and show a large variation. However, the low group velocity maxima suggest that upper mantle velocities are low for all paths. The large variations at periods shorter than 40 sec are mostly due to the upper crustal structure. The one purely oceanic path, from Almeria to VSL, shows a very smooth dispersion curve down to 10 sec, and indicates the crust is relatively thin and that the upper mantle velocities are low.

As already mentioned, the group velocities recorded at station TAM (Figure 34c) in southern Algeria only diverge at periods shorter than 20 seconds. We therefore assume that the Touareg shield region, which represents the largest section of these paths by far, has a homogeneous upper mantle and lower and middle crust. Variations in sedimentary cover can explain the difference in group velocities at short periods. The records at TAM (Figure 30b) are indeed very clean and show little evidence for complex structures.

In contrast, for paths to station MEB (Figure 34d) we find very strong variations in group velocities. We suspect that in this case multi-pathing may be a significant factor on the measurements, since MEB is located close to the transition between the African continental crust and the Mediterranean oceanic crust. The records at MEB (*e.g.* Figure 30a) look very complicated indeed with very strong ringing in the PnL wavetrain, which may be caused by low upper crustal

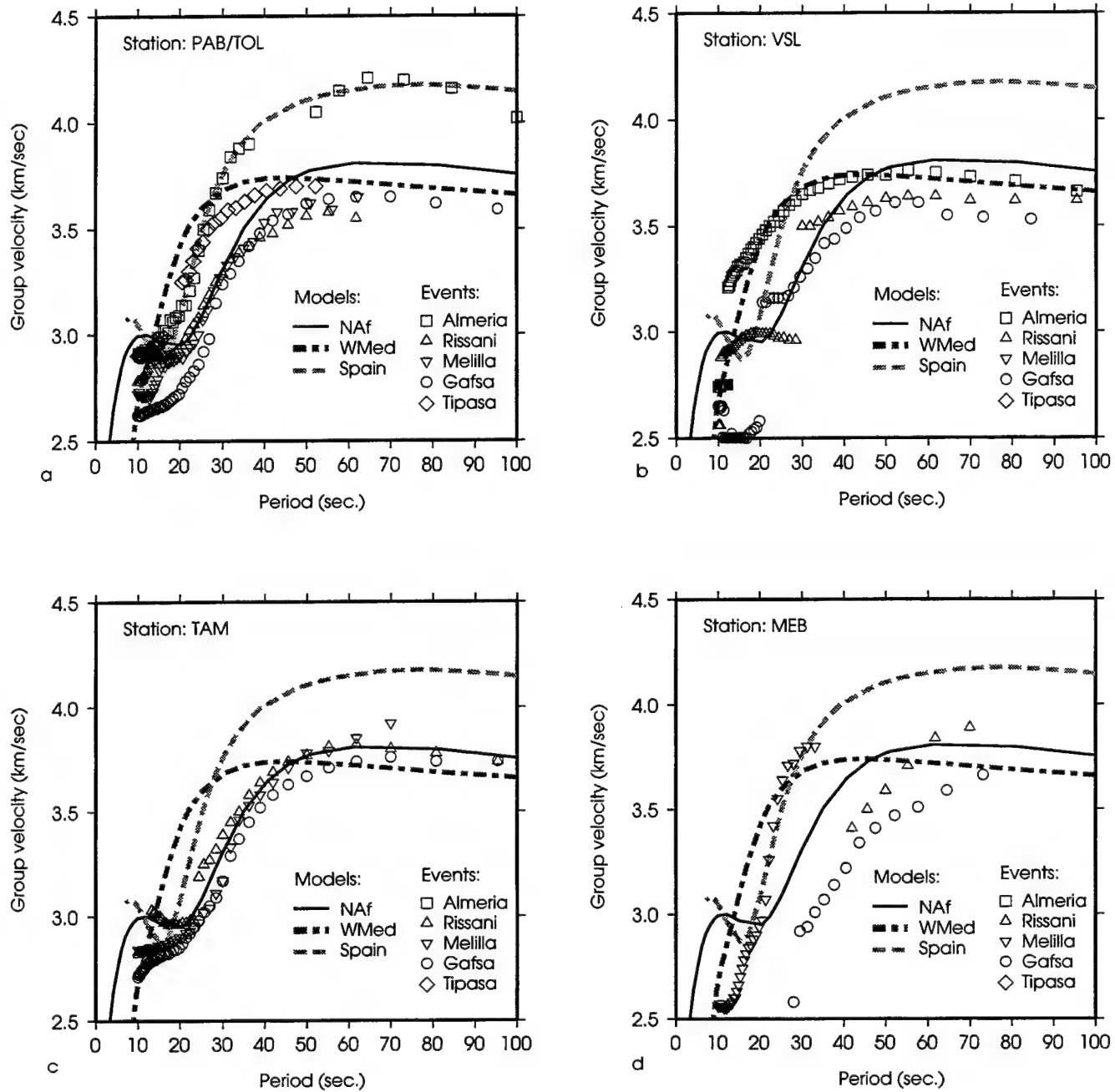


Figure 34. Group velocity measurements for selected source-receiver pairs, plotted per station. a - observations at PAB/TOL, b - VSL, c - TAM and d - MEB. The curves correspond to group velocities for the different preliminary models (Figure 35).

velocities but also by scattering away from the great-circle path. Also, as mentioned earlier, there are several very deep sedimentary basins located along the North coast of Algeria, close to the station. Such laterally varying shallow structure is expected to influence the surface-wave dispersion.

5.5 Preliminary Structure

Based on surface wave group velocity measurements presented above we have constructed velocity models for the different parts of the region (Figure 35), *viz.* Algeria, the western Mediterranean and Southern Spain. For Algeria we found a crustal thickness of 37 km, and little lateral variation except for the coastal regions. We need to perform additional modeling to determine the structure in that area, especially with regards to paths to station MEB. The low upper mantle velocities that we found for Algeria are consistent with the observation of Hadiouche and Jobert (1988).

For the Western Mediterranean we found a crustal thickness of 20 km, but we could not fit the Love and Rayleigh wave data with a single model and our preliminary model is different for Love and Rayleigh waves. However, the generally low upper mantle velocities in this region are consistent with tomographic models of Snieder (1988) and Zielhuis (1992).

For southern Spain we found a crustal thickness of 28 km and higher upper-mantle velocities, which are consistent with the results of deep seismic sounding (WDSSS, 1977).

The Moho depths are not always consistent with those compiled by the Cornell University Middle East and North Africa Project (Barazangi *et al.*, 1996), e.g. our crustal thickness for Spain is significantly smaller than the compilation's depth, and from dispersion observations it seems that the depth under the Algerian coastal region is thickening instead of thinning.

5.6 Regionalization

From our observations it is clear that some sort of regionalization is required in order to study events in this region. In this section, we present a simple and yet very effective way to apply a regionalized model to compute synthetic waveforms.

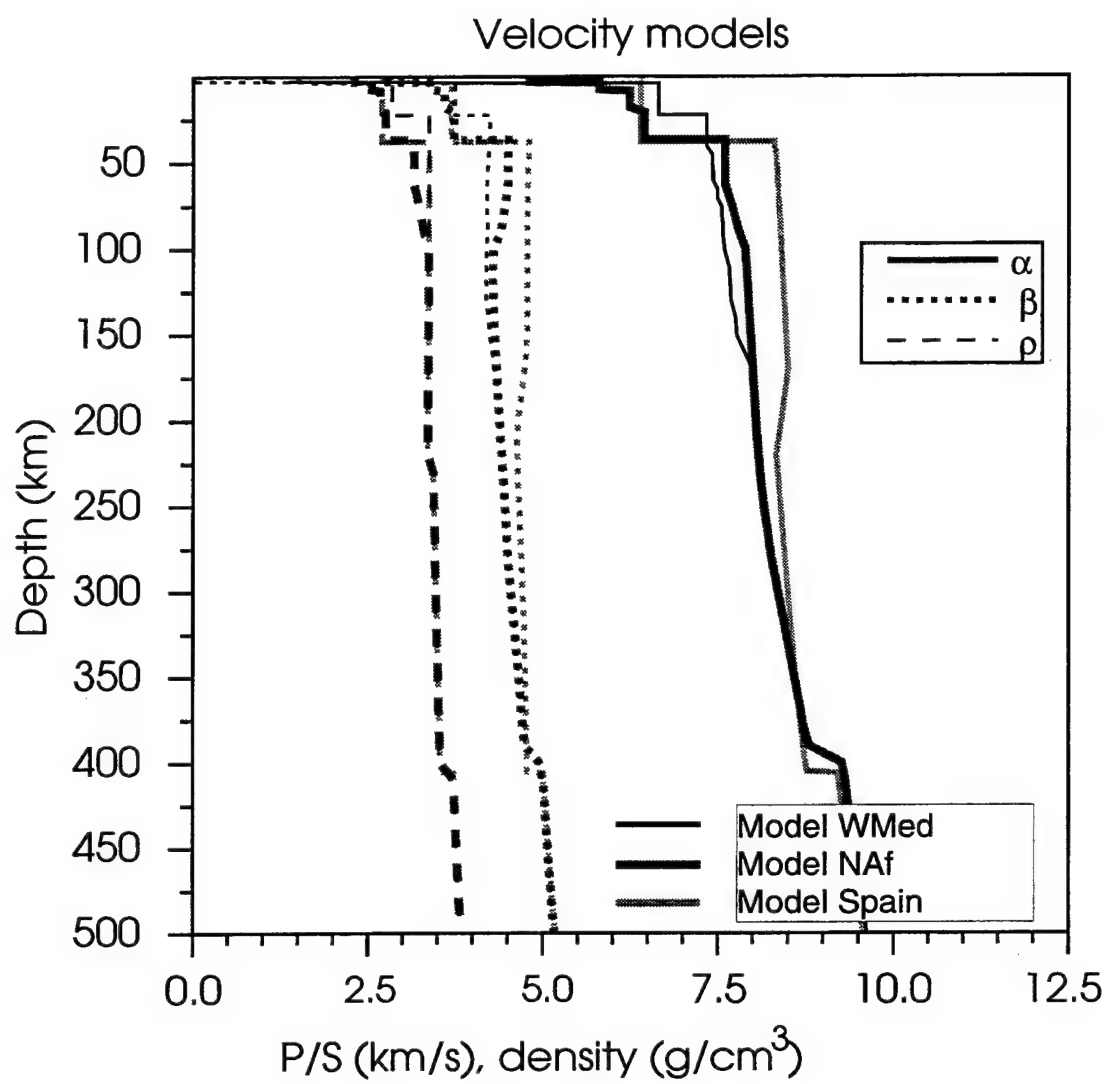


Figure 35. Preliminary velocity models used to compute the group velocities in Figure 34.

Lateral heterogeneity plays a significant role in source inversion studies, especially if the source-receiver paths extend beyond several hundred kilometers. However, for larger distances and heterogeneous media, even if simple time-shifts are allowed, it is still difficult to use the full waveforms because different phases are sensitive to different parts of the structure and therefore need different time corrections. Zhao and Helmberger (1994) solved this problem for weakly heterogeneous cases by splitting the waveforms into a P_n part and a surface wave part, and allowing these to shift in time independently. For paths through relatively homogenous media, like the Hindu Kush (Section 3) this method does yield good results. However, in strongly heterogeneous media, like the present study region, this solution is not sufficient. Because of the radically different dispersive characteristics of the surface waves for different regions, the shape of the surface wave train can become very different (*e.g.* ringing versus an impulsive surface wave) and this effect cannot be synthesized by using simple time shifts. Thio and Kanamori (1995) applied a regionalized phase velocity model for moment tensor inversions in Southern California using short-period surface waves. If we approximate the fundamental mode seismogram as:

$$u(\Delta, t) = \sum A_l e^{i(k\Delta - \omega t)} = \sum A_l e^{ik(\Delta - ct)} , \quad (10)$$

where u is the displacement at distance δ and at time t , and A_l is the excitation function for mode l , including the source mechanisms and geometrical spreading, then to first order the effect of a change in phase velocity will manifest itself only in the phase function, *i.e.* we can suffice by replacing c , which is the phase-velocity computed for the original 1-D model, with c' which is a path-averaged phase velocity calculated from our regionalized velocity model, in the right-hand equation. It should be noted that this method is not restricted to the calculation of fundamental mode surface waves, but can easily incorporate higher modes as well, so that body waves could be included if necessary. However, in general, lateral heterogeneity is most pronounced in the upper crust, and this has the largest effect on fundamental mode surface waves.

This approach was used by Thio and Kanamori (1995) to study the effect of lateral heterogeneity in Southern California. In Figure 36 we present synthetic Rayleigh waves calculated for a suite of mixed paths, starting with a purely Spanish path and sequencing through a range of mixed paths with increasing contributions by the Mediterranean model to a purely Mediterranean

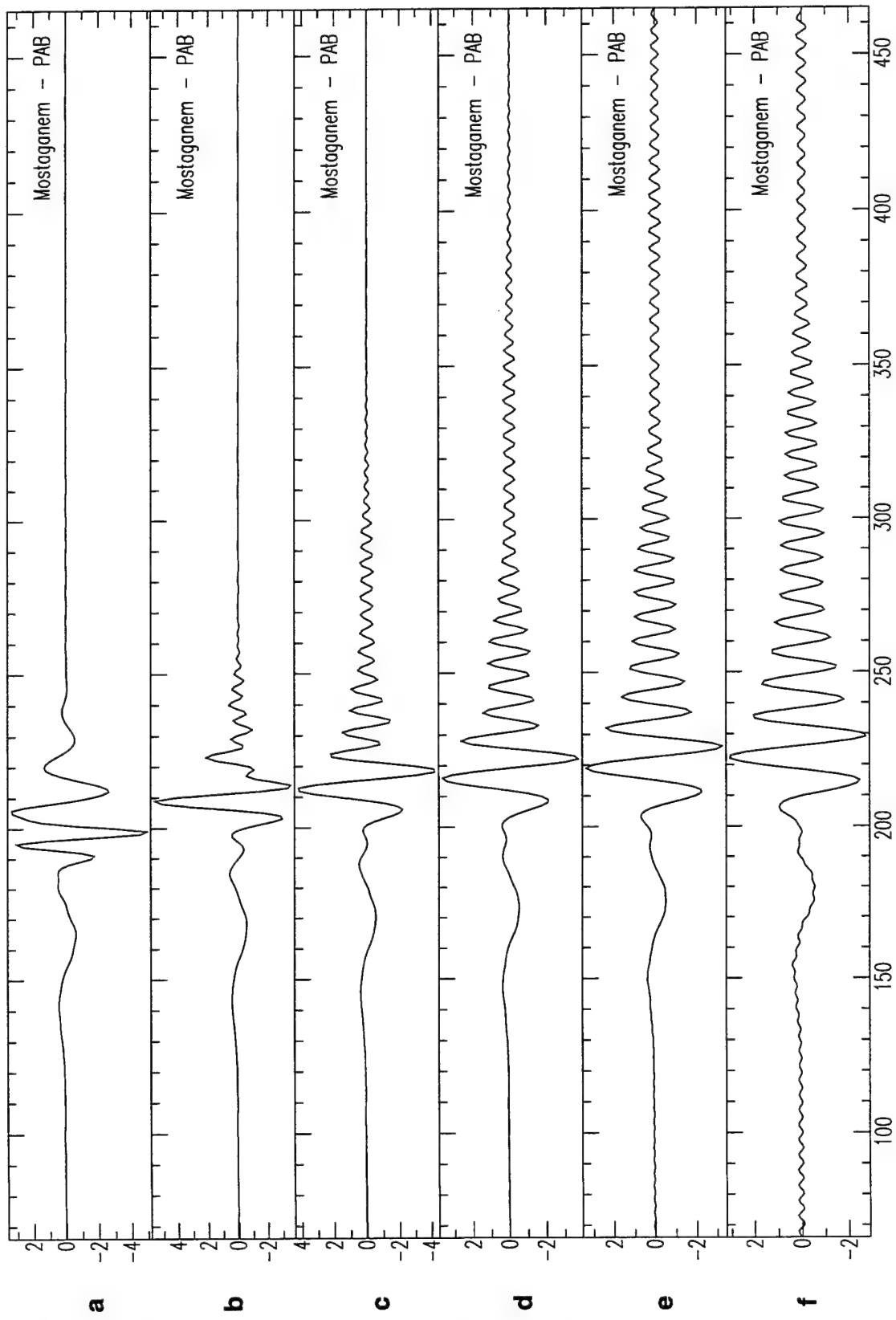


Figure 36. Vertical component Rayleigh waves computed using the mixed path approach for different ratios between a purely Spanish path and a purely Mediterranean path. a - 100% Spanish path, b - 80% Spanish/20% Mediterranean, c - 60%/40%, d - 40%/60%, e - 20%/80% and f - 0%/100% (a purely Mediterranean Sea path).

path. It is clear from this figure that the change of models has a very strong influence not only on the overall arrival time of the Rayleigh waves but also on the shape of the Rayleigh wave train. This effect is similar to our observations on the NARS data for the North Algerian event where the ringing observed in Spain decreases away from the coast, which corresponds to a case where a primarily Mediterranean path becomes transformed by increasing Spanish contributions. We will use this approach to include lateral heterogeneity in source estimation studies of this complex region.

5.7 Moment Tensor Solutions

Using the preliminary structure obtained above from the surface wave group velocity we proceeded to calculate phase velocities for the different regions which we then used to perform source inversions using short period (20-80 sec.) surface waves following the method of Thio and Kanamori (1995). In this method, we determine the complex spectra of a seismogram windowed so that it includes the fundamental mode Love and Rayleigh waves only, and correct the spectra for propagation effects. These corrected spectra represent our estimate of the spectra at the source and we invert these for the source parameters (Figure 37). The depth is determined by inverting for a whole range of depths and choosing the depth which results in the largest variance reduction (Figure 38).

For all events we had at least three stations available and this proved to be sufficient to obtain stable solutions for all events (Table 7). These solutions are consistent with the Harvard and MedNet CMT solutions but all these solutions have difficulty with resolving depth.

In most cases, the teleseismic body wave data for these events were too small in amplitude to be useful for source parameter estimation. However, for the Rissani events (Figure 39) we could observe depth phases at some stations and for the Al Hoceima event (Figure 40) we were able to collect sufficient data to carry out a teleseismic body wave inversion. Based on the depth phases recorded we found depth of around 20 km for the Rissani events (Figure 39). This is consistent with the depths that we found using the regional surface waves (18 km), and is substantially deeper than the depths reported in the ISC bulletins (8 km).

For the Al Hoceima earthquake, we collected worldwide broadband recordings from the IRIS, IDA/IRIS and Geoscope networks, and after the selection of records with good signal-to-noise

Rissani-2

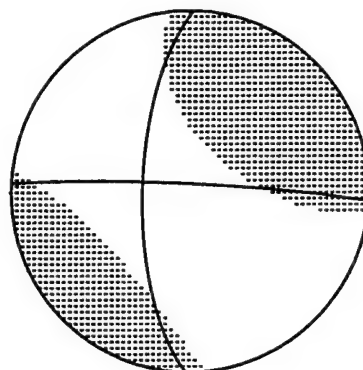
1992 304 10 43 55.8

31.246 -4.381 17.

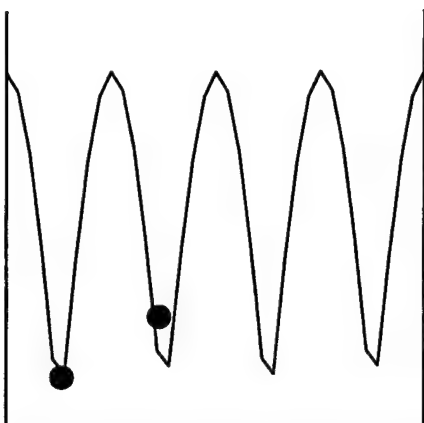
Moment= 2.04 e 24 dyn.cm MW=5.5

Strike Dip Slip
-178.7 68.4 -4.2

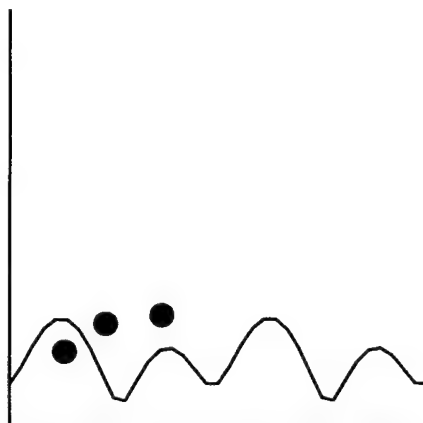
43.320



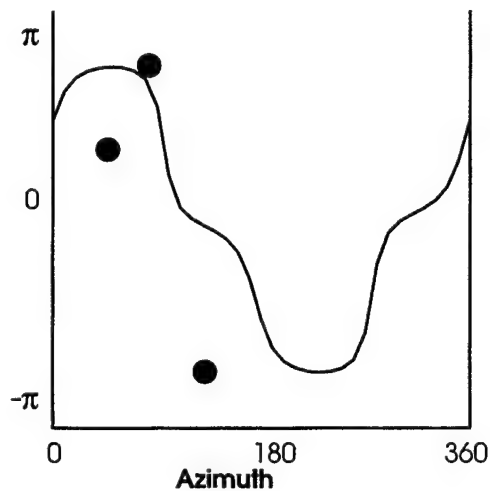
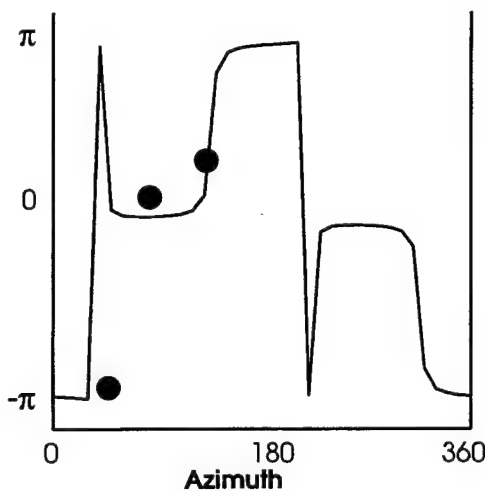
Love



Rayleigh



Amplitude



Phase

Figure 37 Moment tensor solution for the Rissani-2 event. Bottom panels show the comparison between the synthetic radiation pattern and the observed spectra at 30 sec. Left column for the Love wave amplitude (top) and phase (bottom) spectra, and right column for the Rayleigh wave spectra.

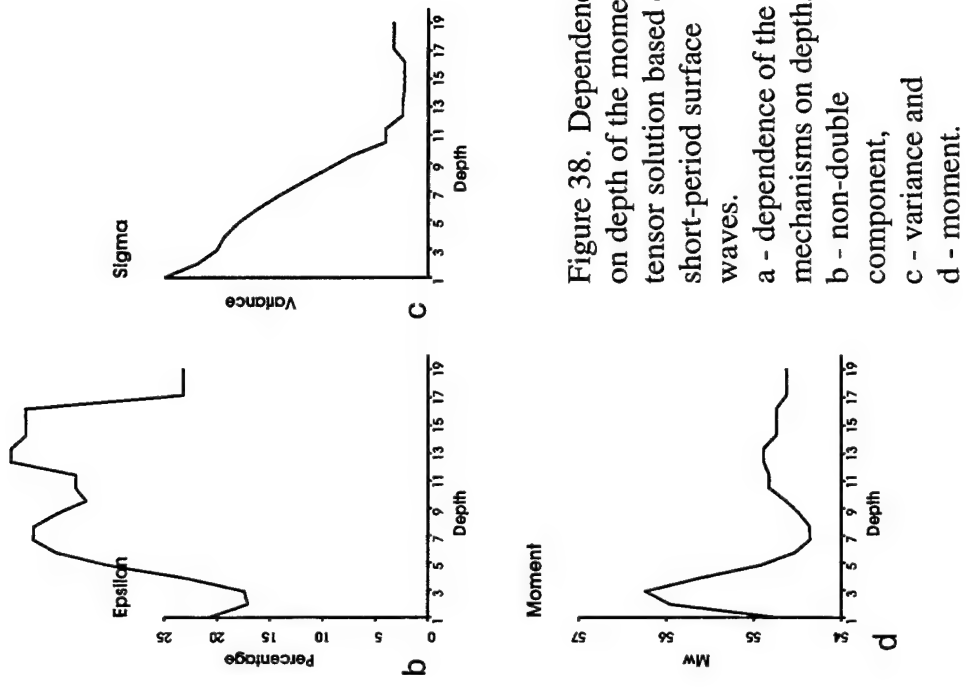
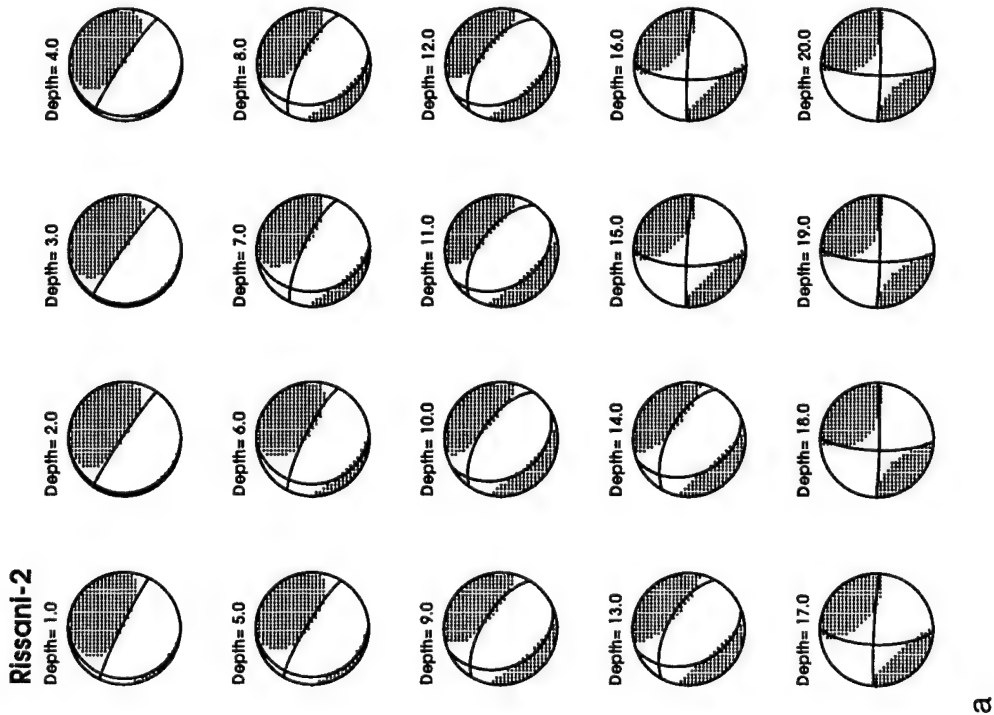


Figure 38. Dependence on depth of the moment tensor solution based on short-period surface waves.
 a - dependence of the mechanisms on depth,
 b - non-double component,
 c - variance and
 d - moment.



a

Table 7. Catalog of Mediterranean events used in the short-period:long-period energy ratio study

Jdate	ID	Hr:Mn:Sec	Mag	Lat	Lon	Depth
8800901		01:42:46.7	5.3	41.246	19.630	24
8802801		15:48:08.1	4.8	32.413	21.150	10
8808601		12:07:29.4	4.7	33.186	13.280	10
8810001		20:27:24.7	4.7	31.449	-9.936	10
8827901		00:42:11.0	3.8	35.505	-3.858	32
8830501		10:12:58.4	5.4	36.443	2.759	12
8834701		06:40:41.6	4.9	36.300	-4.512	93
8904301		12:02:19.0	4.4	36.391	2.648	10
8930201		19:09:12.9	5.7	36.788	2.448	6
8935401		04:15:02.5	4.8	37.207	-7.352	14
9003901		15:47:31.4	5.0	36.259	-12.100	10
9004001		09:31:47.6	5.0	36.775	2.477	12
9006701		01:37:15.3	4.1	36.885	-3.691	625
9010201		22:47:52.7	4.7	36.768	2.492	14
9010301		22:17:13.4	4.2	35.624	-4.792	86
9011201		16:35:43.3	4.7	36.502	26.854	149
9012501		07:21:18.0	4.6	40.744	15.853	13
9012502		07:21:29.5	5.3	40.775	15.766	10
9013701		08:44:05.2	4.8	38.419	22.189	36
9014601		09:21:05.6	4.7	38.306	-11.626	14
9016501		22:15:17.8	4.4	36.372	21.377	40
9017501		22:25:09.1	3.6	33.590	-2.5500	5
9019001		11:22:20.3	4.9	35.066	26.640	60
9020001		12:25:42.8	3.9	34.587	23.513	79
9021201		06:49:31.7	4.8	37.245	21.462	58
9022601		22:44:54.2	3.8	35.629	11.460	10
9023701		14:57:57.9	4.7	35.860	28.087	50
9024001		20:21:21.9	4.4	36.267	27.218	40
9029201		07:56:45.5	3.8	35.973	11.920	10
9030201		08:16:14.1	4.5	36.232	14.671	24
9030801		04:08:07.5	3.8	34.940	11.350	10
9031501		11:57:37.2	4.9	33.985	11.941	10
9034701		00:24:25.7	5.5	37.300	15.438	11
9036301		19:10:46.9	5.0	36.015	11.080	10
9103101		23:05:13.9	6.8	41.709	10.577	8

Table 7. (Continued) Catalog of Mediterranean events
used in the short-period:long-period energy ratio study

Jdate	ID	Hr:Mn:Sec	Mag	Lat	Lon	Depth
9105701		07:25:47.2	5.5	40.186	13.822	401
9108601		09:49:21.3	3.8	41.441	11.573	18
9109101		18:52:40.4	4.1	34.579	27.707	71
9114601		12:26:00.2	5.1	40.730	15.765	8
9117701		11:43:34.8	5.1	38.420	21.175	31
9118201		22:22:48.9	4.1	34.371	27.476	10
9119901		20:40:05.5	4.7	36.077	27.187	106
9121101		04:50:42.3	4.2	36.321	28.200	47
9122001		22:46:10.4	4.8	35.629	11.657	22
9122601		13:41:39.1	4.4	36.053	35.889	41
9124601		04:38:39.3	4.3	36.198	31.807	113
9125301		18:59:15.9	4.0	37.722	23.381	171
9128201		08:17:50.3	4.2	36.174	31.394	79
9201901		20:21:32.6	4.7	36.283	1.871	12
9203201		04:27:18.6	3.9	34.672	23.975	46
9206301		19:01:07.3	3.7	37.957	7.021	49
9207201		13:05:55.2	5.3	35.308	-2.532	22
9207301		00:33:58.8	4.5	34.472	9.656	33
9207302		00:37:01.3	4.3	35.274	-2.440	17
9208101		10:18:54.9	3.2	35.310	-2.448	10
9211601		12:46:19.6	5.4	38.583	14.936	246
9210101		01:02:28.6	3.7	36.123	-3.867	21
9213501		15:00:55.0	3.9	35.199	-2.439	10
9213502		15:48:10.6	3.8	35.268	-2.423	10
9214401		22:53:06.7	4.6	36.740	30.450	42
9215301		15:44:27.1	4.2	36.019	28.272	86
9216401		19:16:43.9	5.3	34.159	8.333	10
9216901		20:47:29.3	3.6	36.292	1.503	10
9217101		18:05:36.3	4.2	34.212	8.611	33
9218301		15:13:32.3	4.3	31.473	15.758	20
9219201		23:57:04.3	4.1	36.093	30.830	77
9219301		17:21:59.9	3.9	36.556	10.779	33
9221901		04:23:15.1	3.7	37.358	13.162	19
9225501		17:20:29.7	4.2	34.407	14.384	10
9227301		15:04:08.1	4.7	34.478	14.483	10

Table 7. (Continued) Catalog of Mediterranean events used in the short-period:long-period energy ratio study

Jdate	ID	Hr:Mn:Sec	Mag	Lat	Lon	Depth
9229101		20:43:17.8	4.2	35.257	1.435	10
9229701		09:11:09.0	5.3	31.355	-4.318	29
9230401		10:43:58.4	5.1	31.284	-4.372	26
9232301		21:10:41.4	5.9	38.307	22.452	15
9235601		09:02:57.8	4.4	35.384	-2.519	13
9304301		15:39:26.5	3.7	36.748	2.479	10
9304701		03:11:11.5	4.2	36.658	-8.575	34
9306601		03:17:17.0	3.8	36.010	1.845	10
9307701		15:47:00.4	5.7	38.340	22.155	59
9312101		00:22:21.1	4.2	35.294	-6.216	61
9314301		07:40:56.9	5.4	35.357	-2.502	27
9315601		19:16:16.8	4.9	43.121	12.678	8
9317301		21:52:00.3	4.4	36.400	-8.133	32
9317701		17:47:53.8	4.9	37.990	14.218	14
9319201		02:21:24.5	3.9	36.532	9.205	33
9319601		05:24:05.9	4.5	36.407	9.329	10
9321801		07:51:49.5	3.9	42.284	10.929	30
9325301		15:39:47.6	4.7	34.834	12.441	10
9325302		16:02:32.3	5.0	35.039	12.366	10
9325401		16:14:53.2	3.9	36.706	7.094	10
9325801		22:43:35.6	4.2	34.986	12.414	10
9327401		03:59:33.0	4.9	36.637	23.967	88
9329201		18:13:55.4	3.4	38.318	-1.380	10
9331301		22:01:14.1	4.3	36.648	-7.695	29
9331501		07:33:22.1	4.1	38.186	-0.022	10
9335601		20:11:36.9	3.6	37.004	-3.895	10
9335701		14:22:35.1	5.0	36.756	-2.937	27
9400401		08:03:15.8	4.9	36.651	-2.822	22
9400501		13:24:09.9	5.7	39.085	15.145	273
9408001		21:41:01.9	5.1	39.745	15.461	279
9414601		08:26:52.4	5.7	35.305	-4.103	10
9415401		08:57:38.3	4.6	35.252	-4.036	15
9423001		01:13:05.7	5.7	35.520	-0.106	9
9423002		01:42:48.6	4.5	35.536	-0.112	10
9532601		04:15:11.0	7.2	34.700	10.000	28.5

Table 8. Locations and source mechanisms for events in the Western Mediterranean used in this report.

ISC Bulletin				Regional Broad-band data								Harvard CMT			
Yr/Jday	Yr/Mo/Dy	Hr:Mi:Sc	Long.	Lat.	Depth	Strike	Dip	Slip	Depth	M _w	Strike	Dip	Slip	M _w	Location
88305	88/10/31	10:12:57.6	36.402	2.682	10.0	105	65	150	10	5.7	103.	55.	167.	5.6	N. Algeria
89302	89/10/29	19:09:13.0	36.782	2.443	6.0	85	83	172	10	5.2	91.	48.	119.	5.9	Tipasa 1
90040	90/02/09	09:31:47.6	36.775	2.481	12.0	-100.9	39.0	63.1	5	4.8	49.	19.	95.	5.2	Tipasa 2
90102	90/04/12	22:47:53.2	36.792	2.493	14.0	-150.3	33.9	37.8	10	4.3					Tipasa 3
92164	92/06/12	19:16:45.7	34.197	8.328	19.0	-117.8	47.8	42.6	14	5.2	82.	36.	114.	5.2	Gafsa
92297	92/10/23	09:11:05.5	31.294	-4.325	5.0	-178.7	68.4	-4.2	19	5.5	-173.	69.	12.	5.5	Rissani 1
92304	92/10/30	10:43:55.8	31.246	-4.381	8.0	87.9	88.8	173.5	17	5.4	90.	72.	176.	5.6	Rissani 2
92356	92/12/21	09:02:57.2	35.386	-2.548	8.0	-135.9	9.8	-142.	10	4.9					Melilla
93143	93/05/23	07:40:57.0	35.356	-2.504	27.0	-94.2	73.2	103.	9	5.3					Saidia
93357	93/12/23	14:22:35.1	36.756	-2.937	27.0	151.1	51.8	-86.8	6	5.1	-25.	43.	-88	5.2	Almeria
94146	94/05/26	08:26:52.4	35.308	-4.105	10.0	120.5	75.9	-166.5	10	5.8	112.	48.	-173	5.9	Al-Hoceima
94230	94/08/18	01:13:05.7	35.520	0.106	9.0	-134.5	60.3	81.0	8	5.8	40.	23.	70.	5.8	Mostaganem

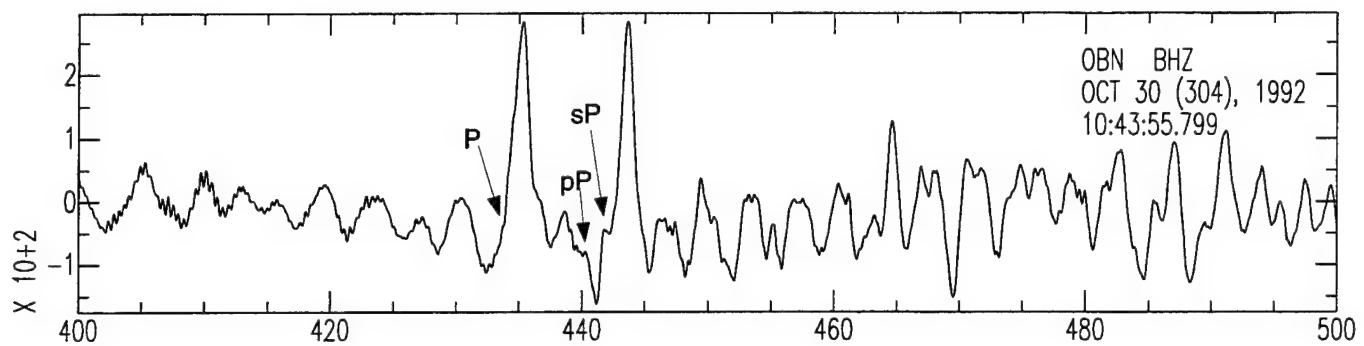


Figure 39. Teleseismic P wave recording at station OBN for the Rissani-1 event. Distance is 34.4 degrees and the separation between P, pP and sP correspond to a depth of 20-21 km (using the IASPEI95 model).

AI Hoceima

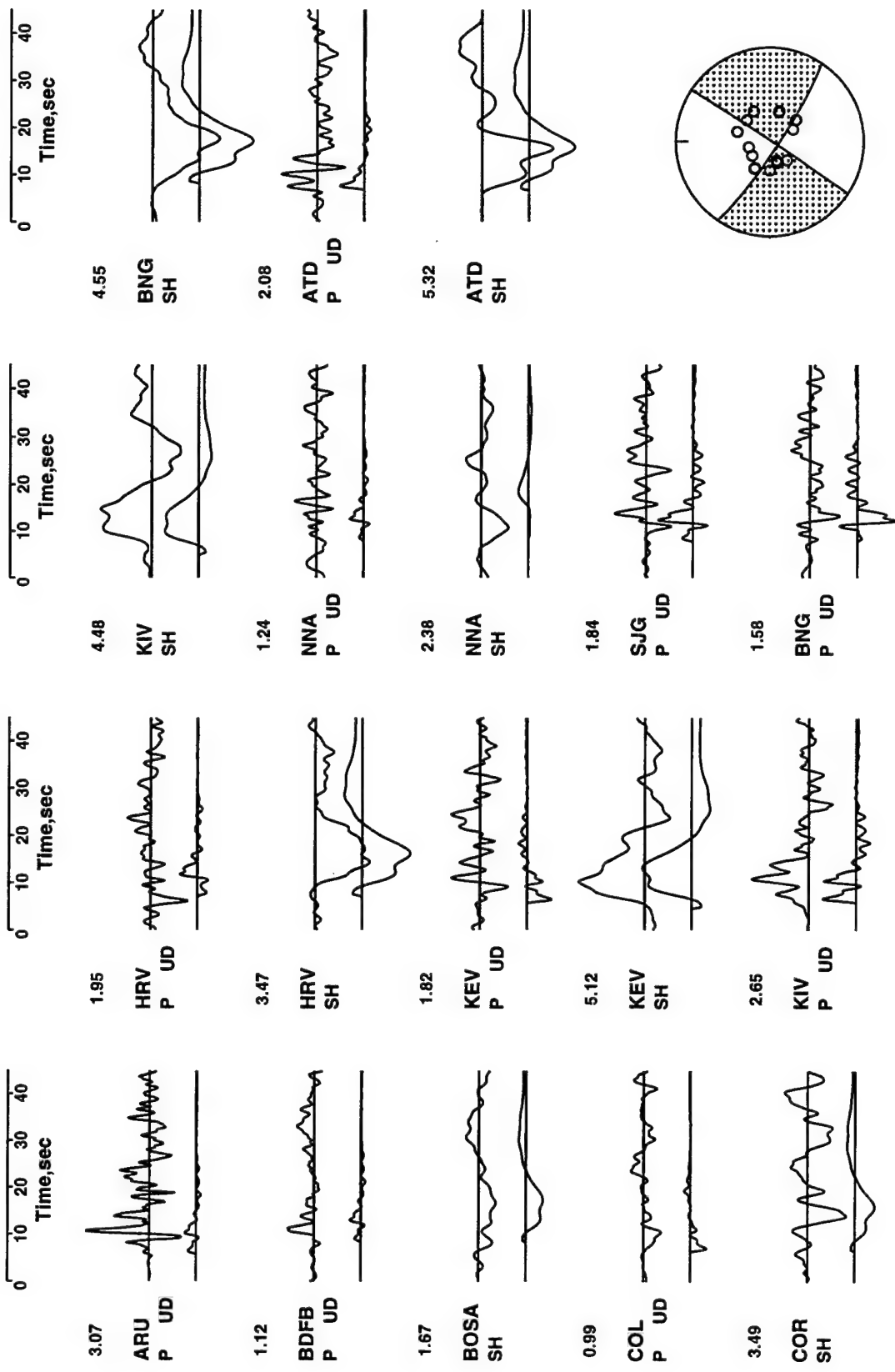


Figure 40. Observed teleseismic body-waves (top traces) for the AI Hoceima event and synthetic seismograms corresponding to our solution (bottom right). P - vertical P waves, SH - SH waves. The maximum amplitudes are given in the upper left corner of every pair of traces, in microns.

ratios we were left with a good azimuthal distribution of stations (Figure 41). The traces were deconvolved to displacement and we used the inversion procedure of Kikuchi and Kanamori (1991) to determine the mechanism, size and depth. This method uses synthetic Green's functions and inverts for the best fitting solution in terms of depth, location and mechanism. We constrained the depth to be within a range of 5 to 20 km, with a grid interval of 5 km. For a time function we chose a triangular function with a half width of 0.5 sec. The results are given in Figure 40, and we found a strike-slip mechanism with a depth of 10 km. This mechanism would be consistent with movement along a local fault system (Medina, 1995), and is quite similar to the Harvard CMT solution. Our solution is primarily determined by the SH waves, since many of the P waves are very noisy. The teleseismic P waves are quite marginal for an event of this size ($M_w = 5.8$), which may be due to effects of complex local structure. This means that we have to rely more heavily on regional data especially for smaller events, and on data from triplication distances ($R < 30^\circ$) that are not included in this inversion. However, in order to use this data we have to determine better calibrations for these distances, which correspond to upper mantle depths.

5.8 P_{nl} Propagation

The P_{nl} wavetrain is important in seismic source estimation studies as well for our preferred seismic discriminant and it is therefore important to calibrate this phase. We modeled the P_{nl} arrivals using the same methods as in Section 2 and the previous report. In Figure 42 we show the fit of the P_{nl} wave for several events along the North African coast recorded at station PAB. The waveforms seem quite stable for the different paths, but the travel-times do change with path. From these modeling efforts we conclude that both the P_n velocity as well as the average crustal P velocity under the Mediterranean increase from West to East, with the lowest velocities occurring under the Alboran Sea. This is consistent with observations of Banda (1988).

P_{nl} observations from the Rissani events recorded at station MEB and VSL (Figure 43), which are located at similar azimuths but different distances (860 and 1540 km respectively), show that the P waves at station VSL are very sharp and distinctive. This feature is best explained by a gradient at the top of the mantle (Figure 44) which makes the P wave appear more as a turning ray instead of a headwave. Thus, the waveform displays P, pP and sP just as a teleseismic signal does (Figure 39). A similar effect may be occurring in the observed records of the Gafsa event (Figure 30a) at VSL, where the P_n and S_n arrivals are quite distinct even at high frequencies (Figure 32a). Pino

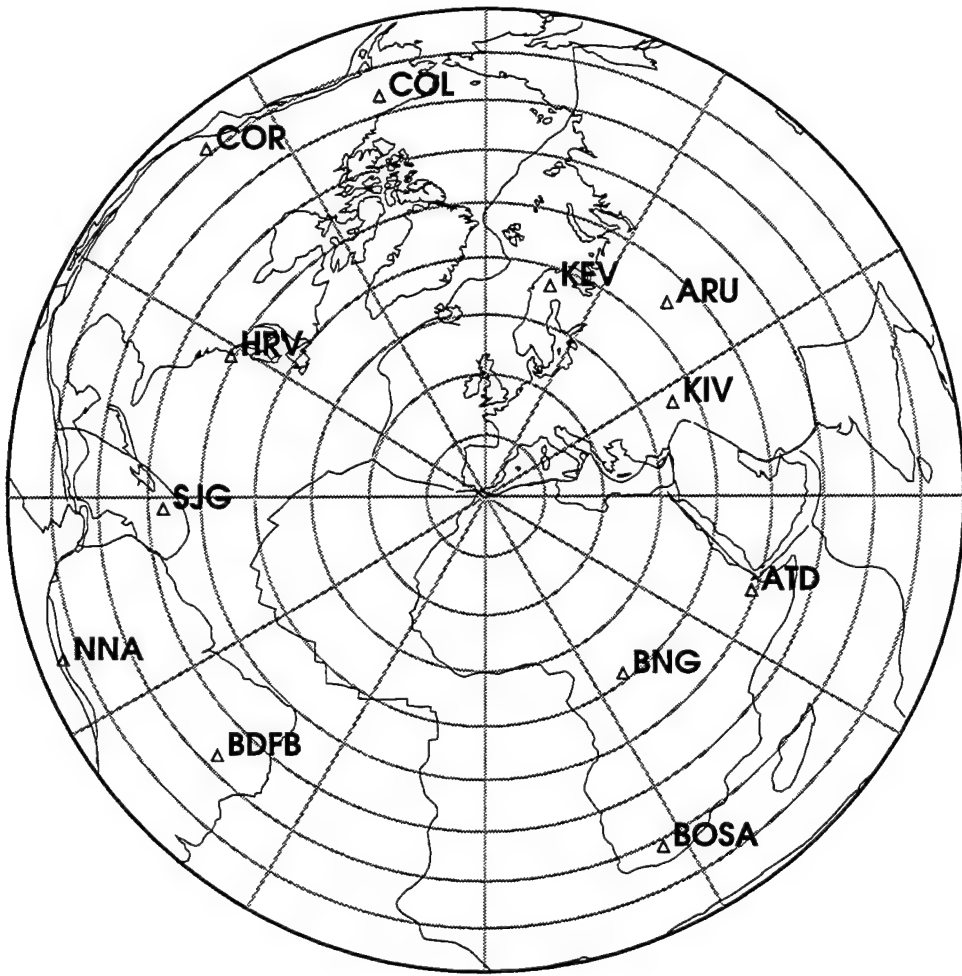


Figure 41. Station coverage for the teleseismic body-wave inversion of the Al Hoceima earthquake

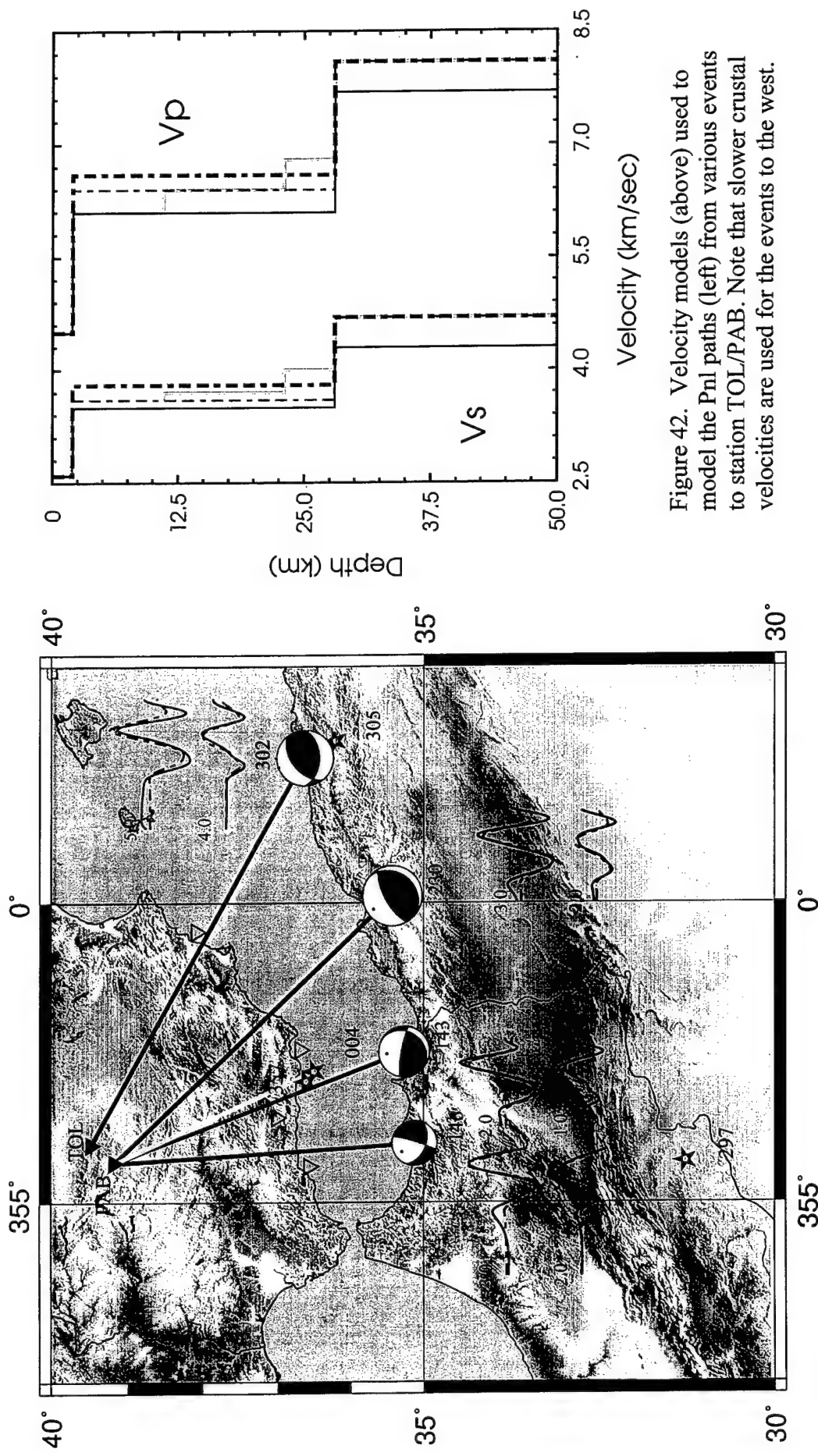


Figure 42. Velocity models (above) used to model the Pn paths (left) from various events to station TOL/PAB. Note that slower crustal velocities are used for the events to the west.

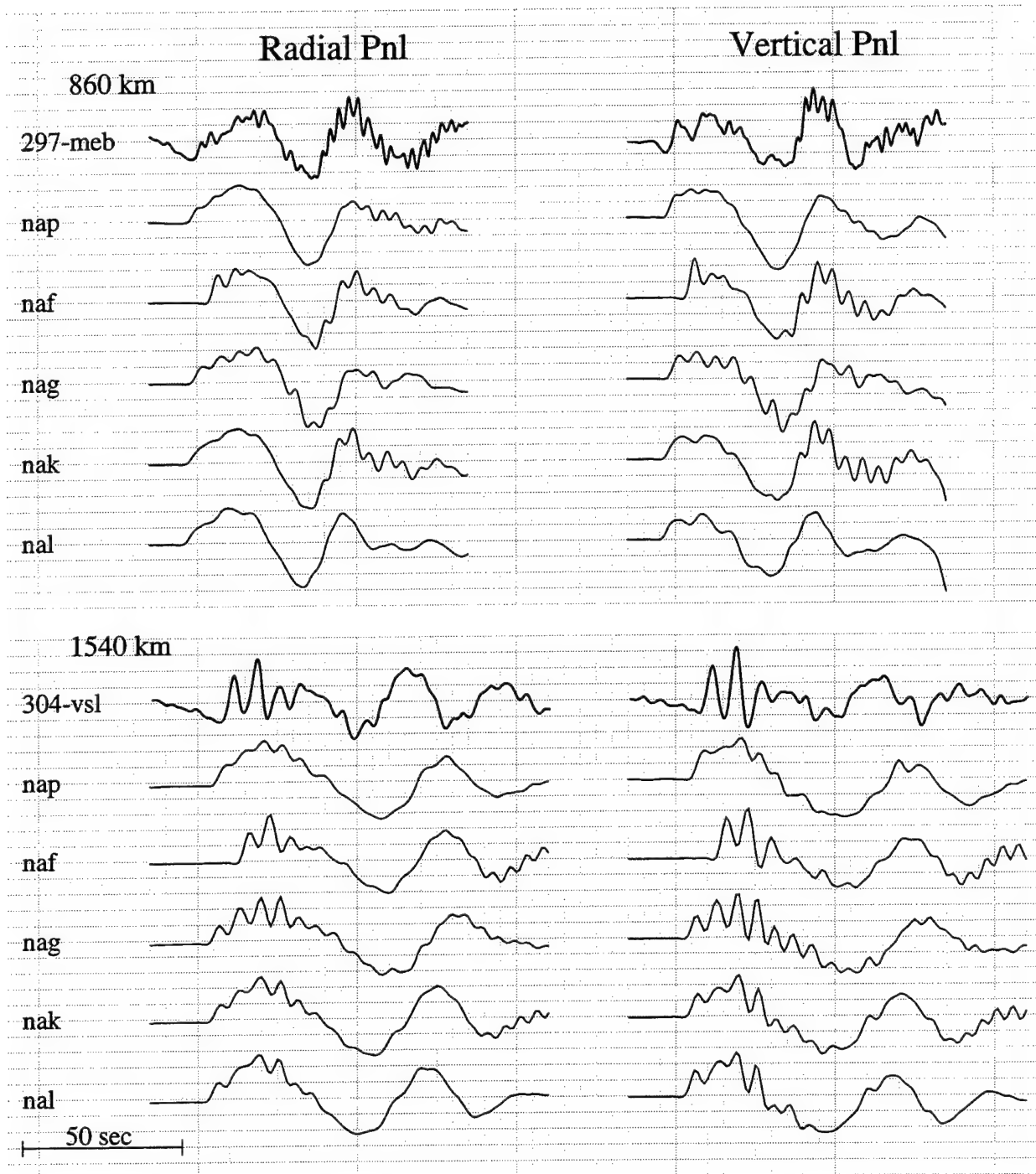


Figure 43. Comparison of a series of P-wave velocity models used in modeling the crust-guided PL waves. Both data and synthetics are low-pass filtered with a corner frequency of 0.2 Hz. Note that these models differ mainly in the crust-mantle transition, which controls the PL wavetrain in the frequency band shown. Data and synthetics are aligned in absolute time. The seismograms are scaled according to their largest amplitude.

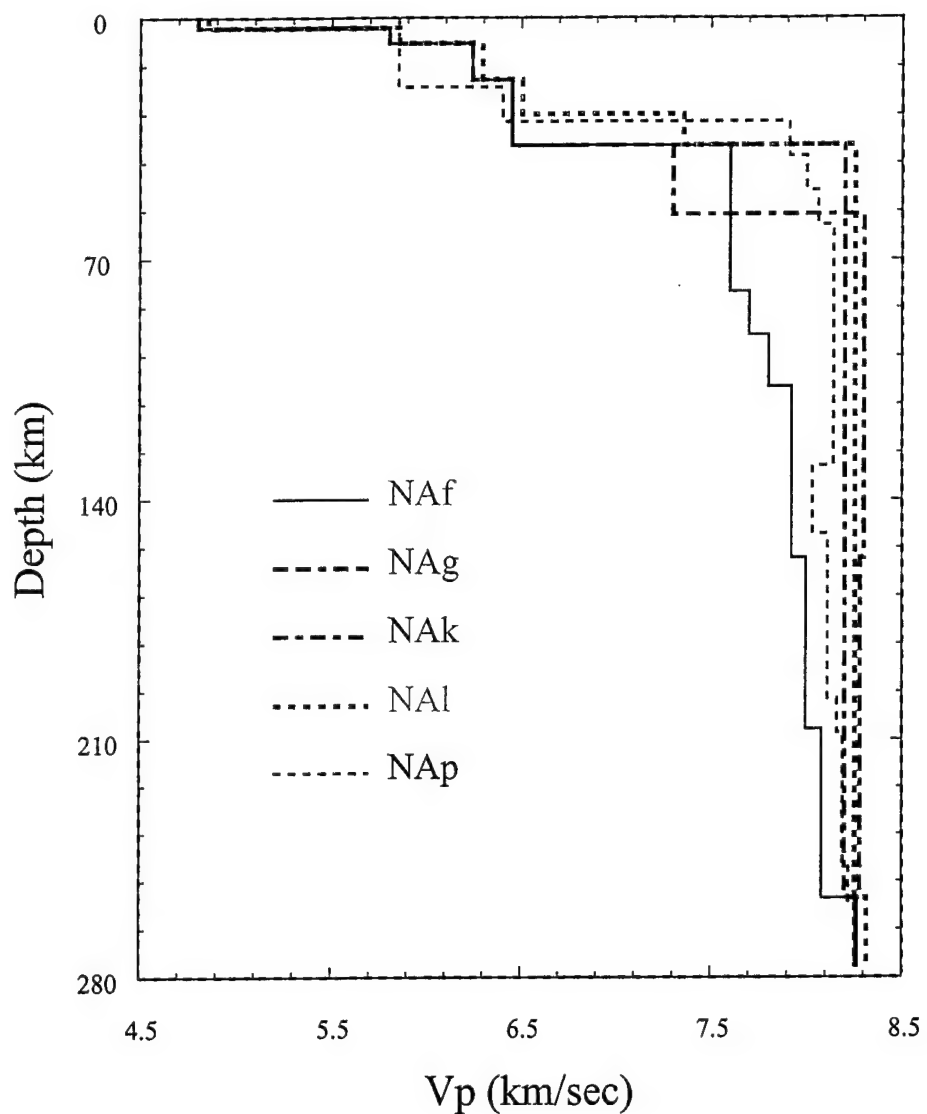


Figure 44. Velocity models used in the synthetic calculations of Figure 43. NAf is the North Africa model determined using the surface-waves, NAg, NAk, and NAl are some trial-and-error models without a gradient at the top of the mantle and model NAp is the model of Pino and Helmberger (1995).

and Helmberger (1995) found a gradient in the upper mantle based on observations of paths that cross the region around VSL, although their gradient is not sufficient to explain the distinct pulses that we observed (Figure 44). We haven't been able to establish how pervasive this effect is for other paths from North Africa, but with more data from Mednet being released it may be possible to calibrate and use these characteristics for depth discrimination.

5.9 Source Estimation Using Whole Waveforms

A disadvantage of using only surface waves in source estimation studies is that the results are poorly constrained if not enough stations are available. This problem becomes acute for smaller events ($Mw < 5$) for which often only one or two stations are available or if only few stations in the region contribute to the monitoring system in the first place. In these cases, it is preferable to use as much of the waveforms recorded as possible as well as to use higher passband information.

In mildly heterogenous regions like the Hindu-Kush (see previous report) we have successfully applied the method of Zhao and Helmberger (1994) for source estimation purposes using two stations. We have applied this method in the present study region and in Figure 45 we present the results for the Almeria event (93356) in Southern Spain using a single station (PAB). The result is compatible with the moment tensor solutions, and we obtain a very satisfactory waveform fit using a simple 1-D model. However, this model does not work very well for paths that cross the Mediterranean, especially for the surface waves as is expected from results in our previous sections (Figure 46). Although it is always possible to construct 1-D models to match the observed seismograms for a single station-receiver pair, this is not a satisfactory solution. In most cases, the effect of lateral heterogeneity on the P_{nl} waveforms consists merely of a shift in absolute time, whereas the surface waves, as mentioned earlier, can have completely different waveforms depending on the structure.

Since the surface waves and the body waves are already conveniently separated in the method of Zhao and Helmberger, it is very straightforward to adapt their method for a more heterogeneous region. The only modification that we have to make is that we use the mixed path normal mode method with the regionalized phase velocity model (Figure 29), that we described earlier, to calculate the Green's functions for the surface wave portion of the wavetrain, instead of using the normal methods of calculating body waves like ray theory.

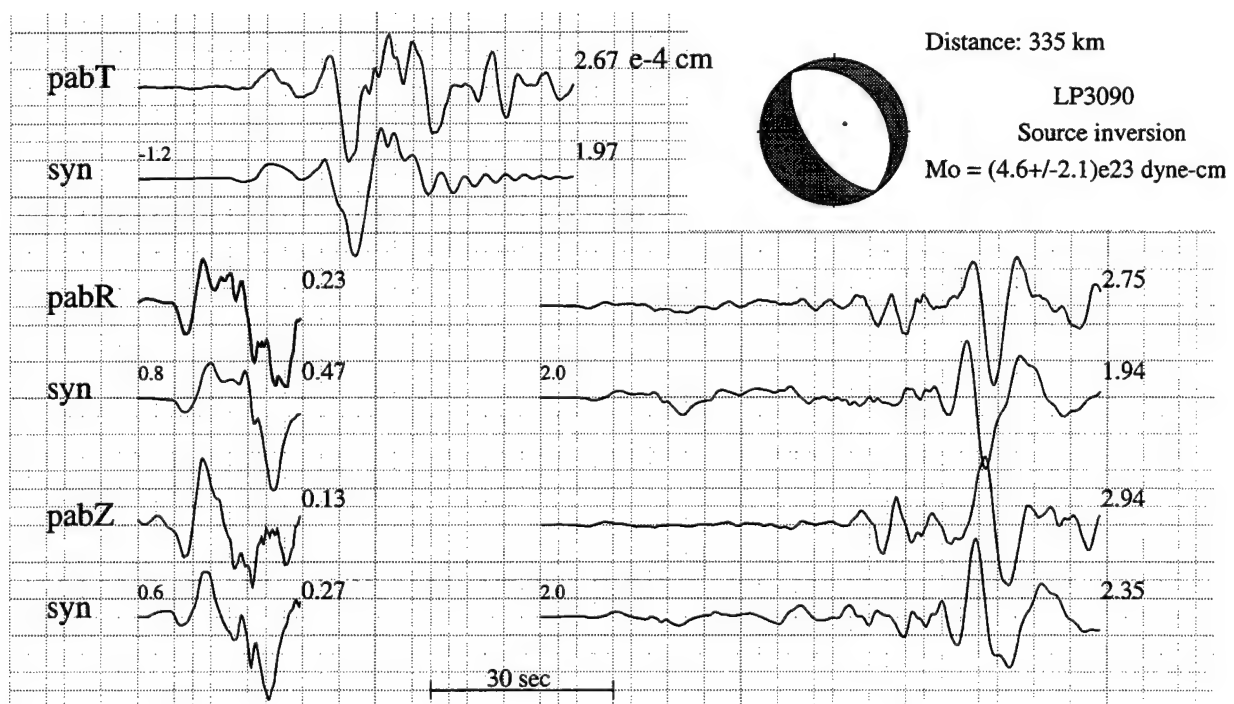


Figure 45. Results from a single station source inversion for the Almeria (93357) event in Southern Spain recorded at PAB. The Green's functions were calculated using a 1-D velocity model.

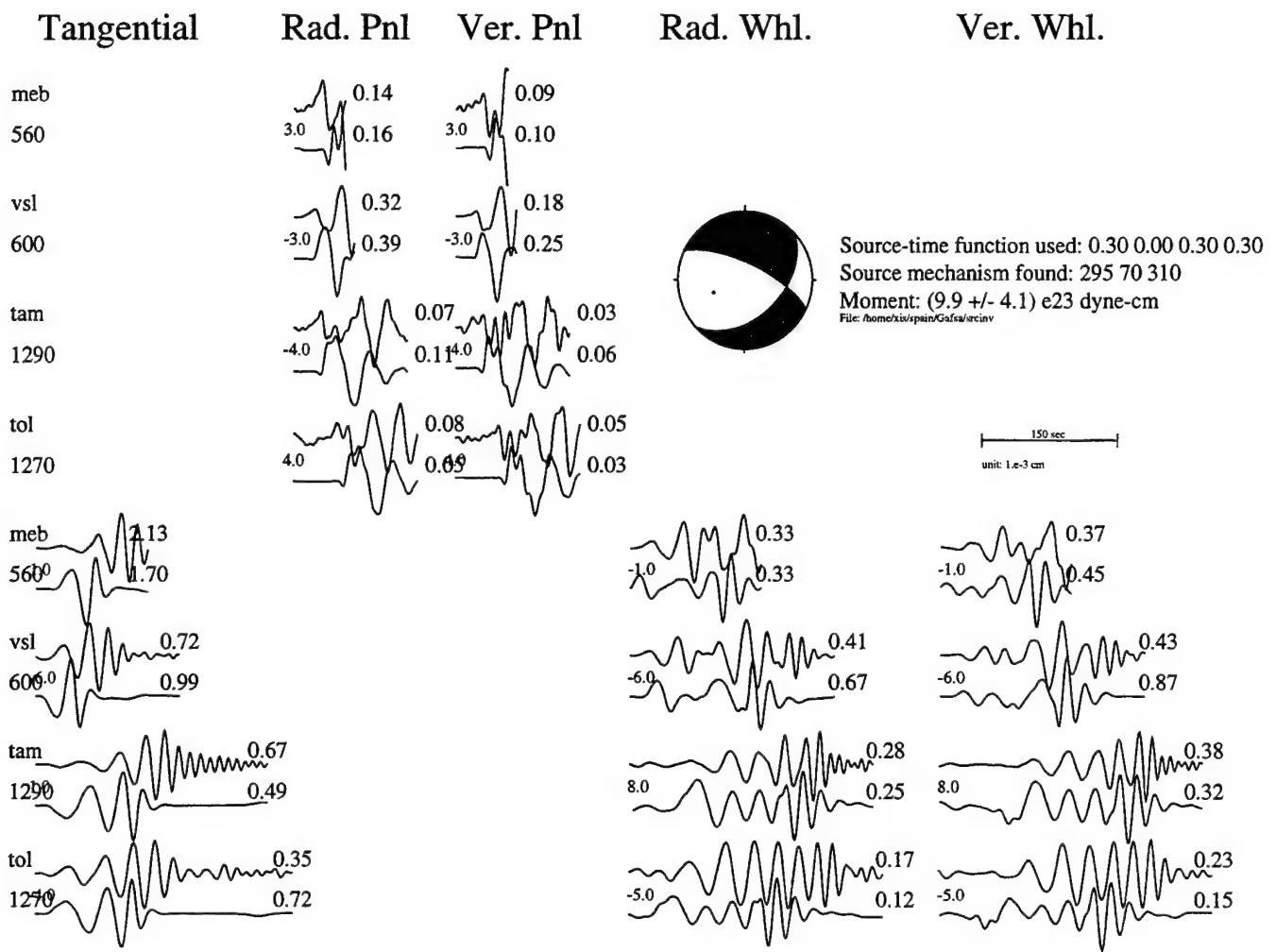


Figure 46. Inversion results using the method of Zhao and Helmberger for the Gafsa event using a 1-D model. It is inconsistent with the Harvard CMT as well as our own moment tensor solution obtained from surface wave inversion. The model used here was developed using our moment tensor solution and the TOL data. It is clear that such a 1-D model, even at longer periods, cannot fit the surface waves at all stations at the same time. Top traces of every pair are data, bottom traces are synthetic seismograms. The timeshift between data and synthetics in seconds is printed at the beginning of every pair.

In Figure 47, we present a multiple station inversion for the Gafsa event using the hybrid method. Note the very different character of the surface waves at different stations and how they are fit by the synthetic waveforms. Although there is still a mismatch for some records, especially at larger distances, we are able to fit the character of the waves much better than with a 1-D model. The same holds true for the 1988 North Algerian event which was recorded by the NARS network (Figure 48). Again, the very different character of the surface waves can be reproduced using our regionalized model.

Since monitoring efforts are based on a limited number of stations, we applied this method to observations from a single station. In Figure 49, we present the result from a single station inversion using the hybrid method for a master event in North Africa recorded by station PAB. The solution for Mostaganem event (94230) is identical to the solution that we obtained using surface waves recorded at several regional stations as well as to that of the Harvard CMT solution.

Another example is given in Figure 50 where we studied an event (Tipasa 1, 89302) for which only data from station TOL was available. Again, we were able to obtain a solution with a good fit for both the PnL and the surface waves.

So far, all the hybrid inversions have been carried out with long period (15 sec) filtered data, because our regionalization is not quite sufficient yet for shorter periods. We will concentrate on refining the regionalization, including off great-circle path effects so that we can use this method at shorter periods, and therefore for smaller events.

5.10 $E_{sp-Pz}:E_{lp-3}$ Ratio Discriminant Results for the Western Mediterranean

We have extended the analysis of the $E_{sp-Pz}:E_{lp-3}$ discriminant to the western Mediterranean in conjunction with waveform modeling in the area. This is a new test environment for the $E_{sp-Pz}:E_{lp-3}$ discriminant in that all previous regions studied have pure continental paths, whereas this area has paths traversing old oceanic crust as well as continental crust. As discussed in the waveform modeling section, these lateral variations in regional paths cause strong propagation effects. Strong attenuation or blockage effects, as discussed above, are well established for short-period Lg

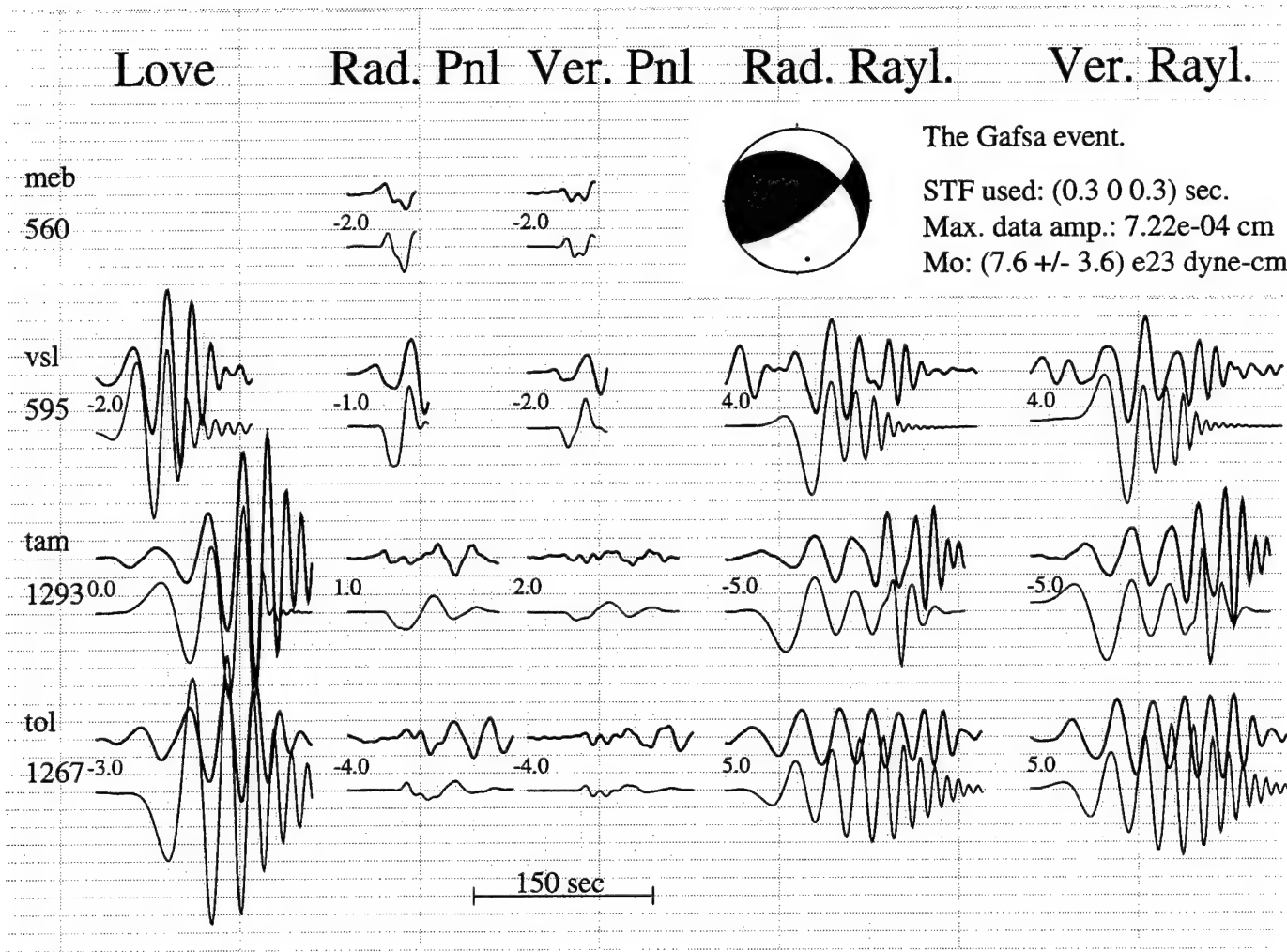


Figure 47. Source estimation for the June 12, 1992 Gafsa event ($M_b=4.8$). Comparison of long-period data and synthetics. Top traces of every pair are data, bottom traces are synthetics. Time shifts at the beginning of the traces are in seconds and represent the shift between the synthetic seismograms and the data. The model used for the Pnl waves is the same as that used for North Algeria event (88305), except that the crust has a thickness of 37 instead of 28 km. The surface wave portions were calculated using the regionalized model.

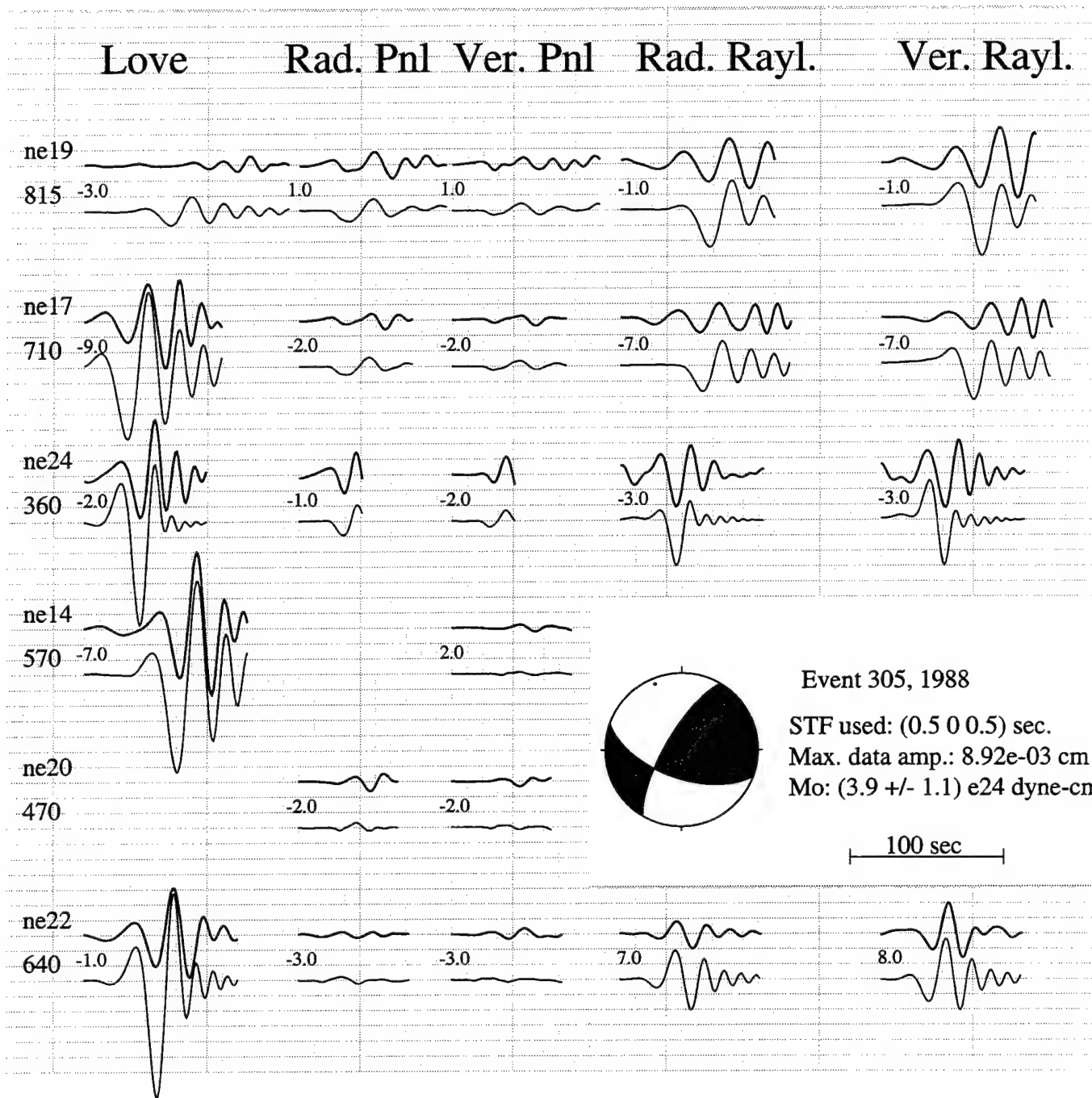


Figure 48. Source estimation for North Algeria event (88305). Comparison of long-period (>10 sec for Pnl, >20 sec for surfacewaves) data. Every waveform pair consists of data (top) and synthetics (bottom). The time shifts between data and synthetics are shown in seconds, with positive numbers indicating fast synthetics. Amplitudes for the Pnl waves are scaled by the distance.

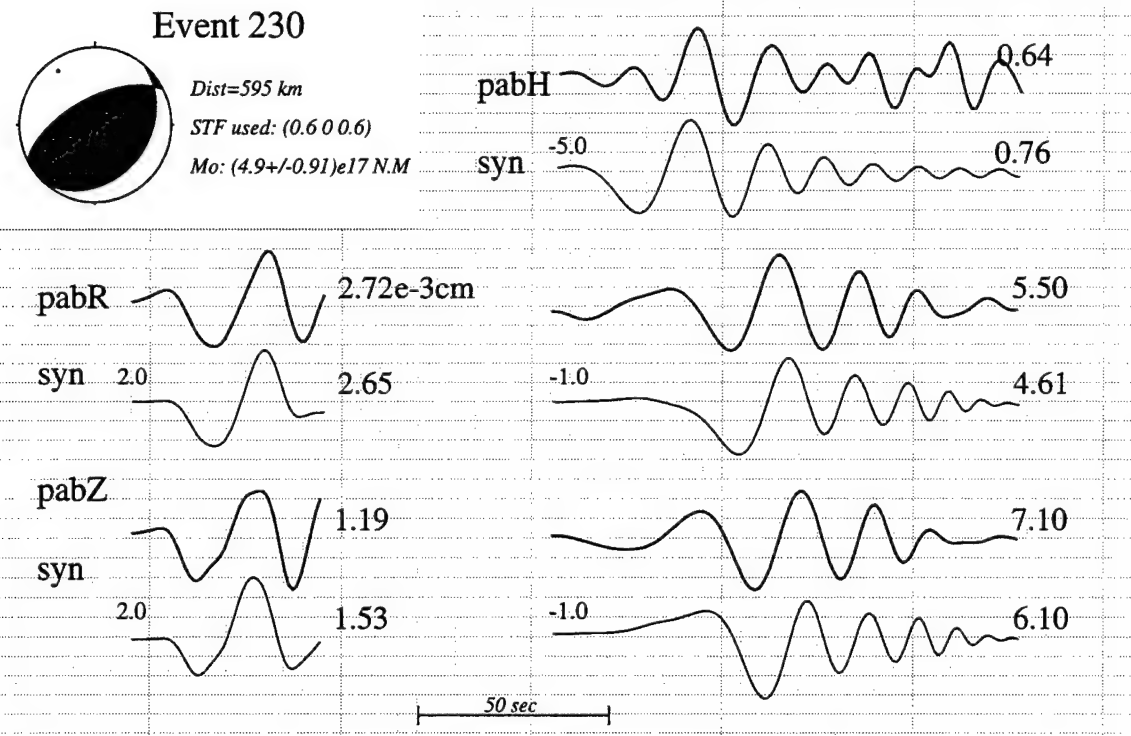


Figure 49. Single station inversion for the Mostaganem earthquake (94230) using the hybrid method. Left traces are Pnl waveform pairs, data (top) and synthetic (bottom). The right-hand traces are the surface-waves, calculated using the mixed path method: tangential (top pair), radial (center pair) and vertical (bottom pair). The number at the beginning of each pair represent the timeshift in seconds, the right-hand numbers are the amplitudes.

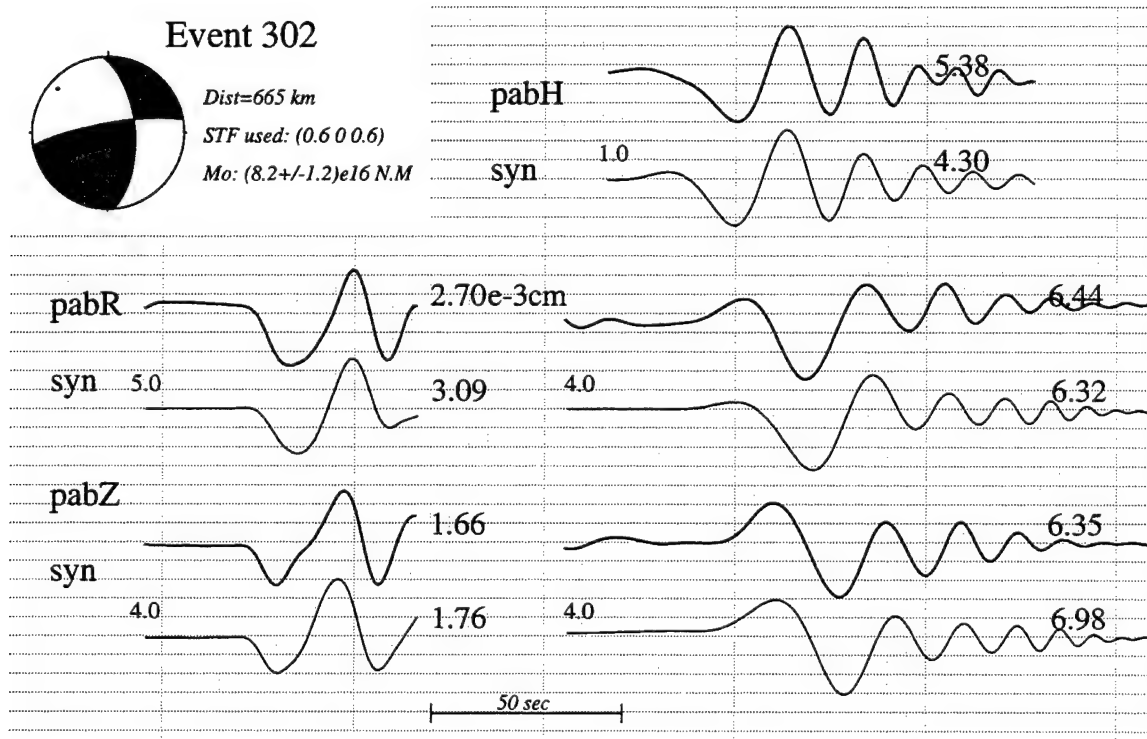


Figure 50. Single station inversion for the Tipasa 1 earthquake (89302) using the hybrid method. Labels and arrangement of the figure are similar to those in Figure 49.

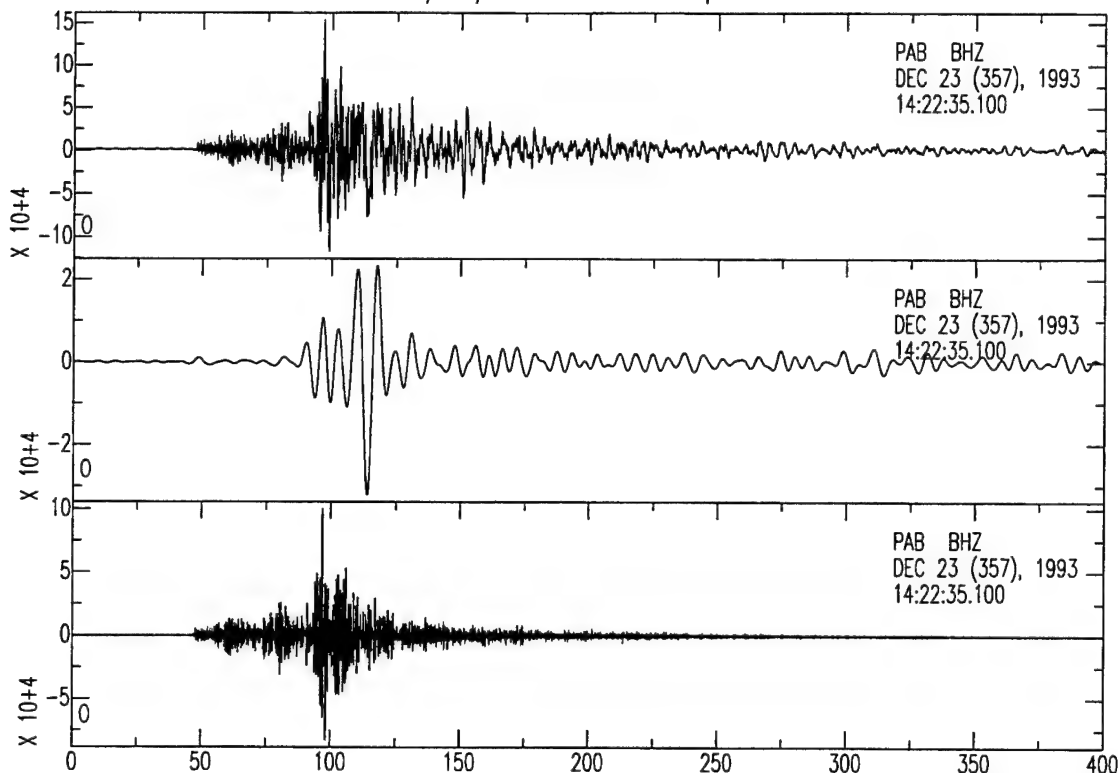
(McNamara *et al.*, 1996; Given, 1992), in addition however, similar effects seem to be occurring to the P_{nl} wavetrain.

As an example of this, Figure 51 plots the short-period and long-period play-outs of the vertical component velocity records for two of the events shown in Figure 29 (the Al-Hoceima and Almeria earthquakes) recorded at PAB. The top event ($m_b = 5$), which traverses a pure continental path has a strong, distinct, short-period S-wave. Peak long-period amplitudes are comparable in size to those of the short-period P_{nl} wavetrain. The other earthquake ($m_b = 4.6$) has larger long-period motion than either the short-period P_{nl} or S/L_g wavetrains. Both events have crustal source depths. The fact that this event is smaller by 0.4 magnitude units makes this result that much more significant, as the larger event should be relatively richer in long-period to short-period energy, however a nodal P-wave would have a similar effect.

Oceanic path propagation effects have two implications on the $E_{sp-P_c} \cdot E_{lp-3}$ discriminant. As the short-period energy level is reduced, the energy ratio will be reduced. Further the SNR measuring threshold for both the long-period and short-period energy will be expected to be near the same magnitude level, unlike in most regions where the short-period threshold level may be an order of magnitude larger than that for the long-period. This is evident in Figure 52 which plots the vertical component record at several passbands for a $m_b = 3.8$ crustal earthquake in Italy recorded by PAB, about 1300 km away, along a path traversing a large tract of the Mediterranean sea. Note that the surface wave is well defined, but that the body waves all lie within the noise level. In this case the energy ratio would be an upper bound. This particular event plots fairly low within the Western Mediterranean earthquake population, in fact. Calibration then is particularly important for paths crossing oceanic provinces. Also, the magnitude measuring threshold of this discriminant also approaches that of short-period discriminants for this region.

Figure 53 is a map of the Western Mediterranean study area with the earthquakes shown that are color-coded corresponding to their depths (red = shallow, yellow = intermediate, and blue = deep). Stations used are denoted triangles. A great majority of these events have shallow (crustal) source depths. A catalog of these events is given in Table 7.

93/12/23 vertical component



94/6/3 vertical component

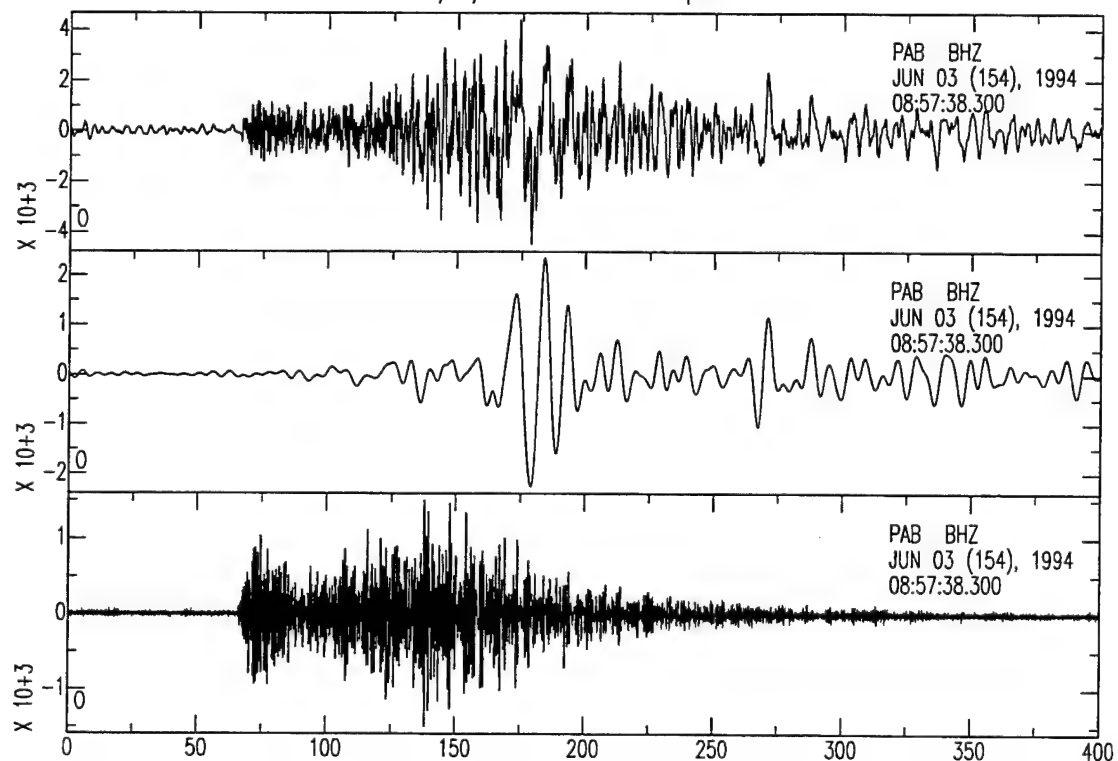


Figure 51. Vertical component velocity records from station PAB for an event along the Southern coast of Spain (top box) and another from Algeria (bottom box). In each case the top trace is the broad-band record, the middle trace band-pass filtered between 0.033 and 0.167 Hz, the passband for the long-period energy measurement, and the bottom trace is high-passed at 1 Hz which is the passband for the short-period energy measurement.

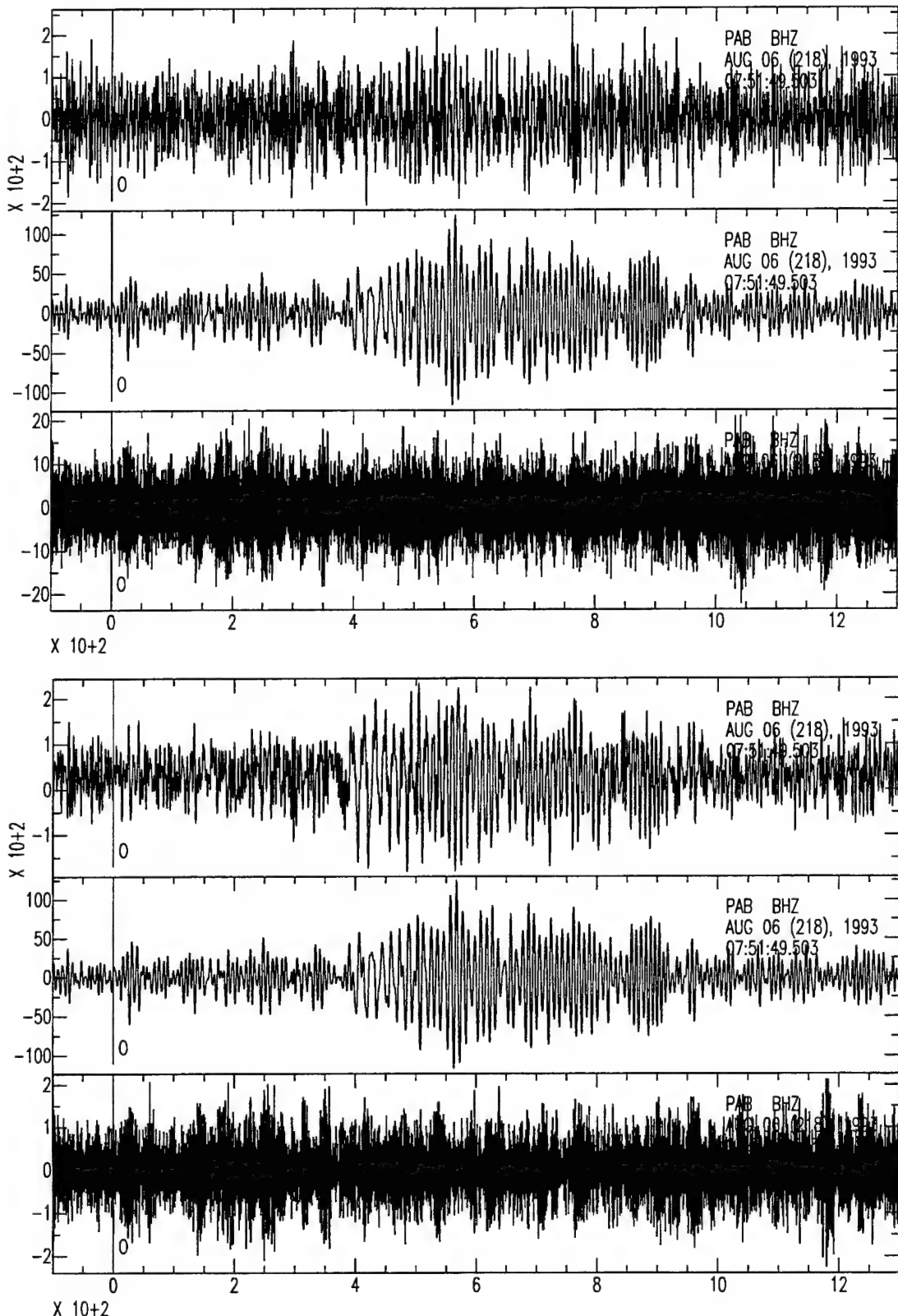


Figure 52. Vertical component seismograms of an Italian earthquake recorded by PAB, about 1300 km away. The top box are velocity records and the bottom box displacements. In each box the top trace is the broadband record, the middle trace band-pass filtered between 0.033 and 0.167 Hz, the passband for the long-period energy measurement, and the bottom trace is high-passed at 1 Hz which is the passband for the short-period energy measurement.

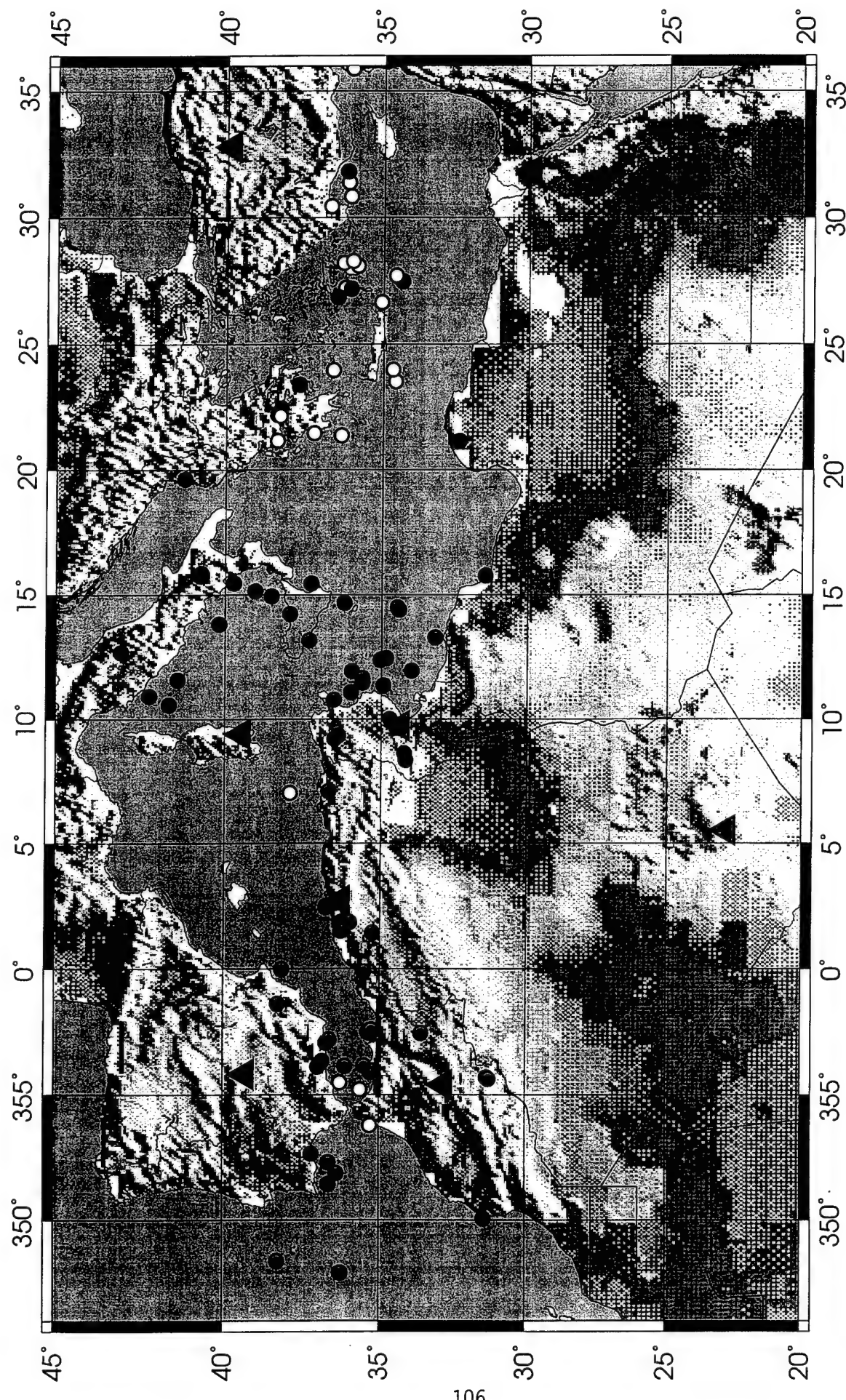


Figure 53. Map of the North African/Mediterranean region and stations and events which comprise the Western Mediterranean $E_{sp-Pz}E_{ip3}$ data set. Events are color-coded by depth with crustal earthquakes in red, intermediate depth earthquakes in yellow and deep earthquakes in blue.

The magnitude-normalized $E_{sp,Pz}:E_{lp,3}$ ratio vs. distance plot for these events is shown in Figure 54. Events again have been sorted with respect to depth. Events with long-period measures at the noise level are denoted by filled symbols. Once again, the deeper events, in general, have the largest energy ratio values. The energy ratio values are depressed considerably relative to the analogous curves for the other regions, as was speculated above. This off-set is estimated to be an order of magnitude difference.

5.11 Discussion and Future Work

We have shown how regionalization can be very useful in tectonically complex areas like the Mediterranean region. Although we have applied this regionalization to surface waves so far, we feel that the current model can easily be extended to other observed wave characteristics, in particular Pn velocities and short-period attenuation. Our present regionalization scheme should be refined in order to use the method for shorter periods, which will improve the constraints on the mechanism and also improves our analyzing capabilities for smaller events.

We have observed that teleseismic observations of body waves from this region are generally of poor quality, which may be due to complexities in the local structure. This emphasizes the importance of using regional data, as well as data from triplication distances ($R < 30^\circ$) for which excellent data is available, especially from the European stations. For instance, we also need to establish how common the distinctive P arrivals are at VSL is for North African events, and we will study this issue further as more data for that station becomes available. It is therefore most important to include the triplication distances in our calibration efforts.

6. Conclusions and Recommendations

Using a regionalized crustal and upper mantle model for the Hindu-Kush region developed from waveform modeling of moderate-sized master events, we have developed a procedure for locating seismic events both horizontally and with respect to depth. With established ground truth source information for these master events, it is possible to conduct studies of possible short-period depth-related phenomena which can be extended to lower magnitude events that cannot be analyzed using broadband waveform inversion procedure.

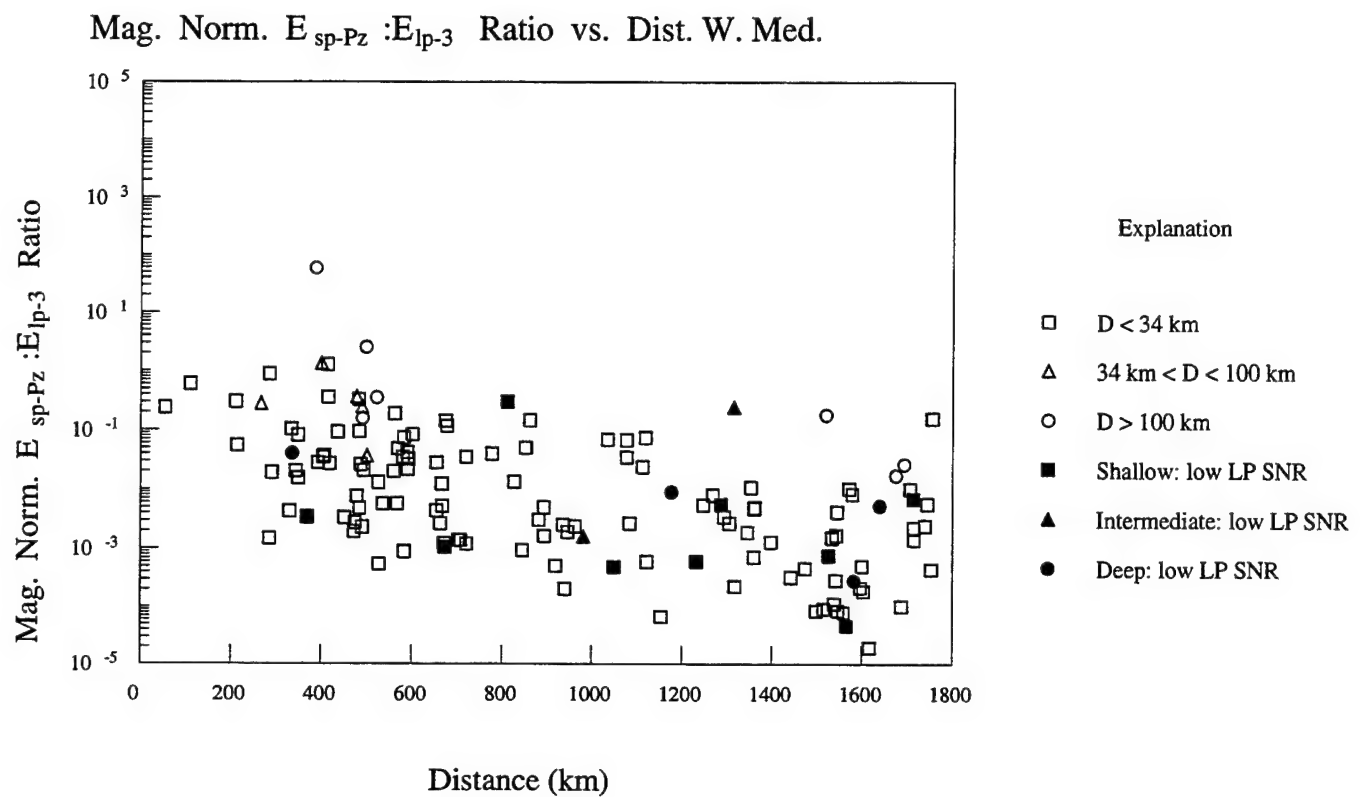


Figure 54. Magnitude-normalized $E_{sp-Pz} : E_{lp-3}$ ratio vs. distance for Western Mediterranean earthquakes. Shallow events ($D \leq 34 \text{ km}$) are denoted by squares, intermediate depth events ($34 < D < 100 \text{ km}$) by triangles and deep events ($D > 100 \text{ km}$) by circles. Events with low SNR long-period signals have filled symbols.

The P- and S-wave detection algorithm has been modified to obtain a back-azimuth measurement as well, thus making it possible to obtain single-station location estimates using three-component, broadband data. The S-wave complexity analysis further yields a potential depth estimator/discriminant, and as such is a complimentary test to the $E_{sp-Pz}:E_{lp-3}$ ratio to distinguish deep earthquakes from other low long-period level events.

Straight-forwardly applying a local magnitude measurement to the master events yields a well-constrained moment - magnitude relationship, although the absolute local magnitude level needs to be refined with a differential attenuation factor for transporting the magnitude scale from the western U.S. to the Hindu-Kush region.

We have compiled a test data-set of small events ($3 < M_L < 4.5$) for the Hindu-Kush region and are currently analyzing their performance with respect to the automated location and source characterization procedures. Results so far suggest that the S-wave complexity measure is an effective depth estimator. Also, sparse or single station locations for the small event appear to give reasonable estimates with depth being the least constrained however.

The calibration of the stations NIL and AAK with respect to regional propagation and source characterization techniques will be extended in azimuth and/or distance to include events to the Northeast from in and around the Lop Nor Test site and to the South into Southern Pakistan and Northern India. Further source depth estimates obtained from the techniques used in this report for present data set will be incorporated into the discriminant depth analysis.

As for the $E_{sp-Pz}:E_{lp-3}$ ratio discriminant, we have extended its performance analysis and calibration to the station ABKT and its surrounding region west of the Hindu-Kush region, and to the Western Mediterranean, a region including significant oceanic crust -- a tectonic environment which has not previously been studied with respect to the energy ratio discriminant. Further, more source depth information has been obtained for the events studied previously which were recorded by NIL, KNET, and AAK. The increase in source depth ground truth information for the data sets further establishes the effect of source depth on the energy ratio discriminant. Deep earthquakes can now be identified via the S-wave complexity measurement and separated from other outlying (with respect to the energy ratio criterion) events.

The IDC is currently implementing the $E_{sp-P_2}:E_{lp-3}$ ratio vs. distance discriminant into the IMS and retaining the parameters, however no quality testing of these results have been done. Therefore the next step is to evaluate the present IDC criteria for making $E_{sp-P_2}:E_{lp-3}$ ratio measurements (signal to noise, time windows used and quality of data). Currently only 10-15% of identified events are yielding these measurements. We will examine this feature and determine whether or not a higher performance percentage can be achieved.

As large explosion data for the present study area is quite sparse, in order to prove the performance of this discriminant we will make cursory studies of stations for which both earthquake and explosion data is available. Currently central Europe is a primary candidate for such work as large blasts and collapses are well documented for this area.

In order to make discrimination parameter information globally comparable, stations and regions need to be calibrated relative to one another. To this end, empirical calibrations will be made for the stations in Southwestern Eurasia analyzed so far and for stations which have recorded anomalous events as well as earthquakes.

Waveform modeling of the Western Mediterranean region has yielded an adequate 1-D model for surface wave propagation. Mixed-path synthetics yield even better waveform and dispersion fits. The nature of the region is such that rather sophisticated regionalization of propagation path calibrations are necessary. Continuing work will focus on refining the current regionalization scheme, including accounting for off great-circle path effects (multi-pathing), so that the surface wave source inversion can be extended to shorter periods ($T < 15$ sec.). The regional calibration will be extended to shorter period phases such as P_n , as well, once the larger scale structure is understood.

From our experience with this project we make several recommendations:

- (1) Surface waves are most susceptible to upper crustal variations, so that the regionalization of surface wave models will end up being more extensive than body-wave calibrations.
- (2) In data gathering and analysis we have found that many events in the $3 < M_w < 4.5$ range are not currently located or in many cases identified by global seismic bulletins, including the IDC's.

Therefore, it is of great importance to establish regional waveguide models for performing IMS stations -- both α and β , in order to better monitor local, low-magnitude seismicity.

(3) Related to (2) is the matter of incorporating regional phase information with teleseismic data in order to lower the magnitude threshold for identifying and locating events. Given the relatively sparse coverage of IMS stations, it is easy to imagine a small event which may only be picked-up with one or two teleseismic arrays and one regional station, whereby combining the different types of information (regional and teleseismic) from these observations can yield improved locations and magnitudes, or furnish them when otherwise unattainable.

(4) We are currently working on a real-time event locating program requiring three-component broadband data from single station. Such a system could provide reasonable locations within minutes and would be of considerable value to the IMS system for analyzing small events.

References

- Allen, R. V. (1978). Automatic earthquake recognition and timing from single traces, *Bull. Seis. Soc. Am.*, **68**, 1521-1532.
- Ambraseys, N.N., J. Vogt and R.D. Adams (1991). The Algerian earthquake of 24 June 1910: a case history, *Tectonoph.*, **193**, 205-213.
- Ambuter, B. P. and S. C. Solomon (1974). An event-recording system for monitoring small earthquakes, *Bull. Seis. Soc. Am.*, **64**, 1181-1188.
- Aoudia, A. and M. Meghraoui (1995). Seismotectonics in the Tell Atlas of Algeria: the Cavaignac (Abou El Hassan) earthquake of 25.08.1922 ($M_s = 5.9$). *Tectonoph.*, **248**, 263-276.
- Bakun, W. H. and W. B. Joyner (1984). The M_L scale in central California, *Bull. Seis. Soc. Am.*, **74**, 1827-1844.
- Banda, E. (1988). Crustal parameters in the Iberian Peninsula, *Phys. Earth Plan. Int.*, **51**, 222-225.
- Barazangi, M., E. Fielding, B. Isacks and D. Seber (1996). Geophysical and Geological databases and CTBT monitoring: a case study of the Middle East, in *Monitoring a Comprehensive Test Ban Treaty*, Husebye, E.S., and A.M.Dainty, eds, Kluwer Academic Pub., 197-224.

- Billington, S., B.L. Isacks, and M. Barazangi (1977). Spatial distribution and focal mechanisms of mantle earthquakes in the Hindu Kush-Pamir region: A contorted Benioff zone, *Geology*, **5**, 699-704.
- Bratt, S. R. and T. C. Bache (1988). Locating events with a sparse network of regional arrays, *Bull. Seis. Soc. Am.*, **78**, 780-798.
- Buñom, E., A. Udías and R. Madariaga (1991). Intermediate and deep earthquakes in Spain. *Pageoph.*, **136**, no. 4, 375-393.
- Buñom, E., C. Sanz de Galdeano and A. Udías (1995). Seismotectonics of the Ibero-Maghrebian region. *Tectonoph.*, **248**, 247-261.
- Burtman, V.S. and P. Molnar (1993). Geological and geophysical evidence for deep subduction of continental crust beneath the Pamir, *Special papers, Geological Society of America*, 281.
- Cahen, L. and N.J. Snelling (1984). The geochronology and evolution of Africa. Clarendon Press, Oxford, 512 pp.
- Chatelain, J.L., S.W. Roecker, D. Hatzfeld, and P. Molnar (1980). Microearthquake seismicity and fault plane solutions in the Hindu Kush region and their tectonic implications, *Journal Geophysical Research*, **85**, 1365-1387.
- Corchete, V., J. Badal, F.J. Serón and A. Soria (1995). Tomographic images of the Iberian subcrustal lithosphere and astenosphere. *J. Geoph. Res.*, **100**, B12, 24,133-24,146.
- Denny, M. D., S. R. Taylor, and E. S. Vergino (1987). Investigation of m_b and M_s formulas for western United States and their impact on M_s/M_b discriminant, *Bull. Seis. Soc. Am.*, **77**, 987-995.
- Dziewonski, A.M. and J.H. Woodhouse (1983). Studies of the seismic source using normal-mode theory. In *Earthquakes: observation, theory and interpretation*, Kanamori, H. and E. Boschi, eds., North Holland, Amsterdam, 45-137.
- Dziewonski, A.M., S. Bloch and M. Landisman (1969). A technique for the analysis of transient seismic signals, *Bull. Seis. Soc. Am.*, **59**, 427-444.
- Fan, G., J.F. Ni, and T.C. Wallace (1994). Active tectonics of the Pamirs and Karakorum, *J. Geoph. Res.*, **99**, 7131-7160.
- Giardini, D., E. Boschi and B. Palumbo (1993). Moment tensor inversion from MEDNET data (2) Regional earthquakes of the Mediterranean. *Geoph. Res. Lett.*, **20**, no. 4, 273-276.

- Given, H. (1991). Heterogeneous Propagation and Blockage of Lg in the Caspian Sea - Caucasus Mountain area of the USSR, *Proceedings of the 13th Seismic Research Symposium* sponsored by PL/DARPA, 211-217, PL-TR-91-2208, ADA241325.
- Hadiouche, O. and N. Jobert (1988). Geographical distribution of surface-wave velocities and 3-D upper mantle structure in Africa. *Geoph. J. Int.*, **95**, 87-109.
- Isacks, B. and P. Molnar (1971). Distribution of stresses in the descending lithosphere from a global survey of focal mechanism solutions of mantle earthquakes, *Rev. Geophys. Space Phys.*, **9**, 103-174.
- Johnston, A.C. (1996). Seismic moment assessment of earthquakes in stable continental regions 3. New Madrid 1811-1812, Charleston 1886 and Lisbon 1755. *Geoph. J. Int.*, **126**, 314-344.
- Kanamori, H., J. Mori, E. Hauksson, T. H. Heaton, L. K. Hutton and L. M. Jones (1993). Determination of earthquake energy release and M_L using TERRASCOPE, *Bull. Seis. Soc. Am.*, **83**, 330-346.
- Kikuchi, M. and H. Kanamori (1991). Inversion of complex body-waves III. *Bull. Seis. Soc. Am.*, **81**, 2335-2350.
- LeFevre, L. and D. V. Helmberger (1989). Upper mantle P velocity structure of the Canadian Shield, *J. Geophys. Res.*, **94**, 17,749-17,765.
- Lesquer, A., D Takherist, J.M. Dautria and O. Hadiouche (1990). Geophysical and petrological evidence for the presence of an "anomalous" upper mantle beneath the Sahara basins (Algeria). *Earth Plan. Sc. Lett.*, **96**, 407-418.
- Levshin, A. L. (1985). Effects of lateral inhomogeneities on surface wave amplitude measurements, *Annal. Geophys.*, **3**, 511-518.
- Lienert, B. R. and J. Havskov (1995). A computer program for locating earthquakes both locally and globally, *Seism. Res. Lett.*, **66**, 5,26-36.
- Lukk, A.A., M. Mirzokurbanov, and I.L. Nersesov (1983). Lateral inhomogeneities of the upper mantle of Central Asia and their possible relation to the process of orogenisis, *Izv. Acad. Sci. USSR Phys. solid Earth*, engl. Transl., **19**, 442-459.
- Marshall, P. D. and P. W. Basham (1972). Discrimination between earthquakes and underground explosions employing an improved M_s scale, *Geophys. J. R. astr. Soc.*, **28**, 431-458.
- McNamara, D., W. R. Walter, C. S. Schultz, and P. Goldstein (1996). Regional Phase Propagation in North Africa and the Mediterranean, *Seism. Res. Lett.* (abs.) **67**, 47.

- Medina, F. (1995). Present-day state of stress in northern Morocco from focal mechanism analysis, *J. Struct. Geol.*, **17**, no. 7, 1035-1046.
- Meghraoui, M., J.-L. Morel, J. Andrieux and M. Dahmani (1996). Tectonique plio-quaternaire de la chaîne tello-riffaine et de la mer d'Alboran. Une zone complexe de convergence continent-continent. *Bull. Soc. Géol. Fr.*, **167**, no. 1, 141-157.
- Molnar, P., and P. Tapponnier (1975). Cenozoic tectonics of Asia: Effects of continental collision, *Science*, **189**, 419-426.
- Molnar, P., and H. Lyon-Caen (1989). Fault plane solutions of earthquakes and active tectonics of the Tibetan Plateau and its margins, *Geophys. J. Int.*, **99**, 123-153.
- Murphy, J. R., P. E. Marshall, B. W. Baker, T. J. Bennett, W. Rivers and L. Grant (1995). Calibration of local magnitude scales for use in seismic monitoring, *17th Seismic Research Symposium on monitoring a CTBT*, sposored by PL/AFOSR/AFTEC/DoE, 252-261, PL-TR-95-2108, ADA310037.
- Nikonov, A.A., A.V. Vakov, and I.A (1983). Veselov, Seismotectonics and earthquakes in the convergent zone between the Pamir and Tien Shan (in Russian): Moscow, Nauka, 240p, 1983.
- Nikonov, A.A. (1988). Reconstruction of the main parameters of old large earthquakes in Soviet Central Asia using the paleoseismogeological method, *Tectonoph.*, **147**, 297-312.
- Nolet, G., B. Dost and H. Paulsen (1991). The NARS array. In MedNet: The broadband seismic network for the Mediterranean, *Il Cigno Galileo Galilei*, Rome, 515 pp.
- Patton, H. J. and W. R. Walter (1993). Regional moment:magnitude relations for earthquake and explosions, *Geophys. Res. Lett.*, **20**, 277-280.
- Pino, N.A. and D.V. Helmberger (1996). Upper mantle compressional velocity structure beneath the Western Mediterranean basin. *J. Geoph. Res.*, in press.
- Research Group for Lithospheric Structure in Tunisia (1992). The EGT'85 seismic experiment in Tunisia: a reconnaissance of the deep structures, *Tectonoph.*, **207**, 245-267.
- Roecker, S.W, O.V. Soboleva, I.L. Nersesov, A.A. Lukk, D. Hatzfeld, J.L. Chatelain, and P. Molnar (1980). Seismicity and fault plane solutions of intermediate depth earthquakes in the Pamir-Hindu Kush region, *Journal Geophysical Research*, **85**, 1358-1364.
- Richter, C. (1935). An instrumental earthquake magnitude scale, *Bull. Seis. Soc. Am.*, **25**, 1-32.

- Saikia, C. K., B. B. Woods, L. Zhu, H. K. Thio and D. V. Helmberger (1996). Path calibration, source estimation and regional discrimination for the Middle East: Application to the Hindu-Kush Region, *Scientific Report 1*, PL-TR-96-2069, ADA314440.
- Sandvol, E., J. Ni and T. Hearn (1994). Seismic azimuthal anisotropy beneath the Pakistan Himalaya, *Geophys. Res. Lett.*, **21**, 1635-1638.
- Seber, D., M. Barazangi, B.A. Tadili, M. Ramdani, A. Ibenbrahim and D. Ben Sari (1996). Three-dimensional upper mantle structure beneath the intraplate Atlas and interplate Rif mountains of Morocco. *J. Geoph. Res.*, **101**, no. B2, 3125-3138.
- Shlien, S. and M. N. Toksöz (1973). Automatic event detection and location capabilities of large aperture seismic arrays, *Bull. Seis. Soc. Am.*, **63**, 1275-1288.
- Singh, S.K., M.A. Santoyo, and J. Pacheco (1995). Intermediate-depth earthquakes in central Mexico: implications for plate waves, *Geophys. Res. Lett.*, **22**, 527-530.
- Snieder, R. (1988). Surface wave scattering theory, *Geol. Ultraiectina*, **50**.
- Song, X.J., D.V. Helmberger, and L.S. Zhao (1996). Broad-band modeling of regional seismograms: the Basin and Range crustal structure, *Geophys. J. Int.*, **125**, 15-29.
- Song, X.J. and D.V. Helmberger (1996). The Northridge aftershocks, a source study with TERRAScope data, *submitted to Bull. Seis. Soc. Am.*
- Stevens, J. L. and S. M. Day (1985). The physical basis of m_b : M_s and variable frequency magnitude methods for earthquake/explosion discrimination, *J. Geophys. Res.*, **90**, 3009-3020.
- Stevens, J.L. and K.L. McLaughlin (1996). A transportable regional discriminant using a maximum likelihood analysis of surface waves. *Proceedings of the 18th Annual Seismic Research Symposium* sponsored by PL/AFOSR/AFTEC/DoE, 622-630, PL-TR-96-2153, ADA313692.
- Stevenson, R. (1976). Microearthquake at Flathead Lake, Montana: A study using automatic earthquake processing, *Bull. Seis. Soc. Am.*, **66**, 61-79.
- Stewart, S. W. (1977). Real-time detection and location of seismic events in central California, *Bull. Seis. Soc. Am.*, **67**, 433-452.
- Taylor, S. R., D. D. Denny, E. S. Vergino and R. E. Glaser (1989). Regional discrimination between NTS explosions and southwestern U. S. earthquakes, *Bull. Seis. Soc. Am.*, **79**, 1142-1176.
- Thio, H.K. and H. Kanamori (1995). Moment-tensor inversions for local earthquakes using surface waves recorded at TERRAScope. *Bull. Seis. Soc. Am.*, **85**, 1021-1038.

- Westaway, R. (1990). Present-day kinematics of the plate boundary zone between Africa and Europe, from the Azores to the Aegean. *Earth Plan. Sc. Lett.*, **96**, 393-406.
- Woods, B. B. and D. G. Harkrider (1995). Determination of surface wave magnitudes from regional NTS data, *Geophys. J. Int.*, **120**, 474-498.
- Woods, B. B. S. Kedar, and D. V. Helmberger (1996). $M_L:M_0$ as a regional seismic discriminant, *Bull. Seism. Soc. Am.*, **83**, 1167-1183.
- Working Group for Deep Seismic Sounding in Spain, 1974-1975 (1977). Deep seismic soundings in southern Spain, *Pageoph*, **115**, 721-735.
- Zandt G., S.L. Beck, S.R. Ruppert, C.J. Ammon, D. Rock, E. Minaya, T.C. Wallace, and P.G. Silver (1996). Anomalous crust of the Bolivian Altiplano, central Andes: constraints from broadband regional seismic waveforms, *Geophys. Res. Lett.*, **23**, 1159-1162.
- Zhao, L. and D.V. Helmberger (1991). Geophysical implication from relocation of Tibetan earthquakes - hot lithosphere, *Geophys. Res. Lett.*, **18**, 2205-2208.
- Zhao, L. and D.V. Helmberger (1993). Source retrieval from broadband regional seismograms: Hindu Kush region, *Physics of the Earth and Planetary Interiors*, **78**, 69-95.
- Zhao, L. and D.V. Helmberger (1994). Source estimation from broadband regional seismograms, *Bull. Seism. Soc. Am.*, **84**, 91-104.
- Zhu, L.P., R.S. Zeng, F.T. We, T.J. Owens, and G.E. Randall (1993). Preliminary study of crust-upper mantle structure of the Tibetan plateau by using broadband teleseismic body waveforms, *Acta Seismo. Sinica*, **6**, 305-316.
- Zhu, L.P. and D.V. Helmberger (1994). Regional earthquake waveform modeling on the Tibetan plateau, *Proceedings of the 16th Annual Seismic Research Symposium*, Thornwood, New York, 407-413, PL-TR-94-2217, ADA284667.
- Zhu, L.P. and D.V. Helmberger (1996a). Intermediate-depth earthquakes beneath the India-Tibet collision zone, *Geophys. Res. Lett.*, **23**, 435-438.
- Zhu, L.P. and D.V. Helmberger (1996b). Advancement in source estimation techniques using broadband regional seismograms, *Bull. Seism. Soc. Am.*, **86**, 1634-1641.
- Zielhuis, A. (1992). S-wave velocity below Europe from delay-time and waveform inversions, *Geol. Ultraiectina*, **88**.

APPENDIX

Figure A.0 Analysis of broadband seismograms for shallow event 289.024239.hlkt hp 1.0 lp 8.0

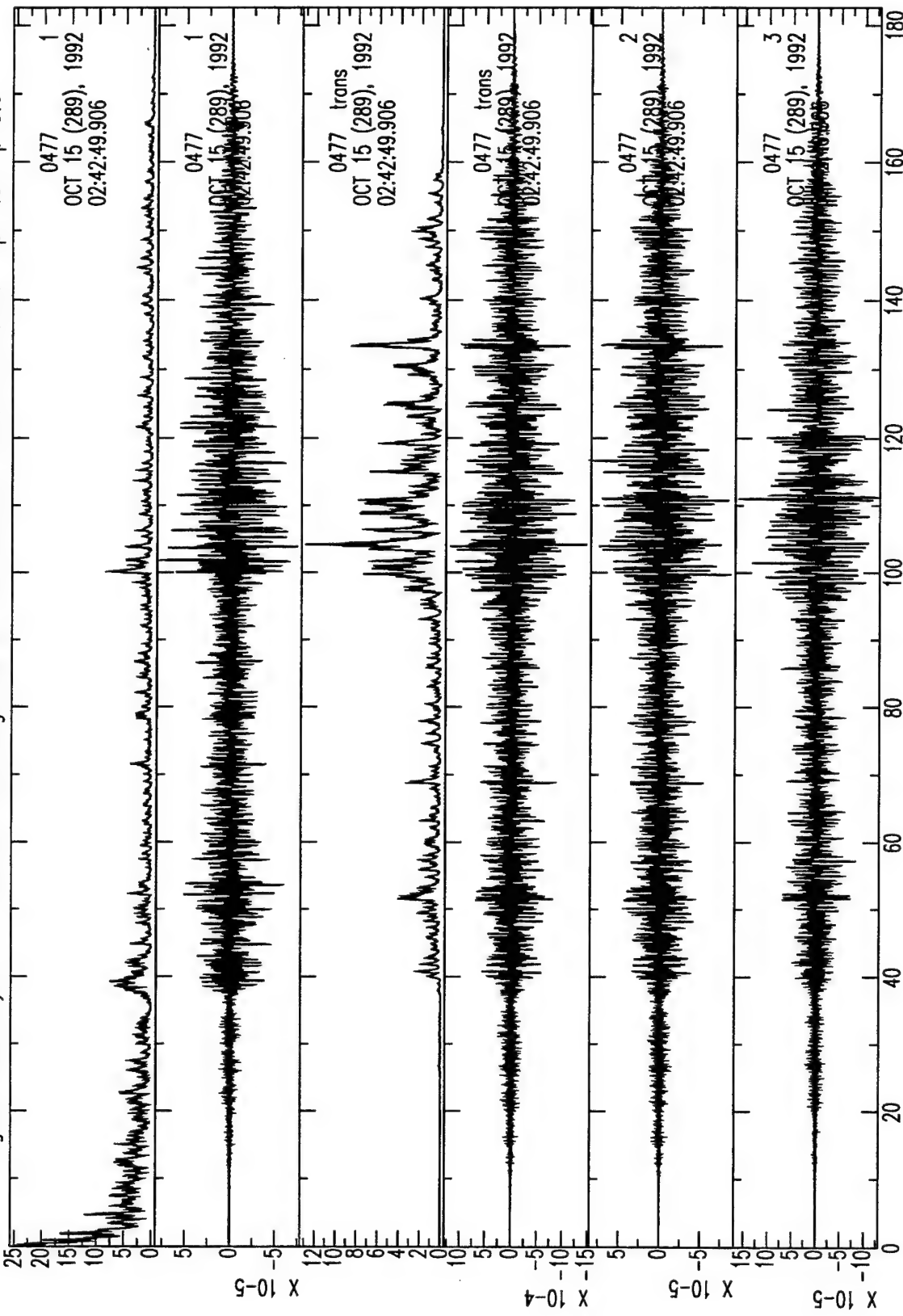
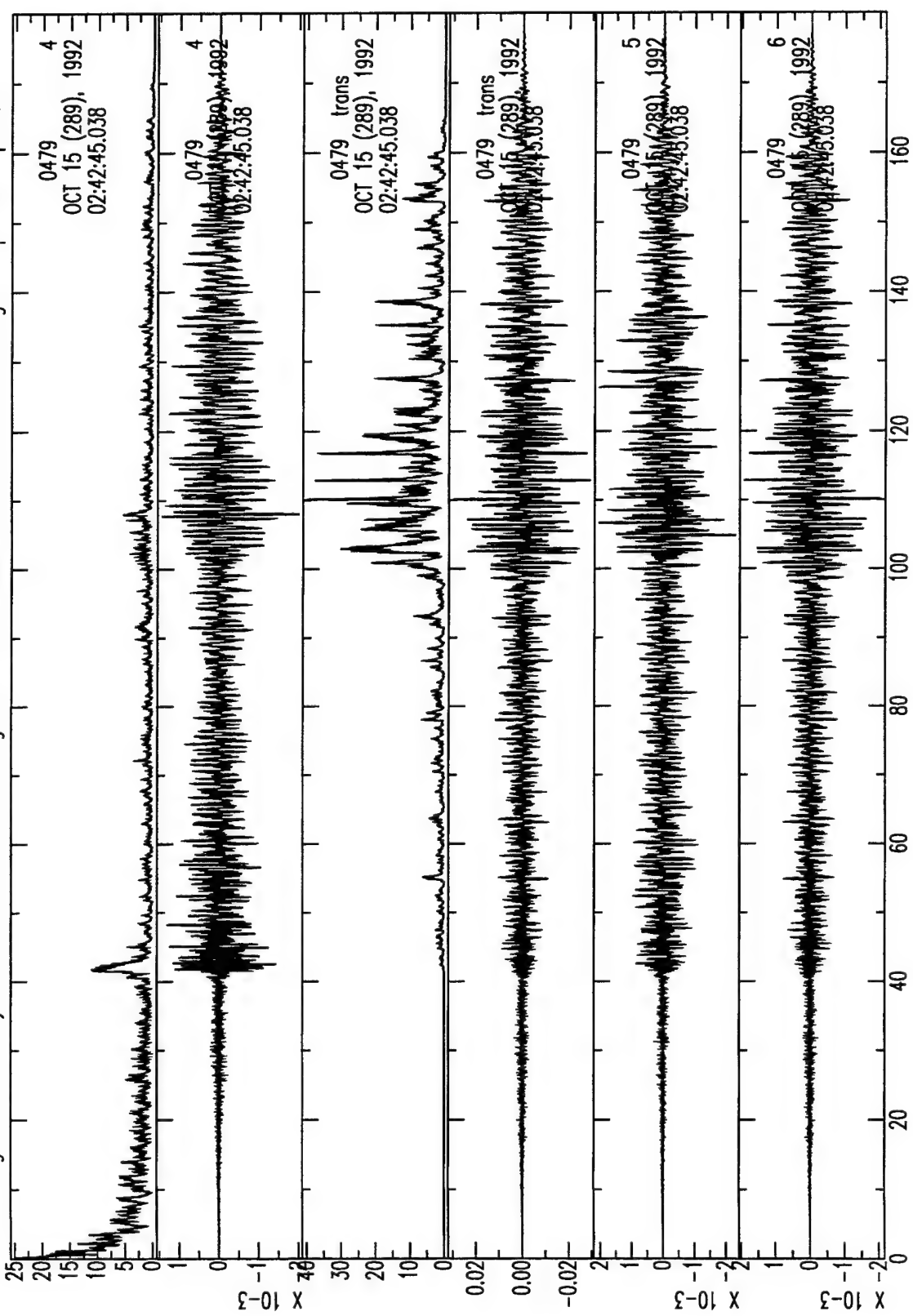


Figure A.1 Analysis of broadband seismograms for shallow event 289.024245.bkgm hp 1.0 lp 8.0



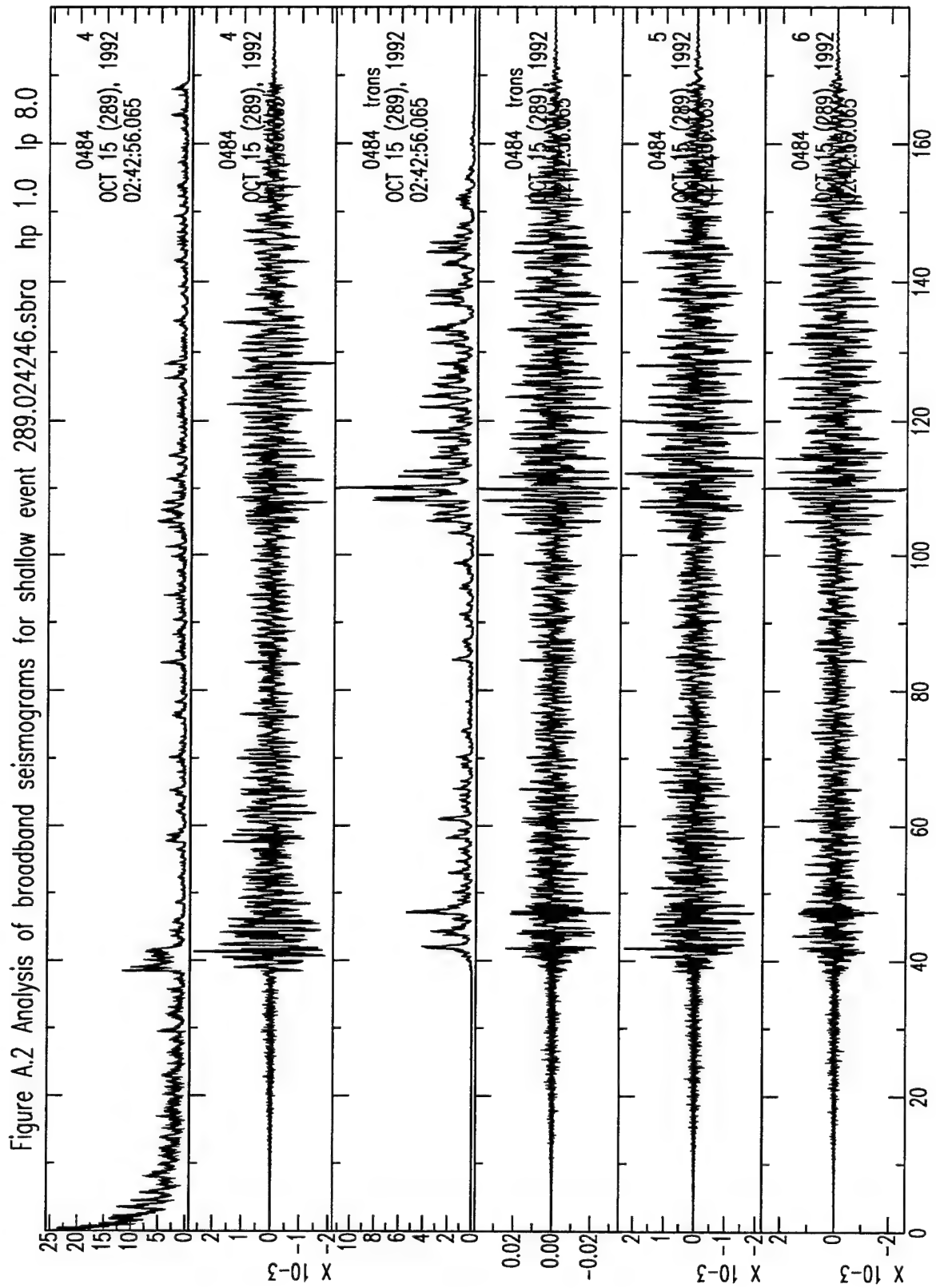
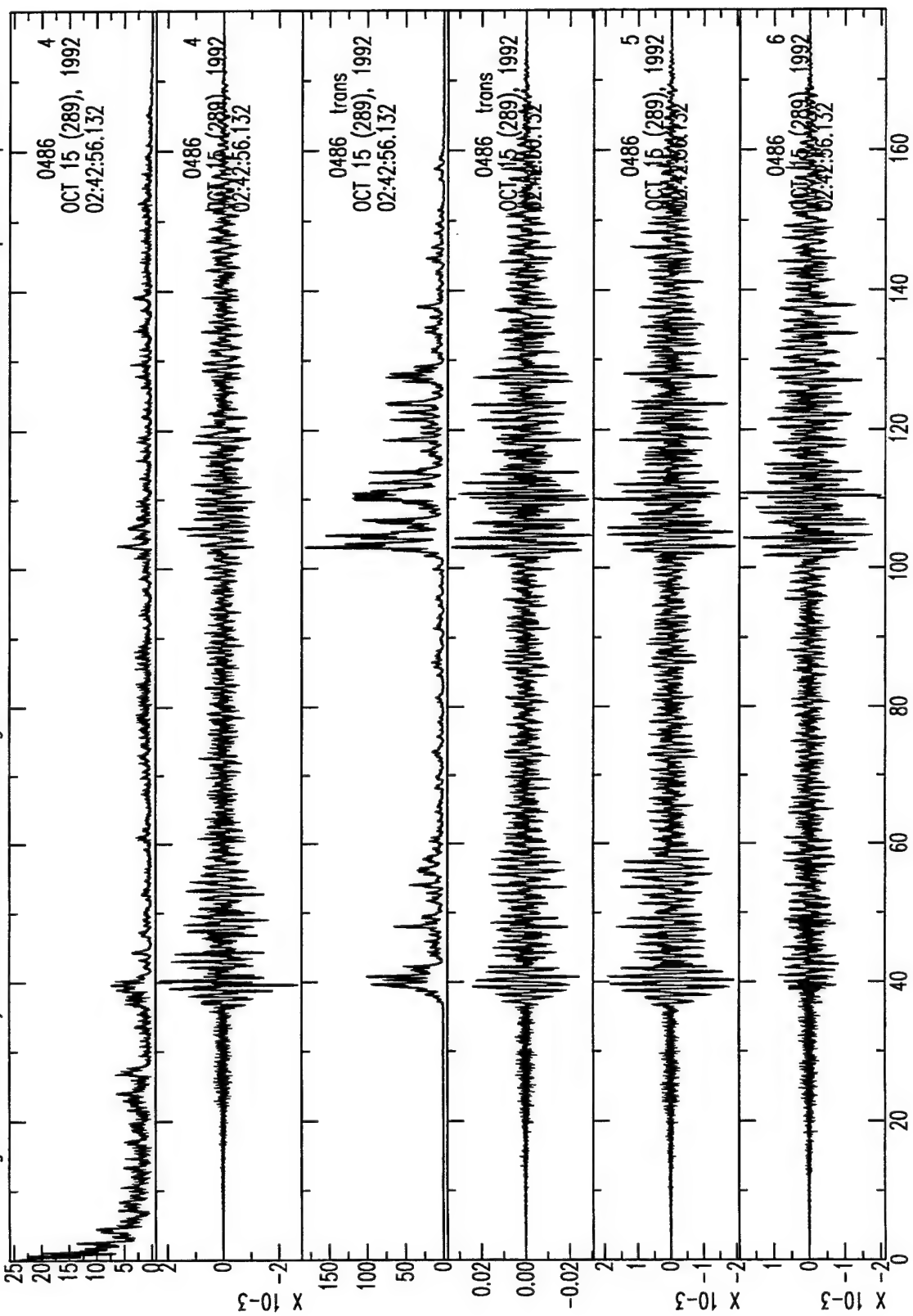


Figure A.3 Analysis of broadband seismograms for shallow event 289.024256.shab



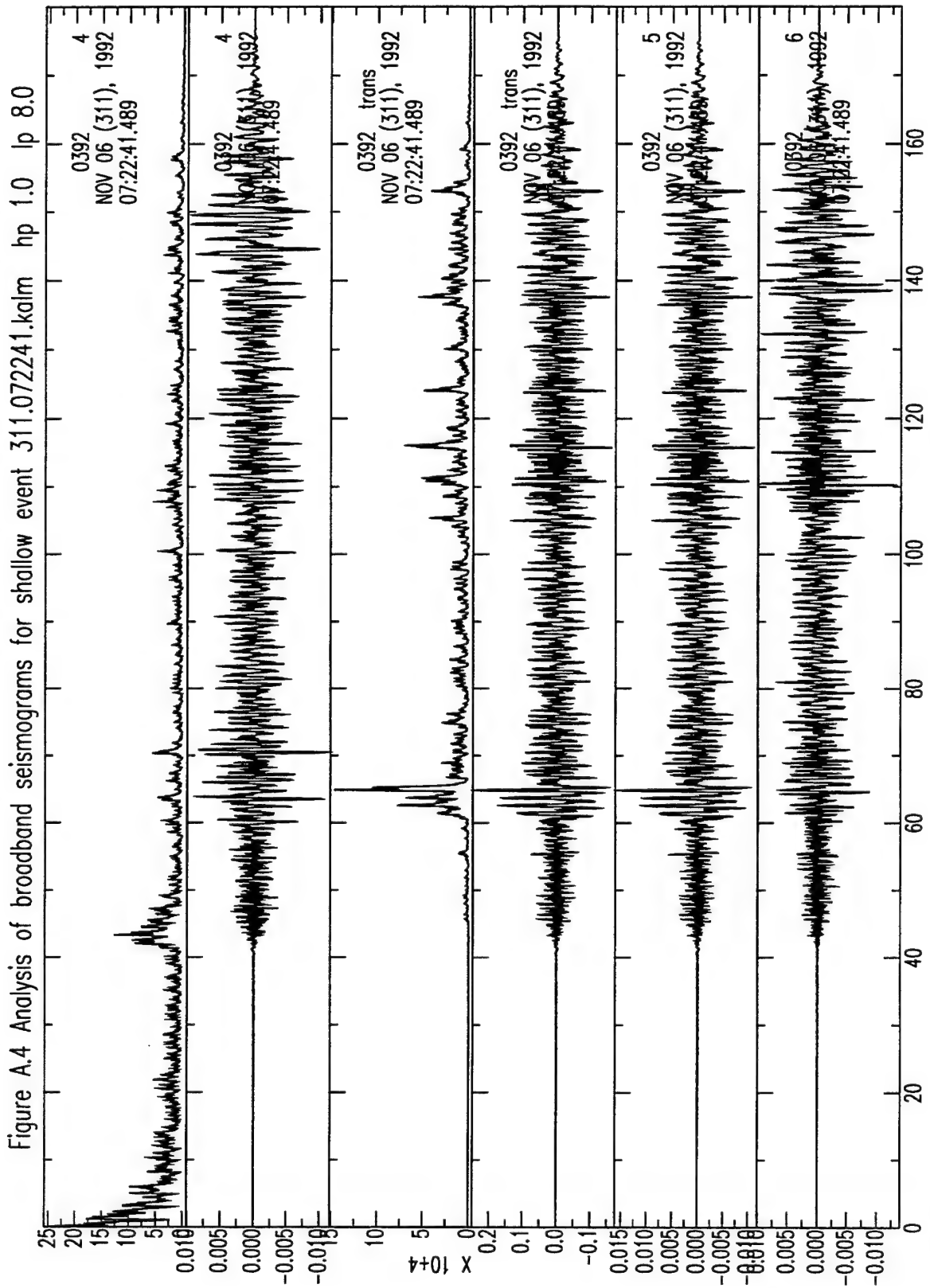
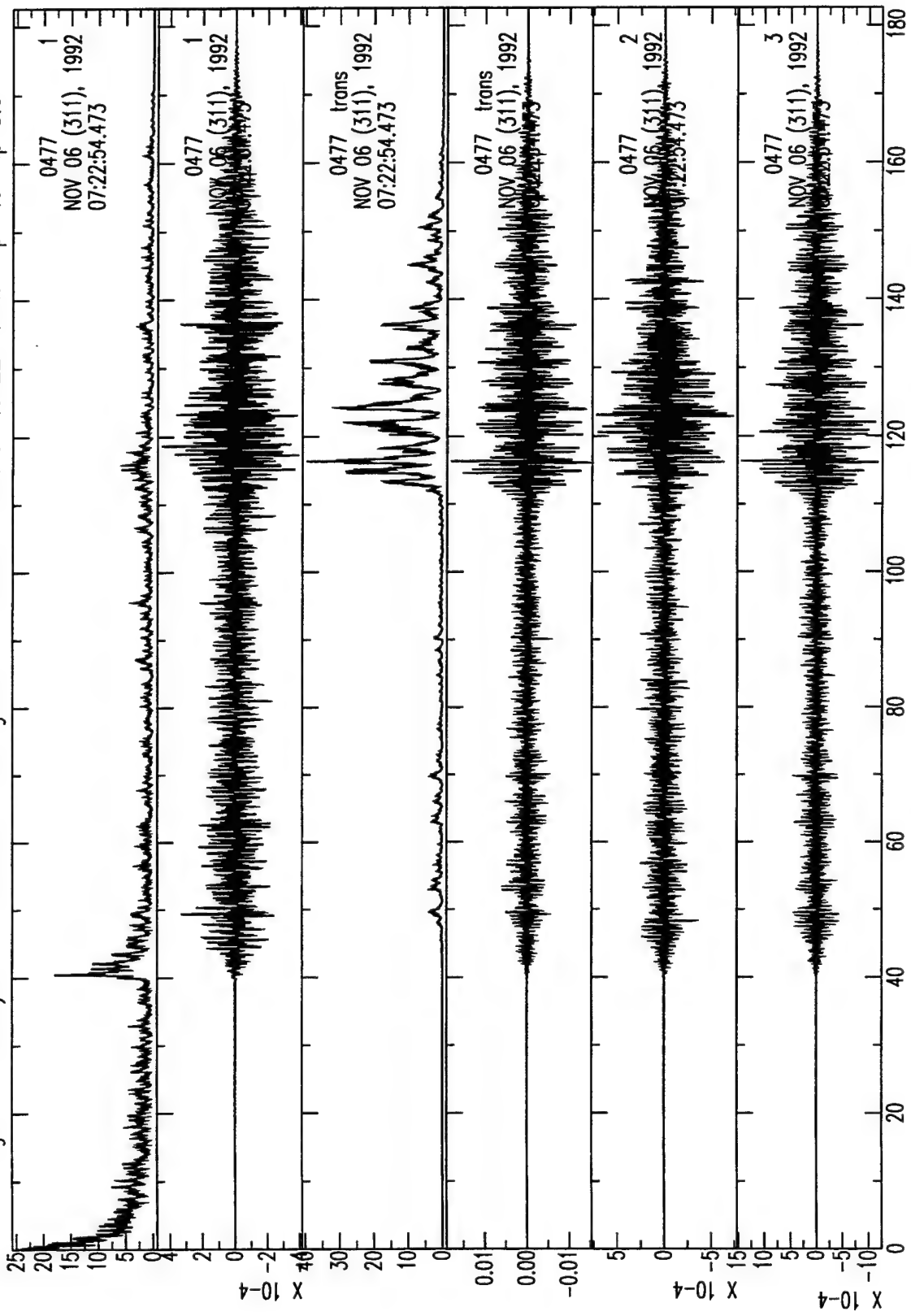


Figure A.5 Analysis of broadband seismograms for shallow event 311.072244.hklt hp 1.0 lp 8.0



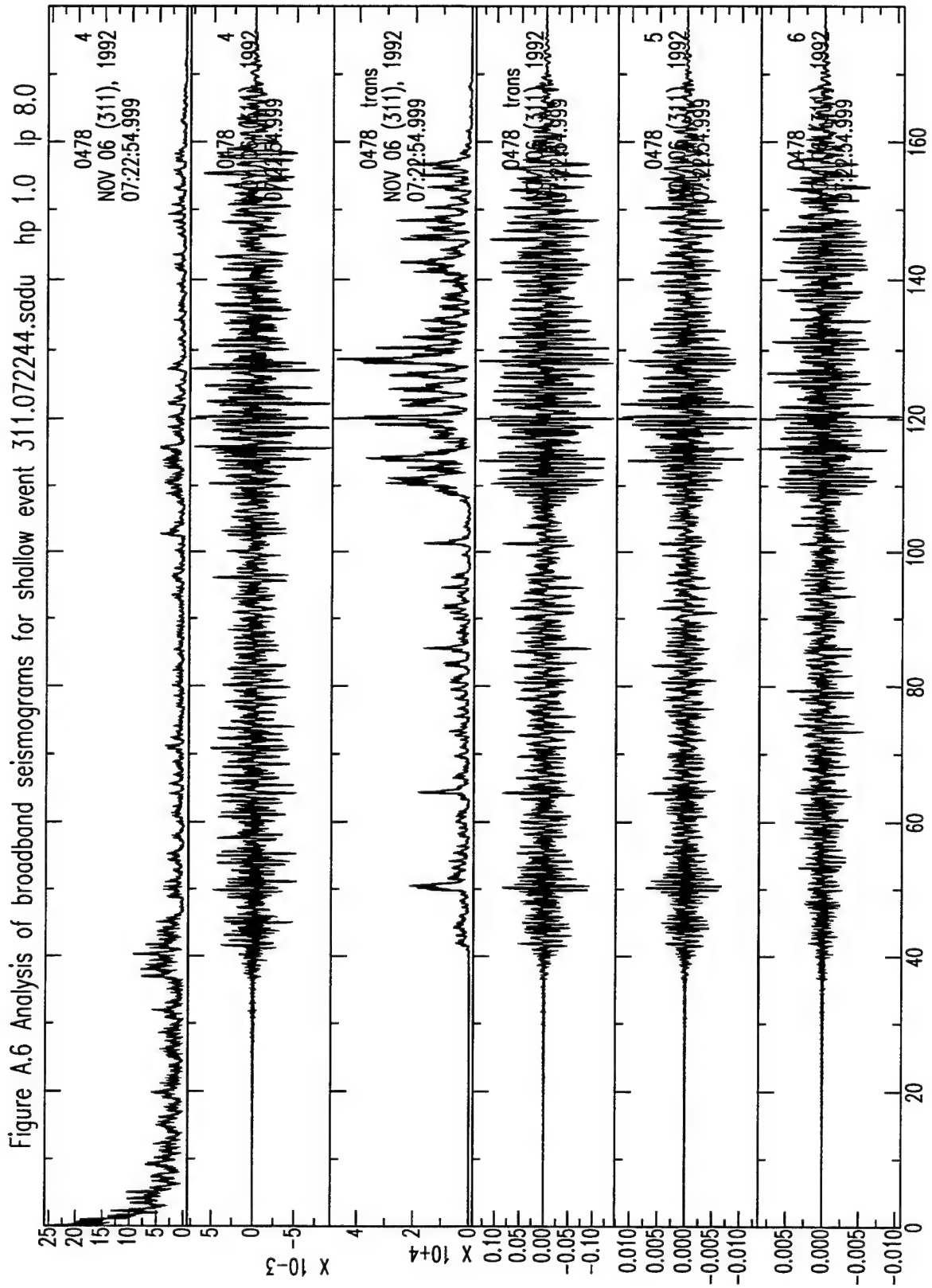


Figure A.7 Analysis of broadband seismograms for shallow event 311.072247.dsosu hp 1.0 lp 8.0

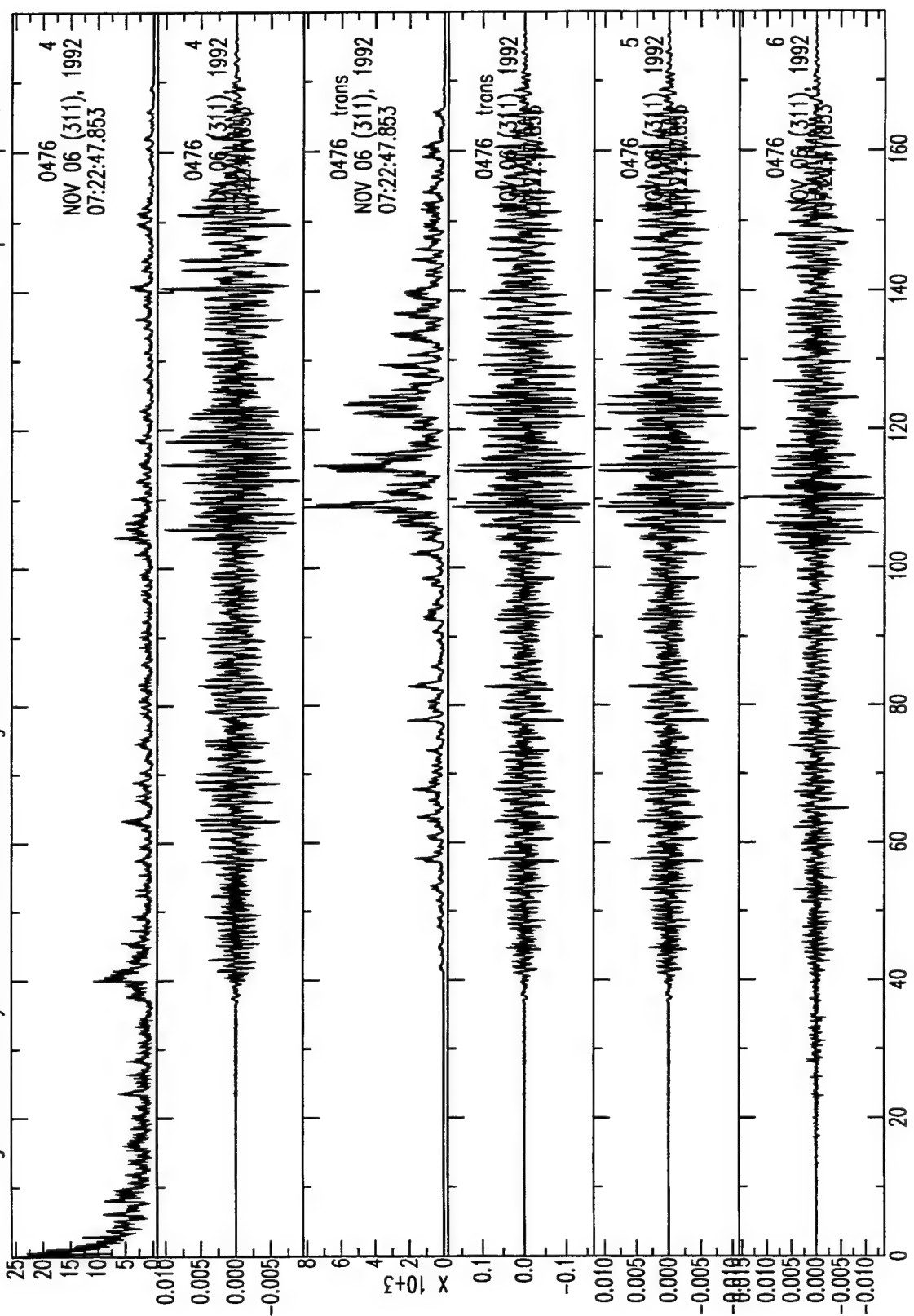


Figure A.8 Analysis of broadband seismograms for shallow event 311.072249.patn

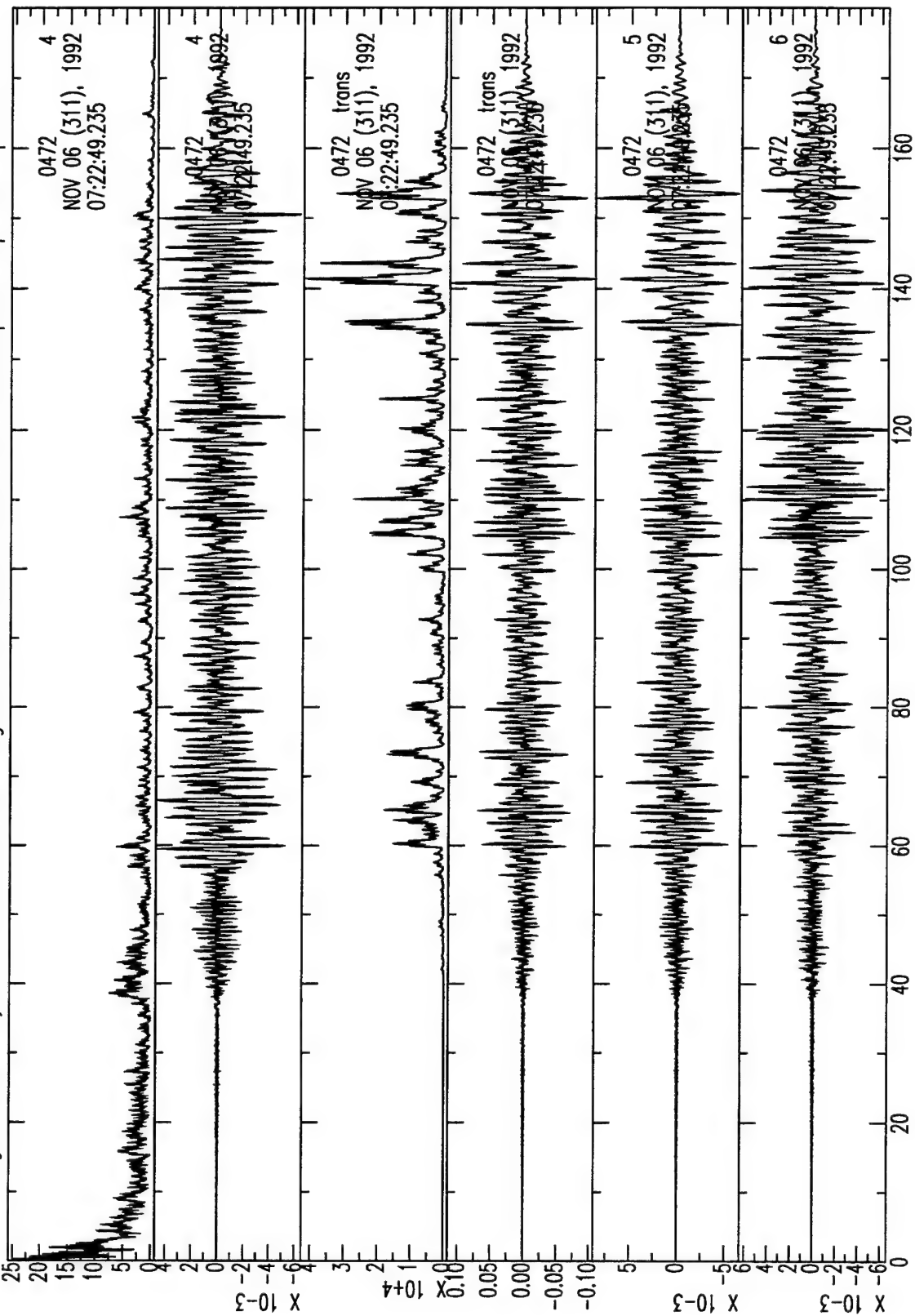


Figure A.9 Analysis of broadband seismograms for shallow event 311.072250.sbra

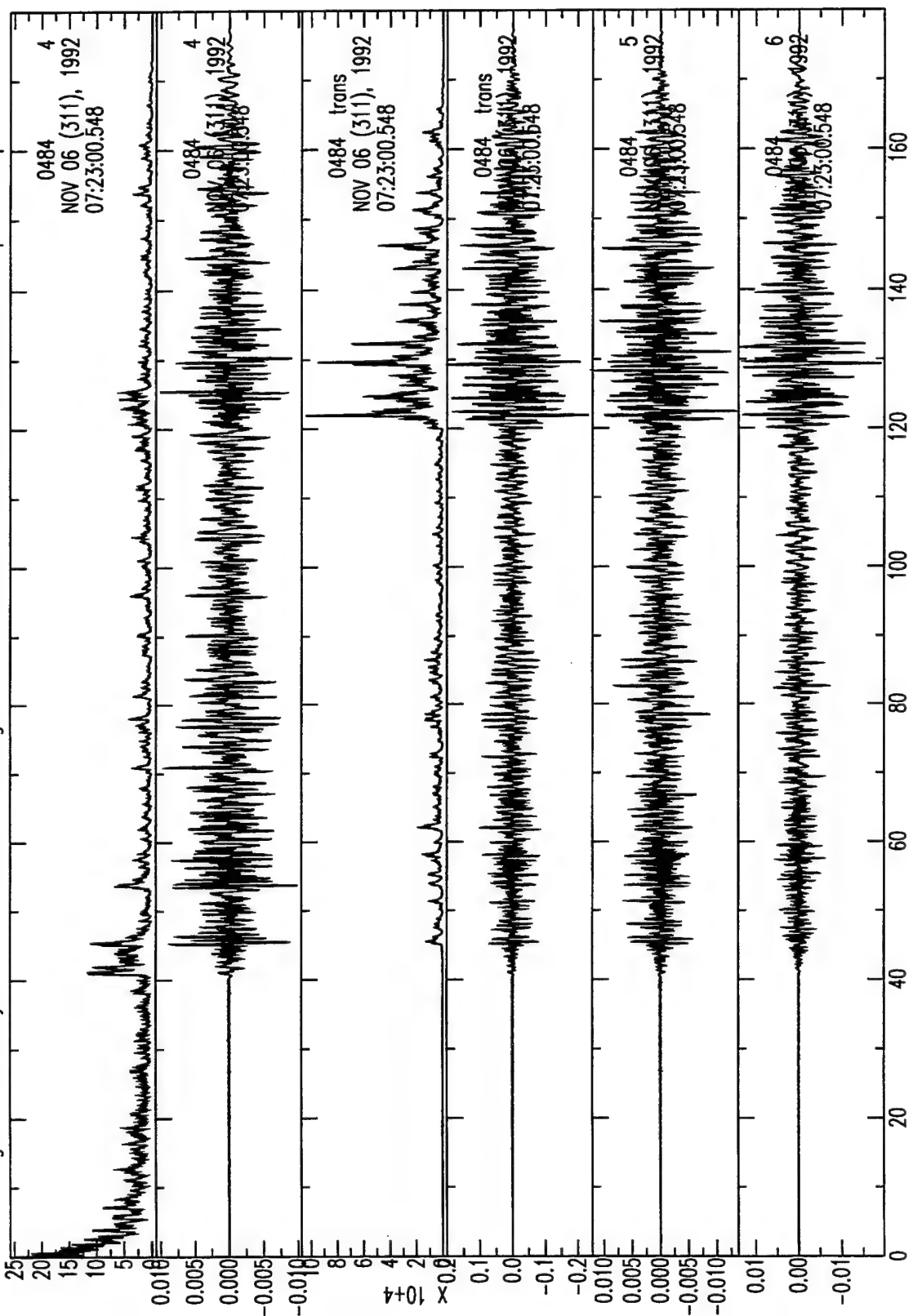


Figure A.10 Analysis of broadband seismograms for shallow event 311.072252.shin

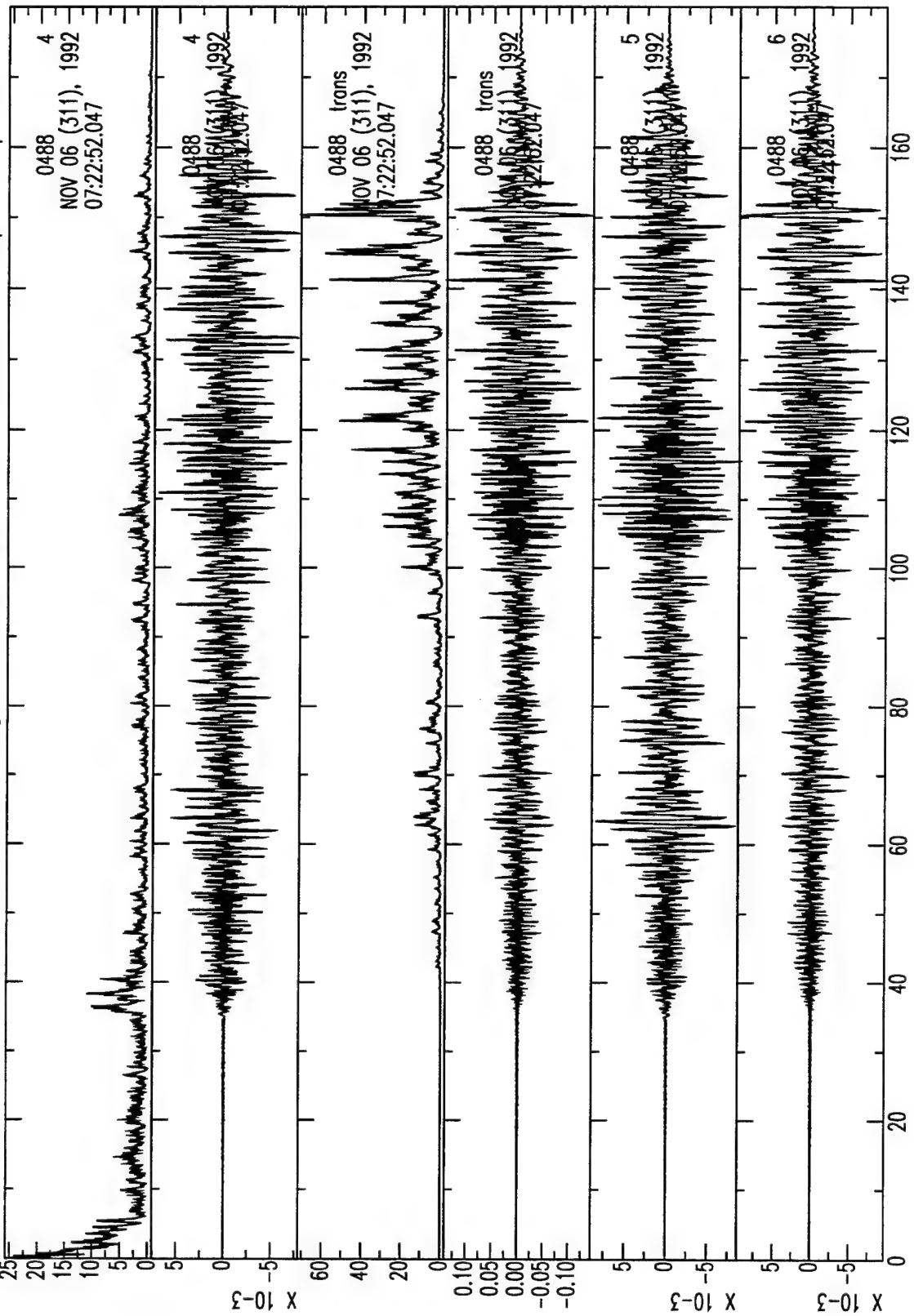


Figure A.11 Analysis of broadband seismograms for shallow event 311.072253.btgm hp 1.0 lp 8.0

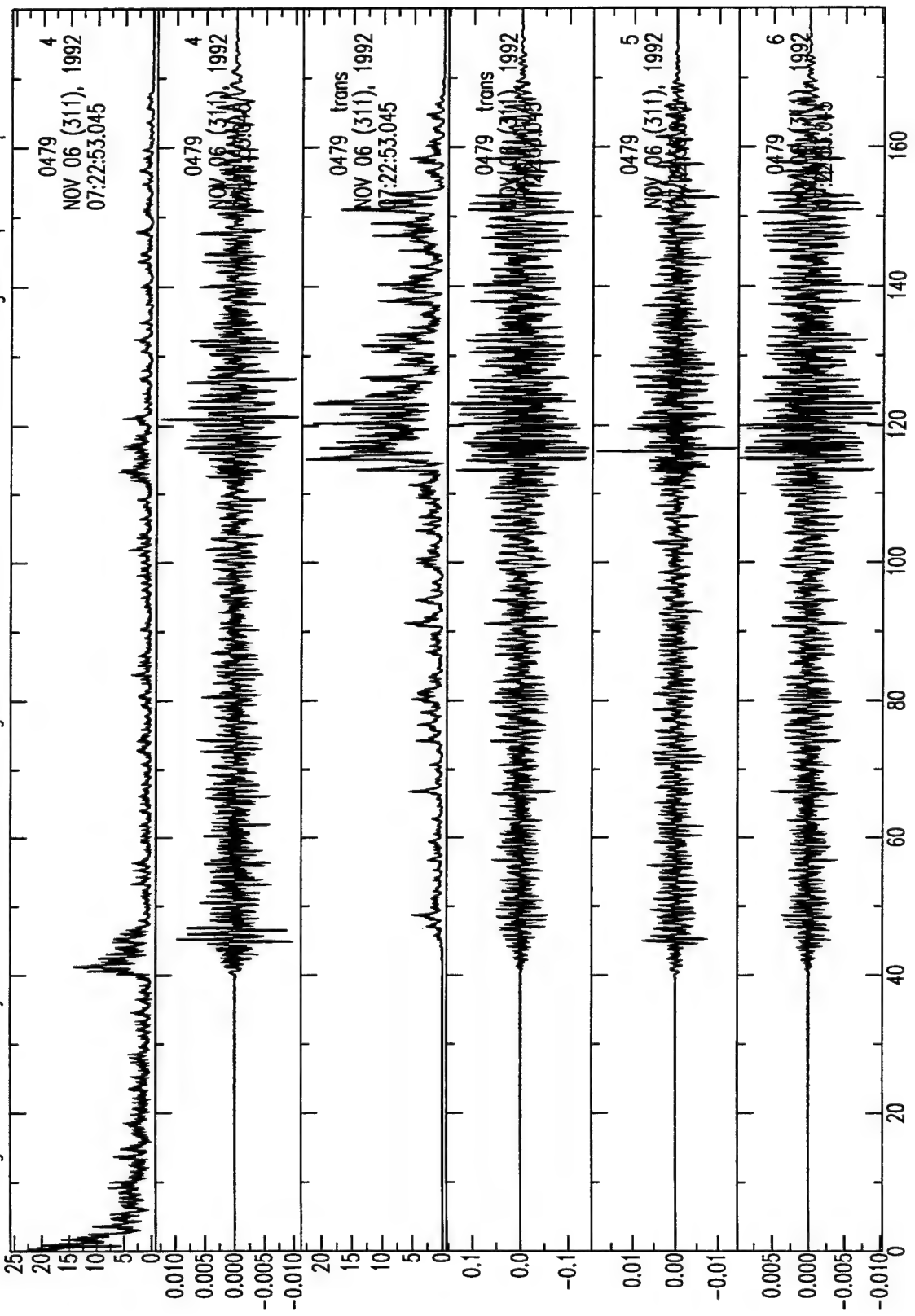


Figure A.12 Analysis of broadband seismograms for shallow event 311.072302.shab

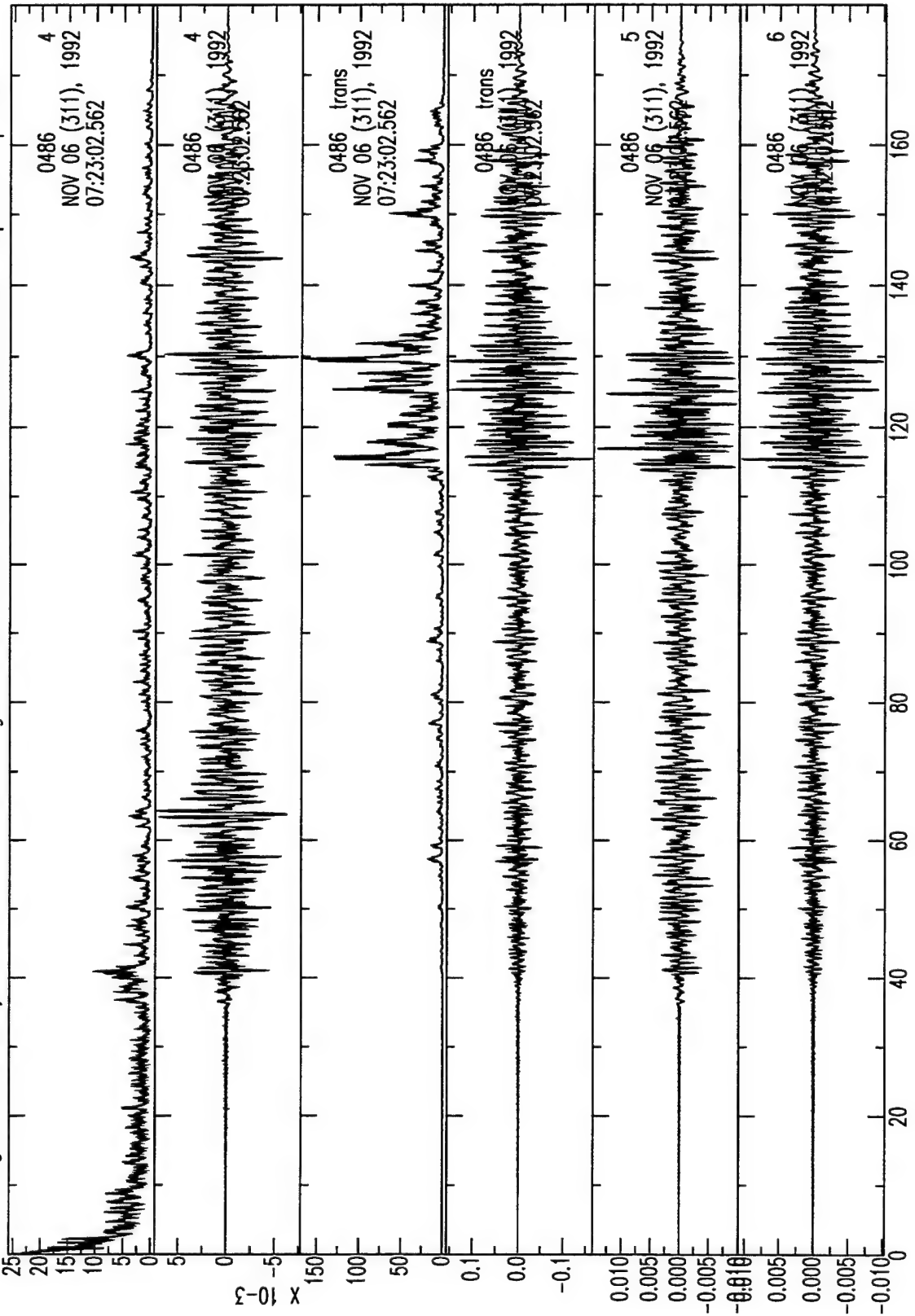


Figure A.13 Analysis of broadband seismograms for shallow event 311.175749.shin

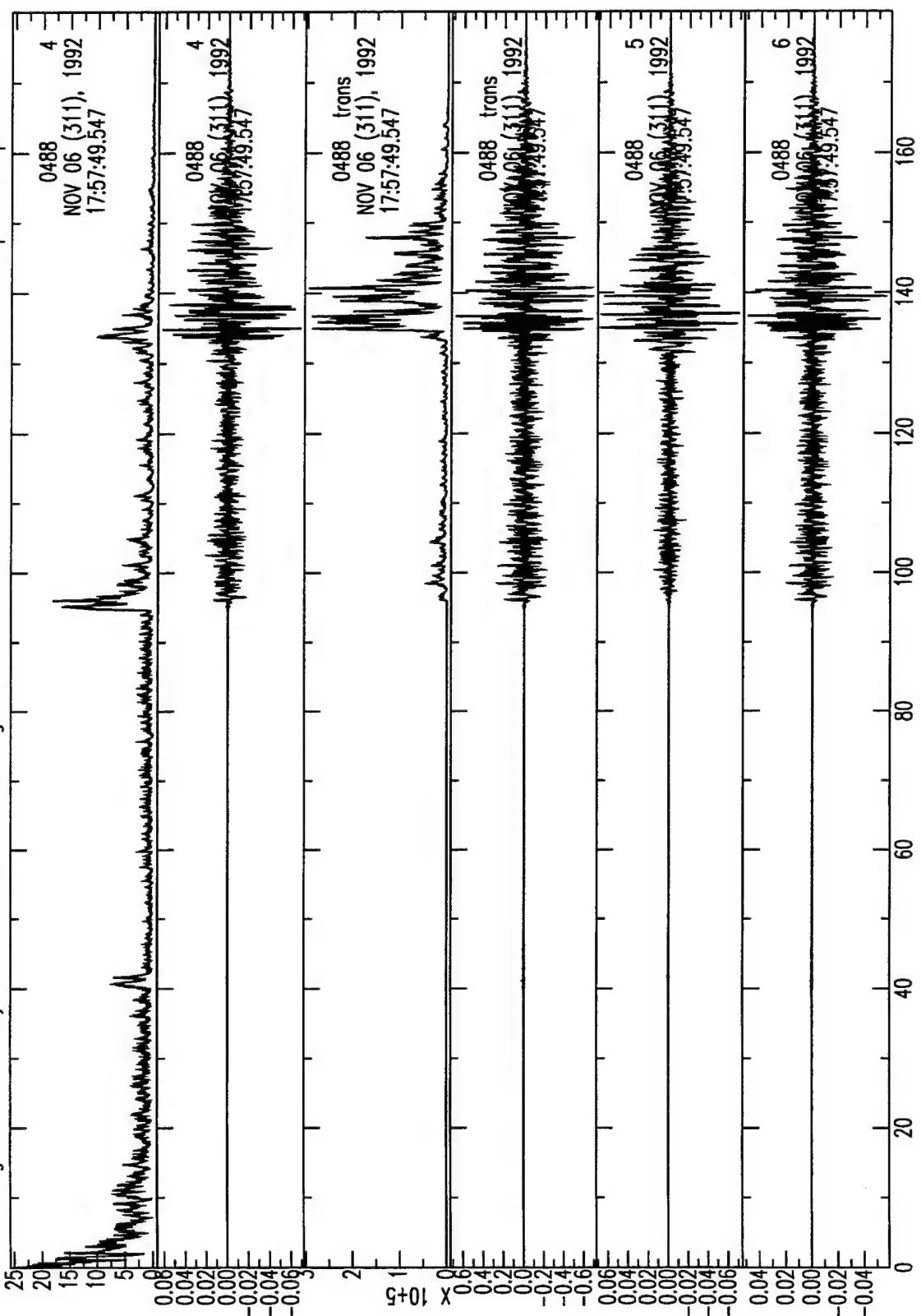


Figure A.14 Analysis of broadband seismograms for shallow event 311.175832.sadu

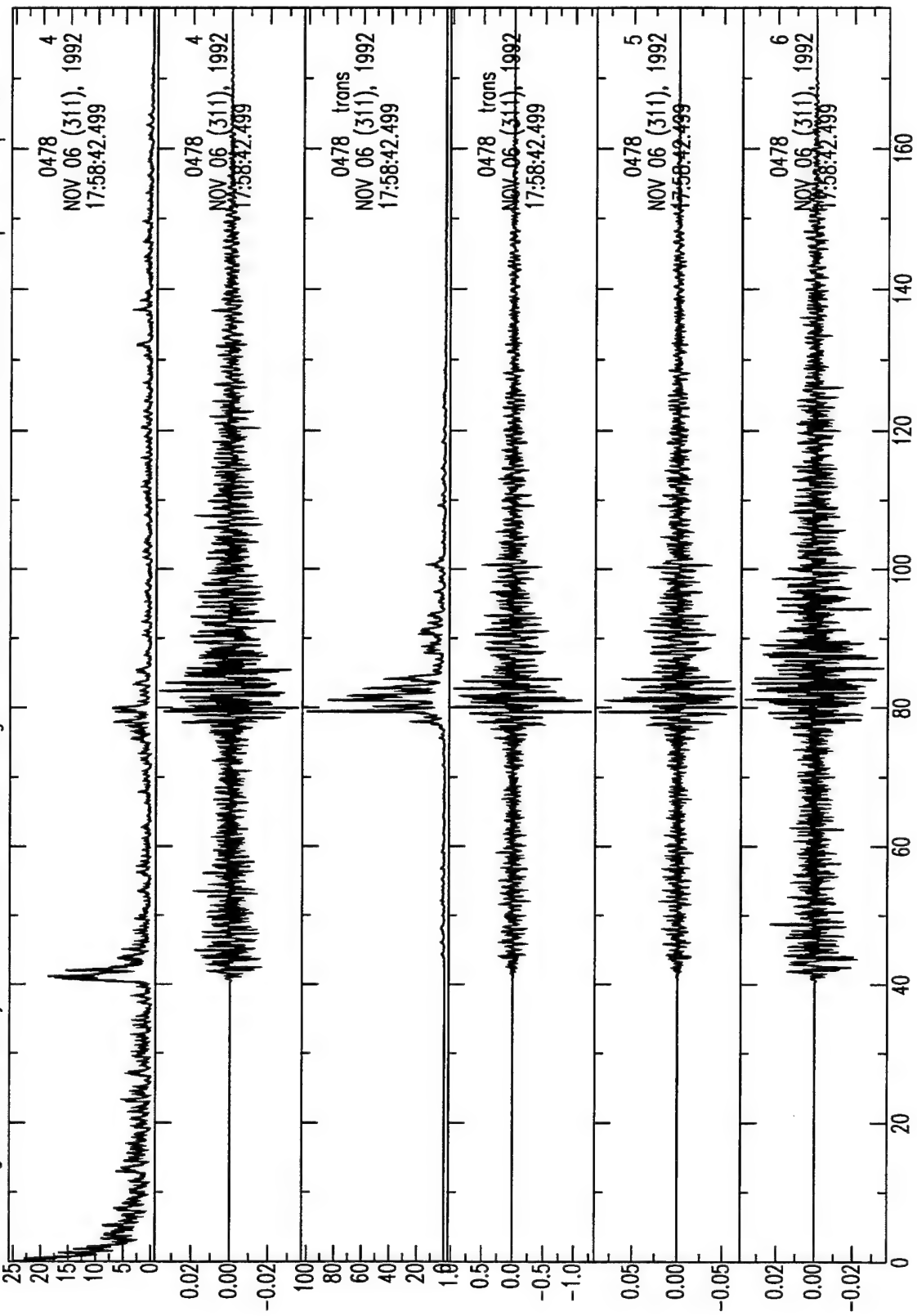
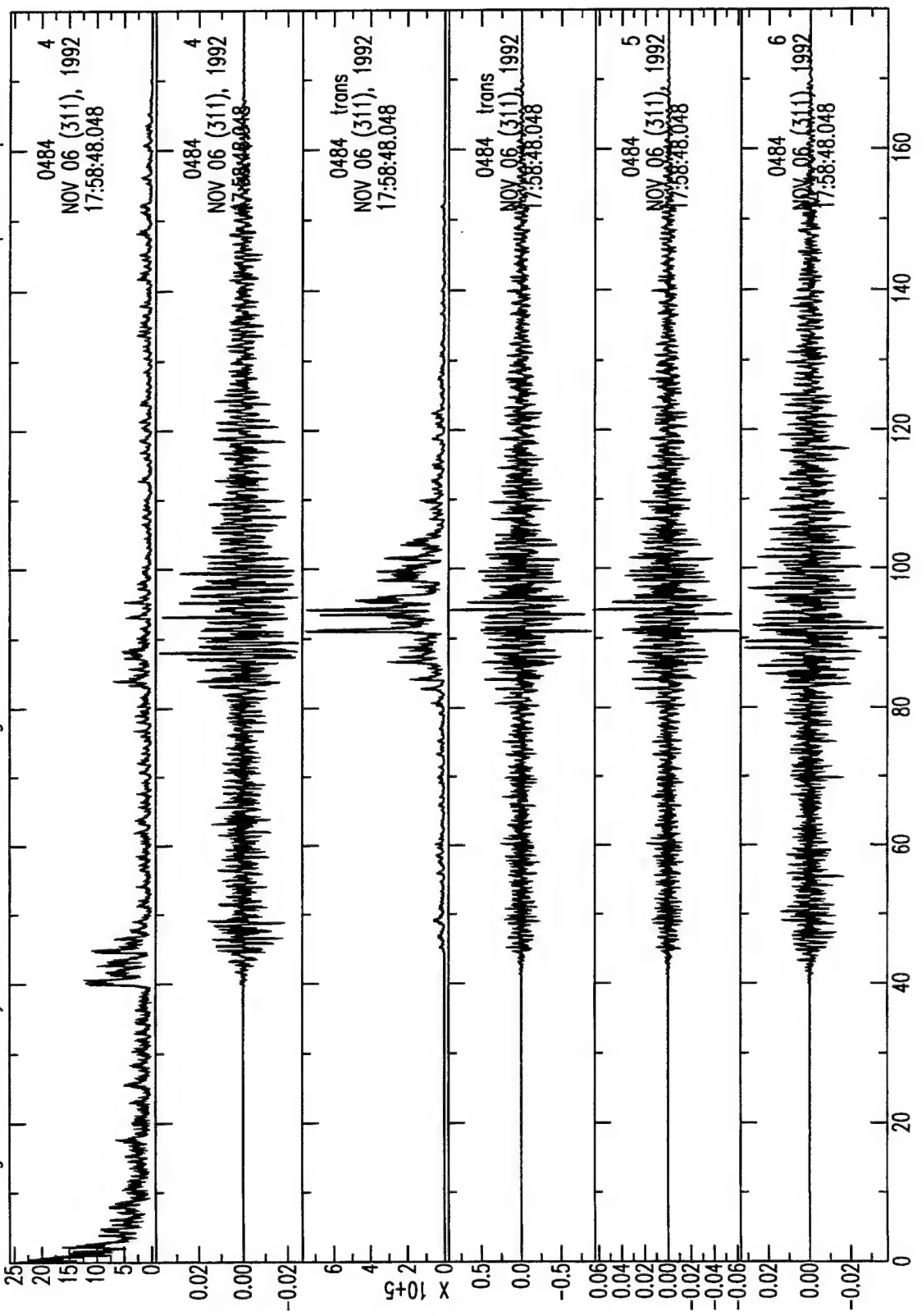


Figure A.15 Analysis of broadband seismograms for shallow event 311.175838.sbra hp 1.0 lp 8.0



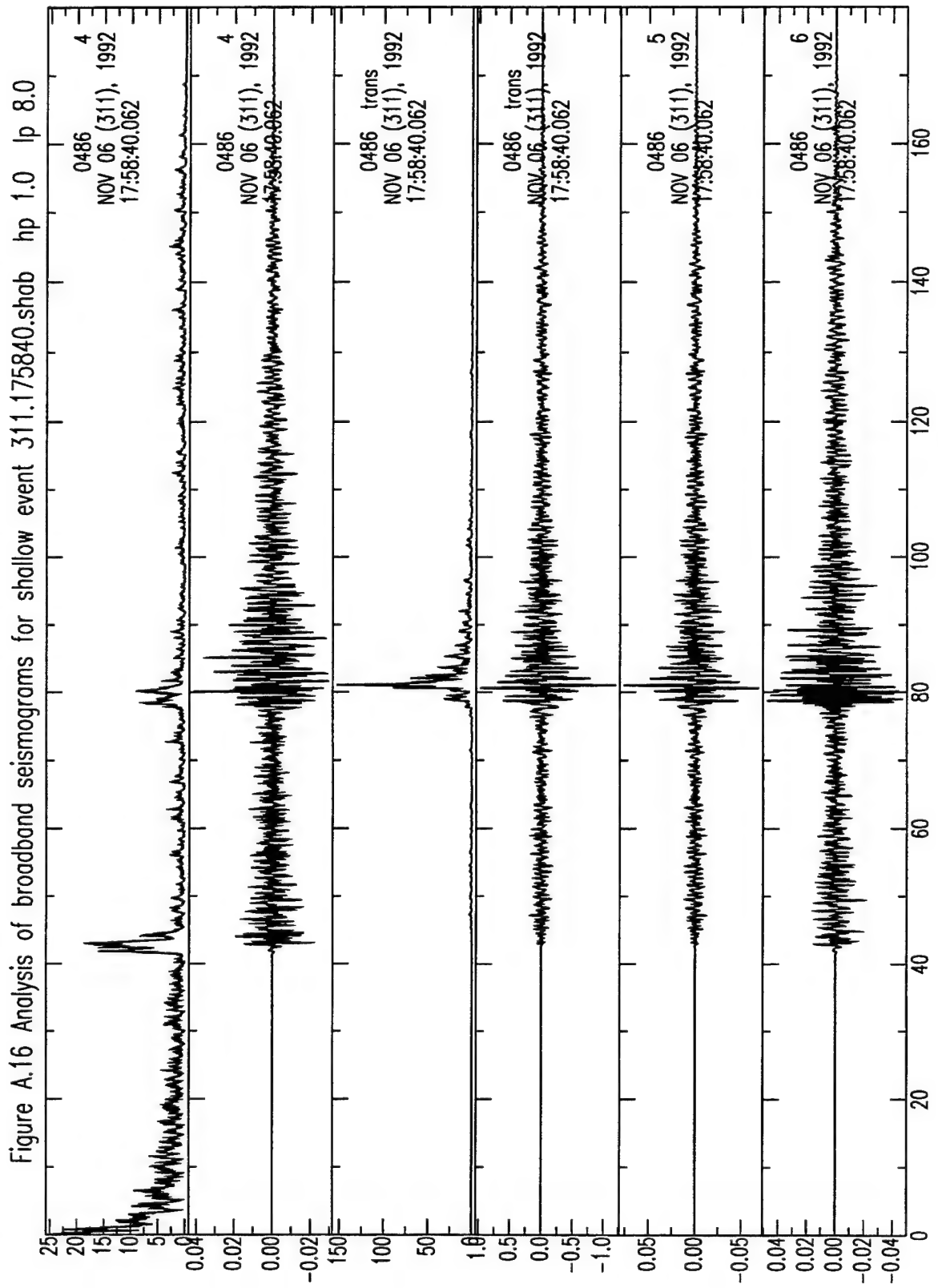
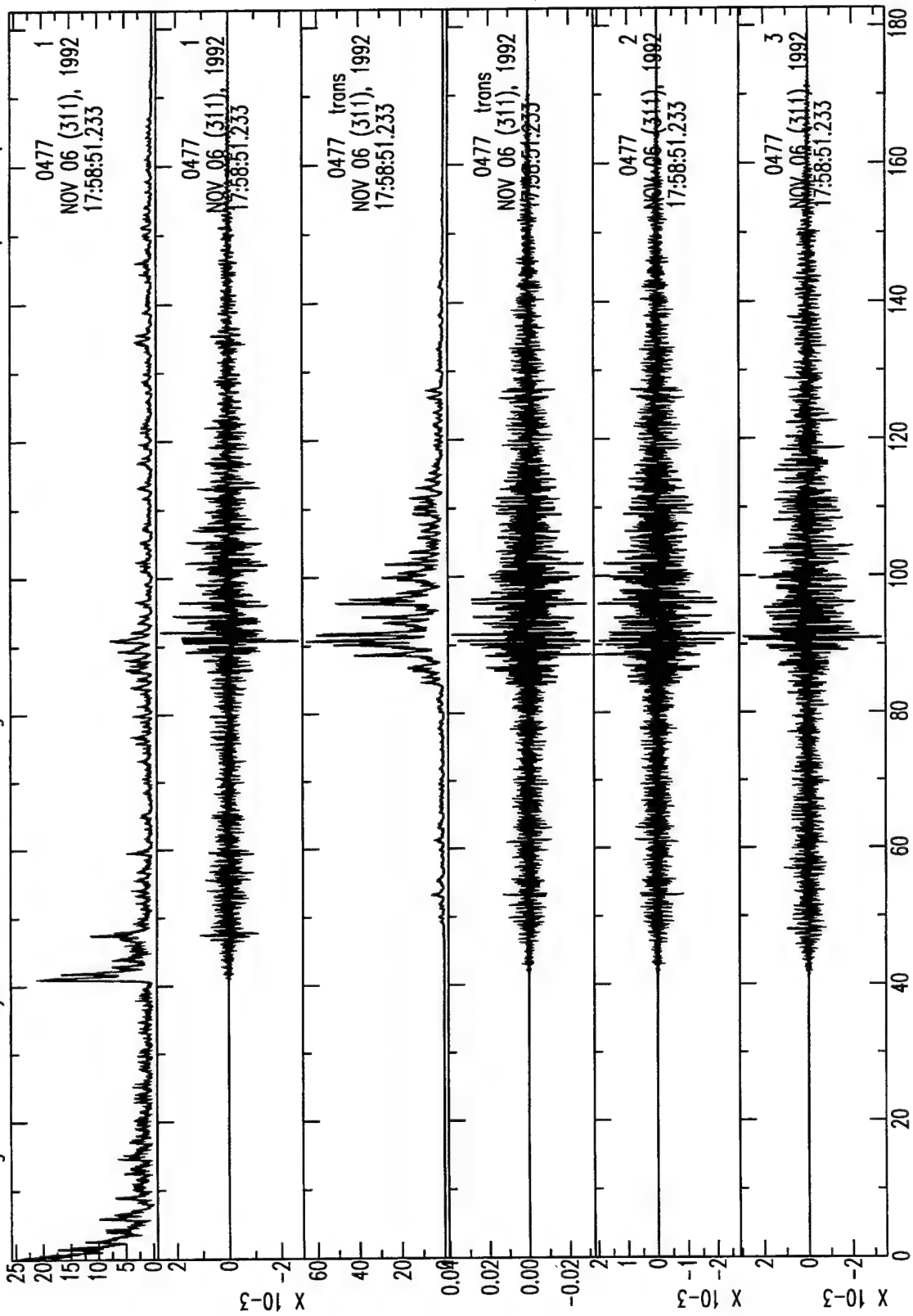


Figure A.17 Analysis of broadband seismograms for shallow event 311.175841.hklt hp 1.0 lp 8.0



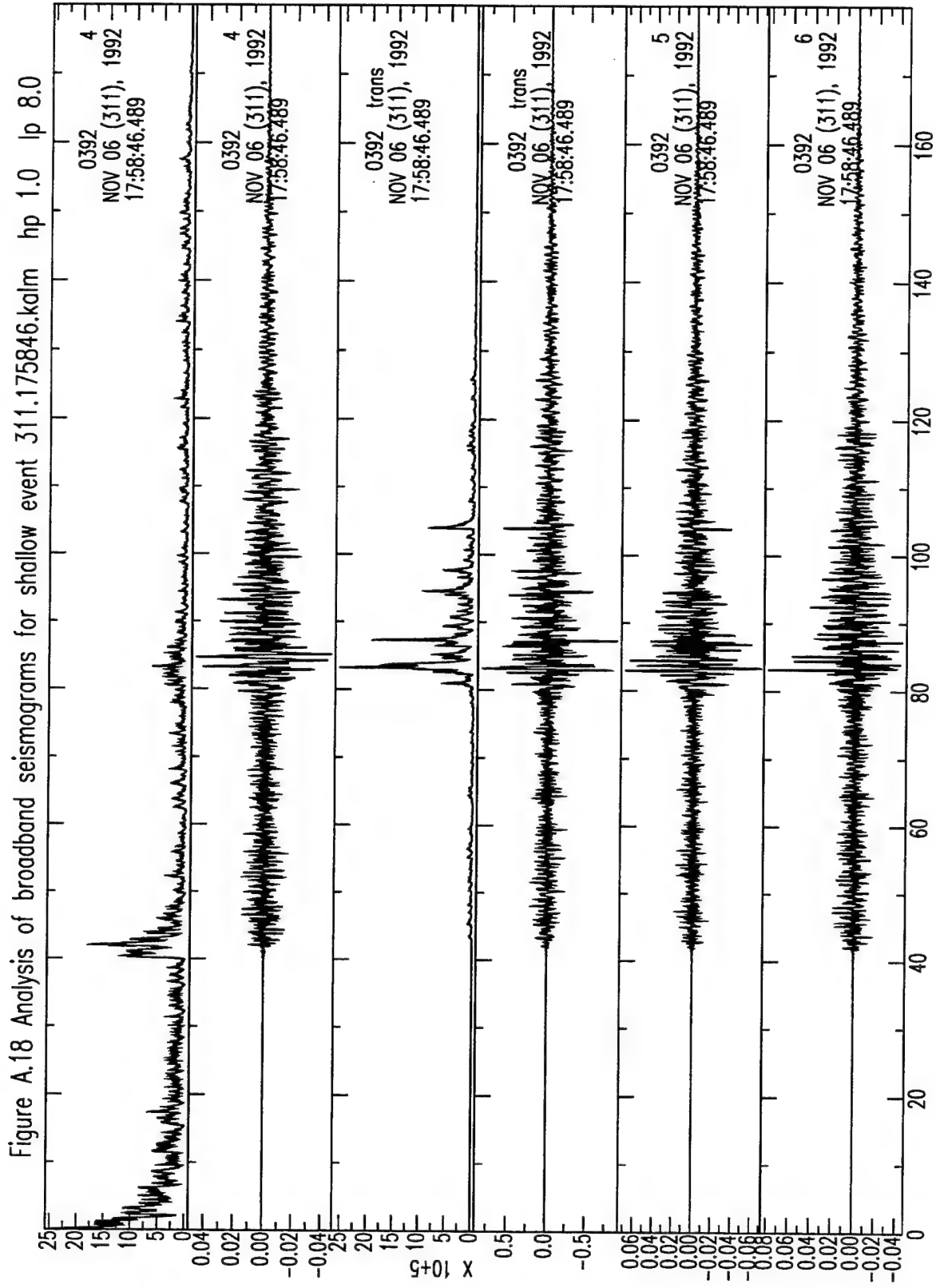
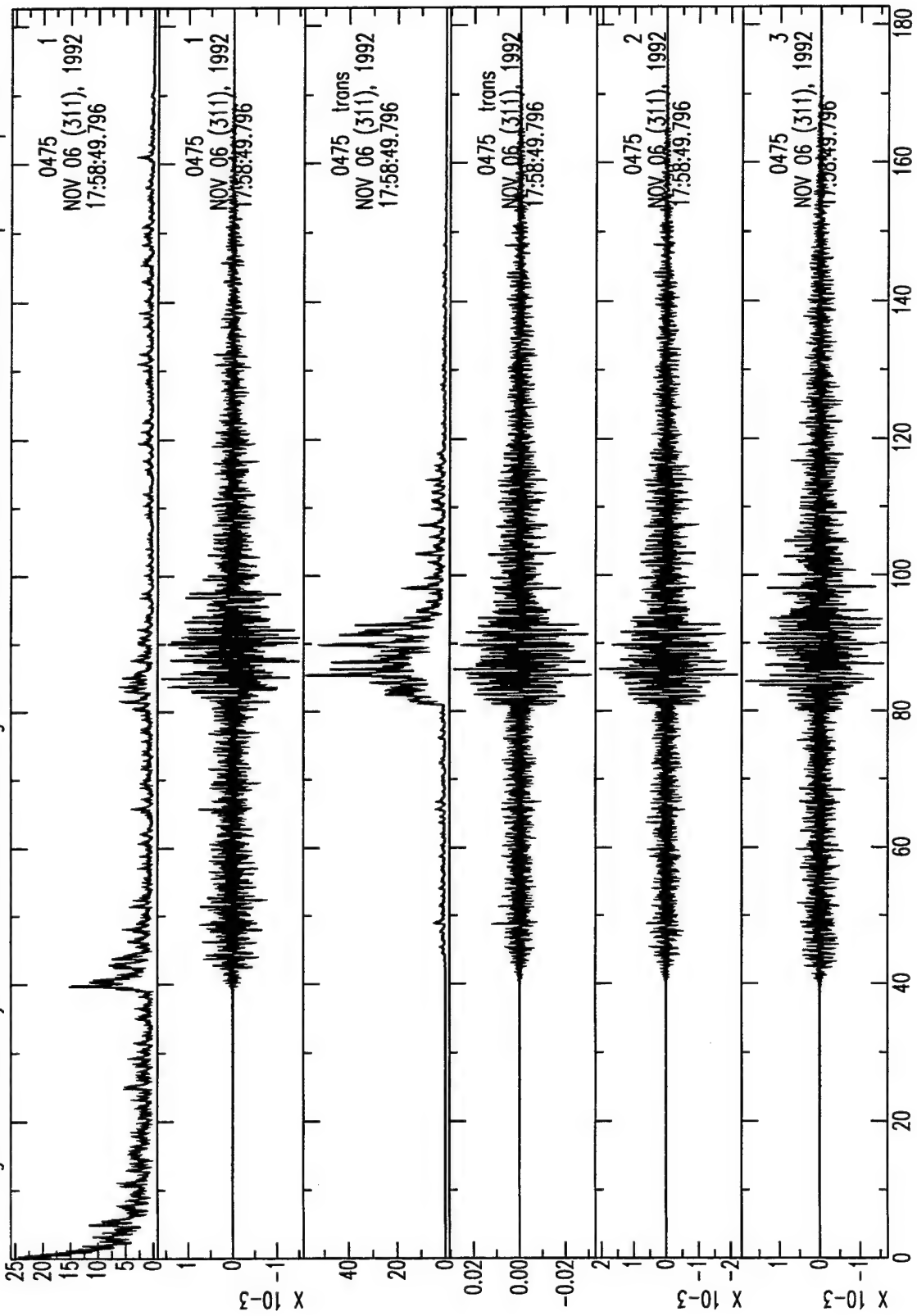


Figure A.19 Analysis of broadband seismograms for shallow event 311.175849.basm



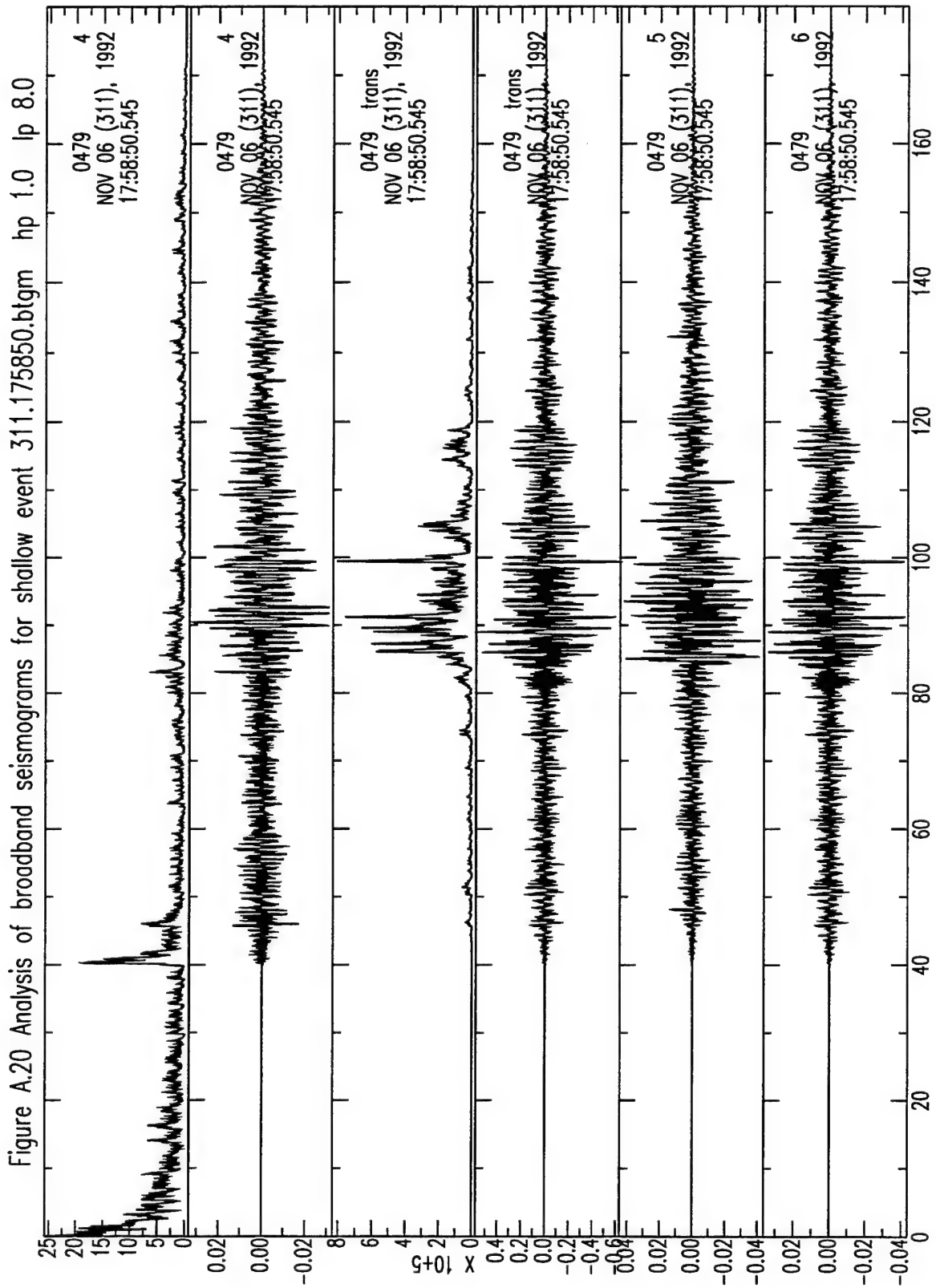
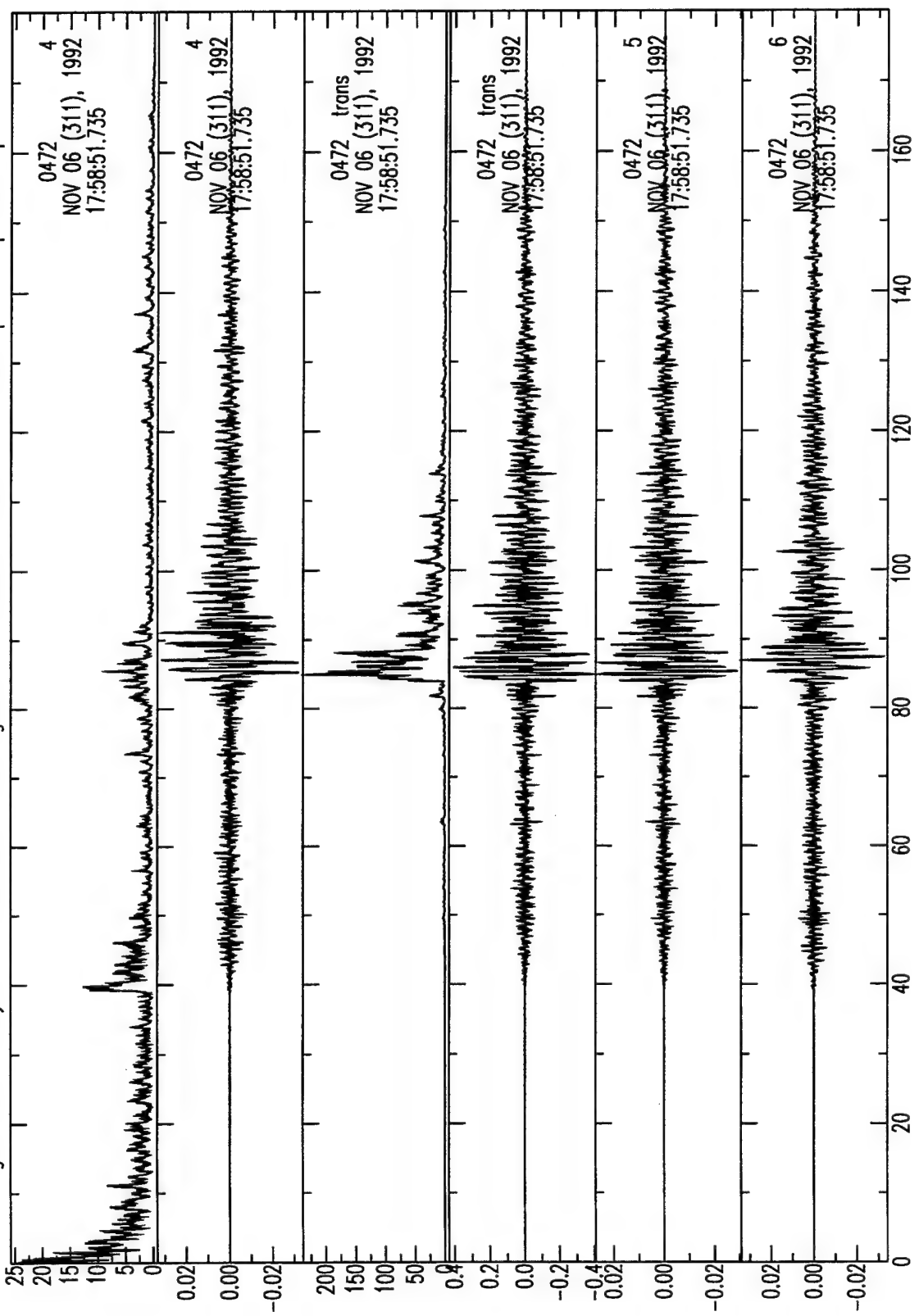


Figure A.21 Analysis of broadband seismograms for shallow event 311.175851.patn



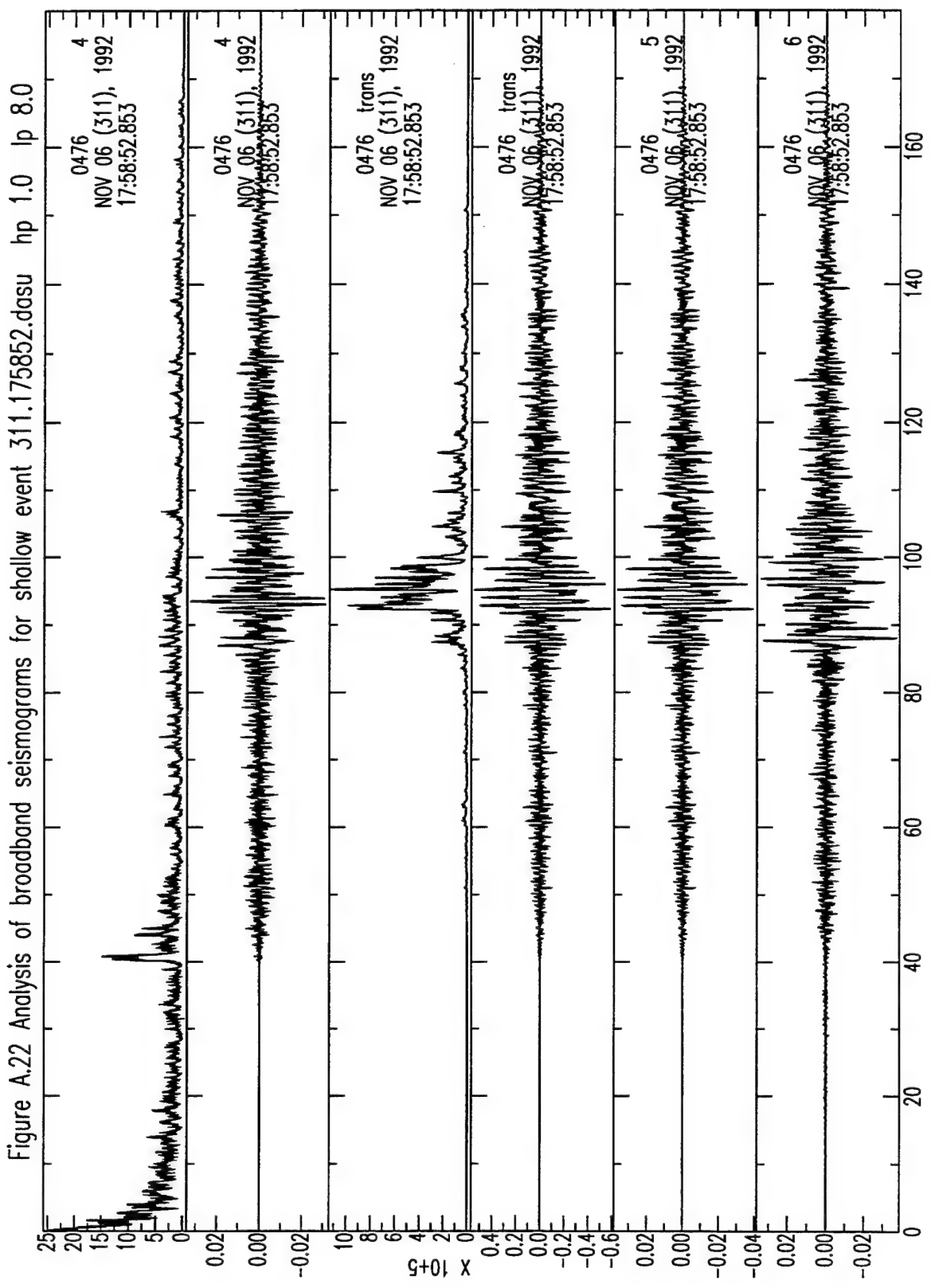
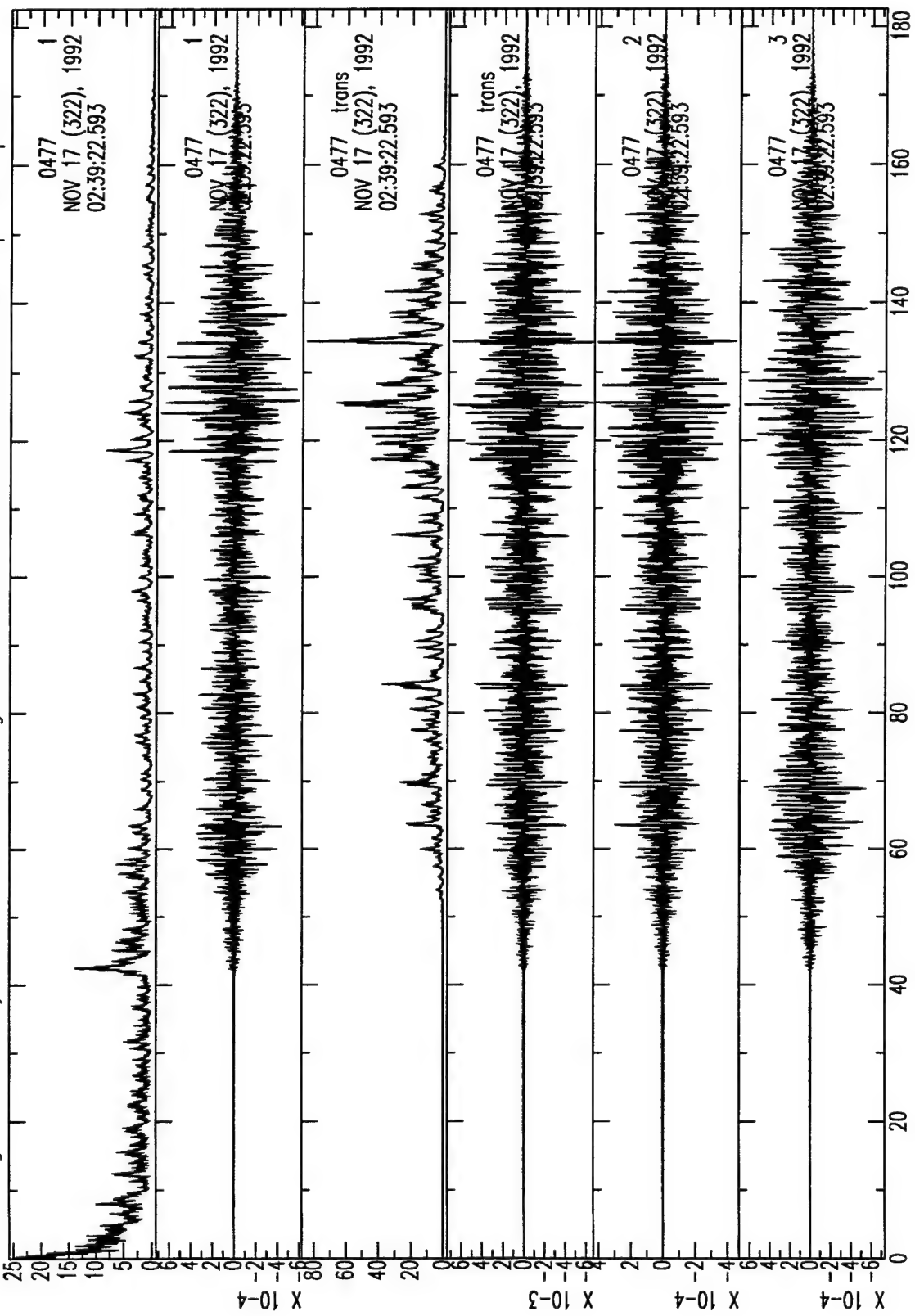


Figure A.23 Analysis of broadband seismograms for shallow event 322.023912.hklt hp 1.0 lp 8.0



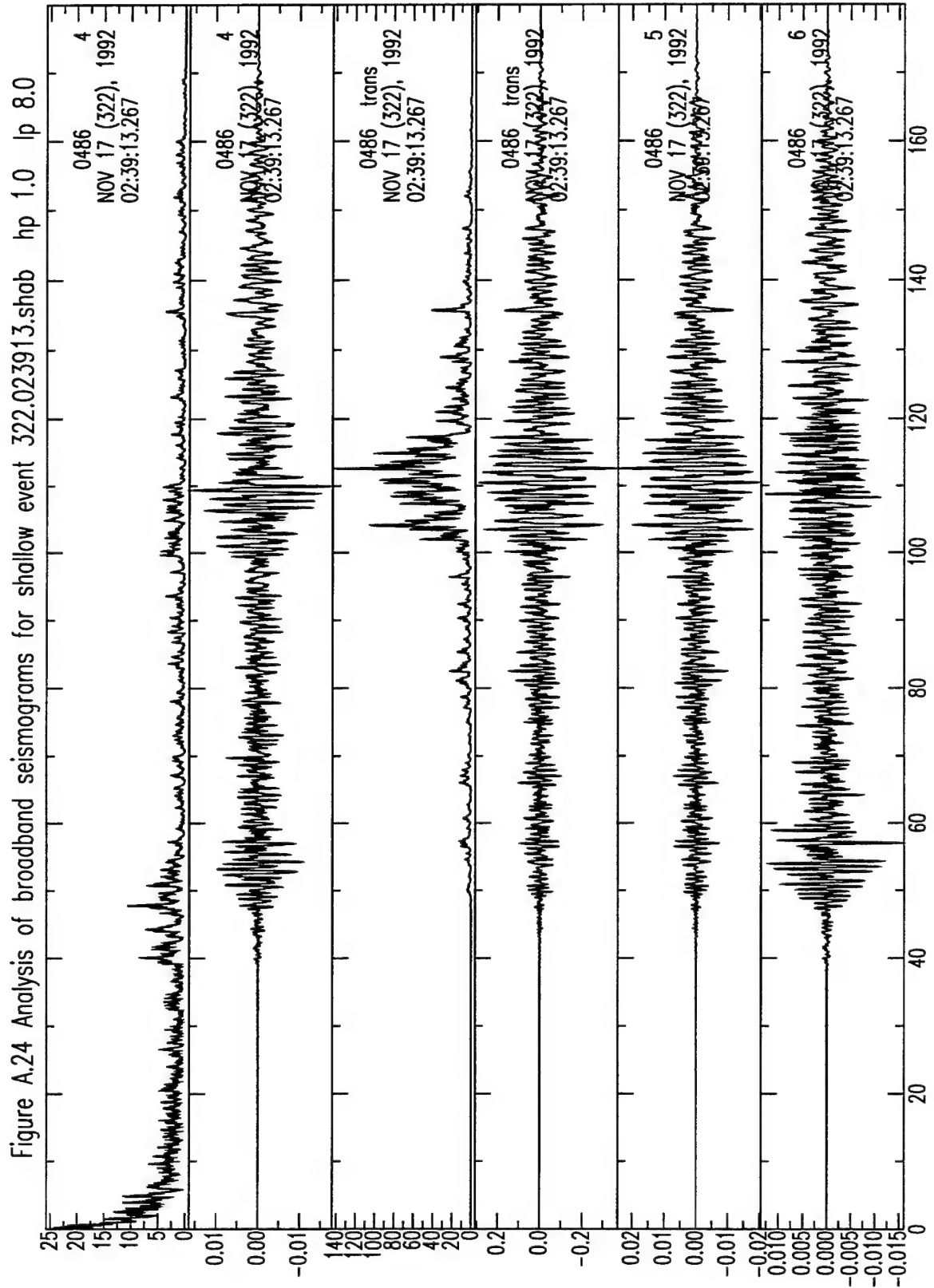
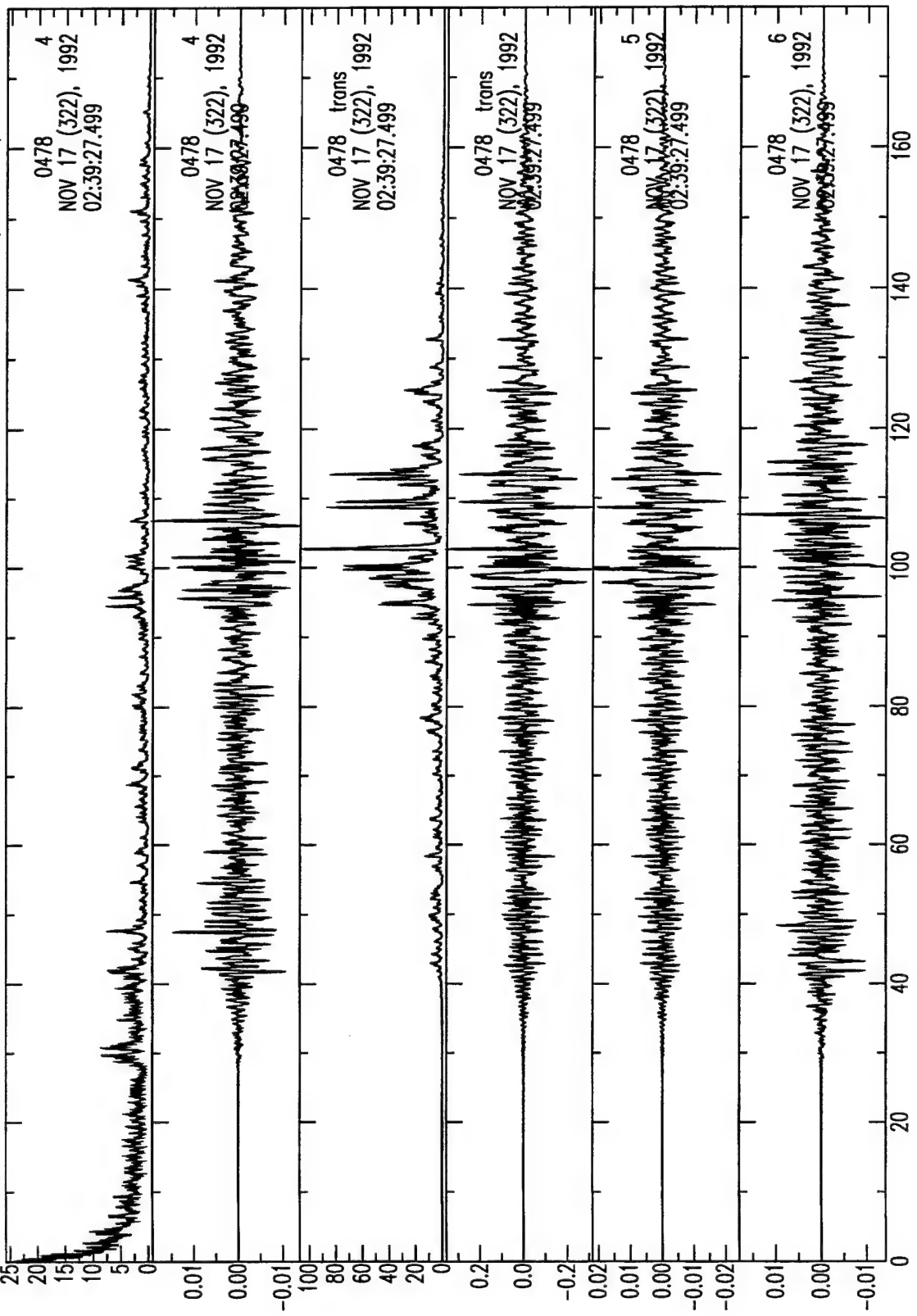


Figure A.25 Analysis of broadband seismograms for shallow event 322.023917.sadu hp 1.0 lp 8.0



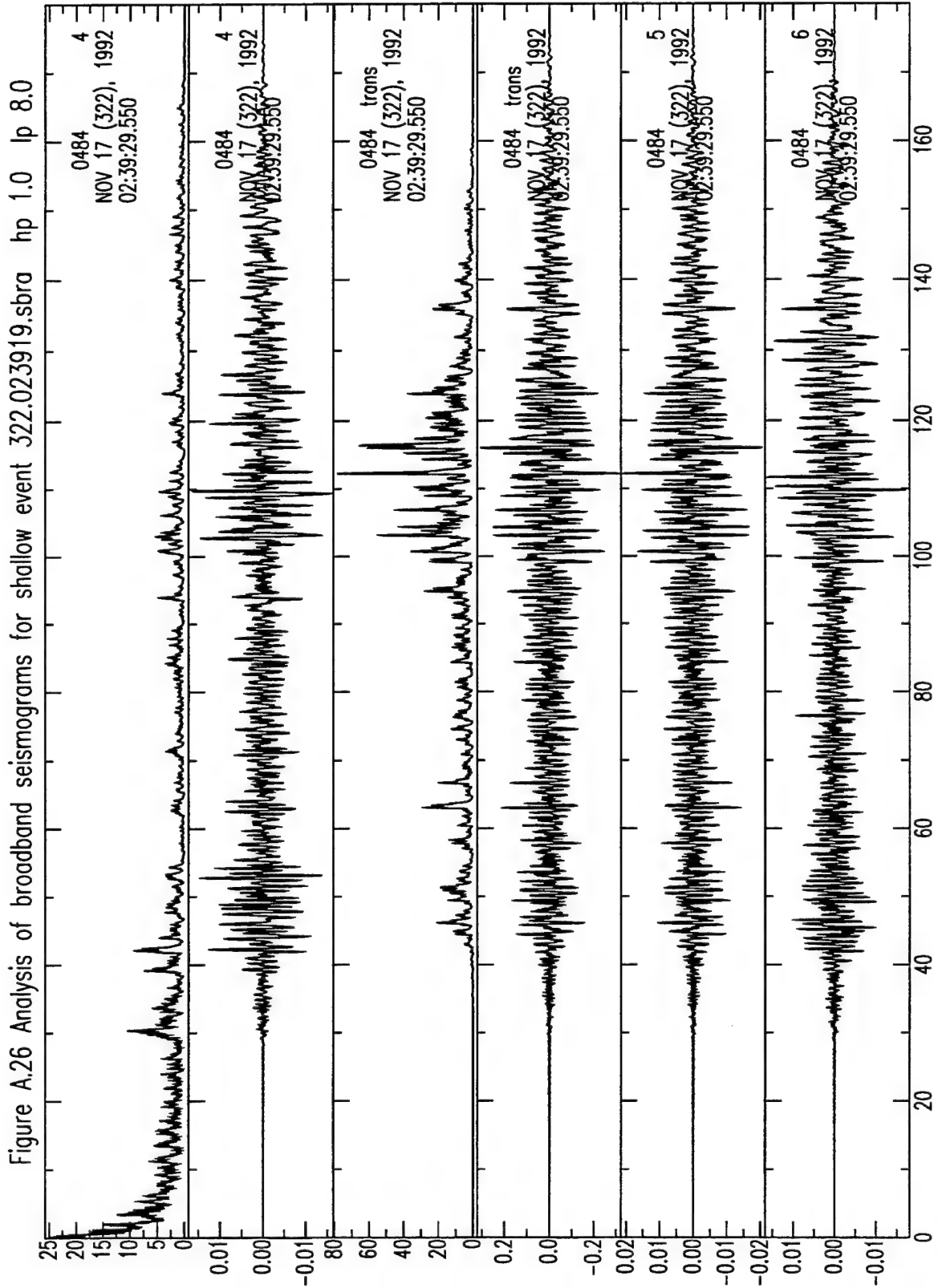


Figure A.27 Analysis of broadband seismograms for shallow event 322.023919.shin

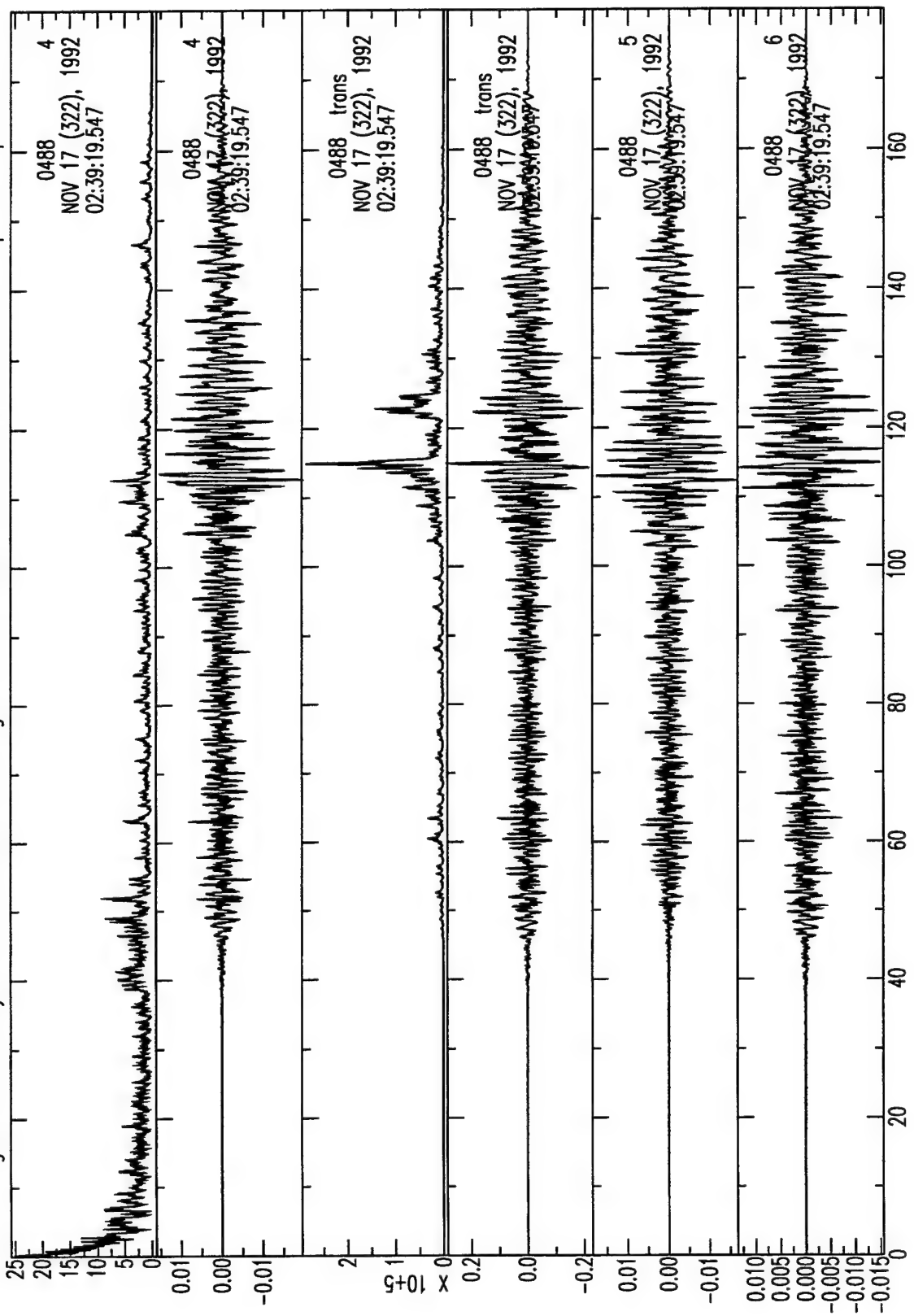


Figure A.28 Analysis of broadband seismograms for shallow event 322.023923.kalm

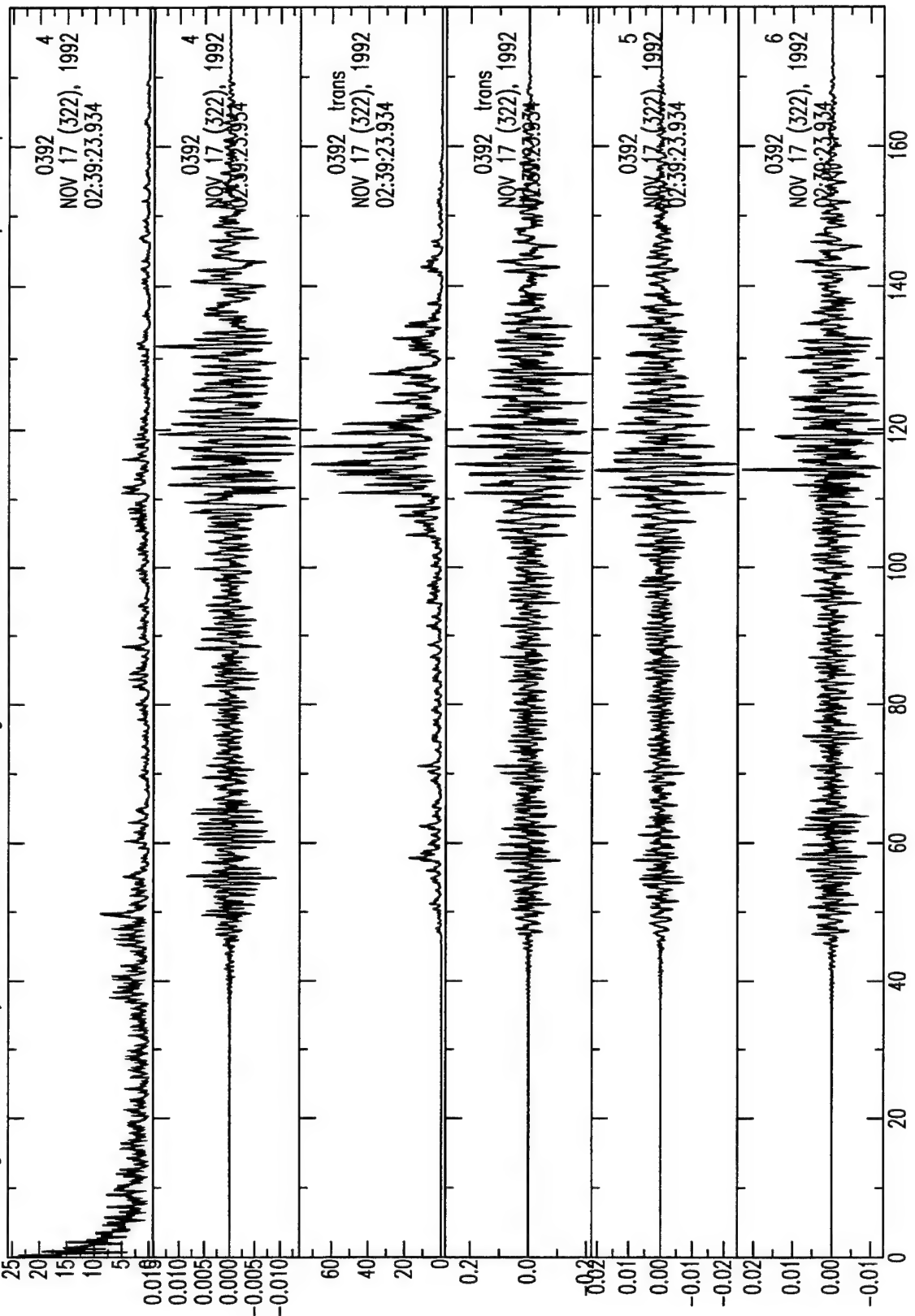
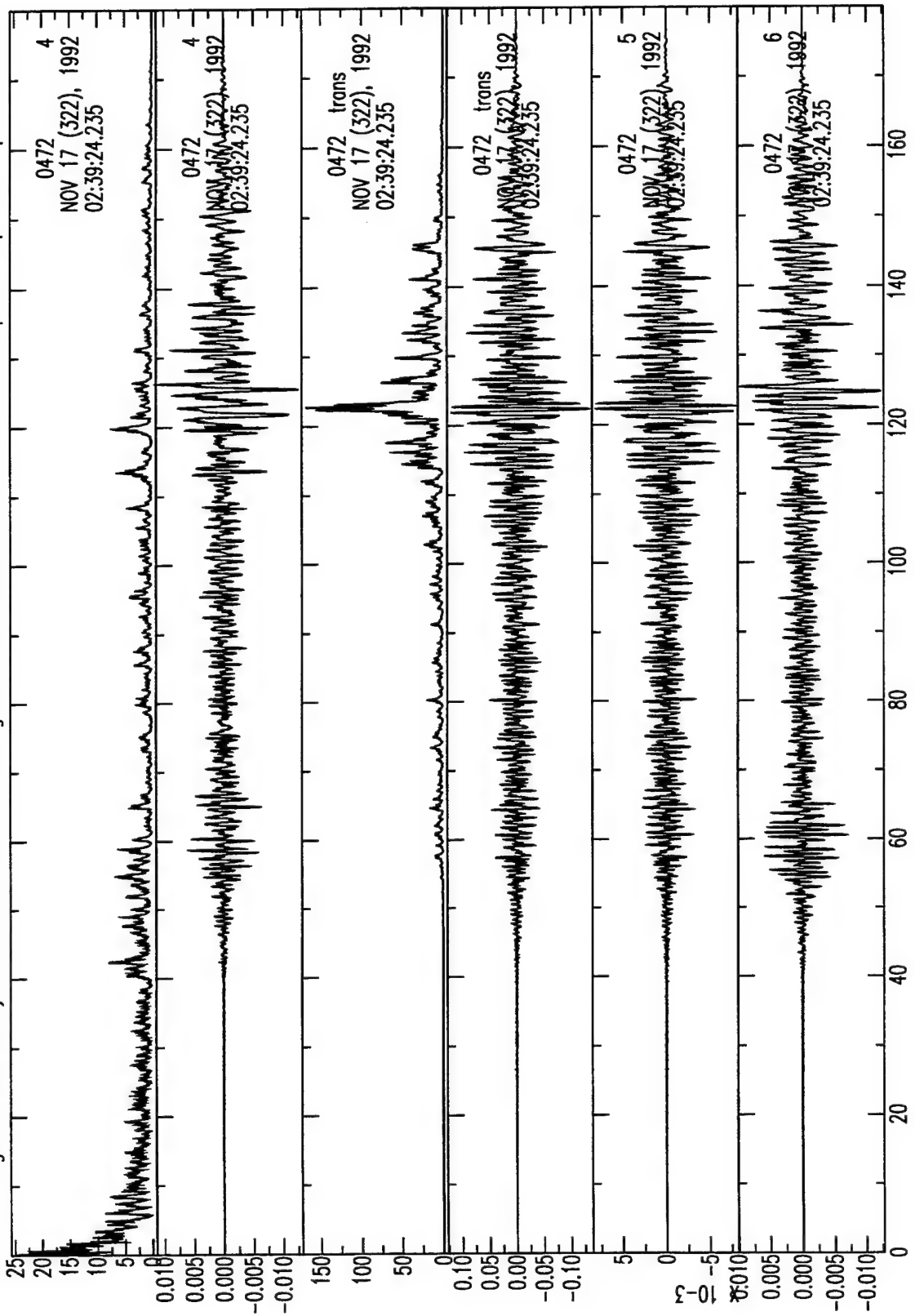


Figure A.29 Analysis of broadband seismograms for shallow event 322.023924.patn



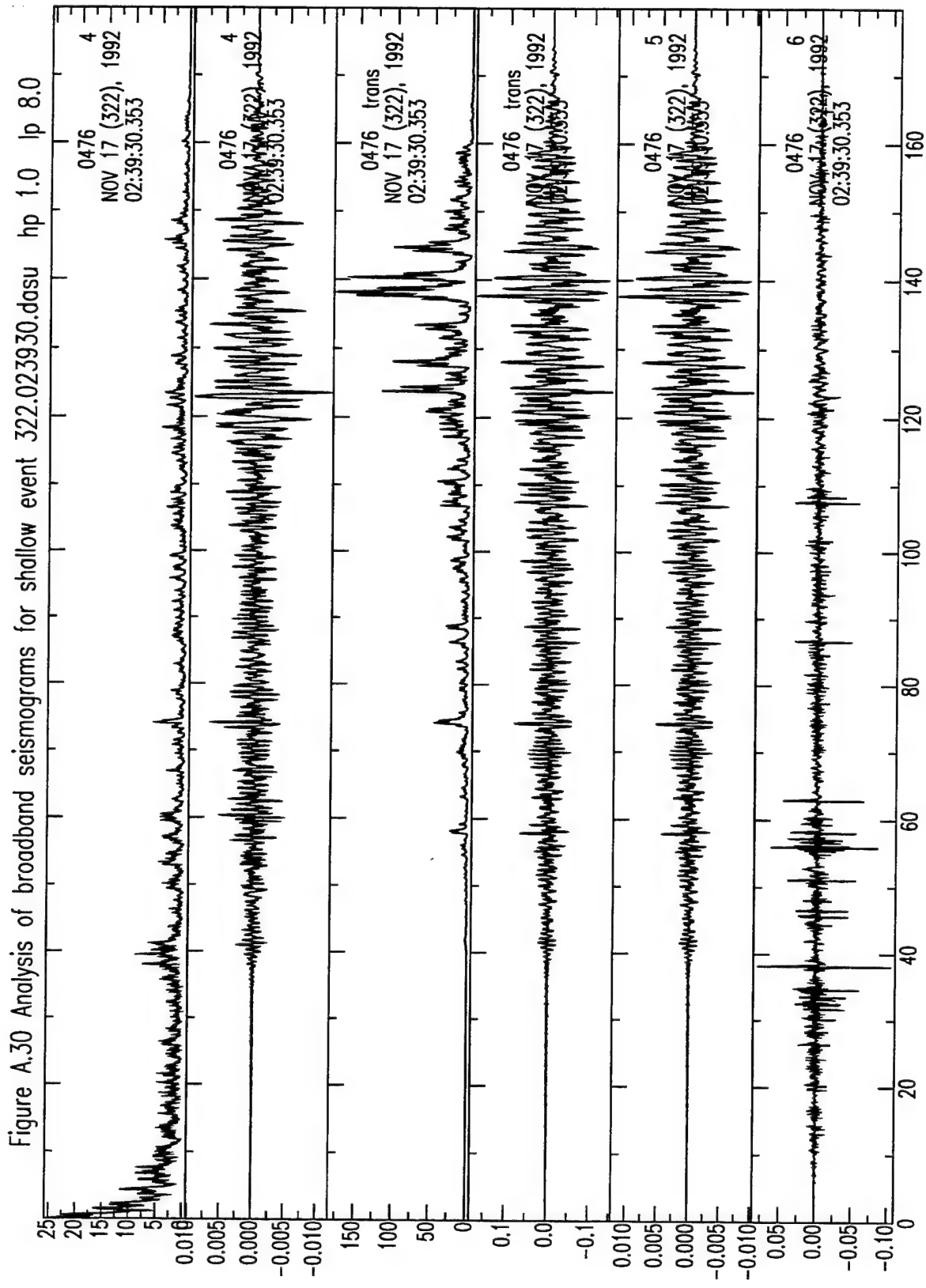
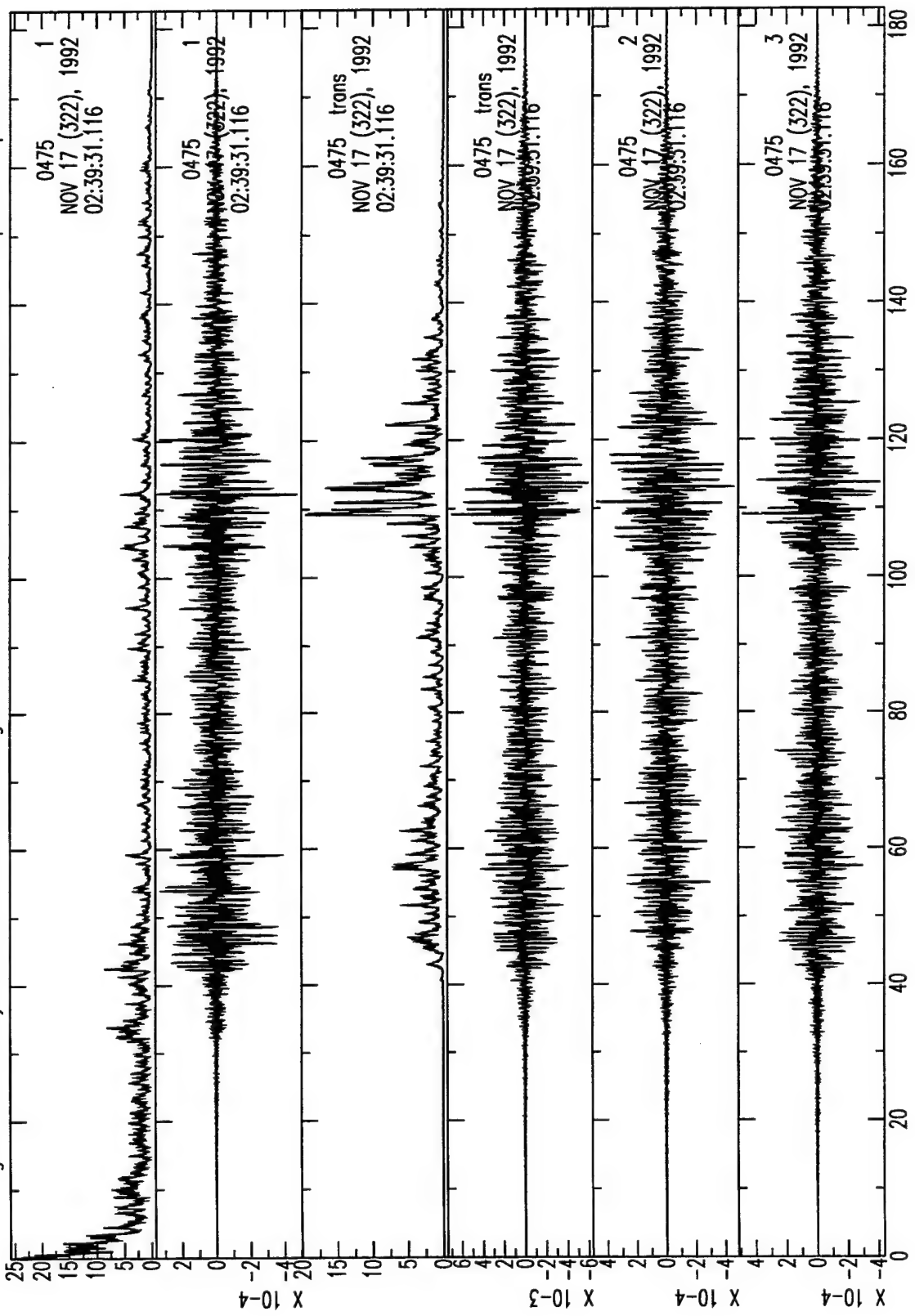
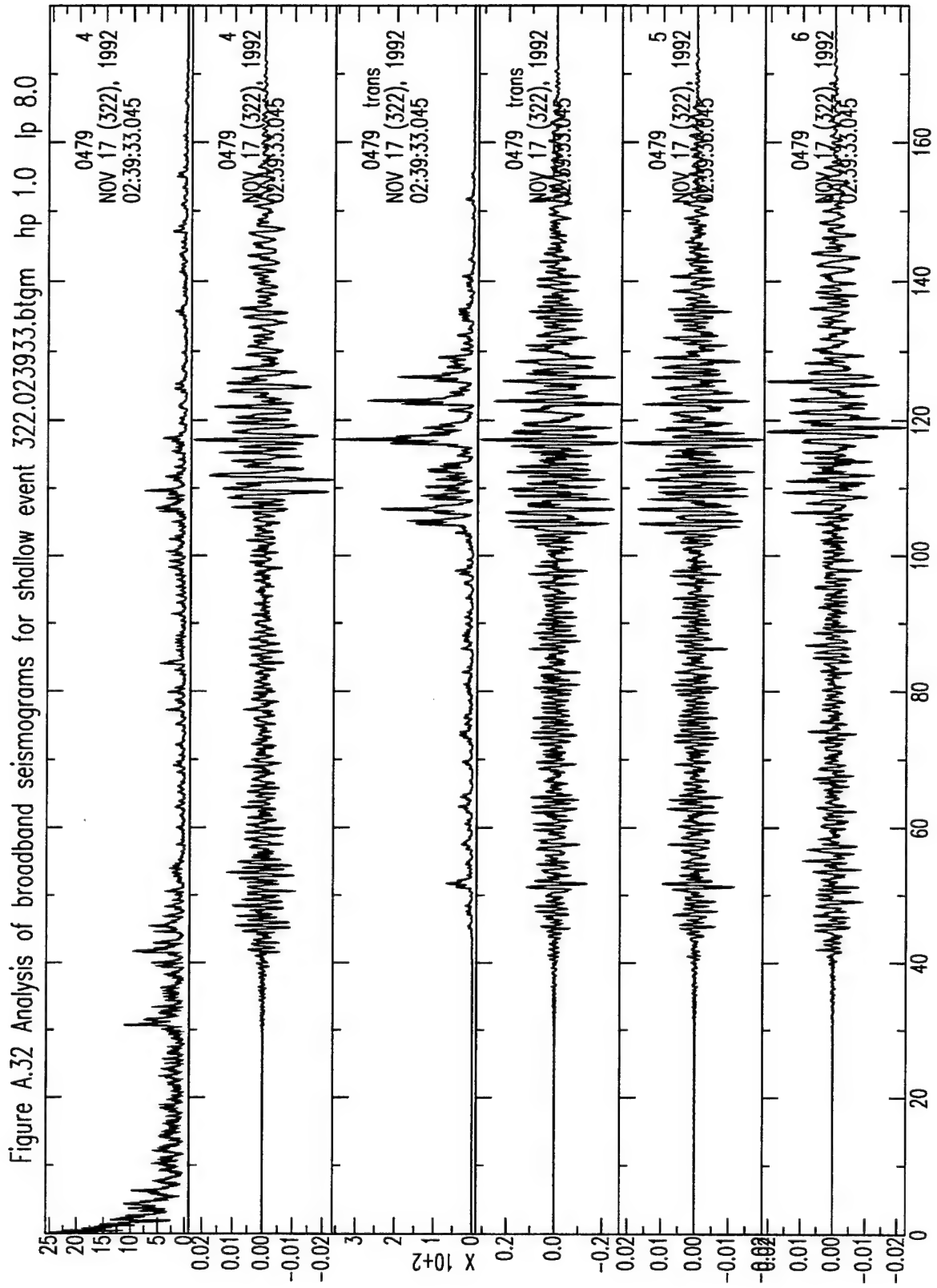
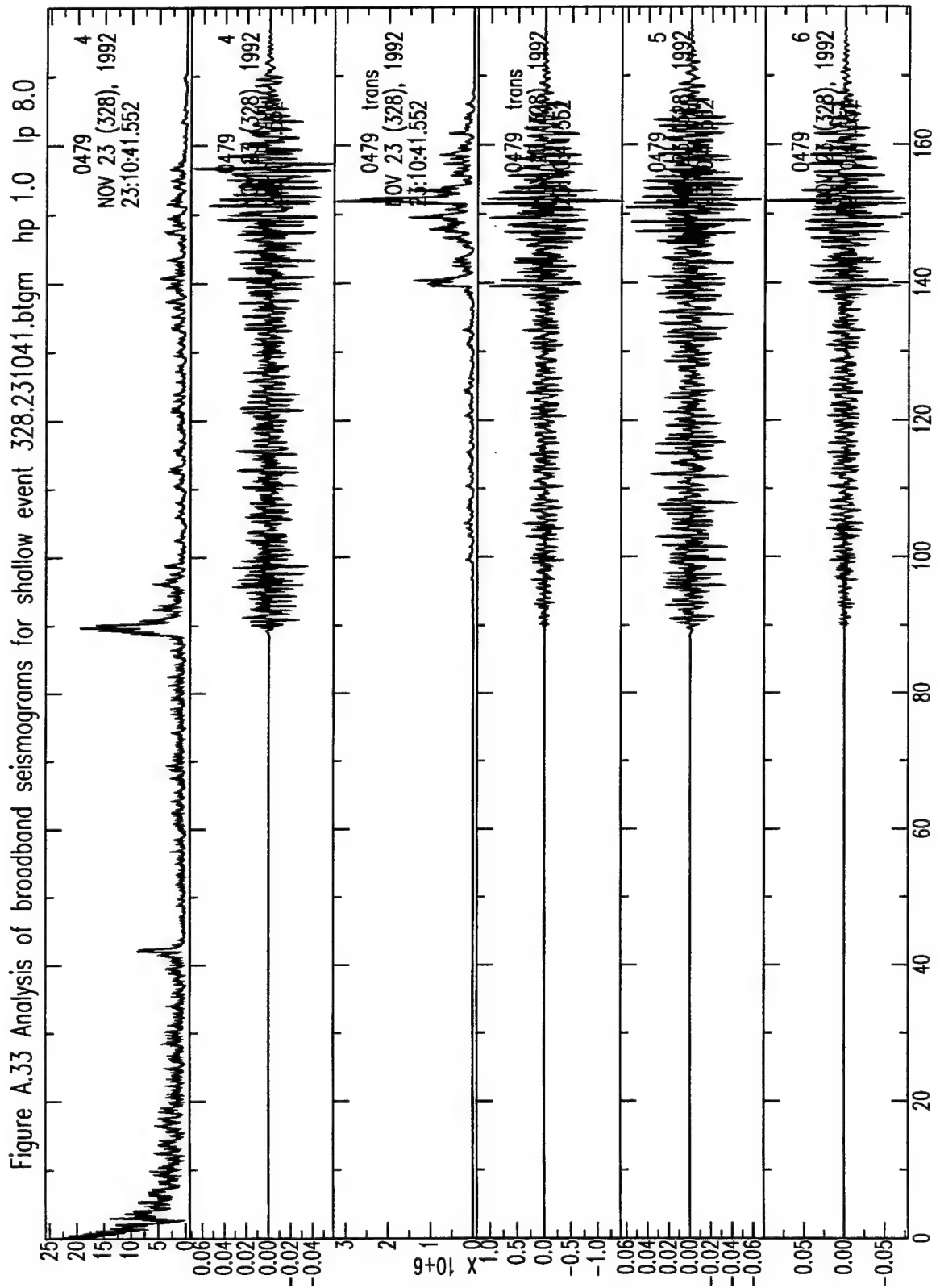


Figure A.31 Analysis of broadband seismograms for shallow event 322.023931.basm







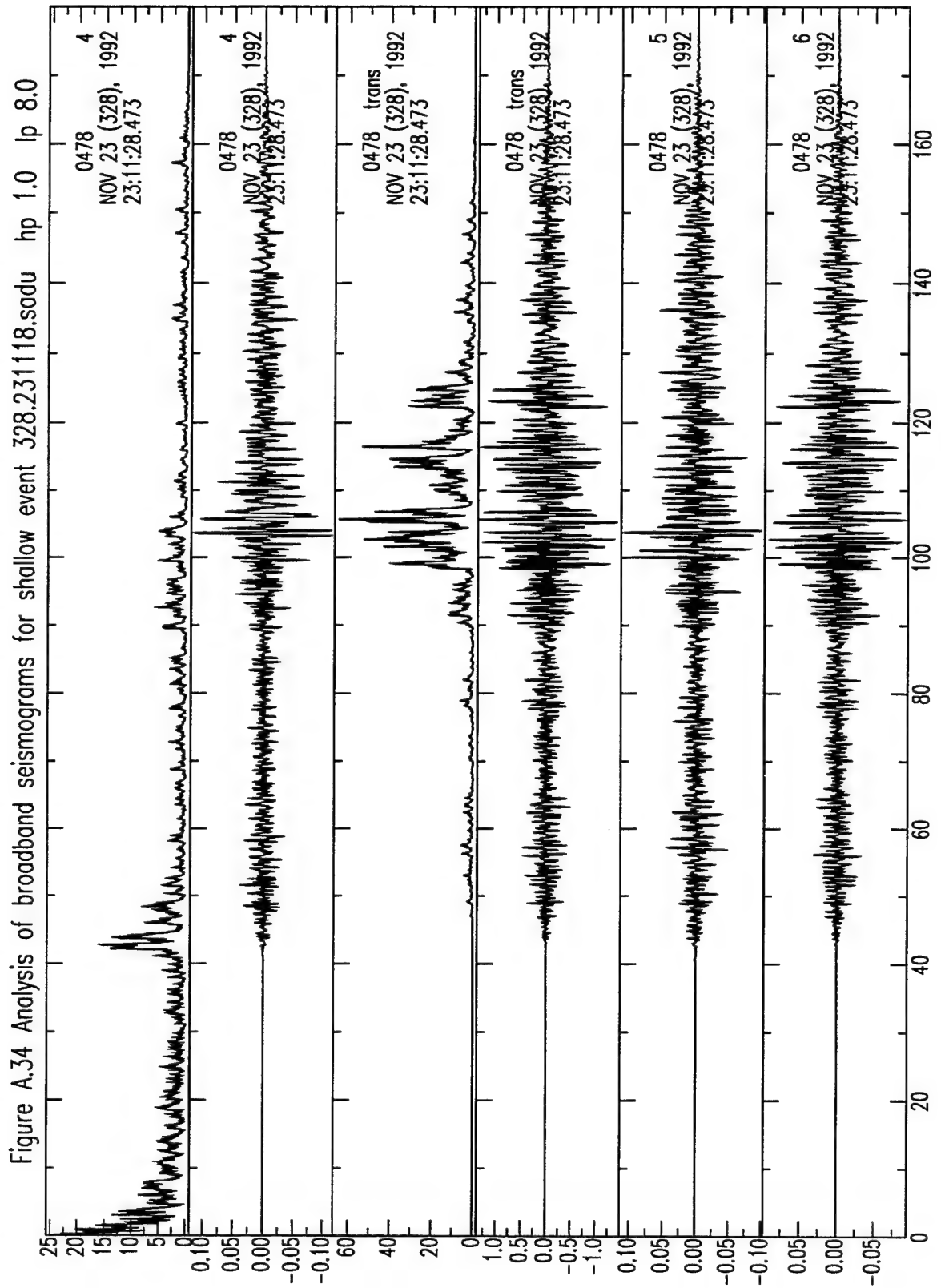


Figure A.35 Analysis of broadband seismograms for shallow event 328.231121.dasu hp 1.0 lp 8.0

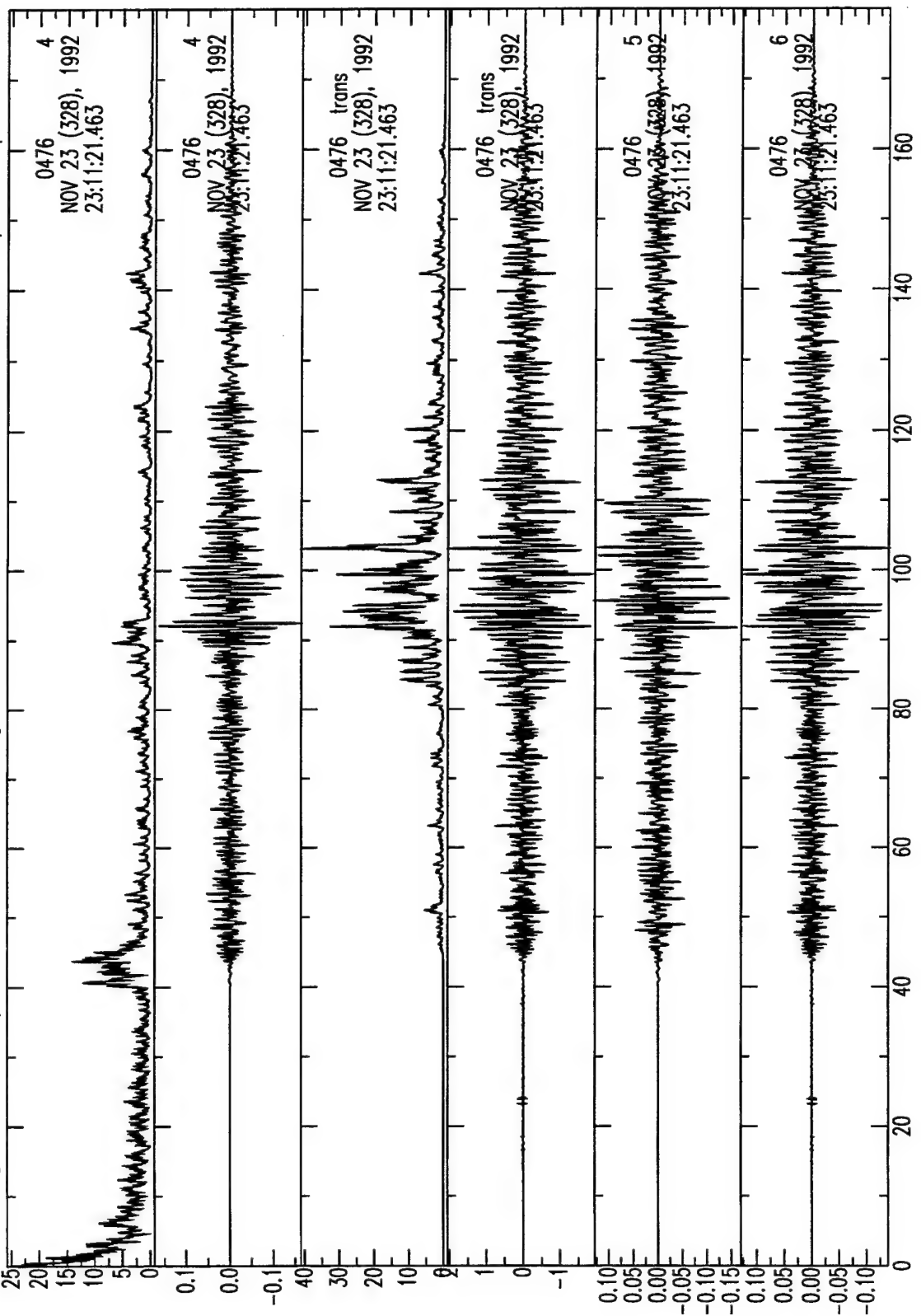


Figure A.36 Analysis of broadband seismograms for shallow event 328.231121.hklt

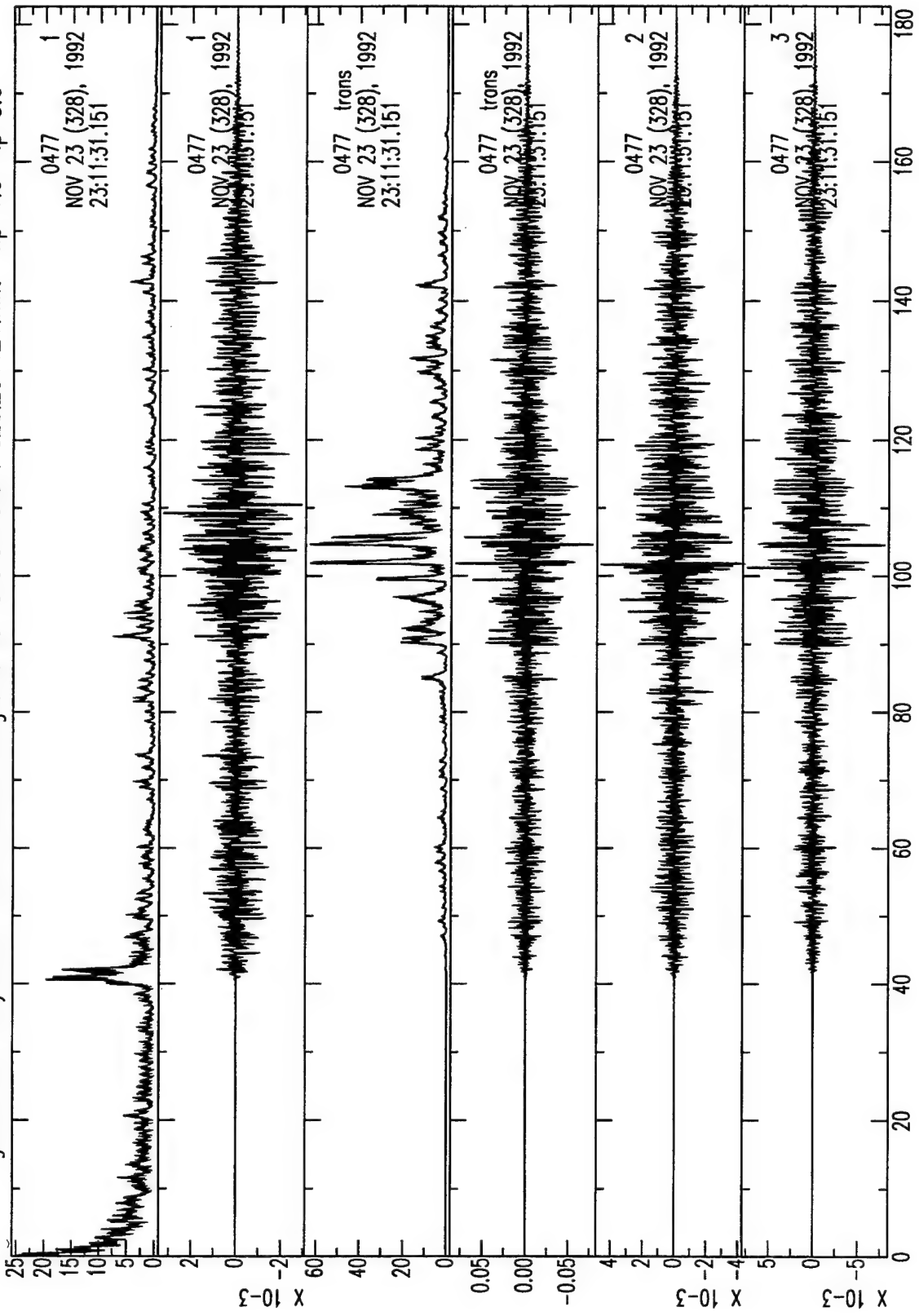
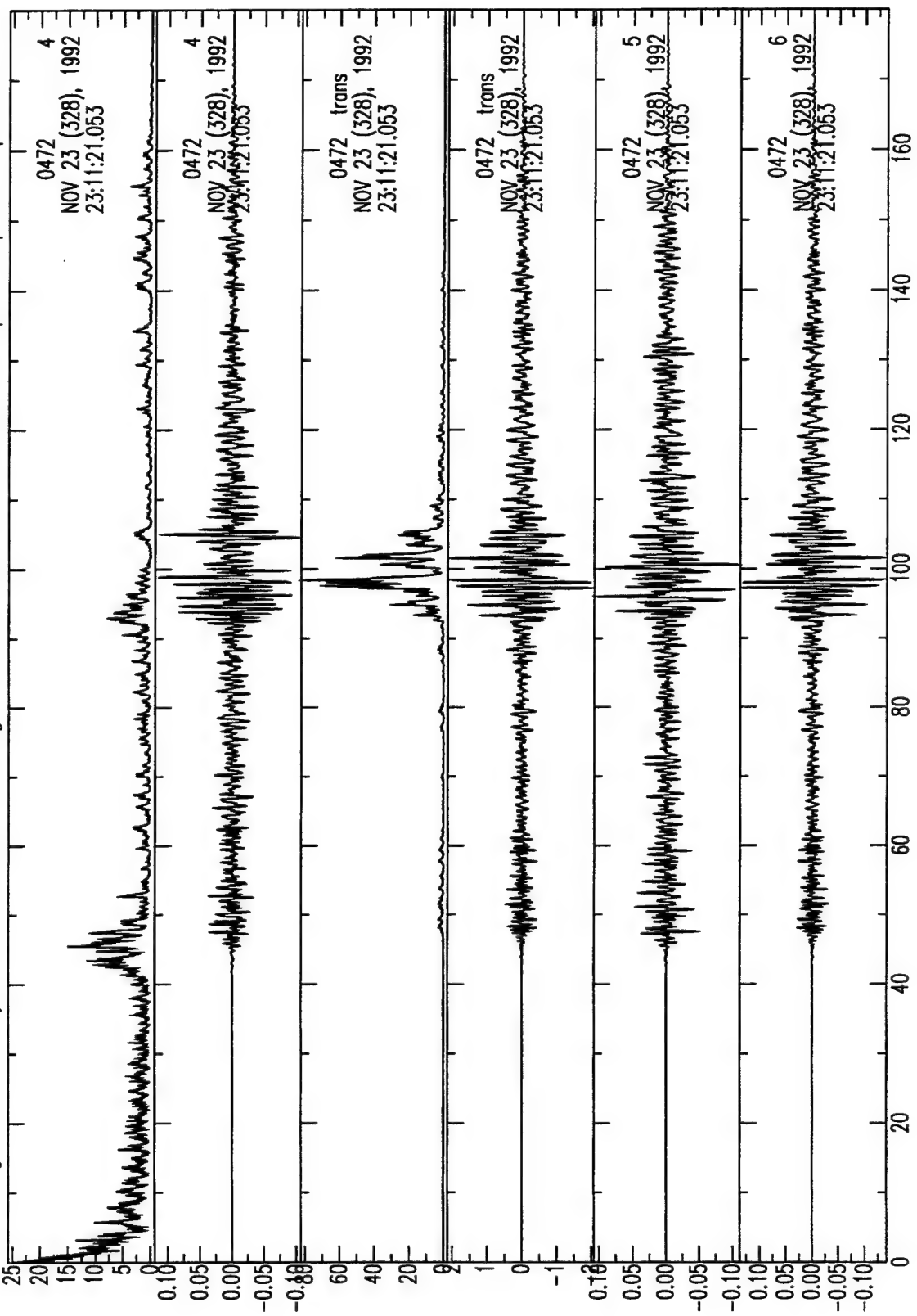


Figure A.37 Analysis of broadband seismograms for shallow event 328231121.patn



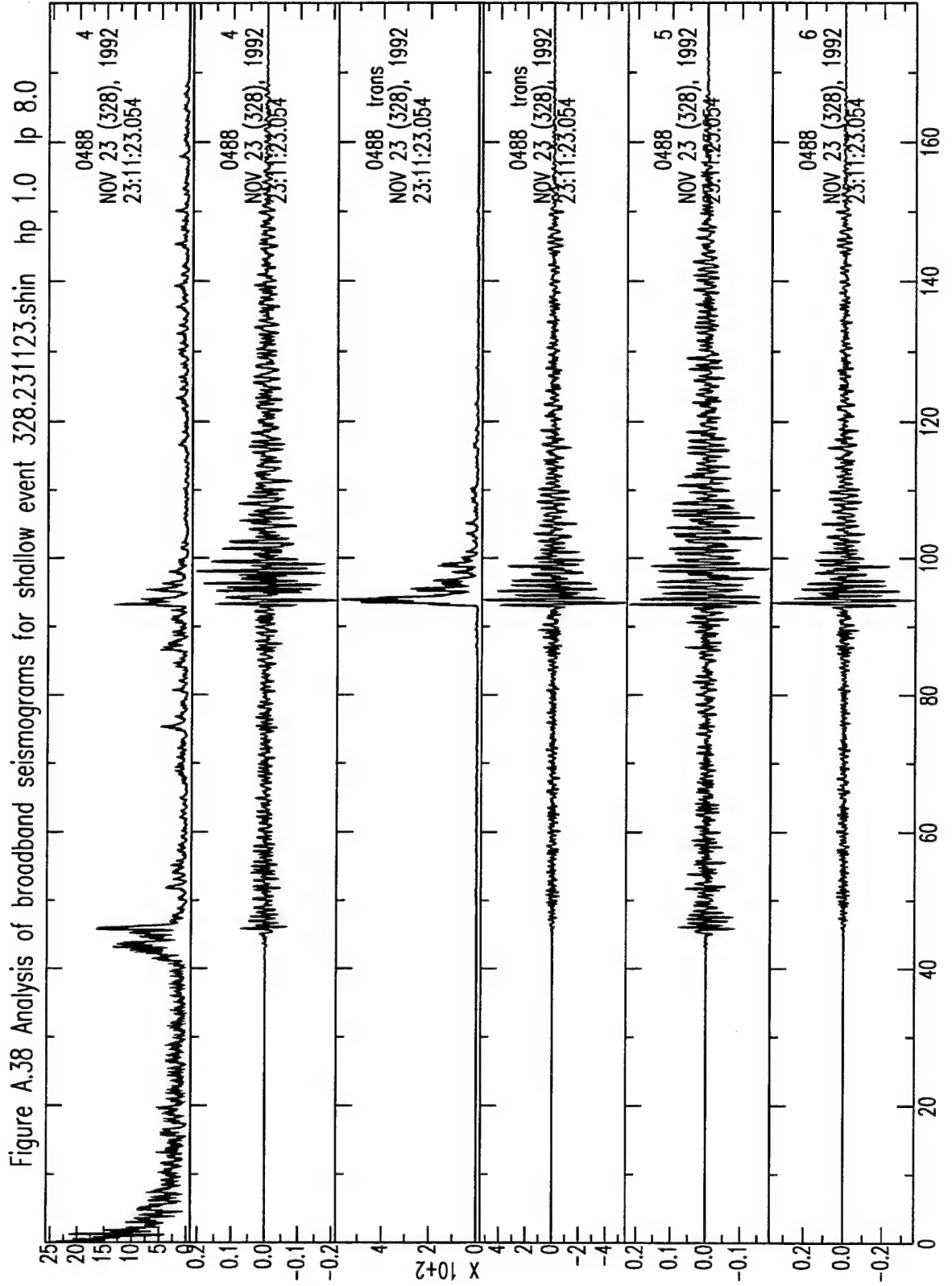
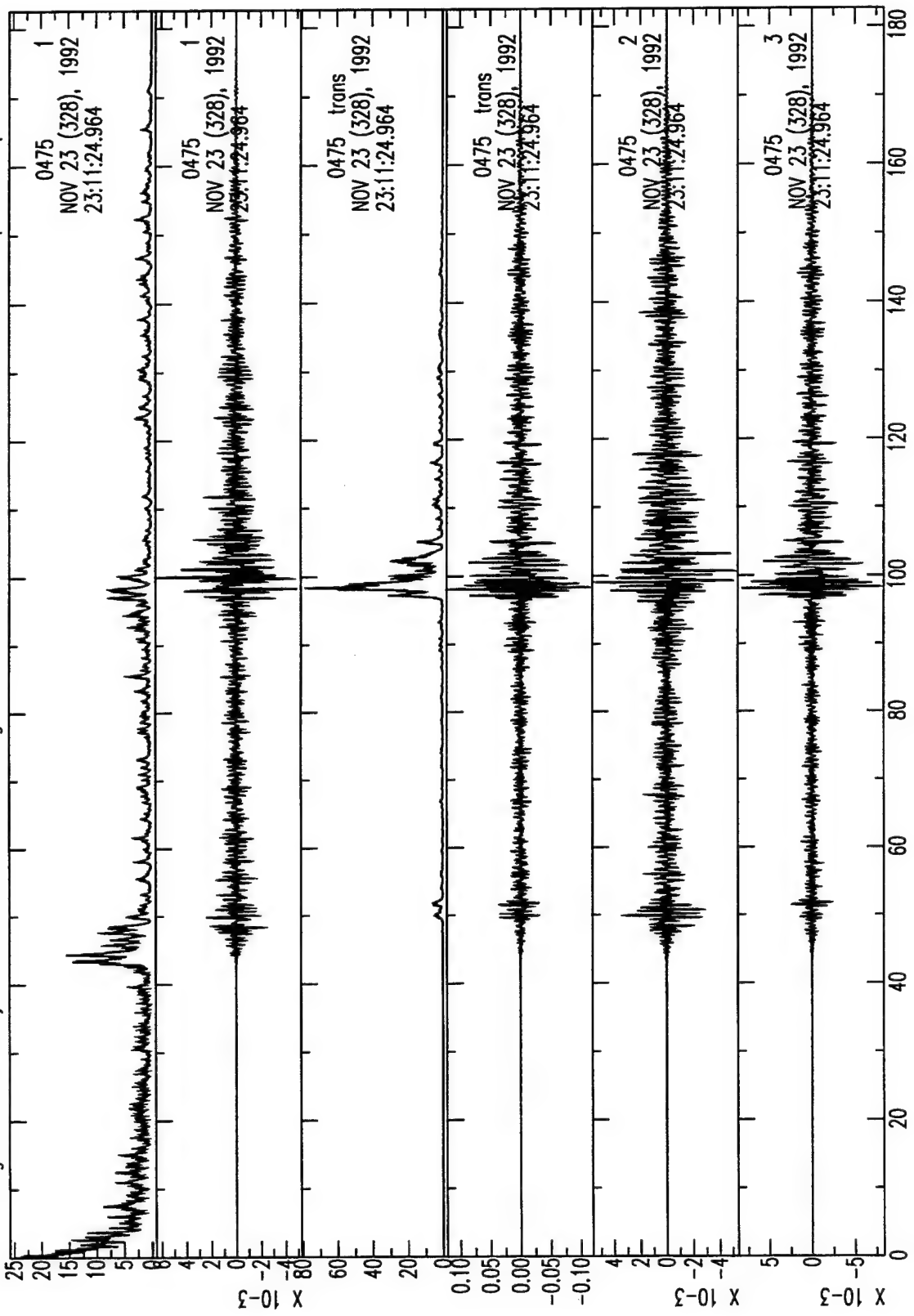


Figure A.39 Analysis of broadband seismograms for shallow event 328.231124.basm hp 1.0 lp 8.0



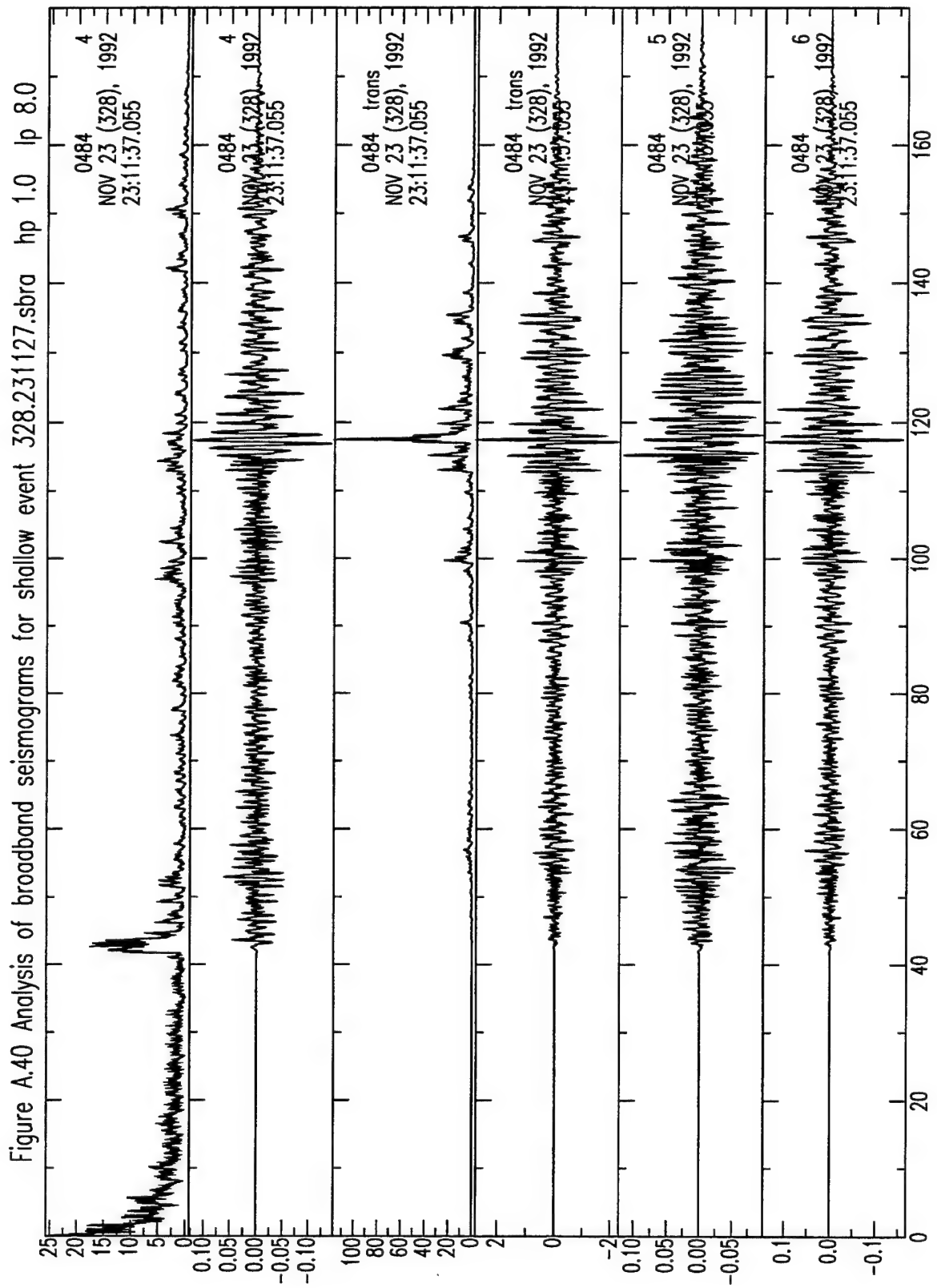


Figure A.41 Analysis of broadband seismograms for shallow event 328.231200.shob

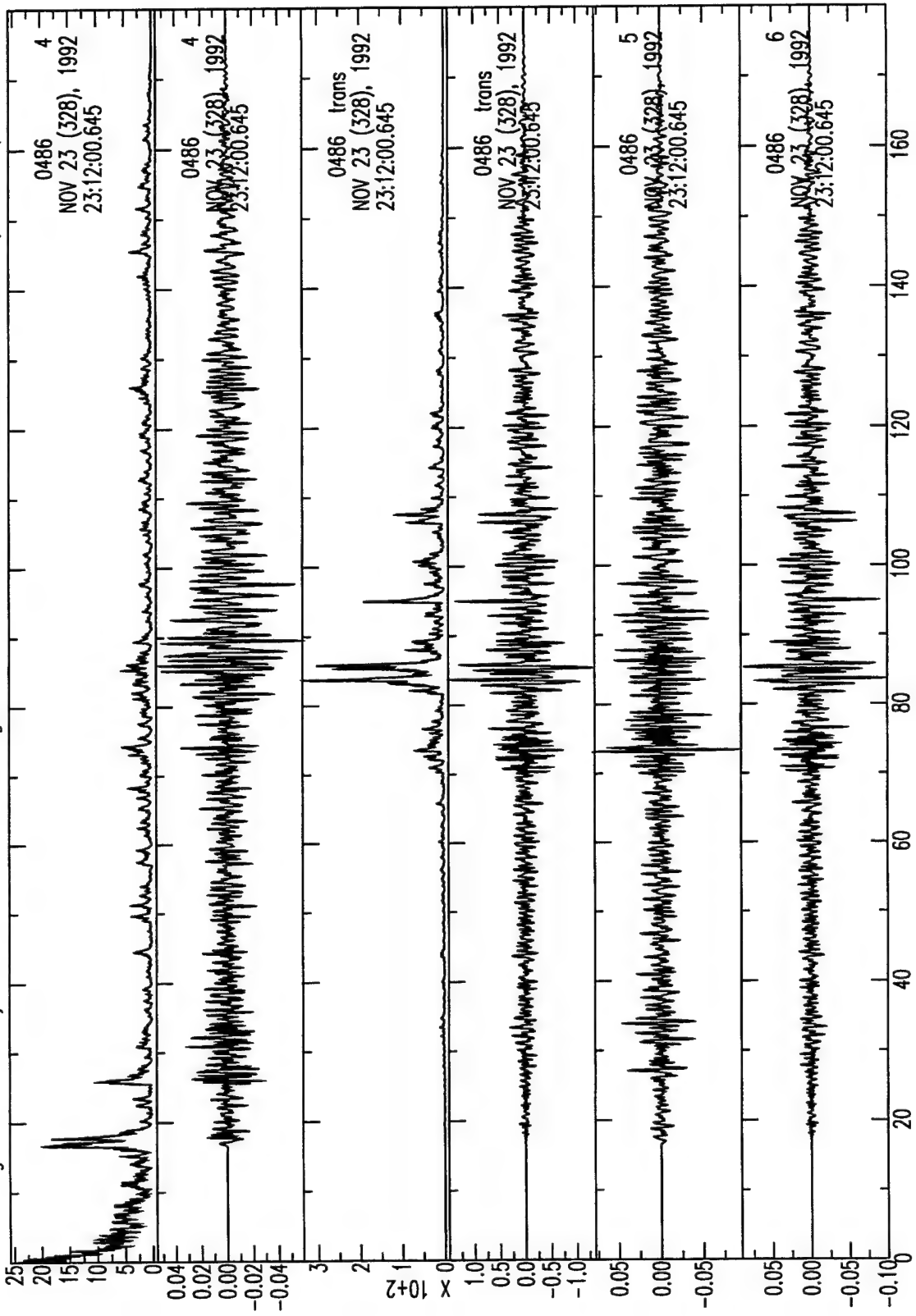
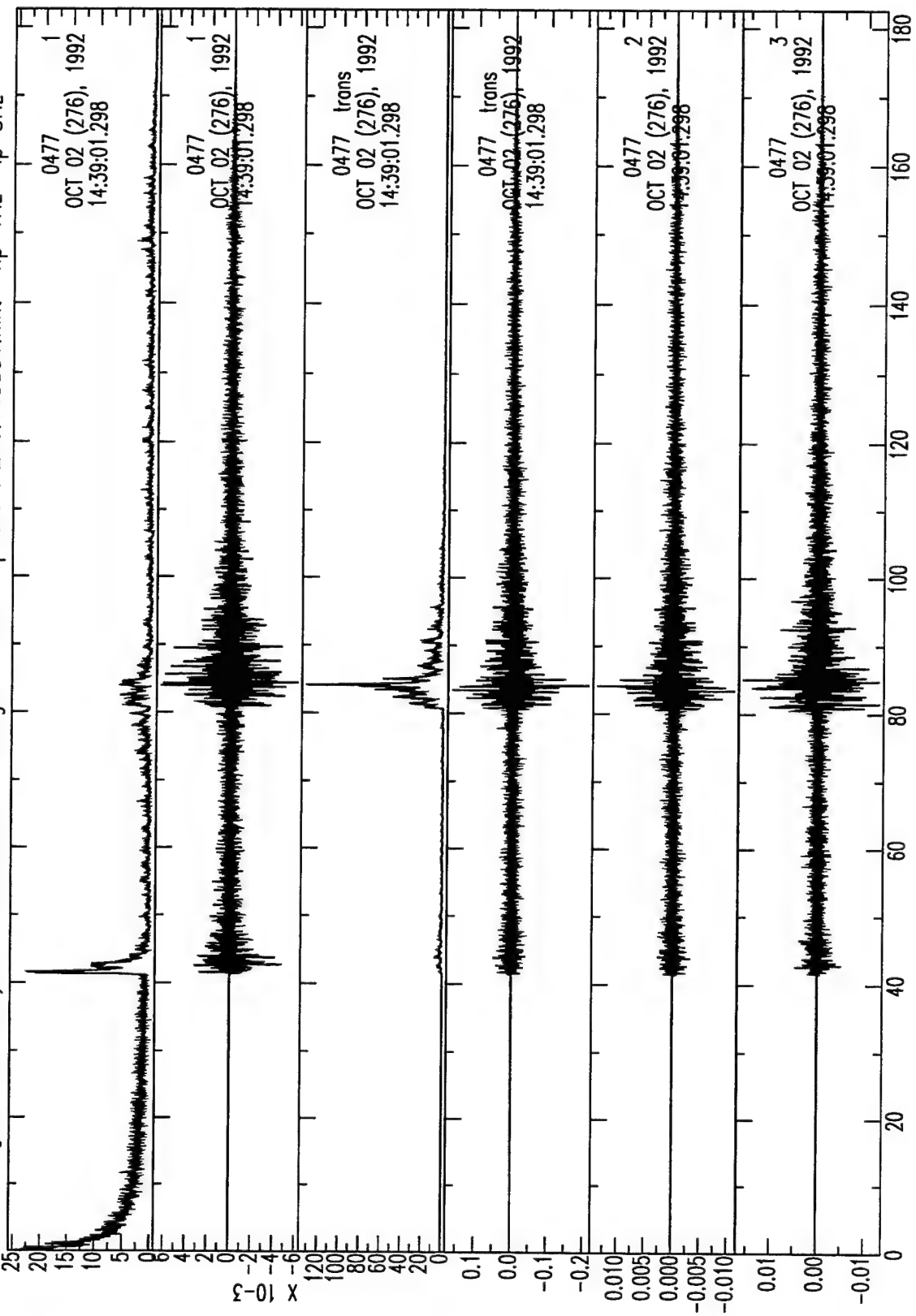
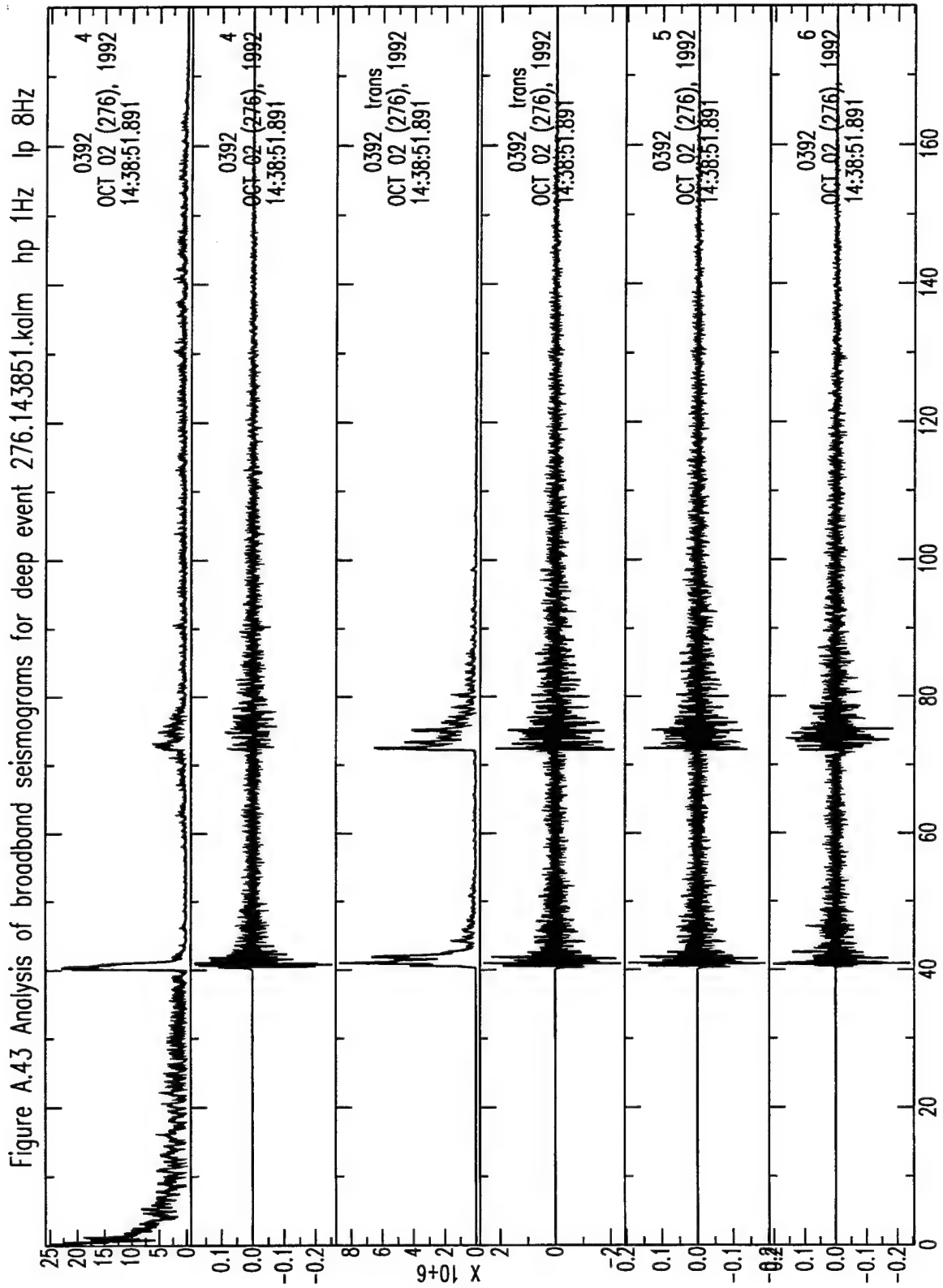


Figure A.42 Analysis of broadband seismograms for deep event 276.143851.hklt hp 1Hz lp 8Hz





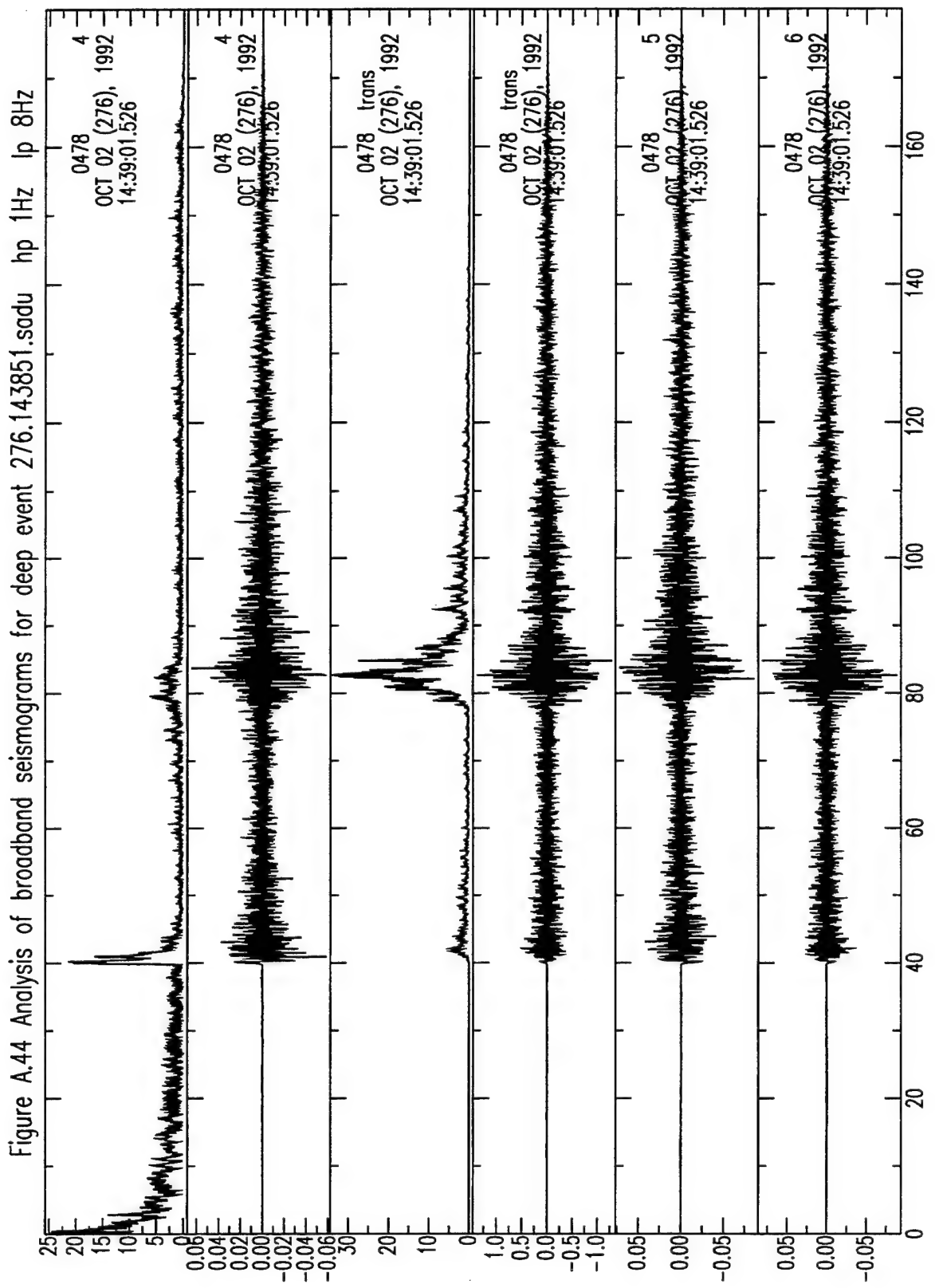
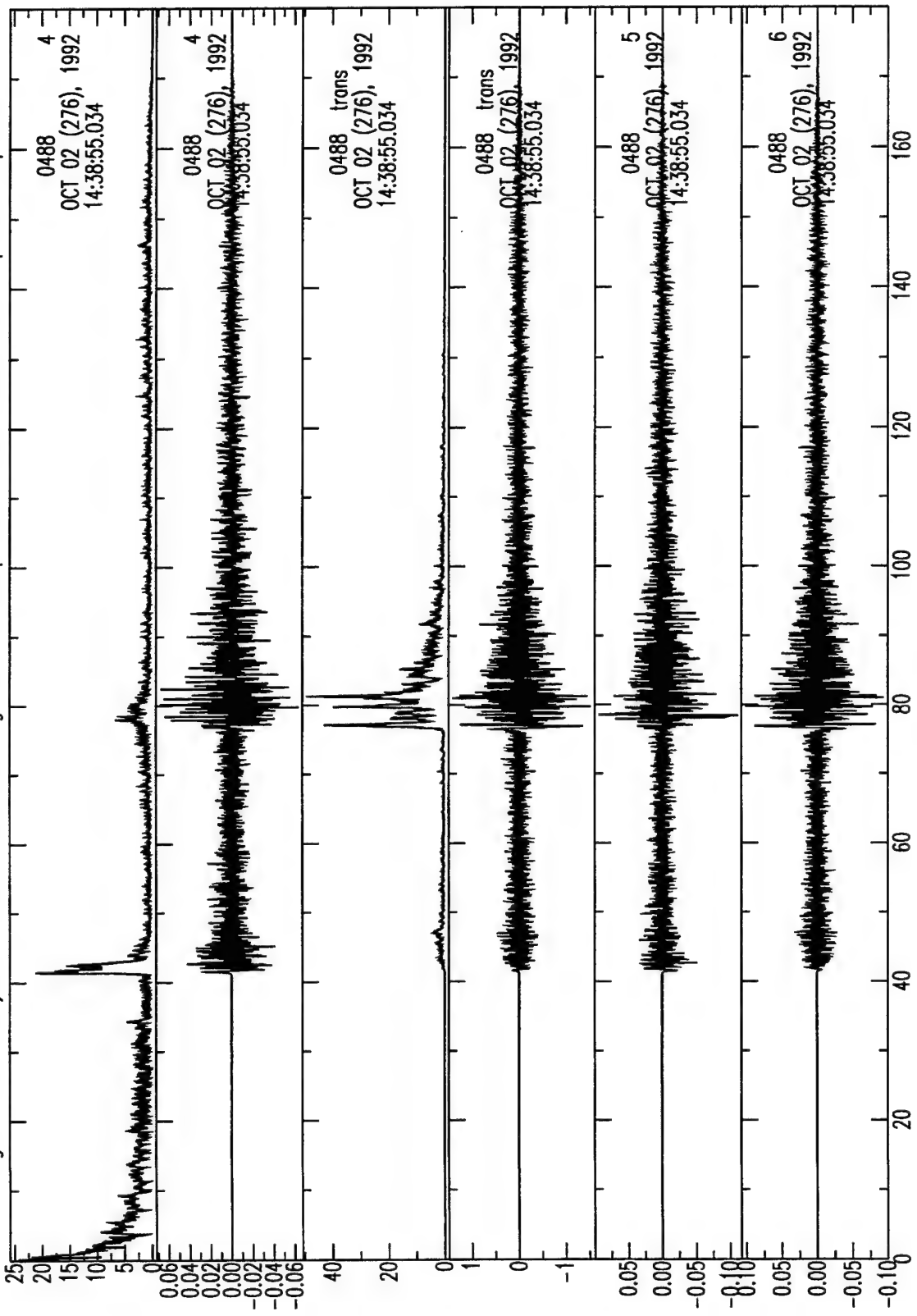


Figure A.45 Analysis of broadband seismograms for deep event 276.143855.shin



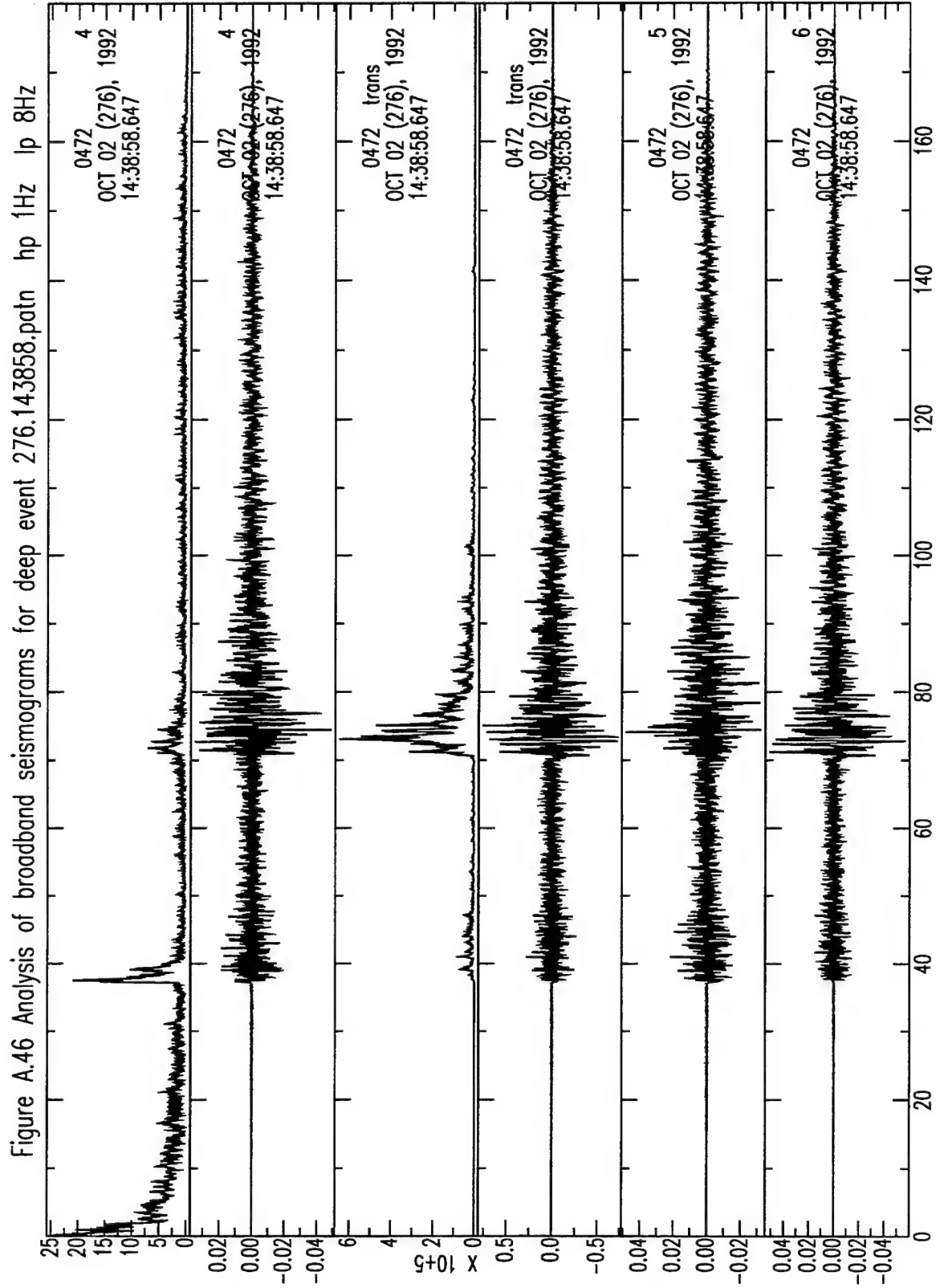


Figure A.47 Analysis of broadband seismograms for deep event 276.143905.btlgm

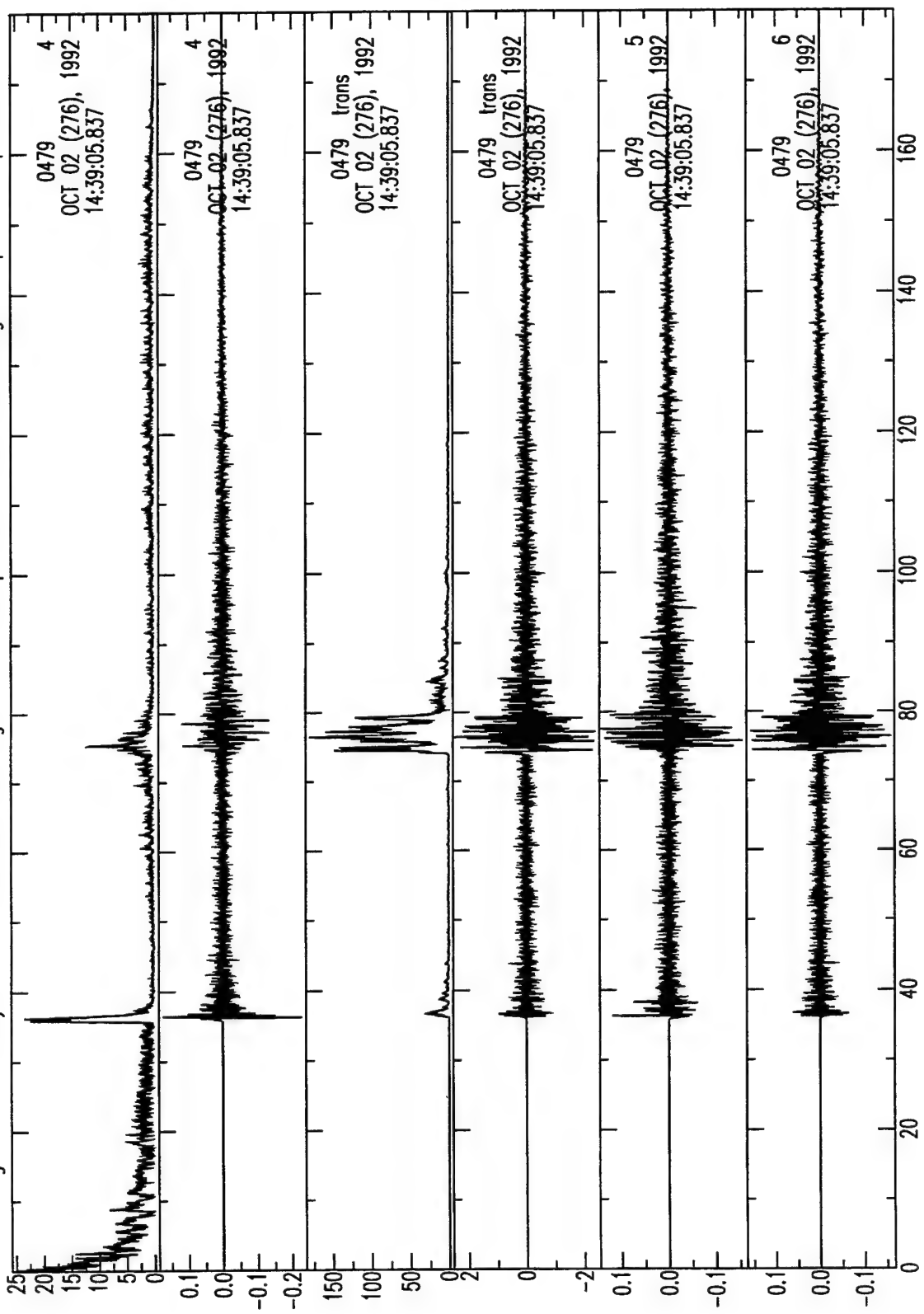


Figure A.48 Analysis of broadband seismograms for deep event 276.143907.shab

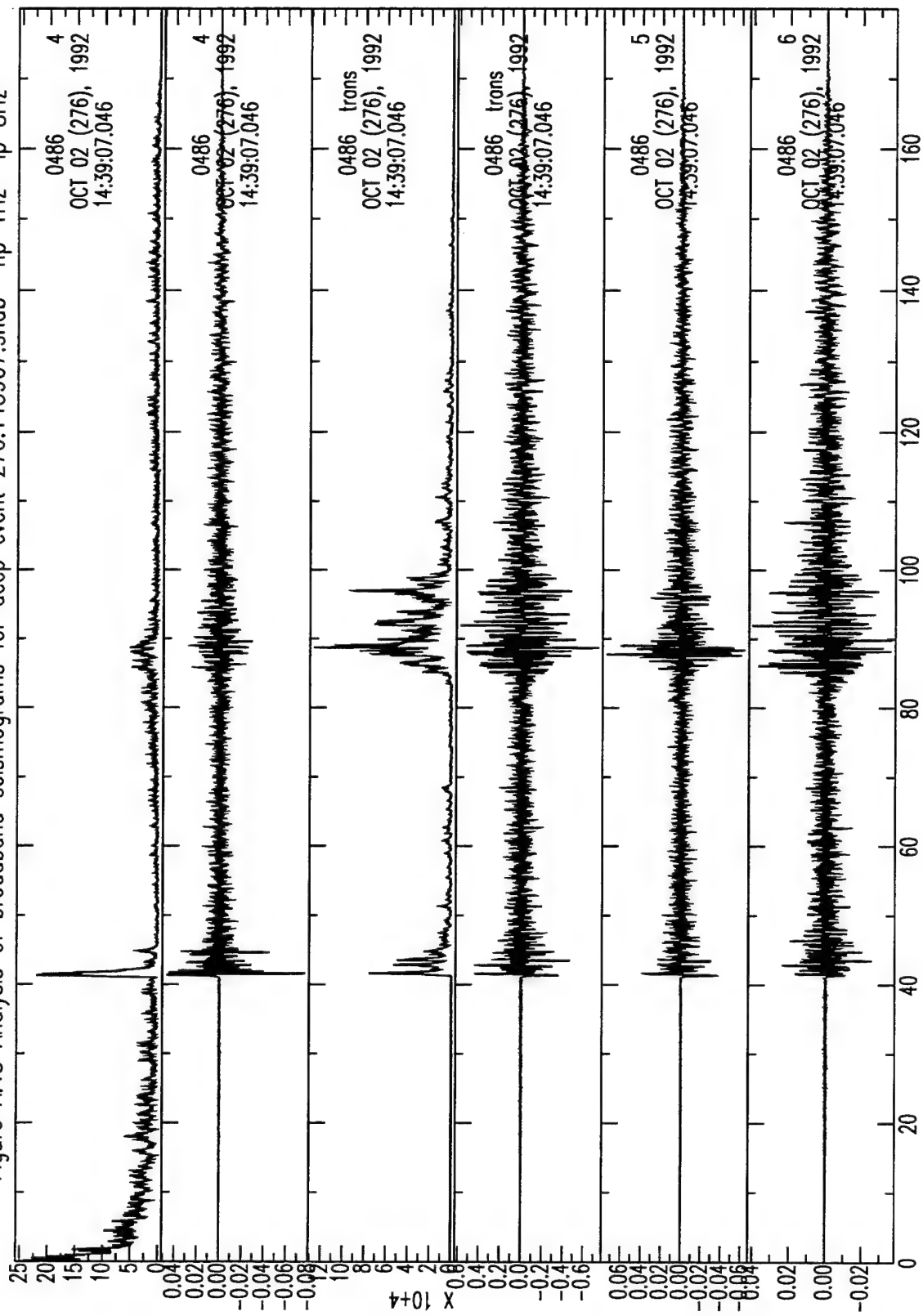
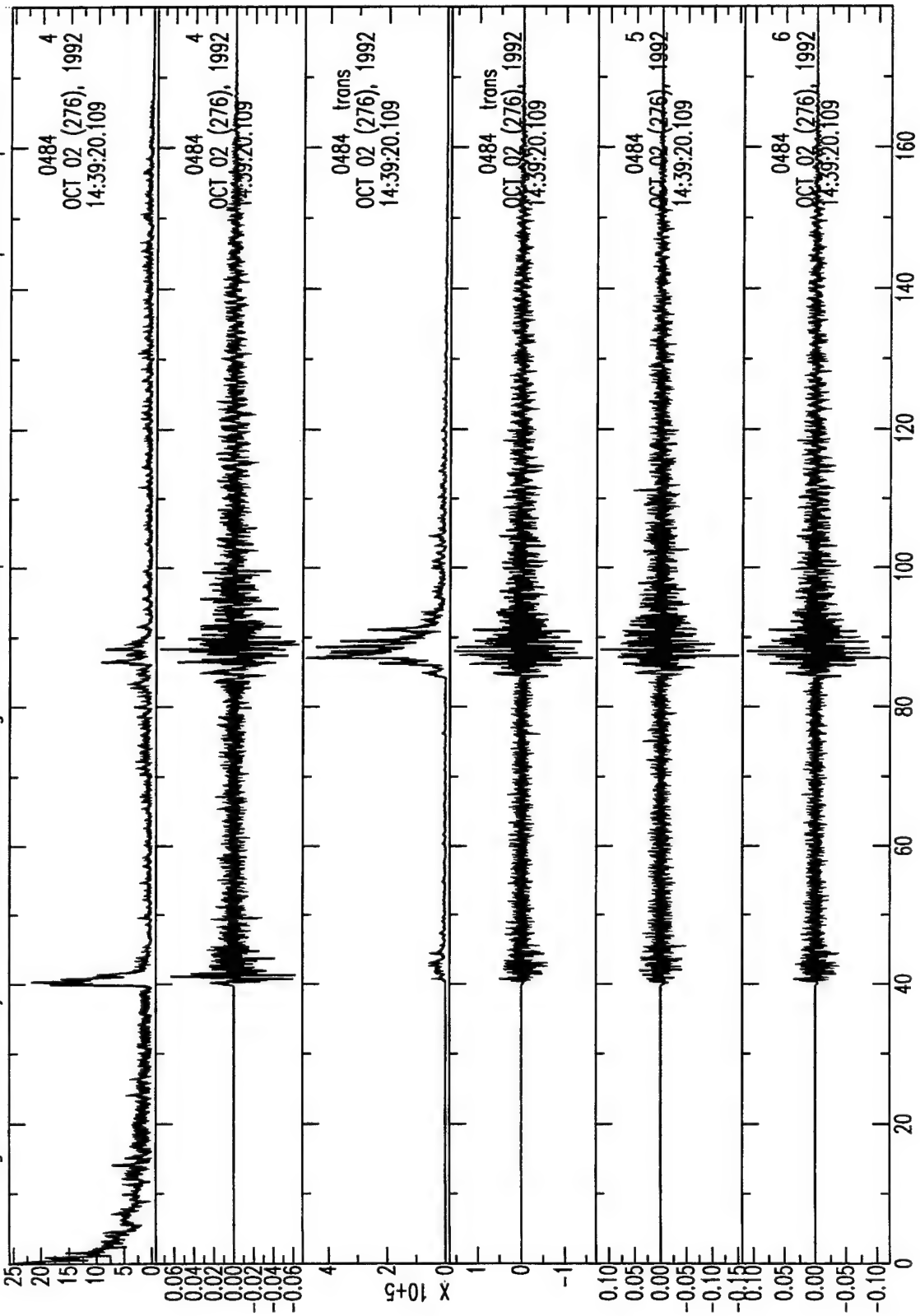


Figure A.49 Analysis of broadband seismograms for deep event 276.143910.sbra



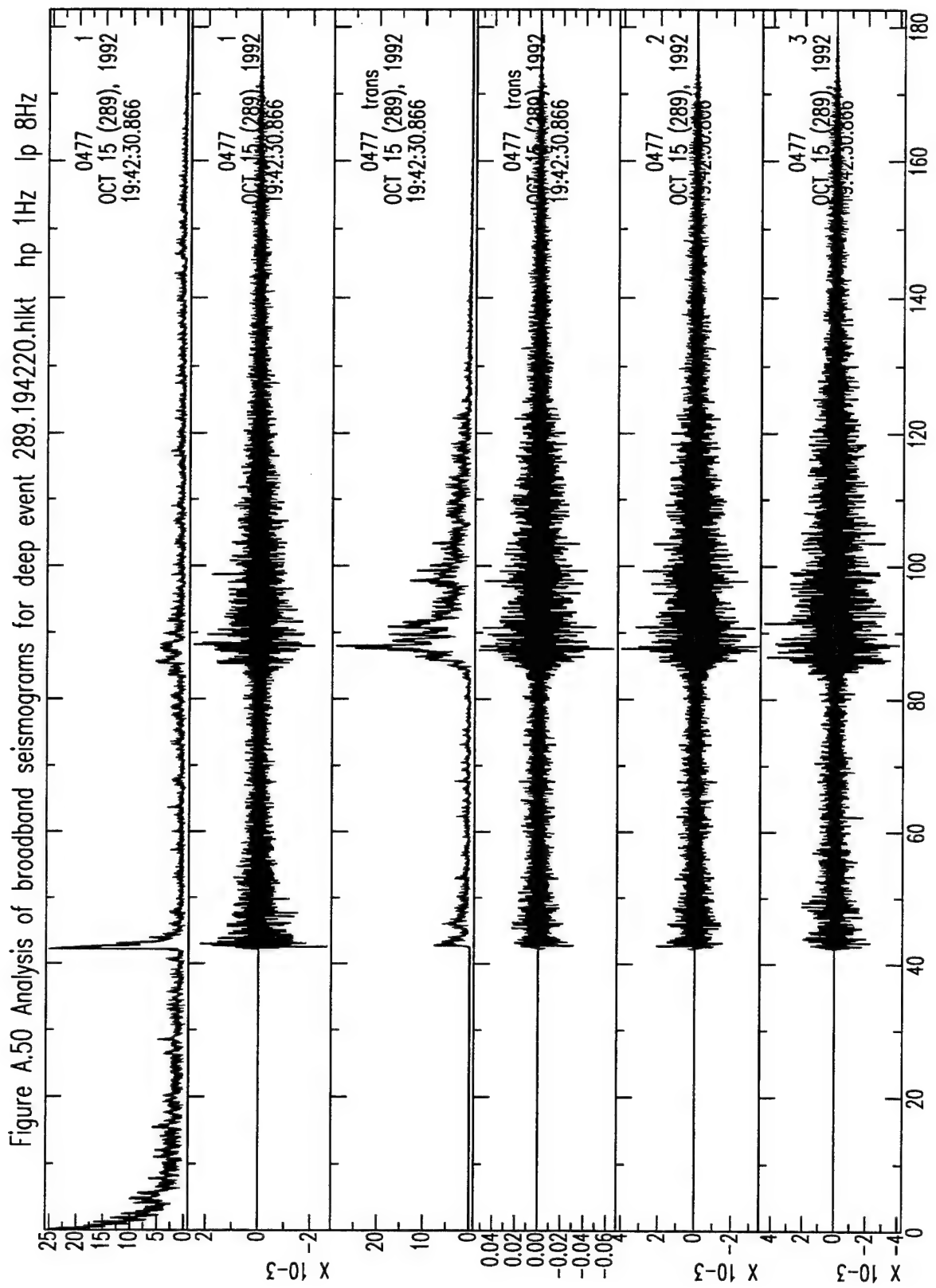


Figure A.51 Analysis of broadband seismograms for deep event 289.194223.ds0u

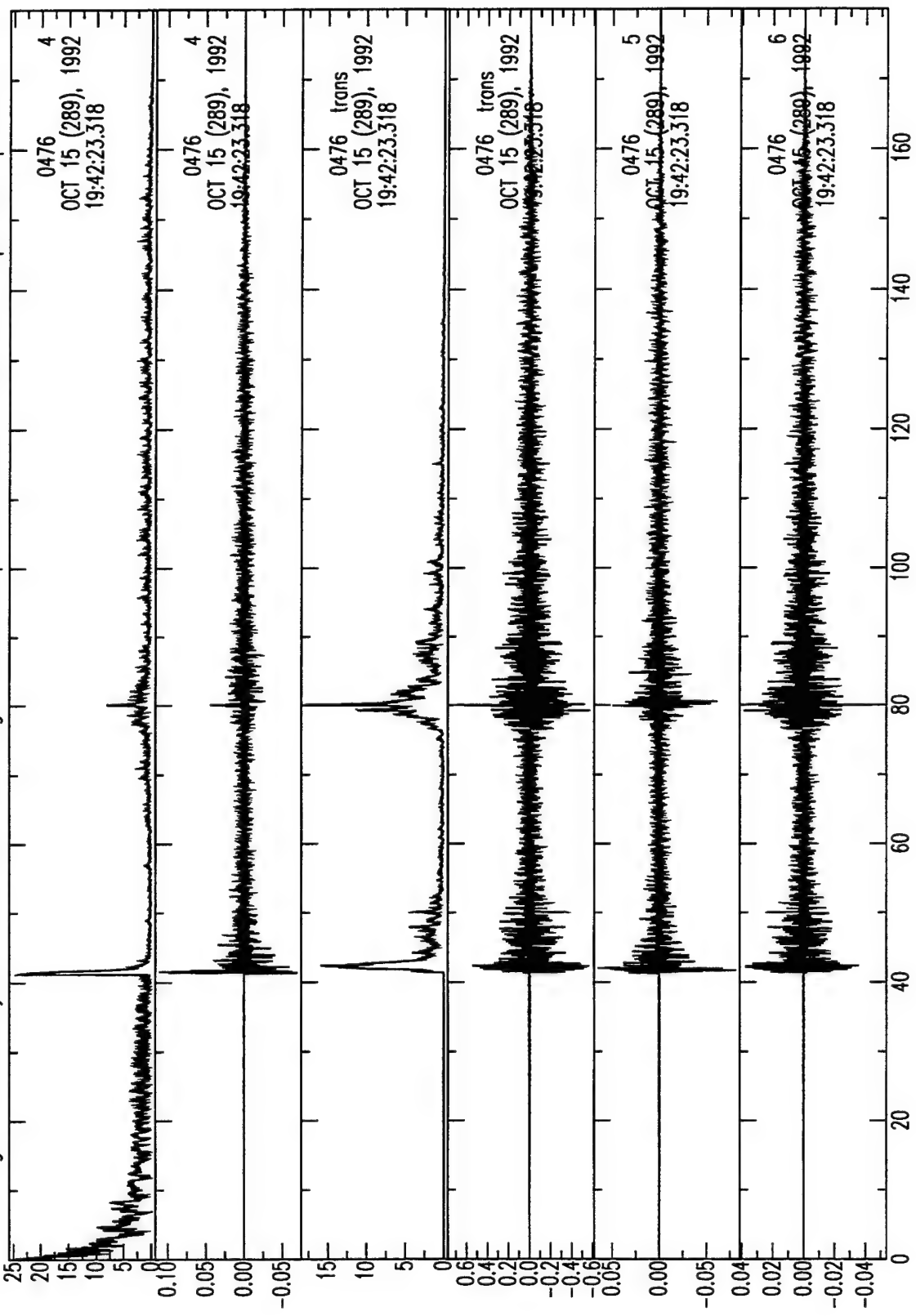


Figure A.52 Analysis of broadband seismograms for deep event 289.194223.sadu

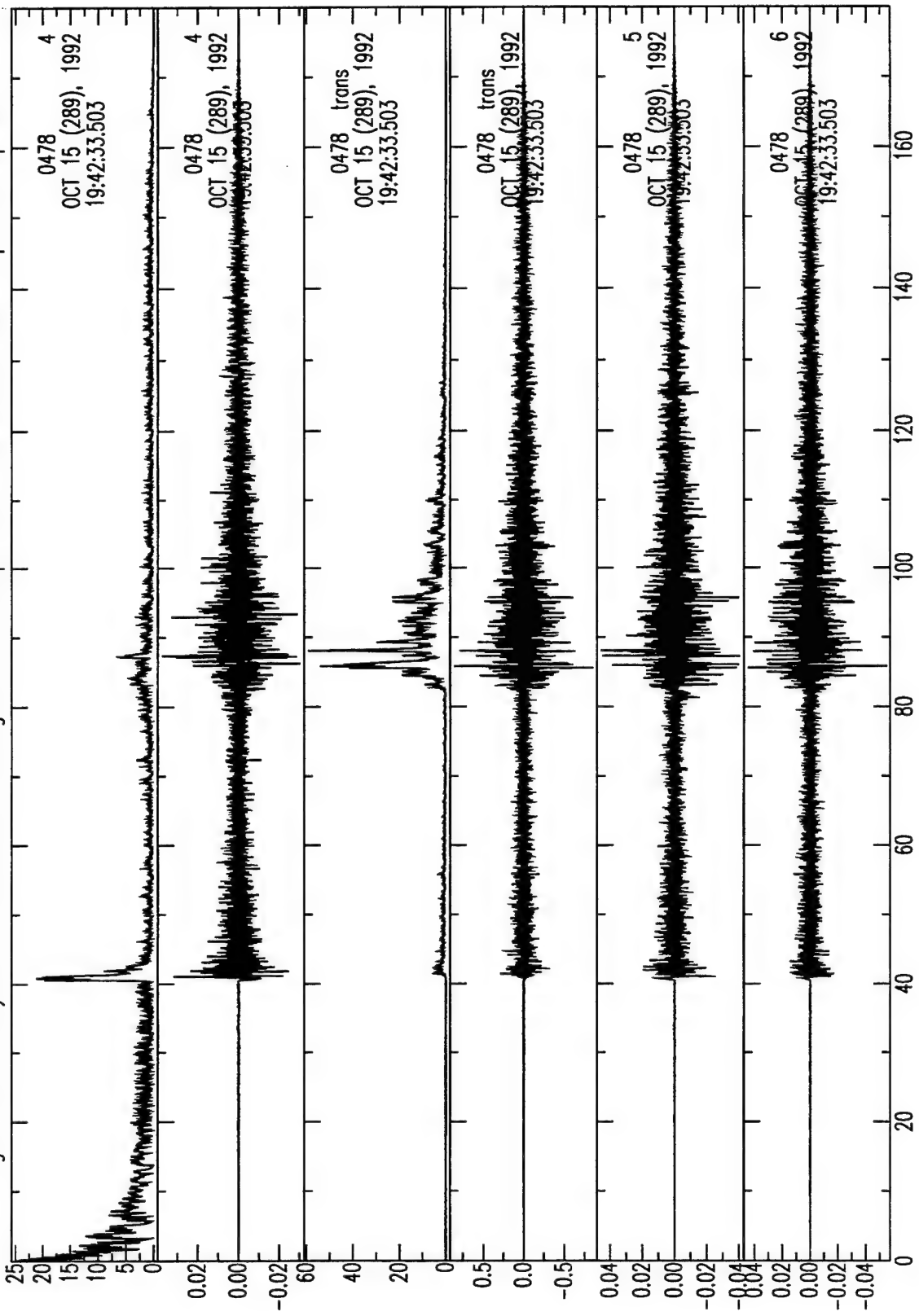


Figure A.53 Analysis of broadband seismograms for deep event 289.194227.shin

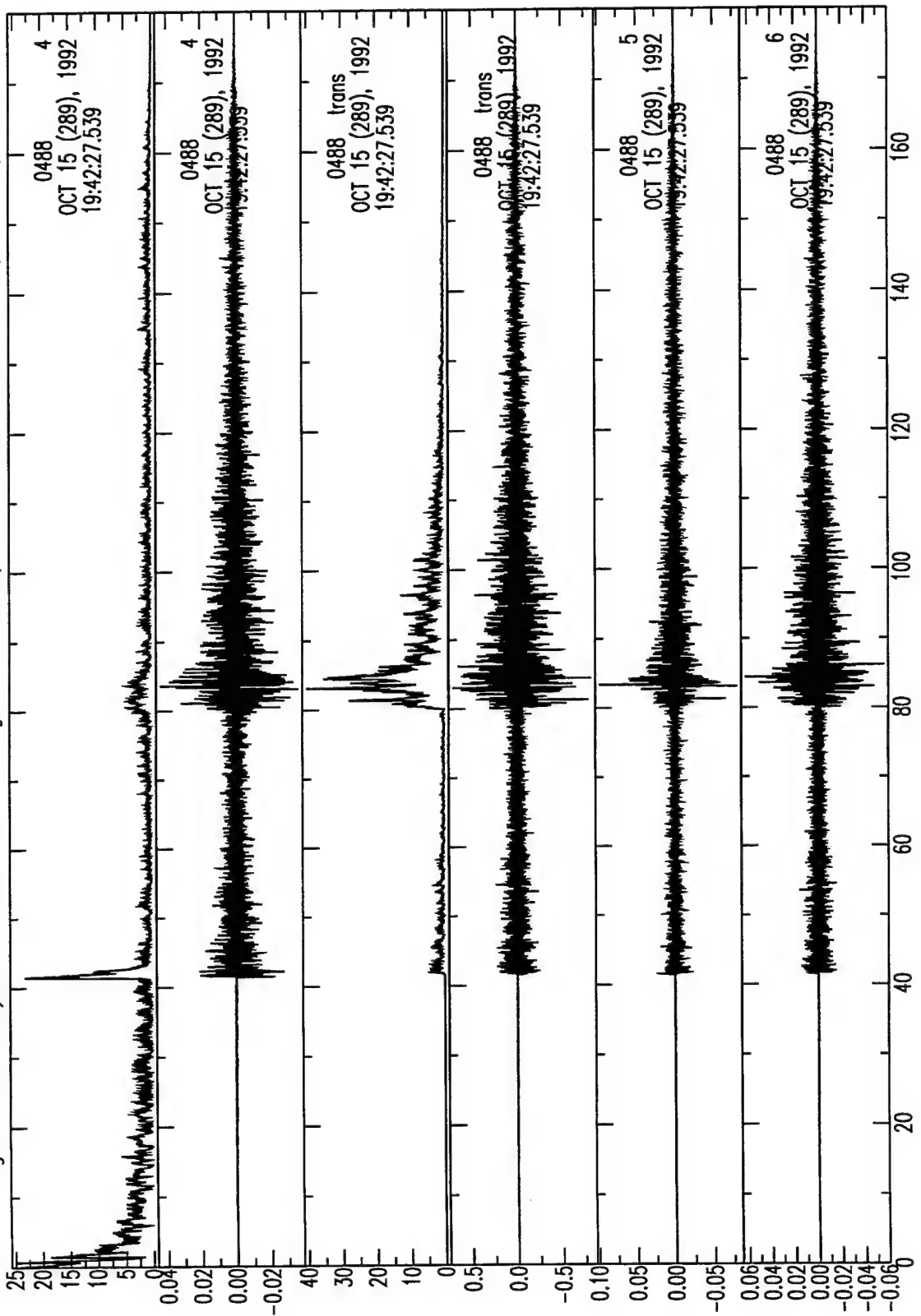


Figure A.54 Analysis of broadband seismograms for deep event 289.194229.basm

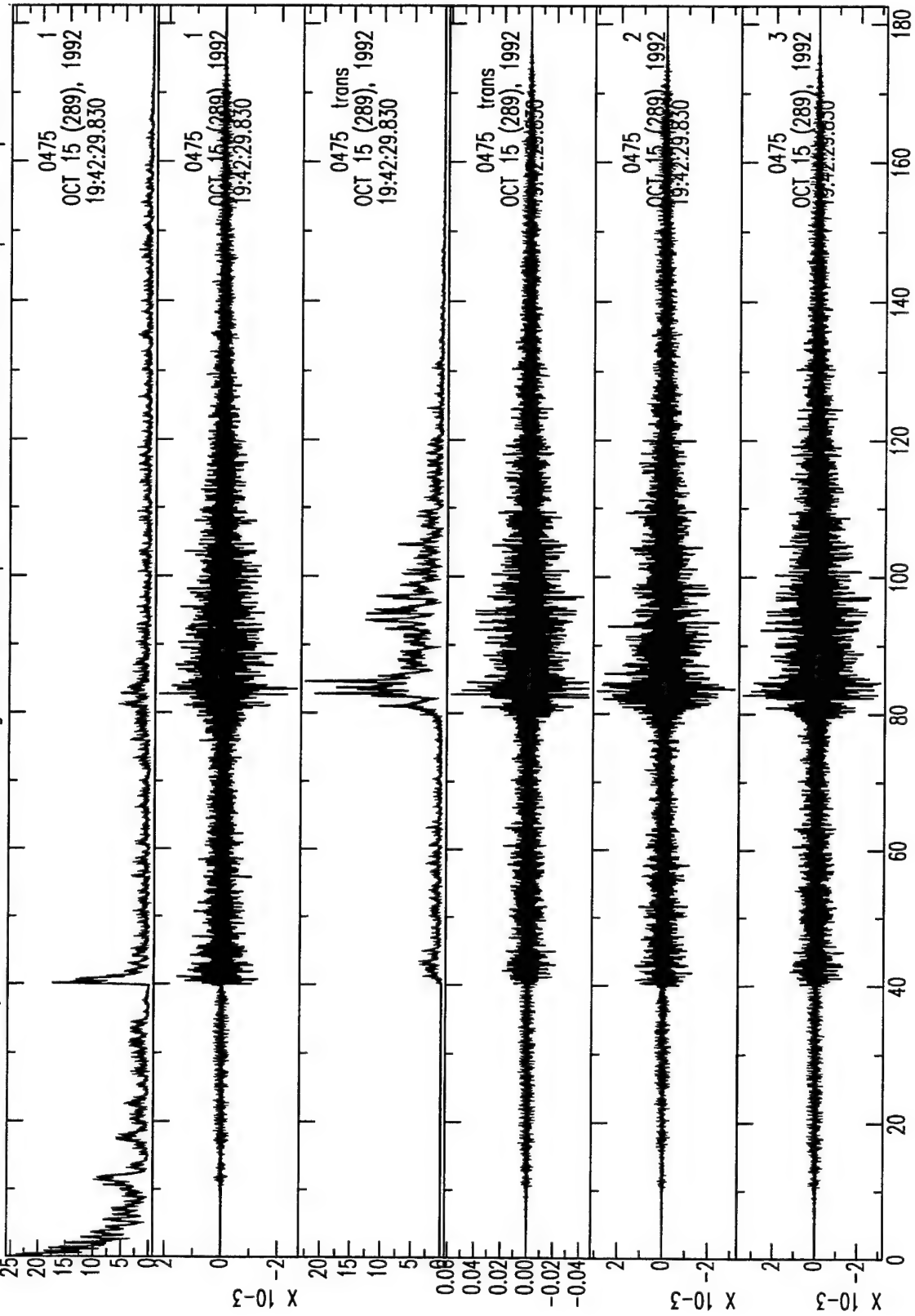


Figure A.55 Analysis of broadband seismograms for deep event 289.194230.btgm hp 1Hz lp 8Hz

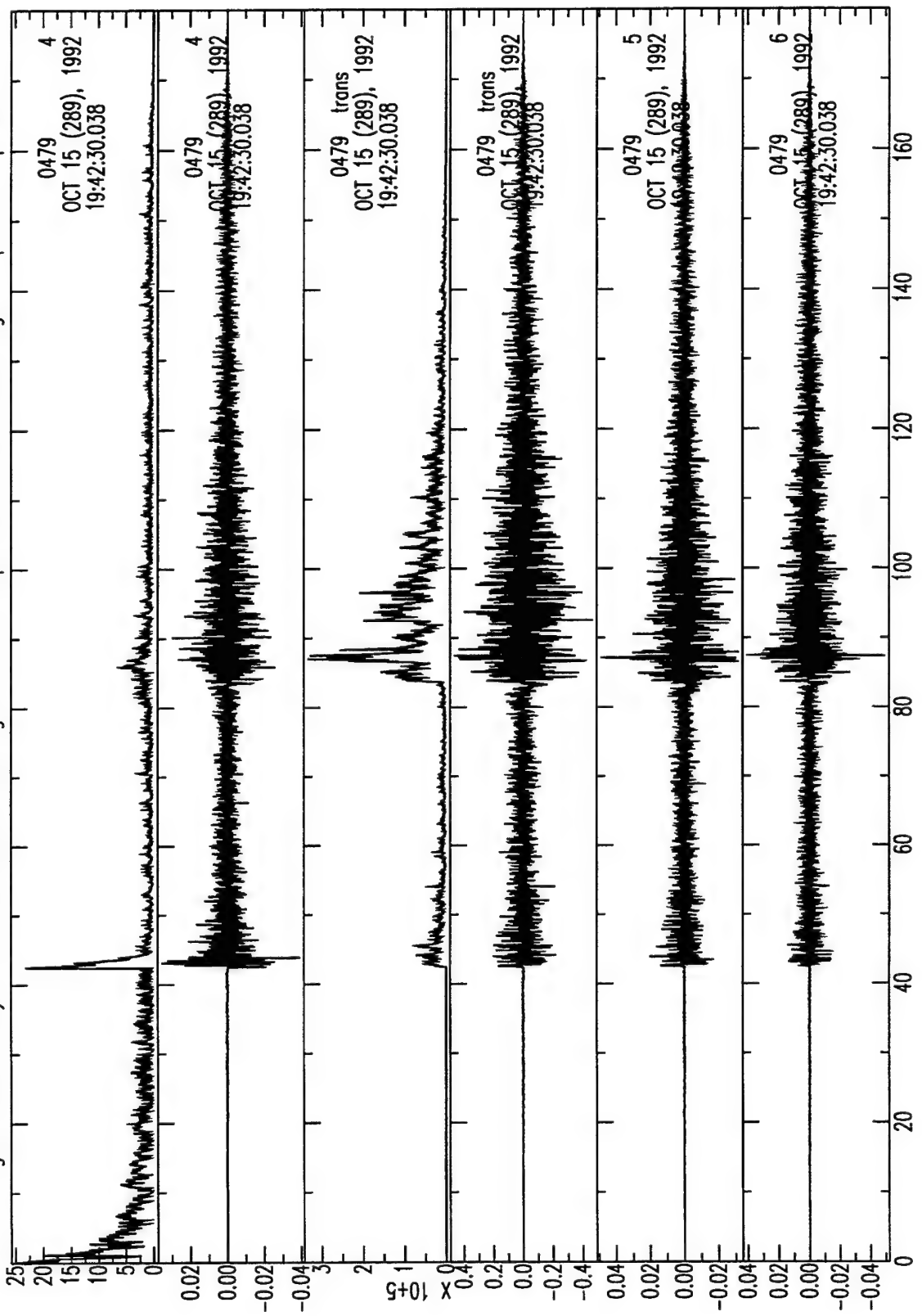


Figure A.56 Analysis of broadband seismograms for deep event 289.194230.potn

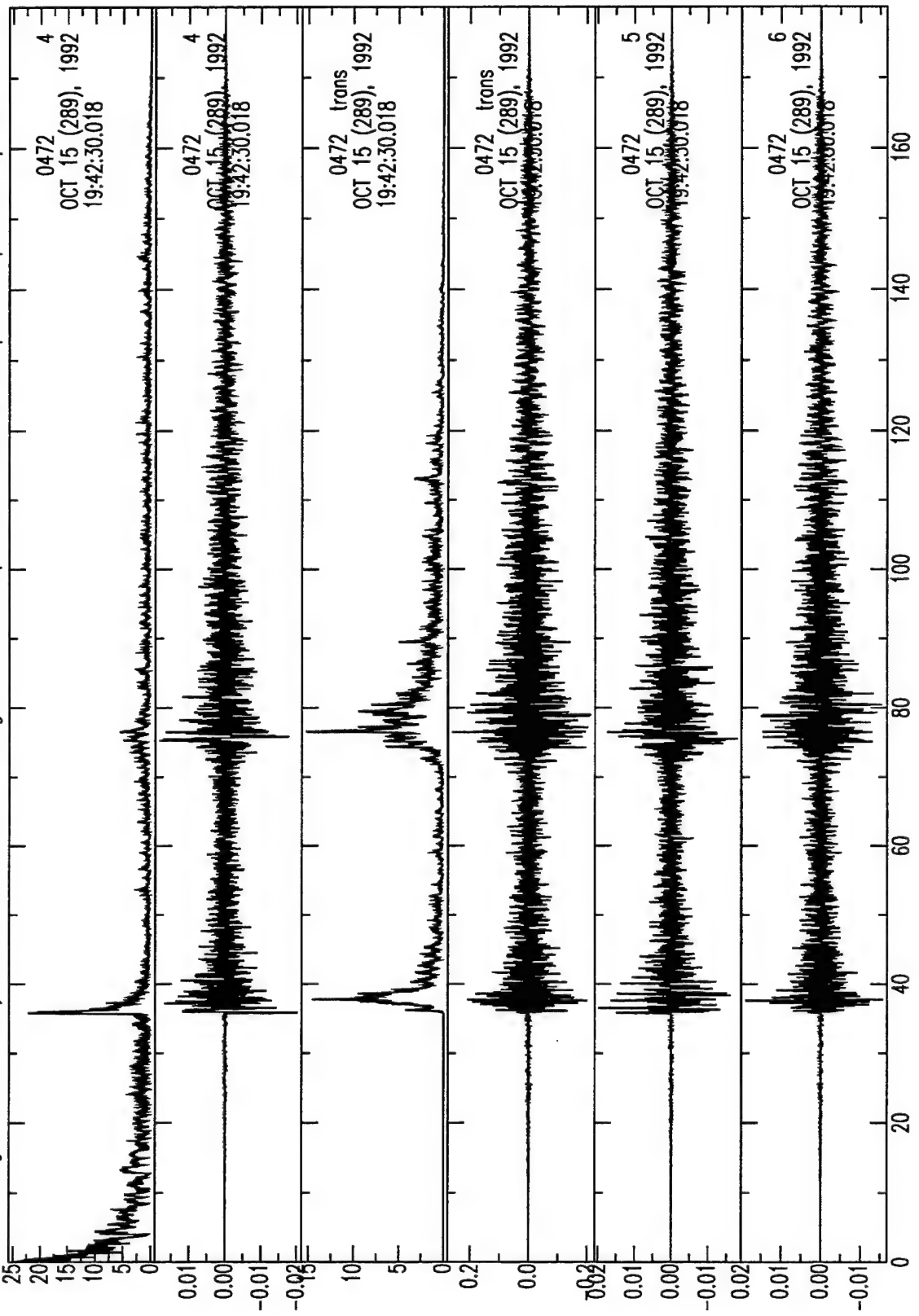
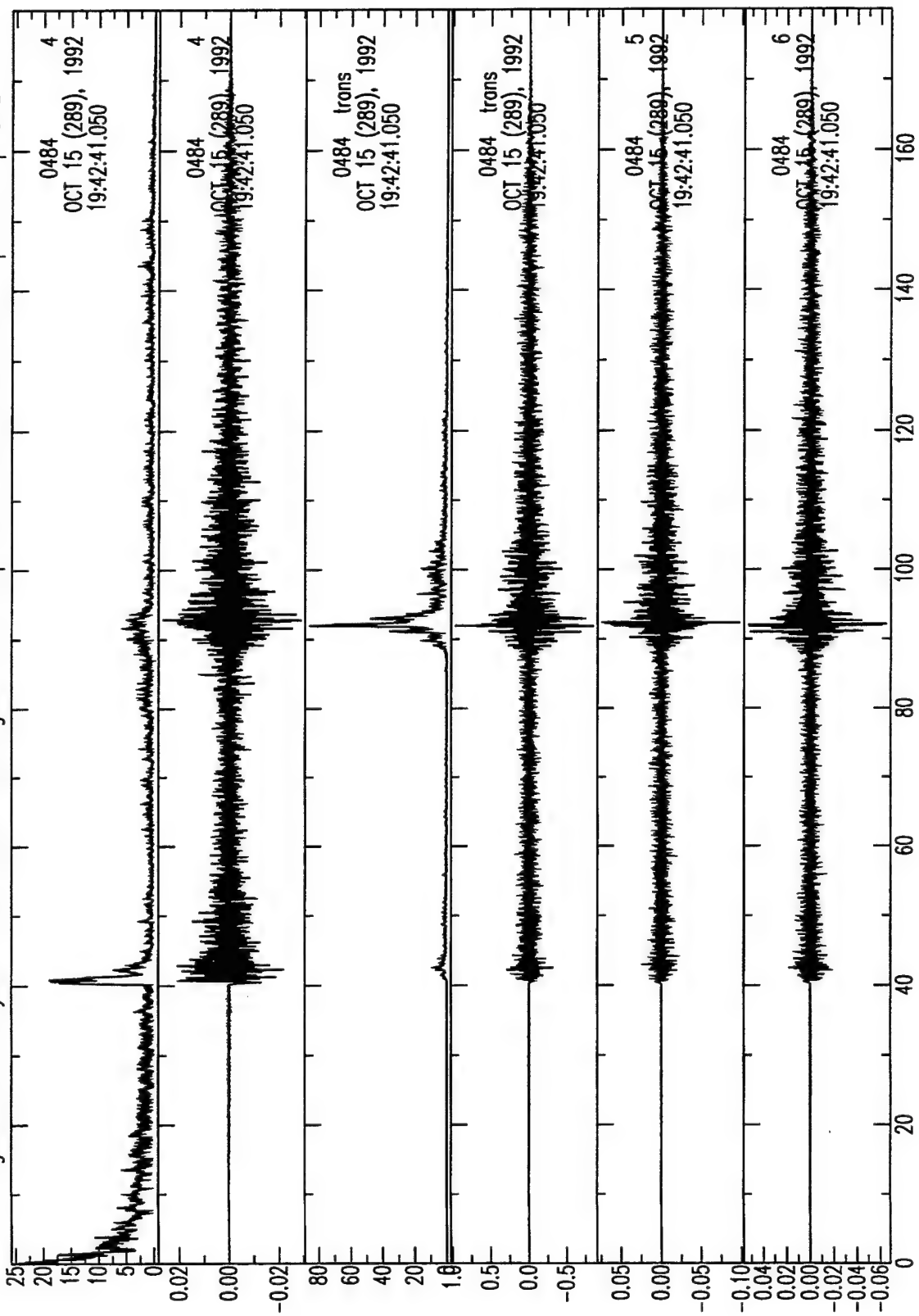


Figure A.57 Analysis of broadband seismograms for deep event 289.194231.sbra



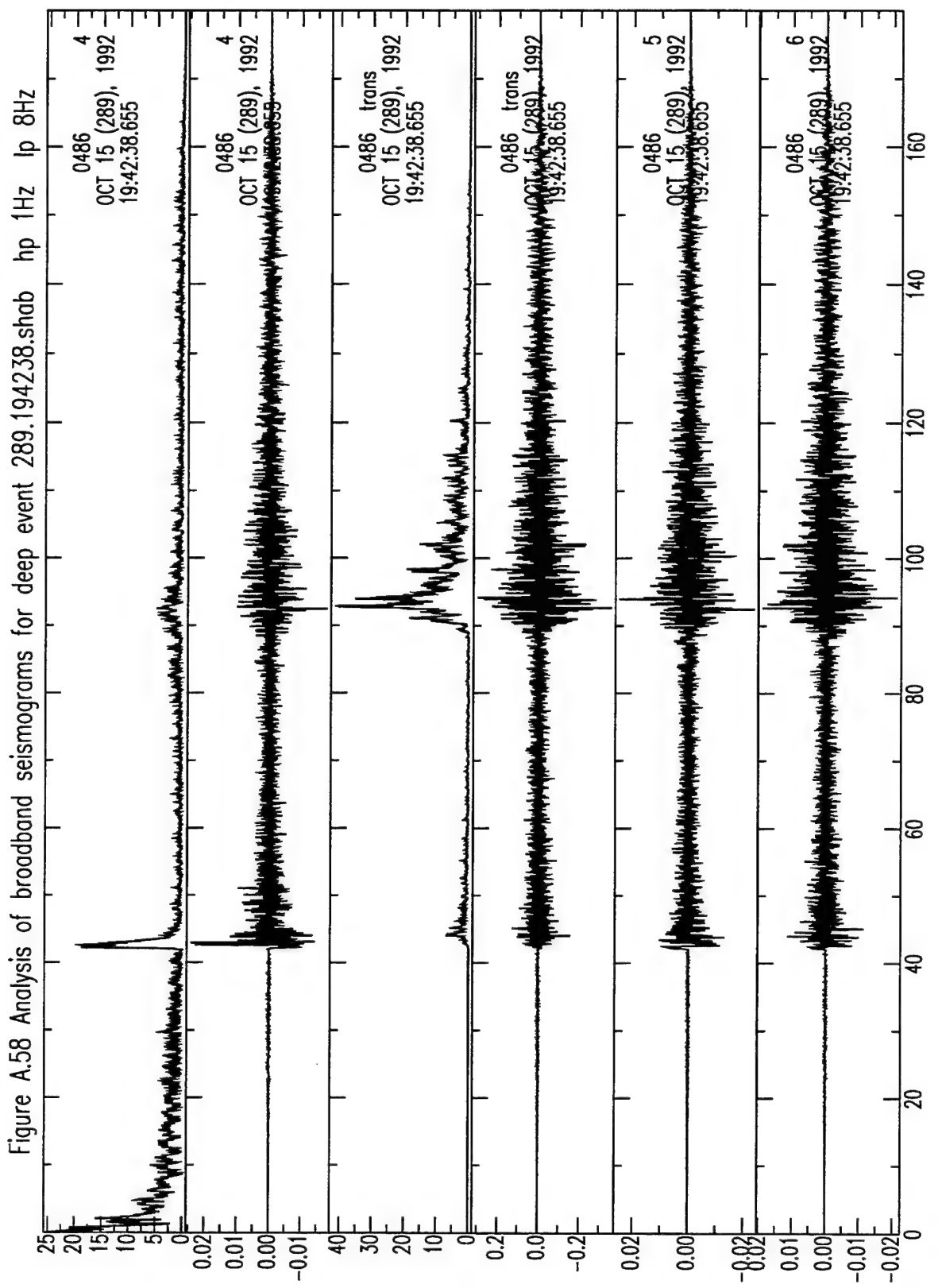
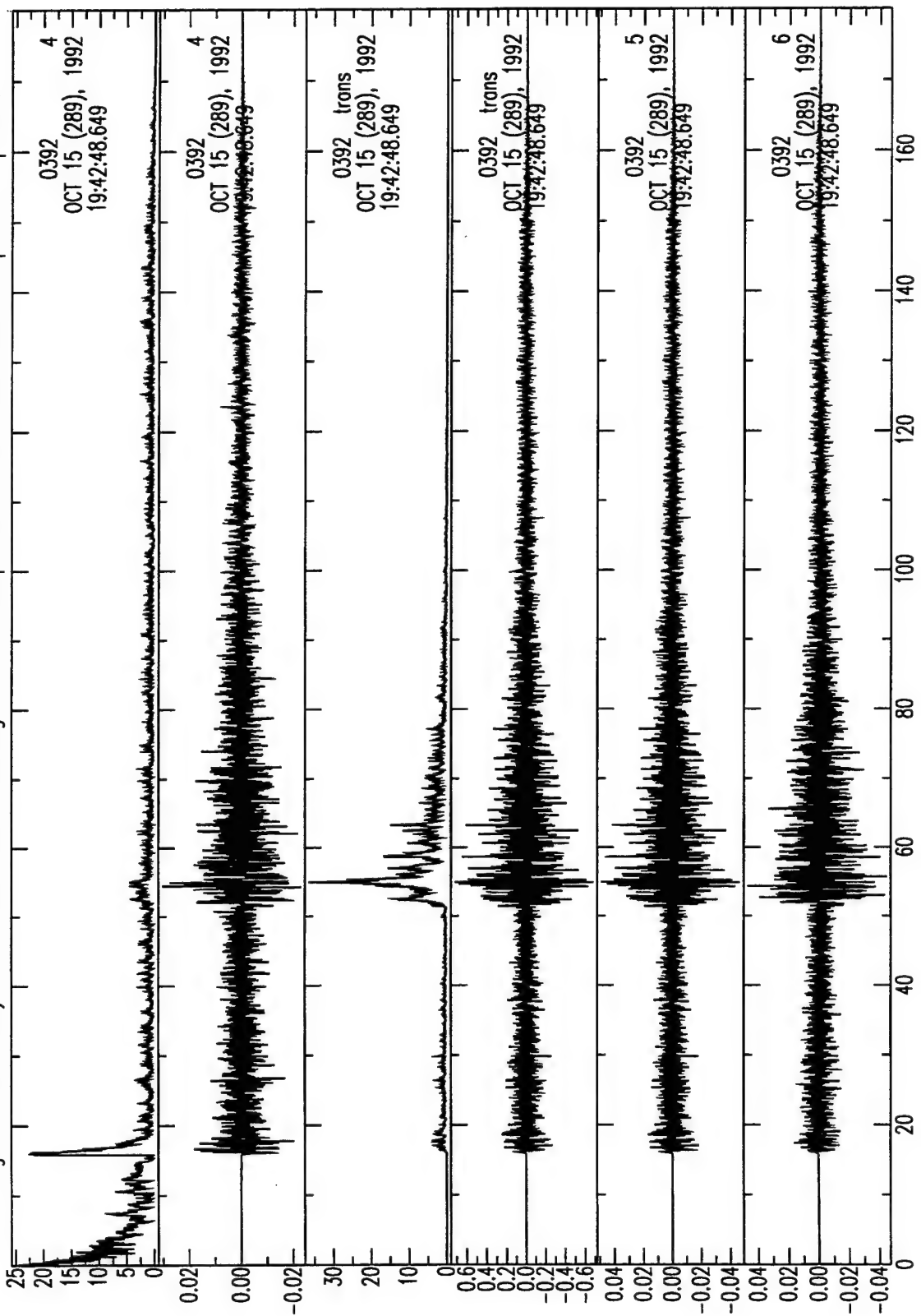


Figure A.59 Analysis of broadband seismograms for deep event 289.194248.kolm hp 1Hz lp 8Hz



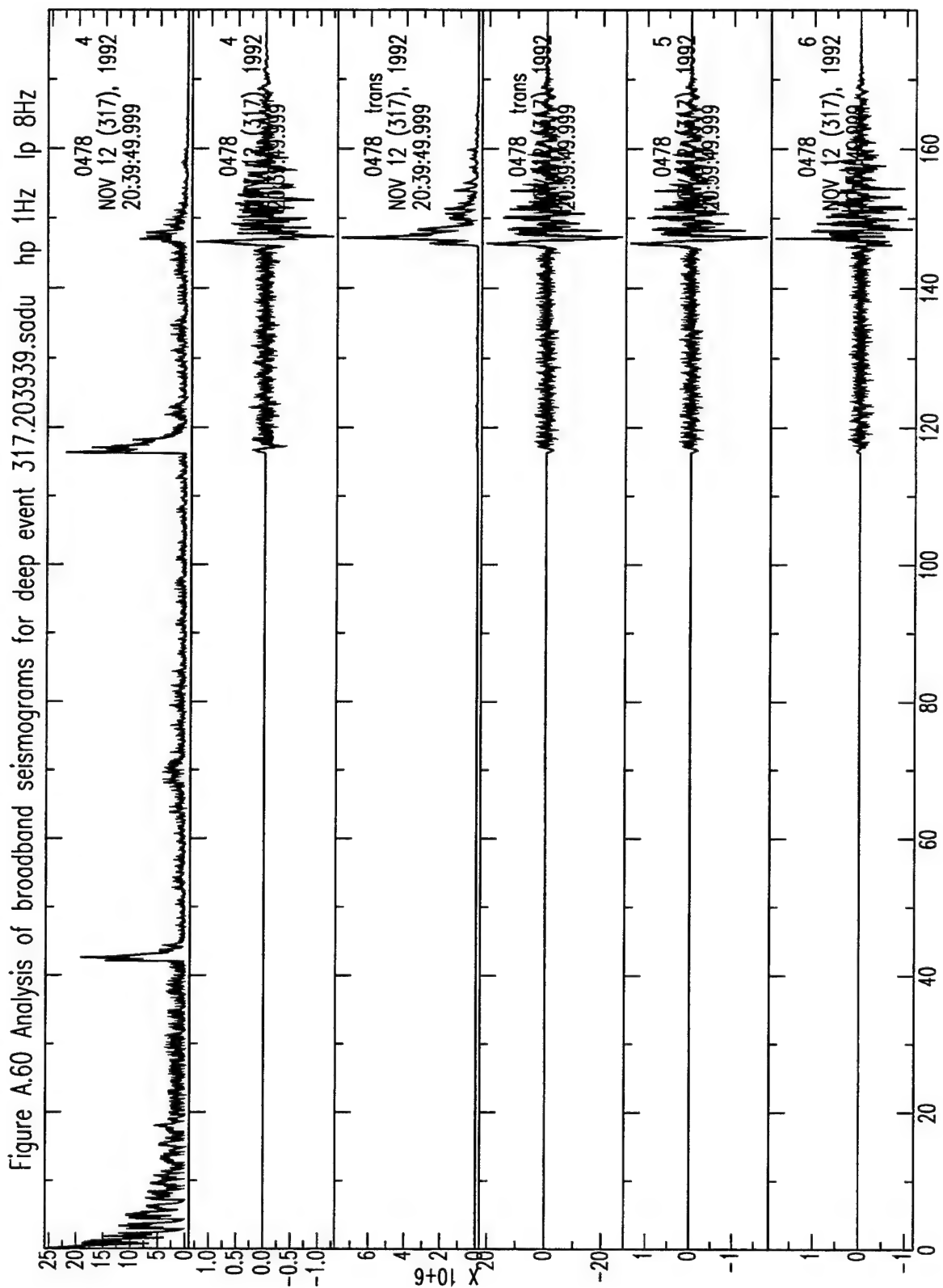
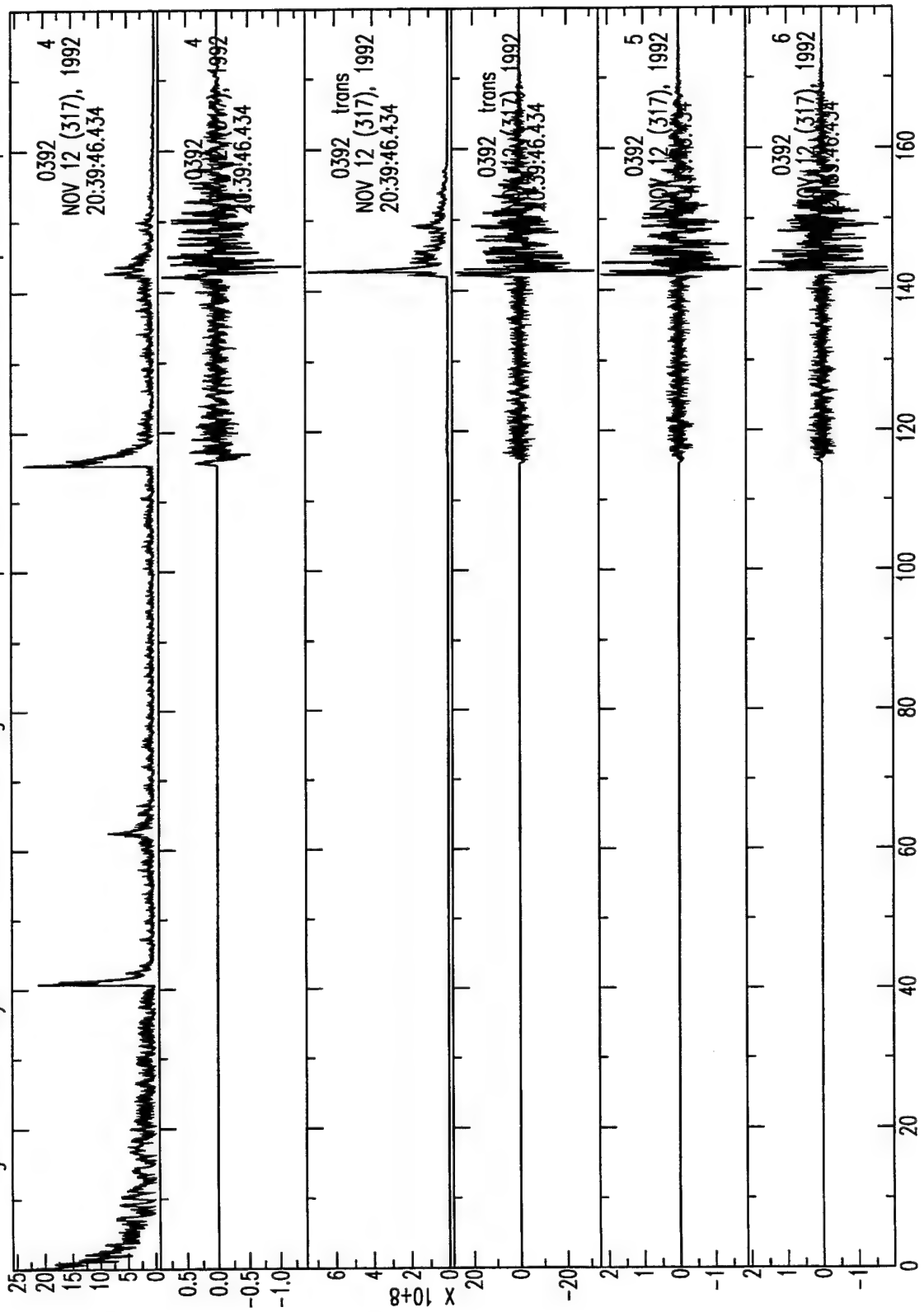


Figure A.61 Analysis of broadband seismograms for deep event 317.203946.kalm



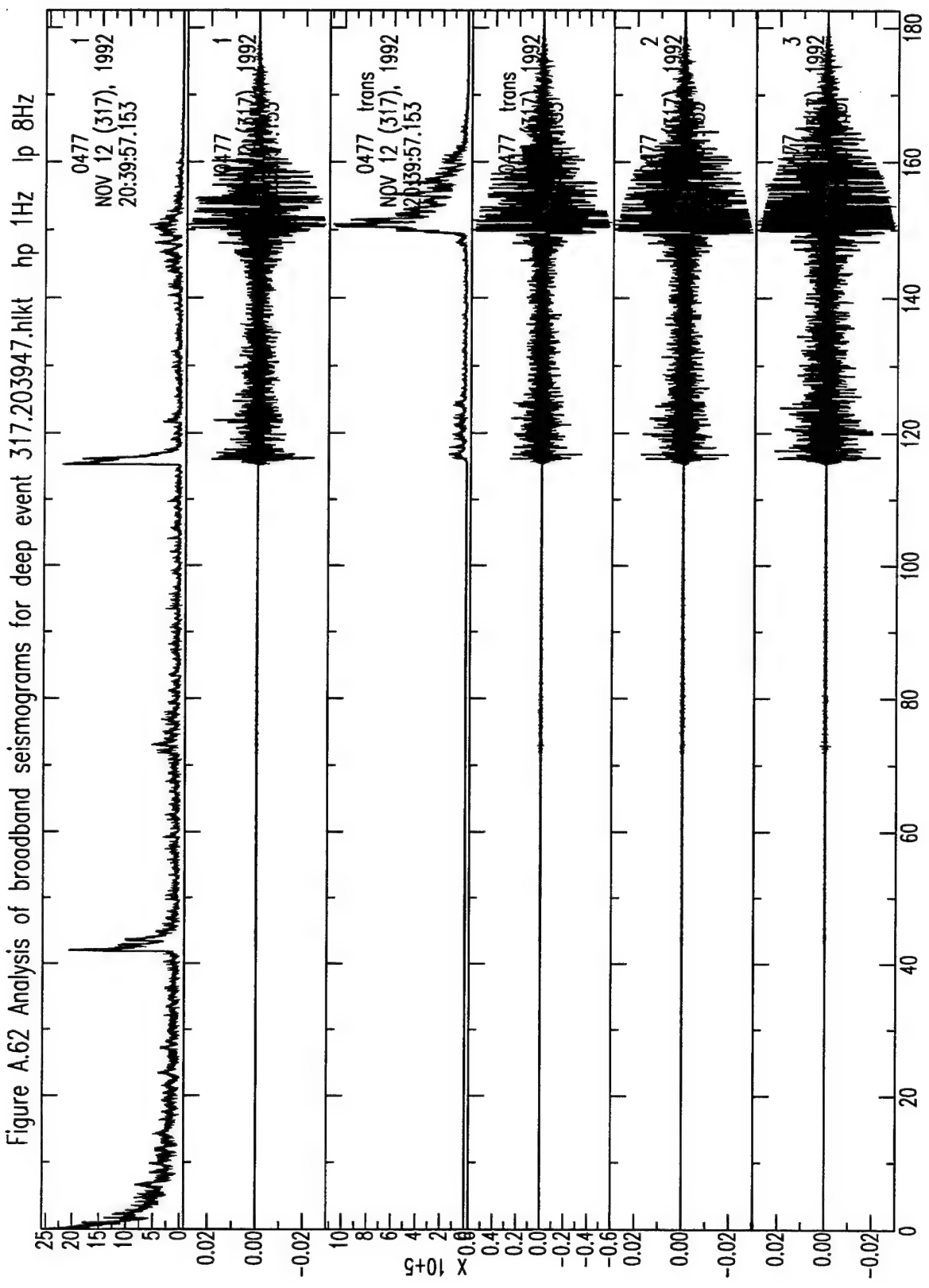


Figure A.63 Analysis of broadband seismograms for deep event 317.203947.shin

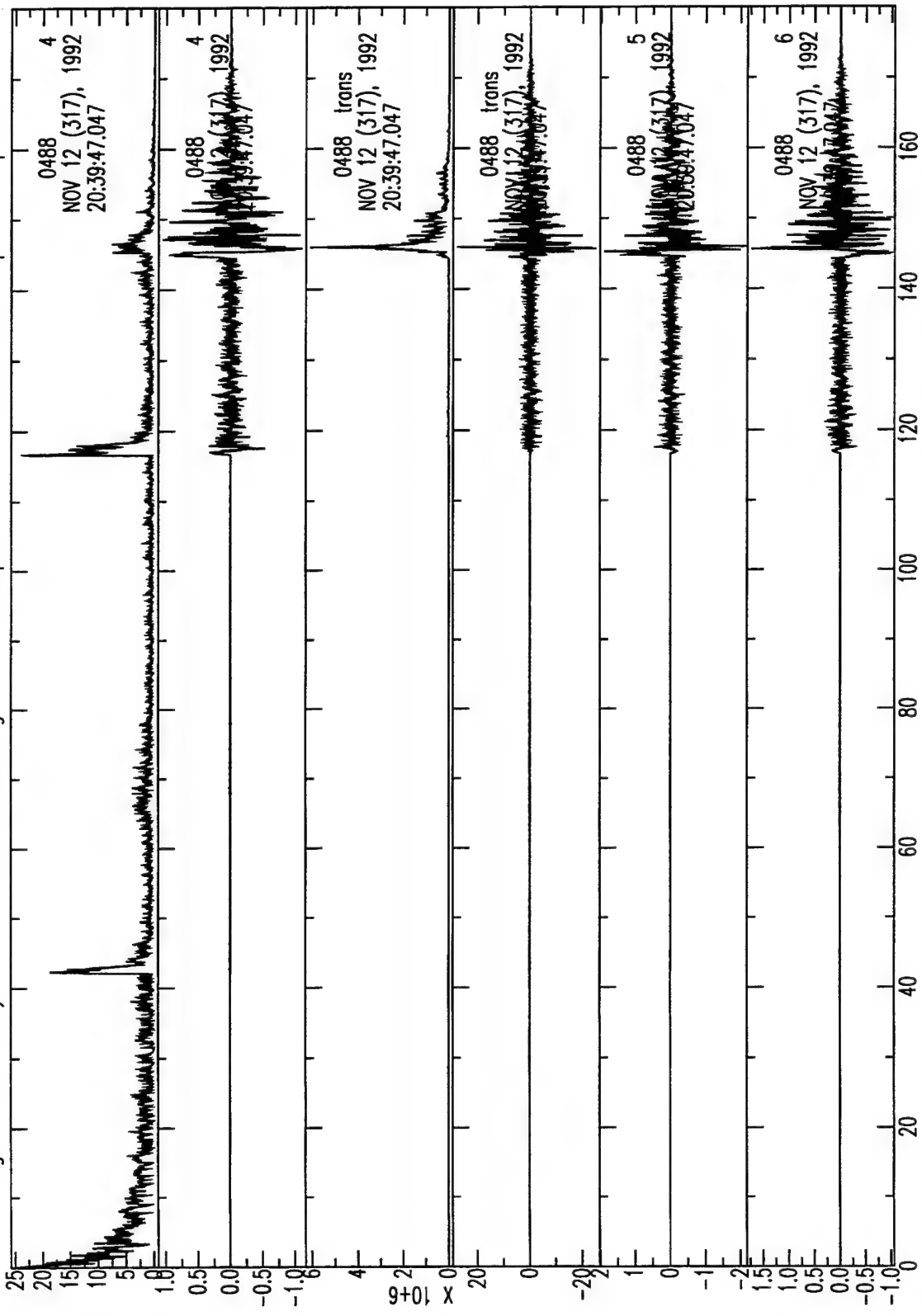


Figure A.64 Analysis of broadband seismograms for deep event 317.203951.patn

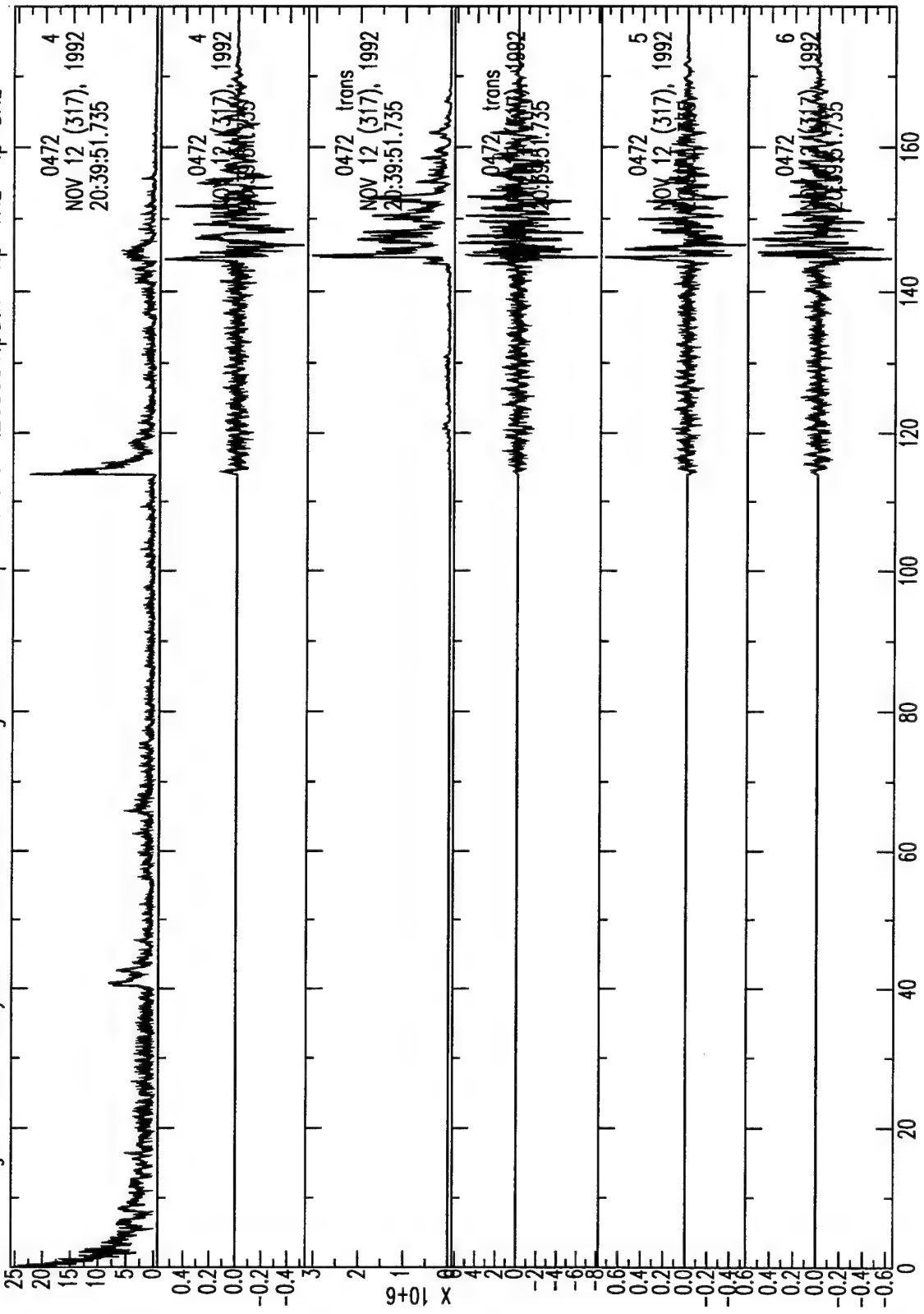
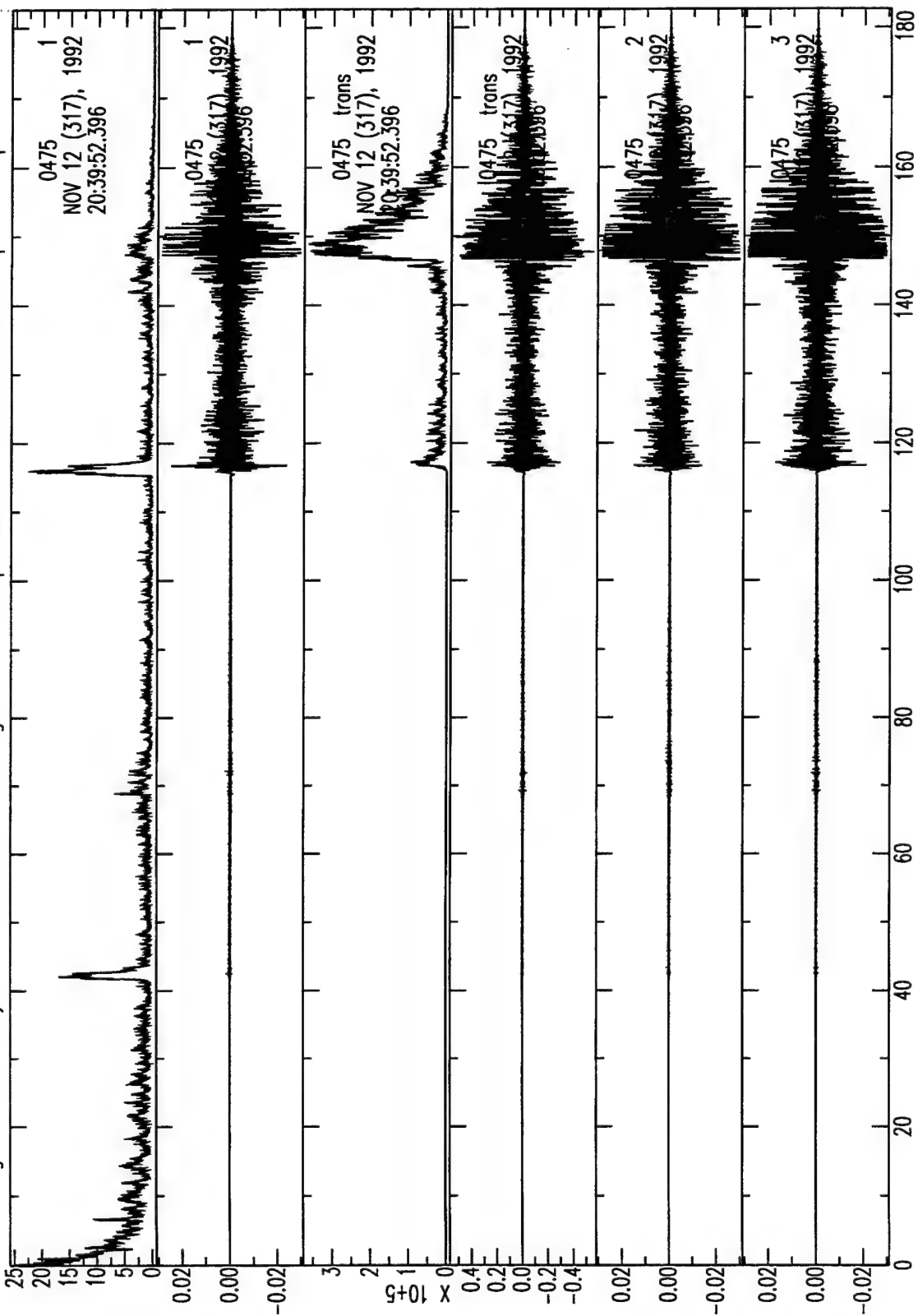


Figure A.65 Analysis of broadband seismograms for deep event 317.203952.bosm



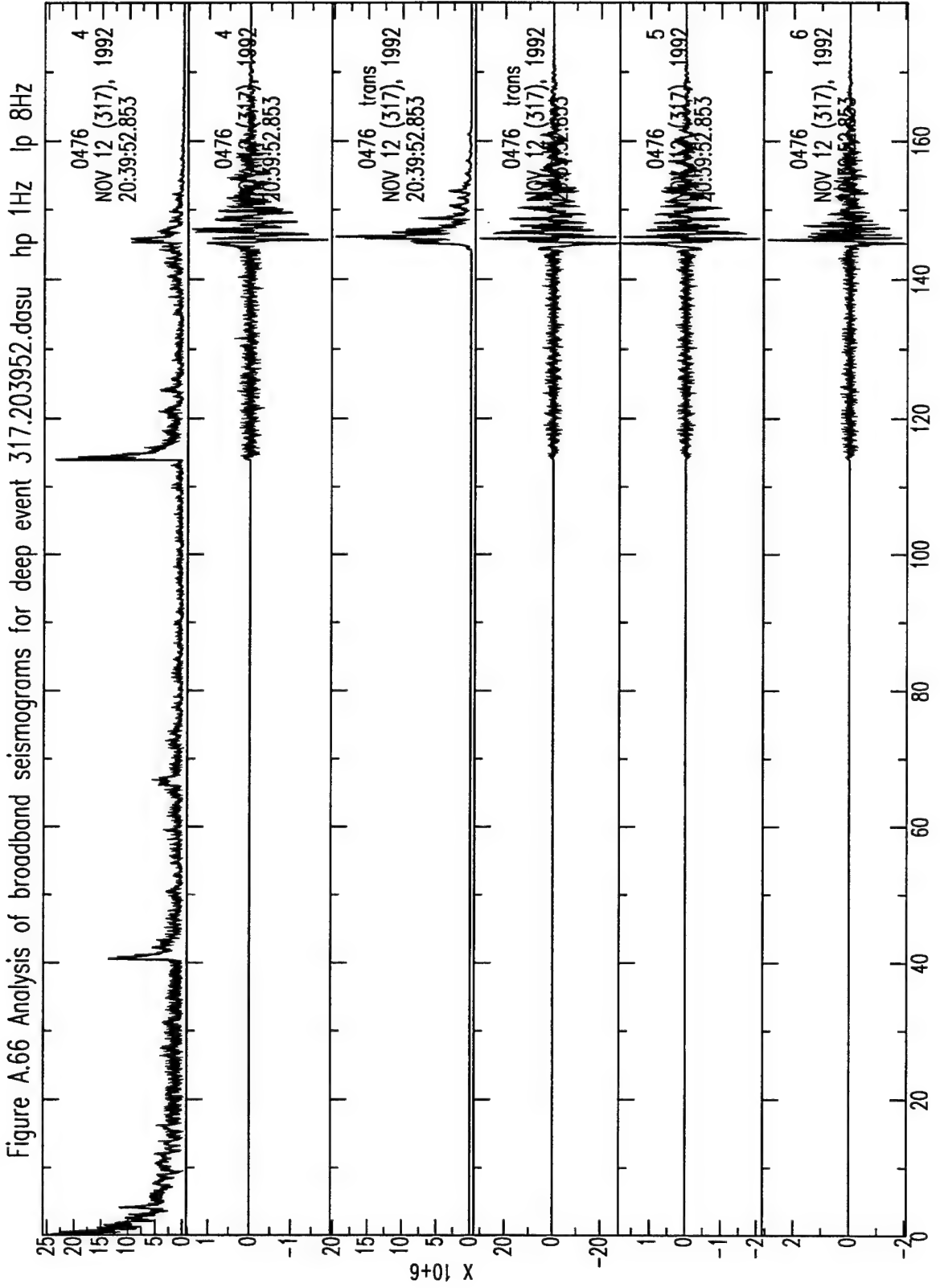
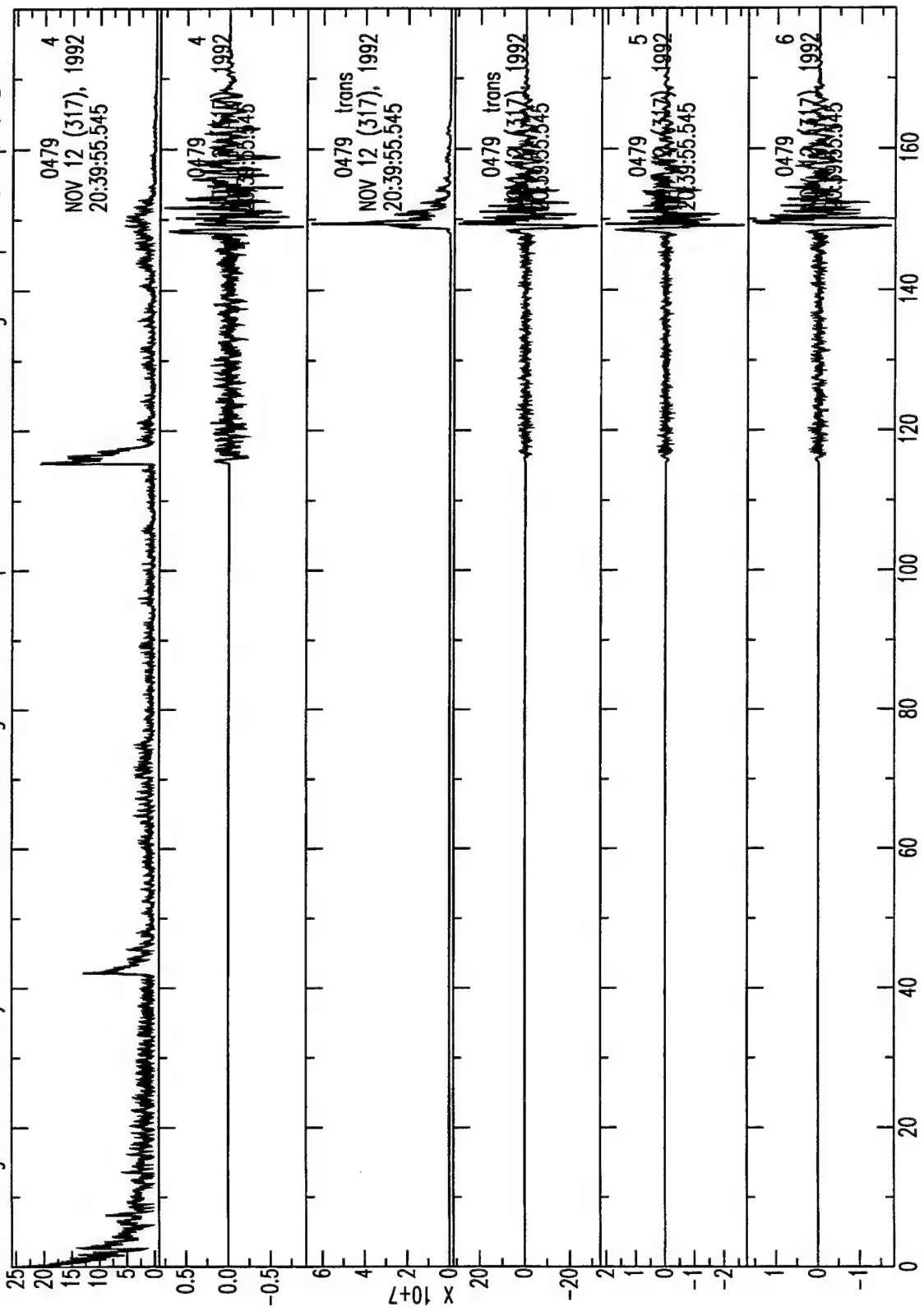


Figure A.67 Analysis of broadband seismograms for deep event 317.203955.btlgm



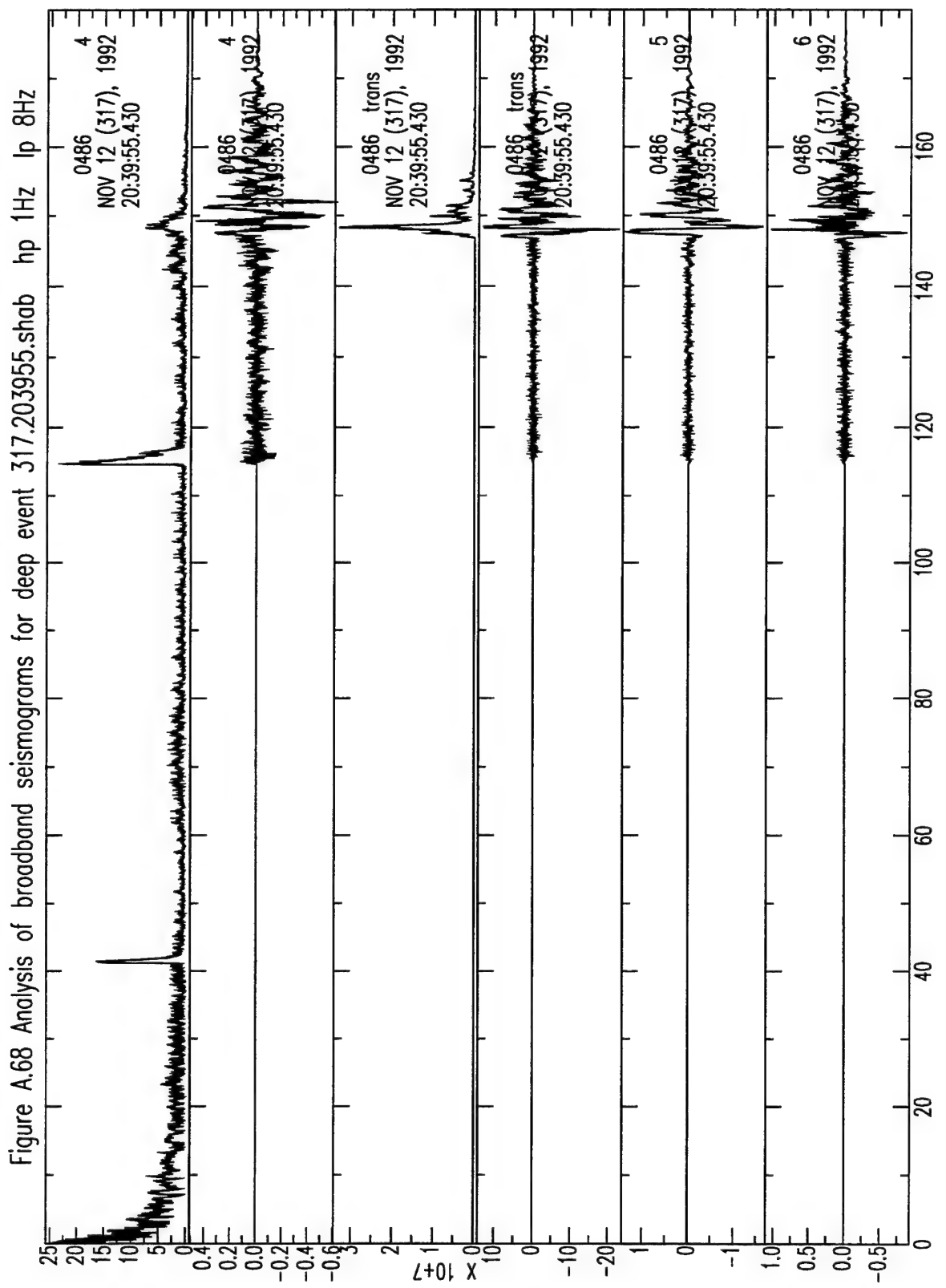


Figure A.69 Analysis of broadband seismograms for deep event 317.204104.sbra

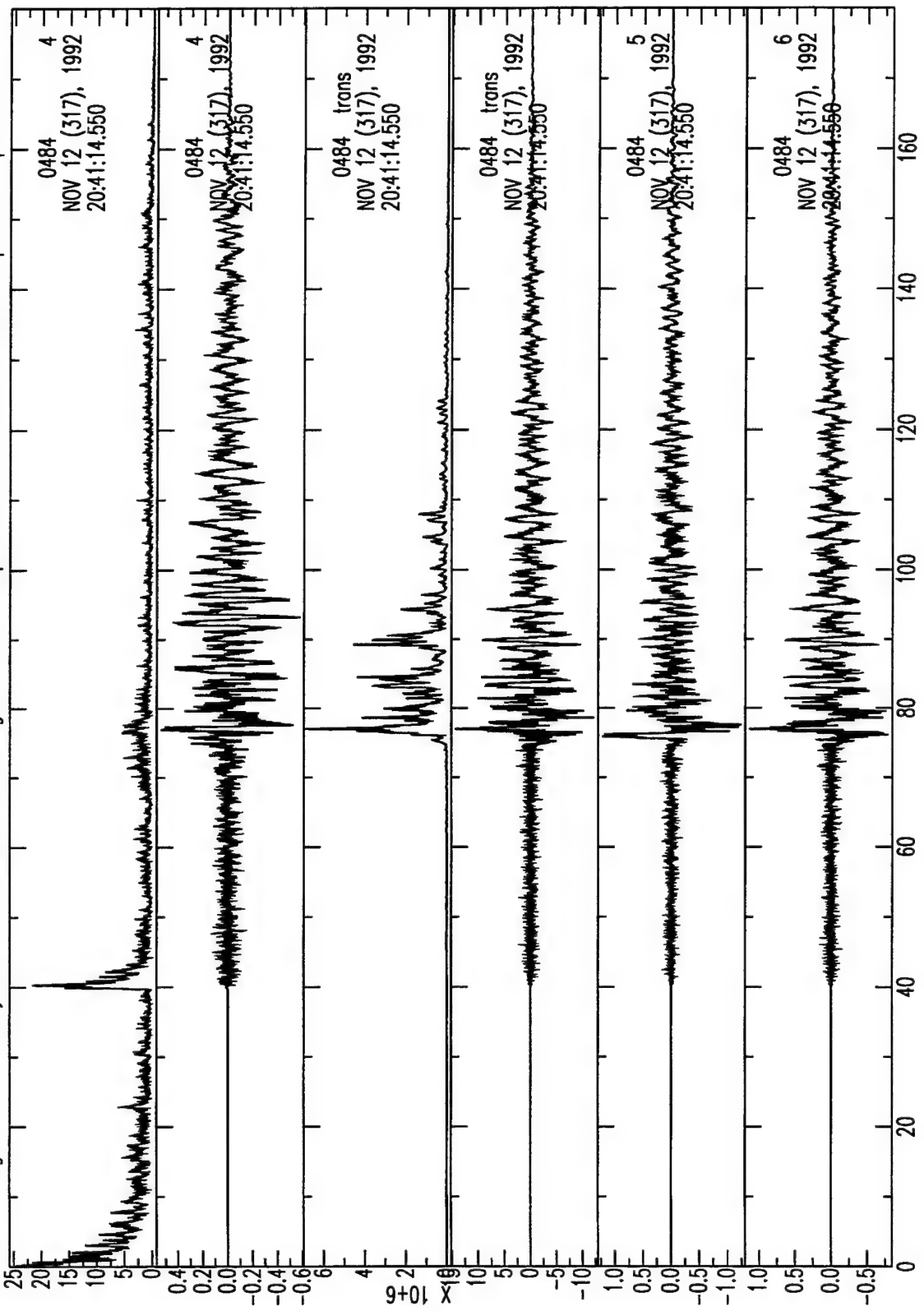


Figure A.70 Analysis of broadband seismograms for deep event 339.113633.sadu

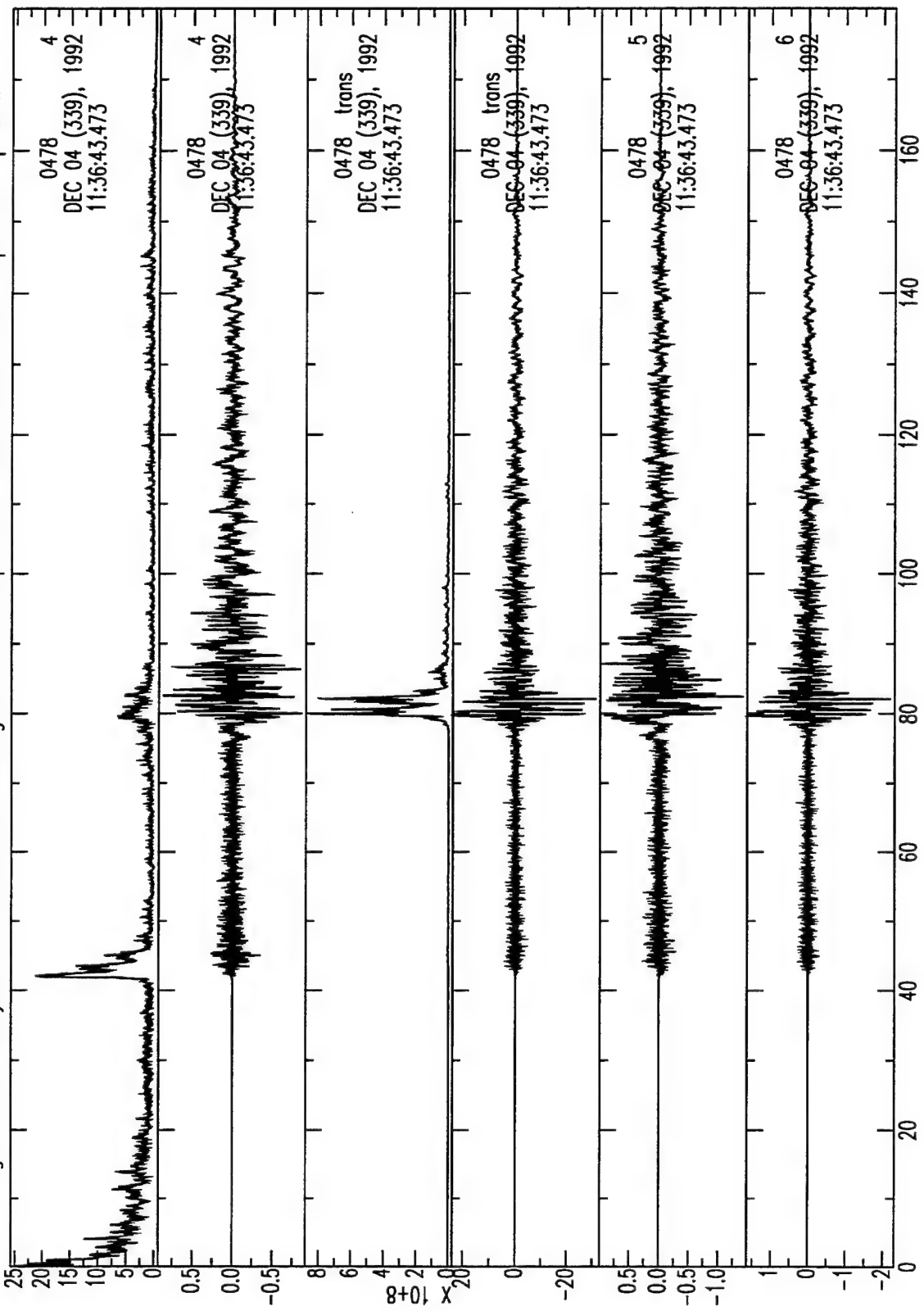
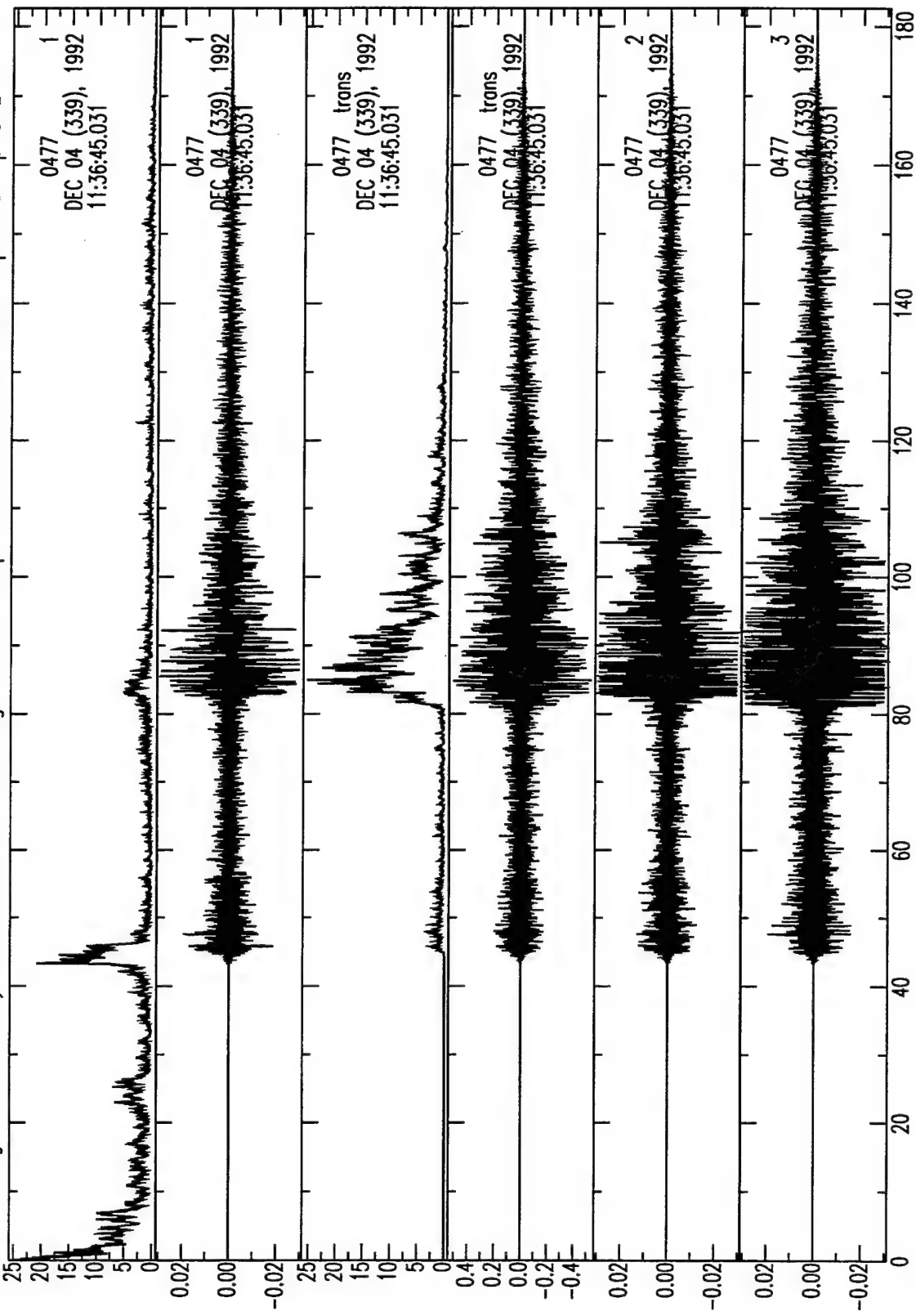


Figure A.71 Analysis of broadband seismograms for deep event 339.113635.hklt hp 1Hz lp 8Hz



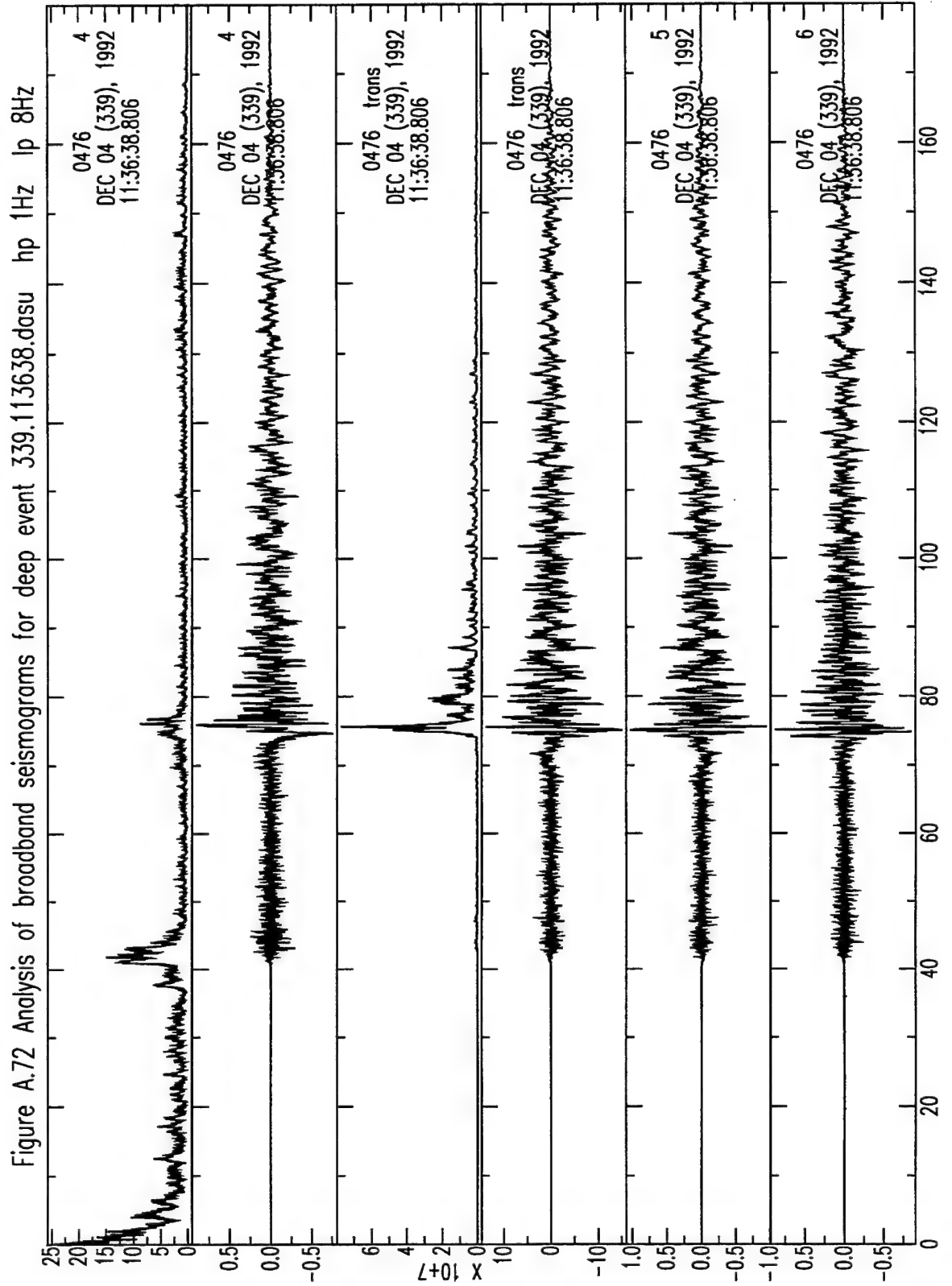


Figure A.73 Analysis of broadband seismograms for deep event 339.113638.patn

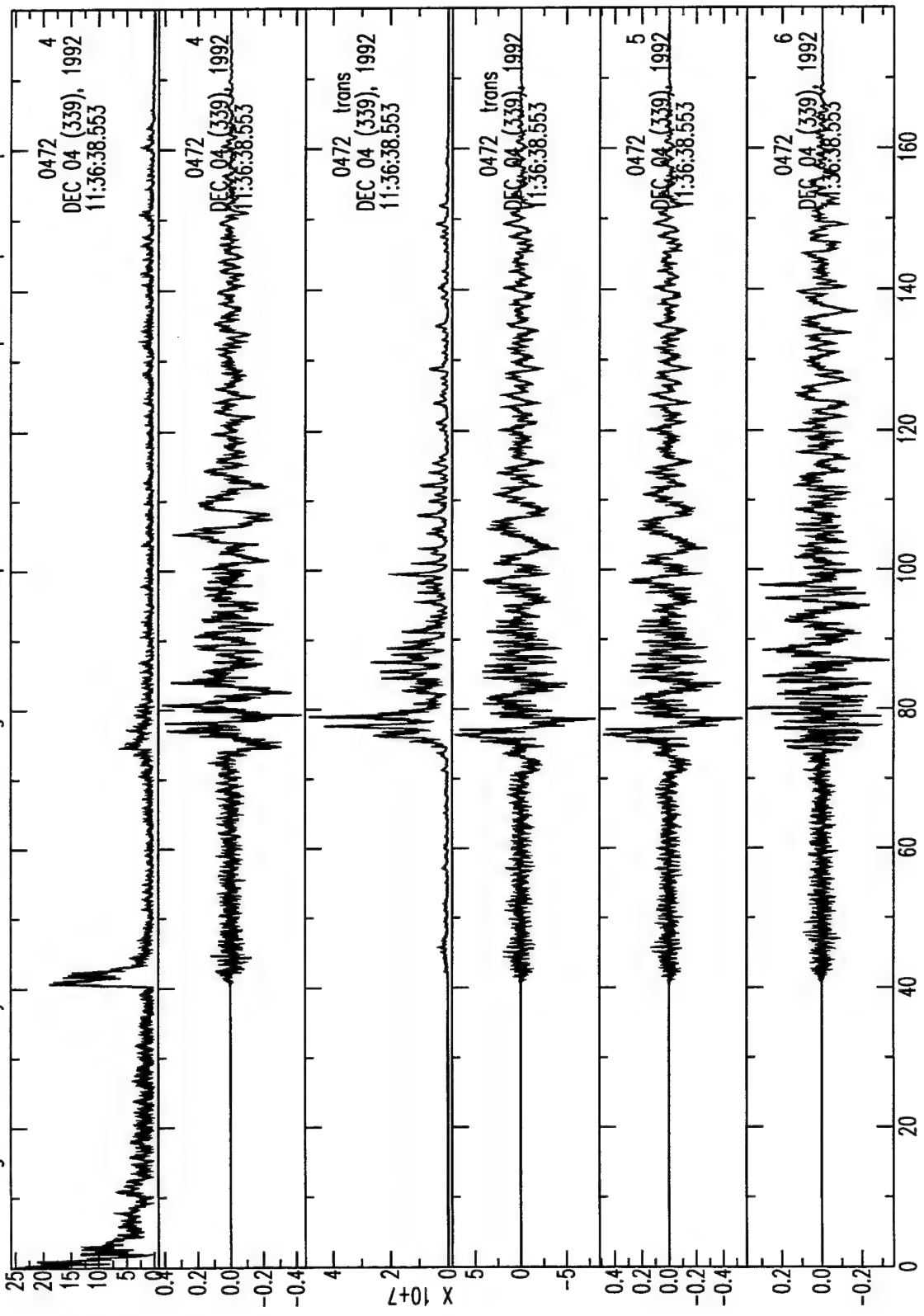


Figure A.74 Analysis of broadband seismograms for deep event 339.113640.shin

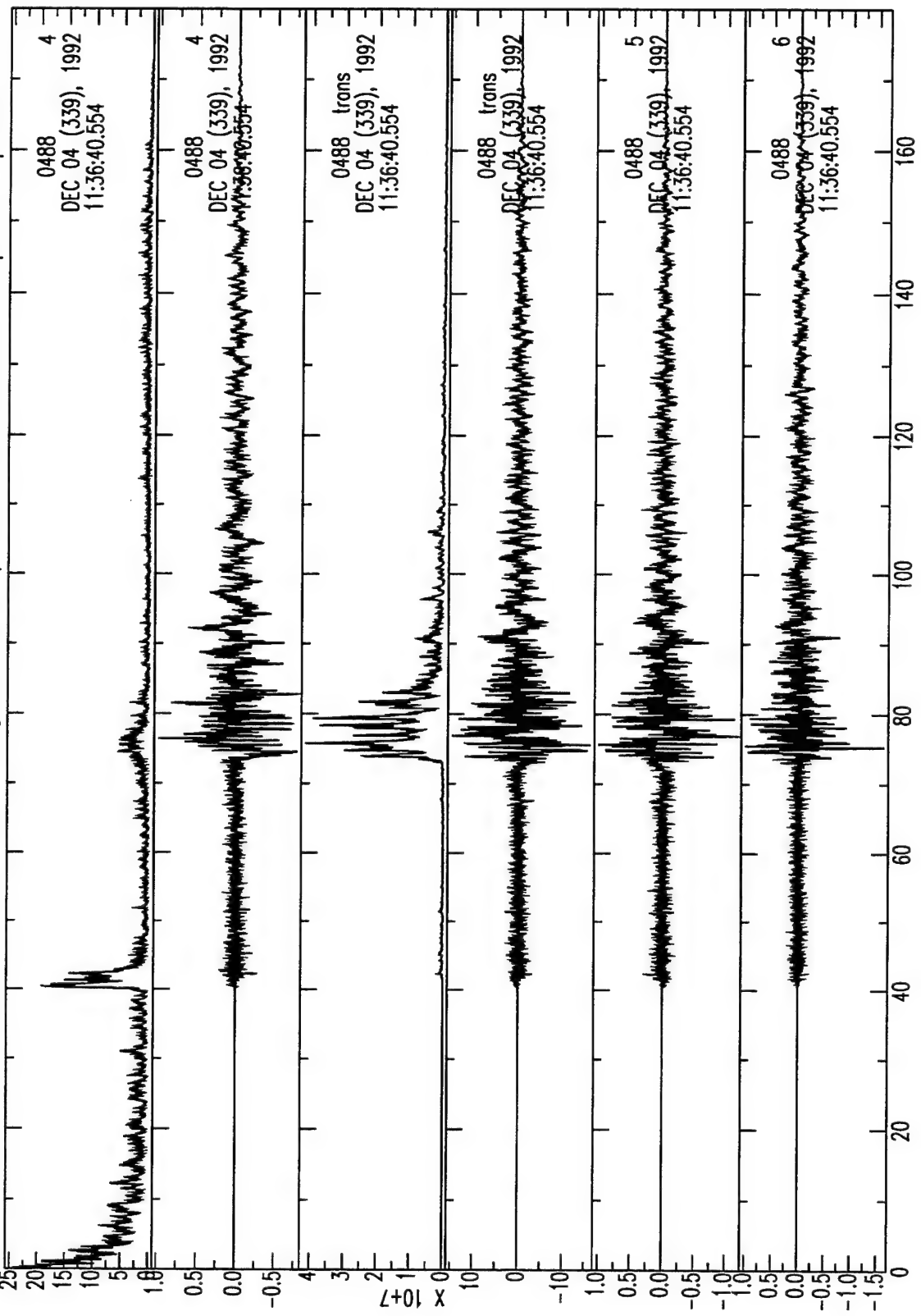
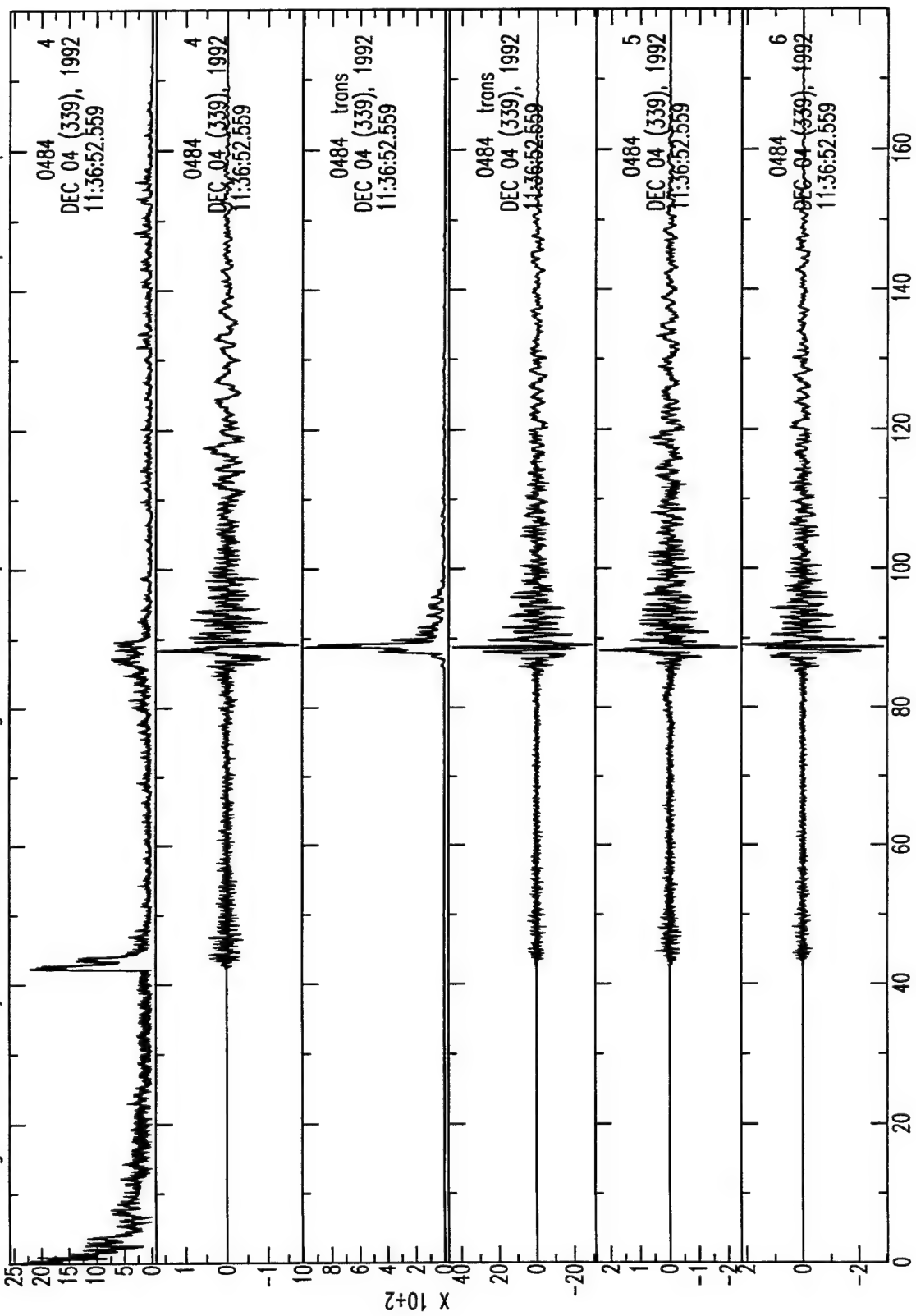


Figure A.75 Analysis of broadband seismograms for deep event 339.113642.sbra



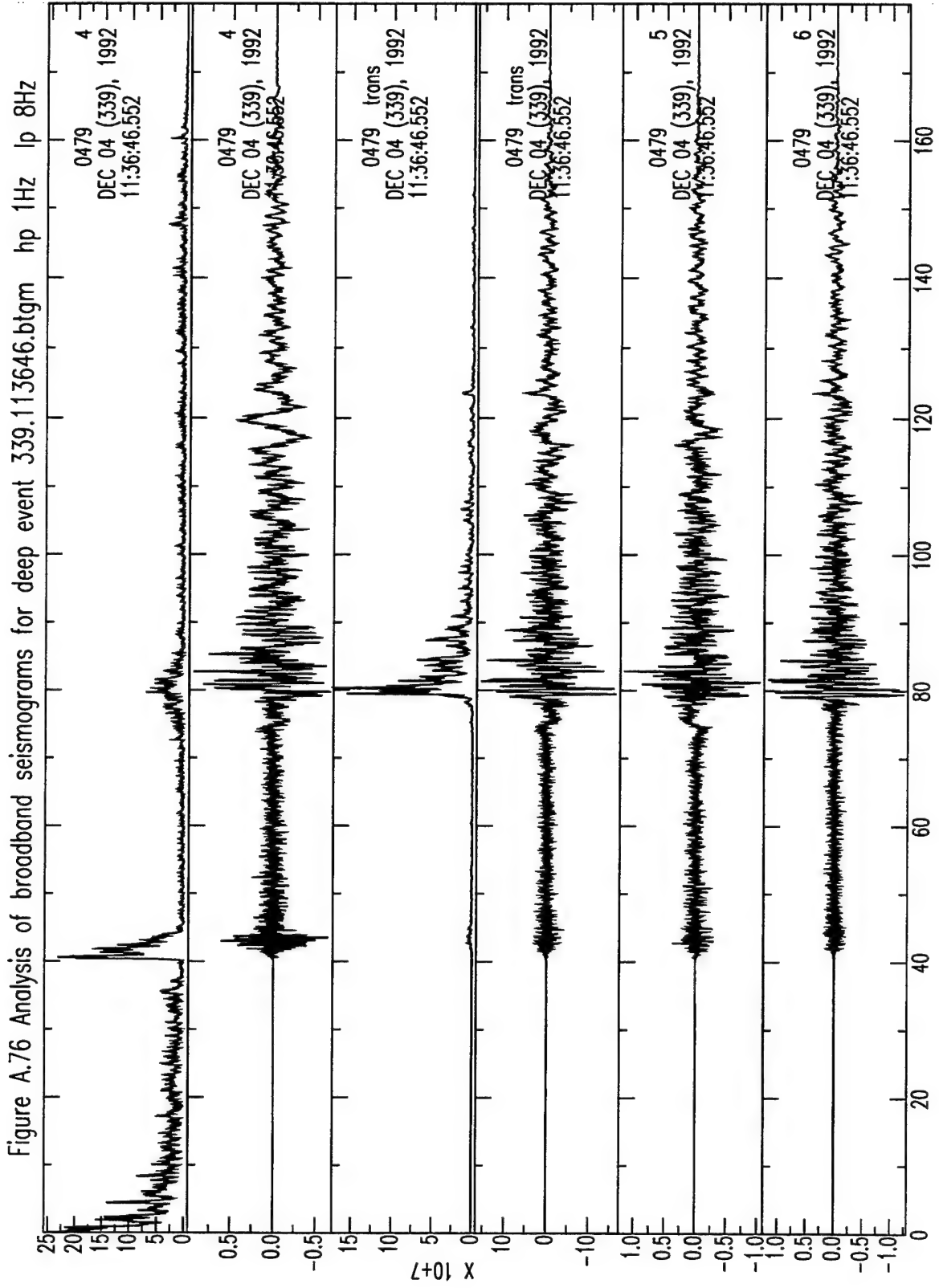


Figure A.77 Analysis of broadband seismograms for deep event 339.113706.basm

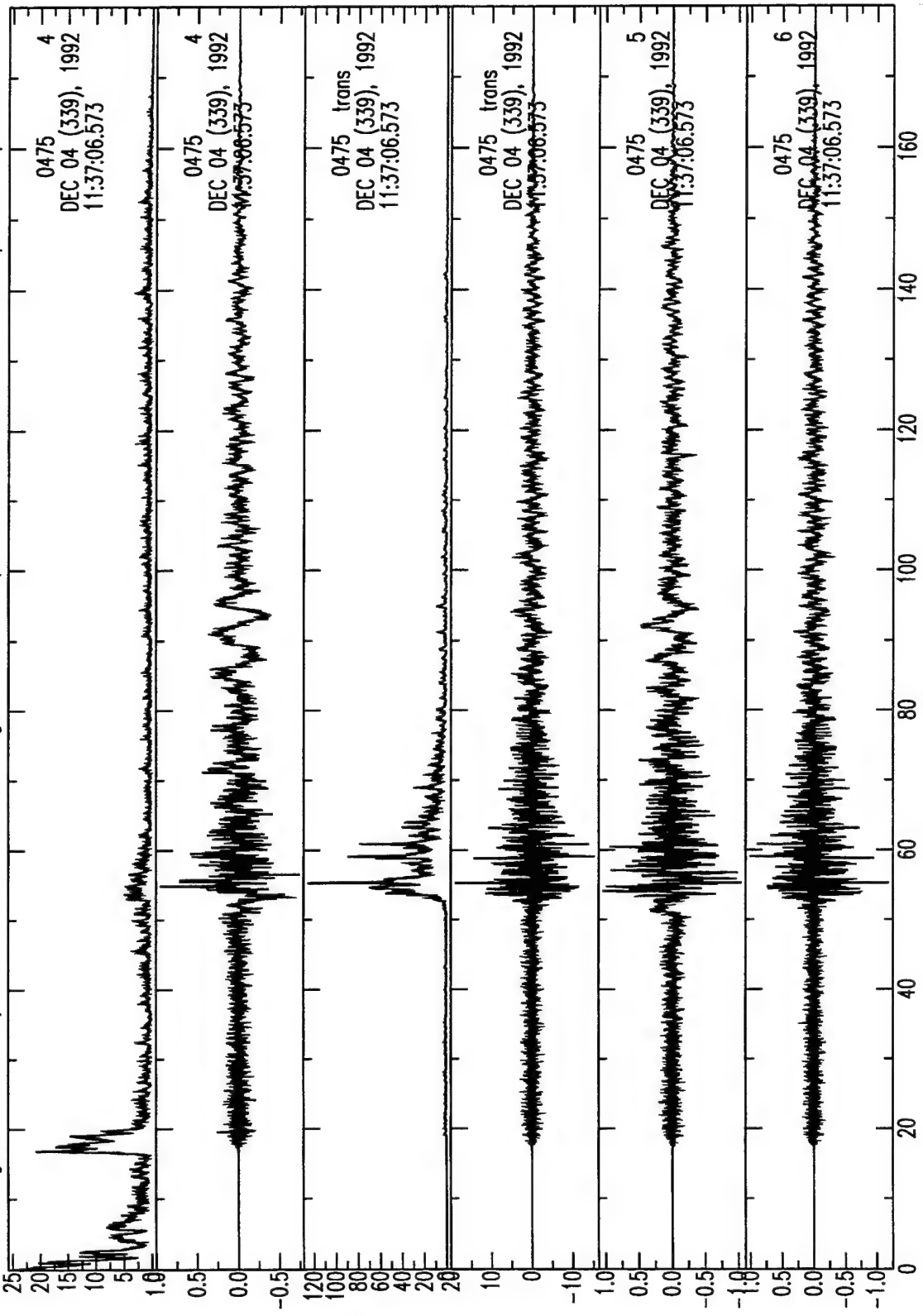


Figure A.78 Analysis of broadband seismograms for deep event 339.113715.shab

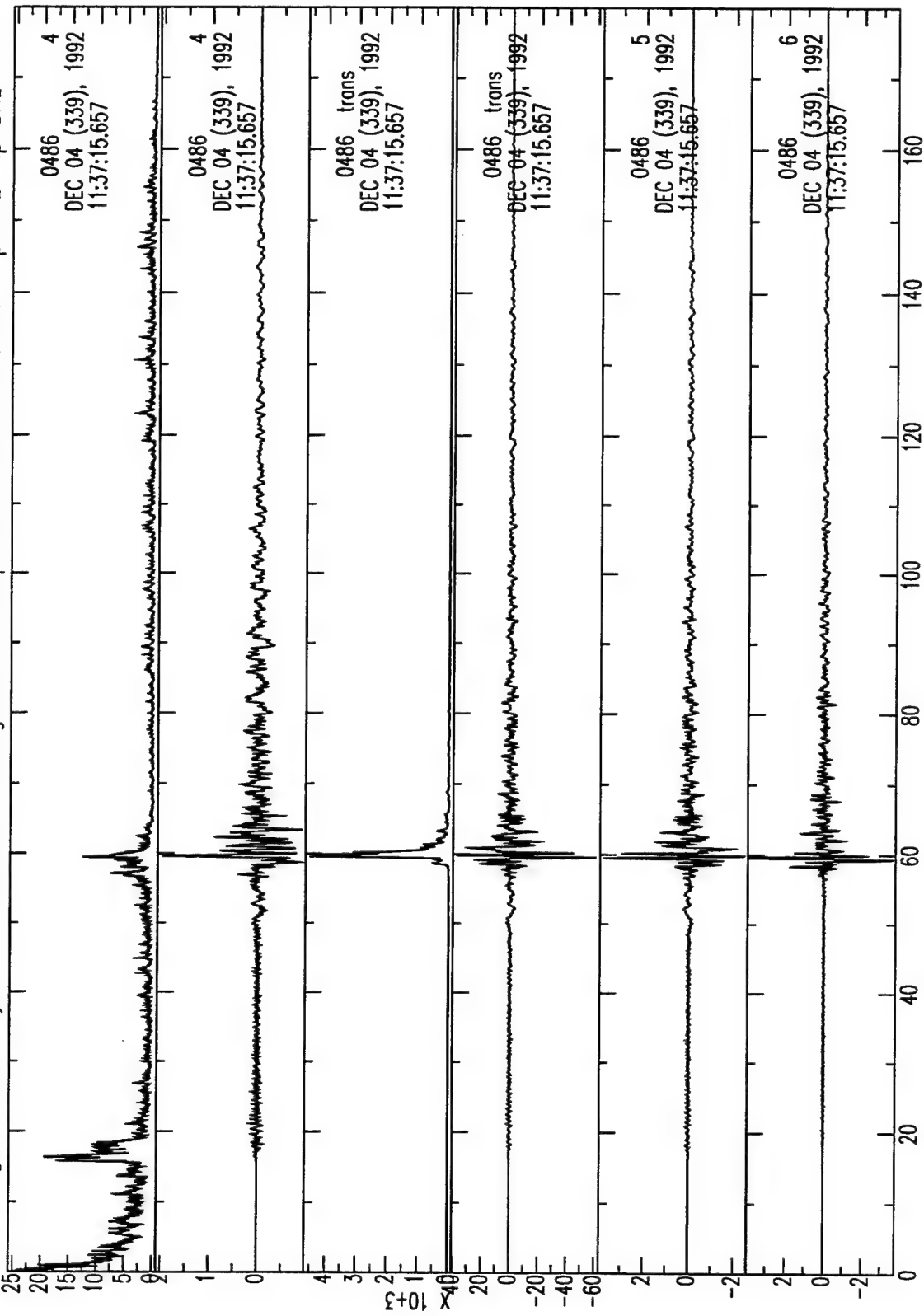


Figure A.79 Analysis of broadband seismograms for deep event 341.034428.hklt hp .1Hz |p 8Hz

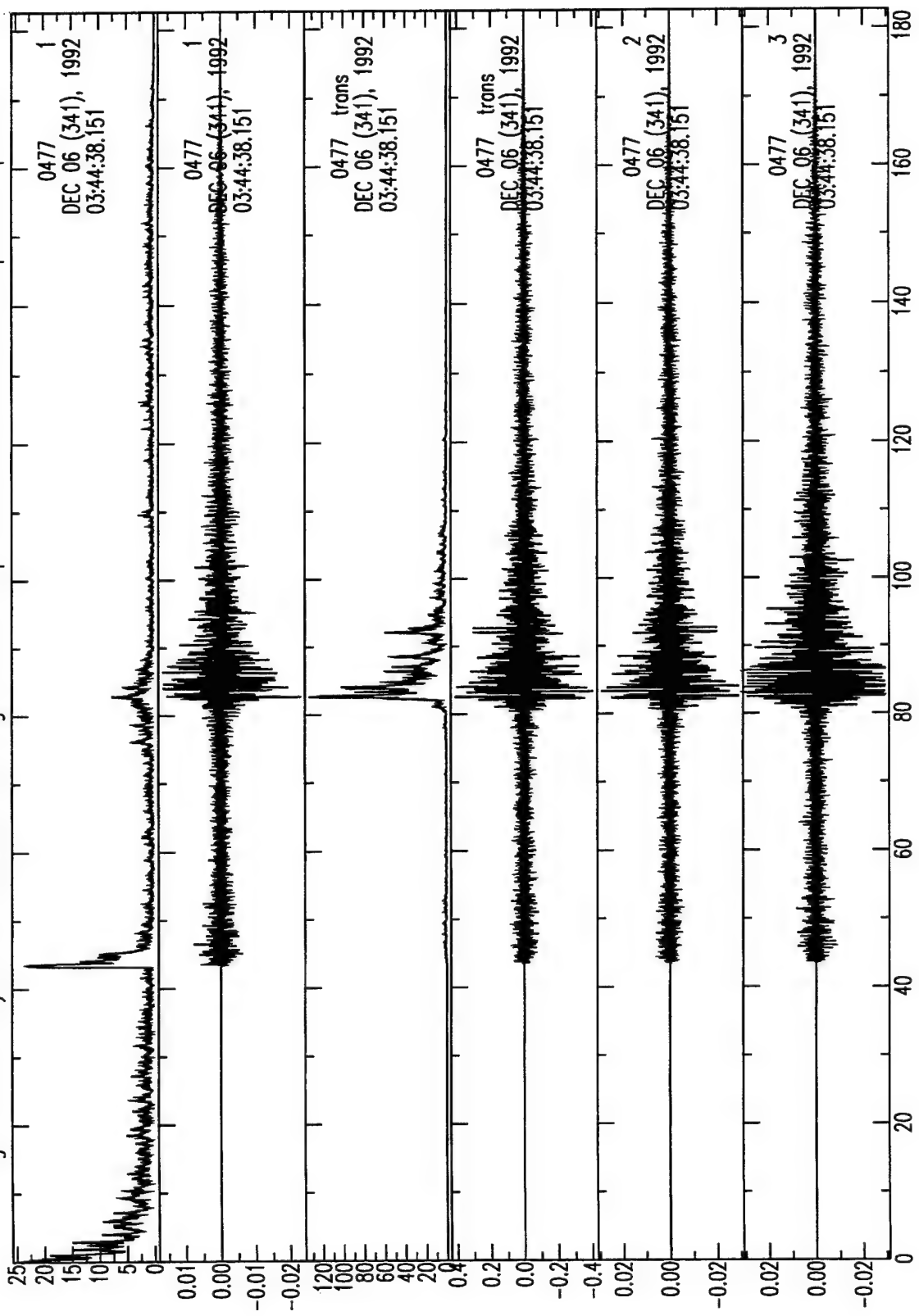


Figure A.80 Analysis of broadband seismograms for deep event 341.034428.sodu

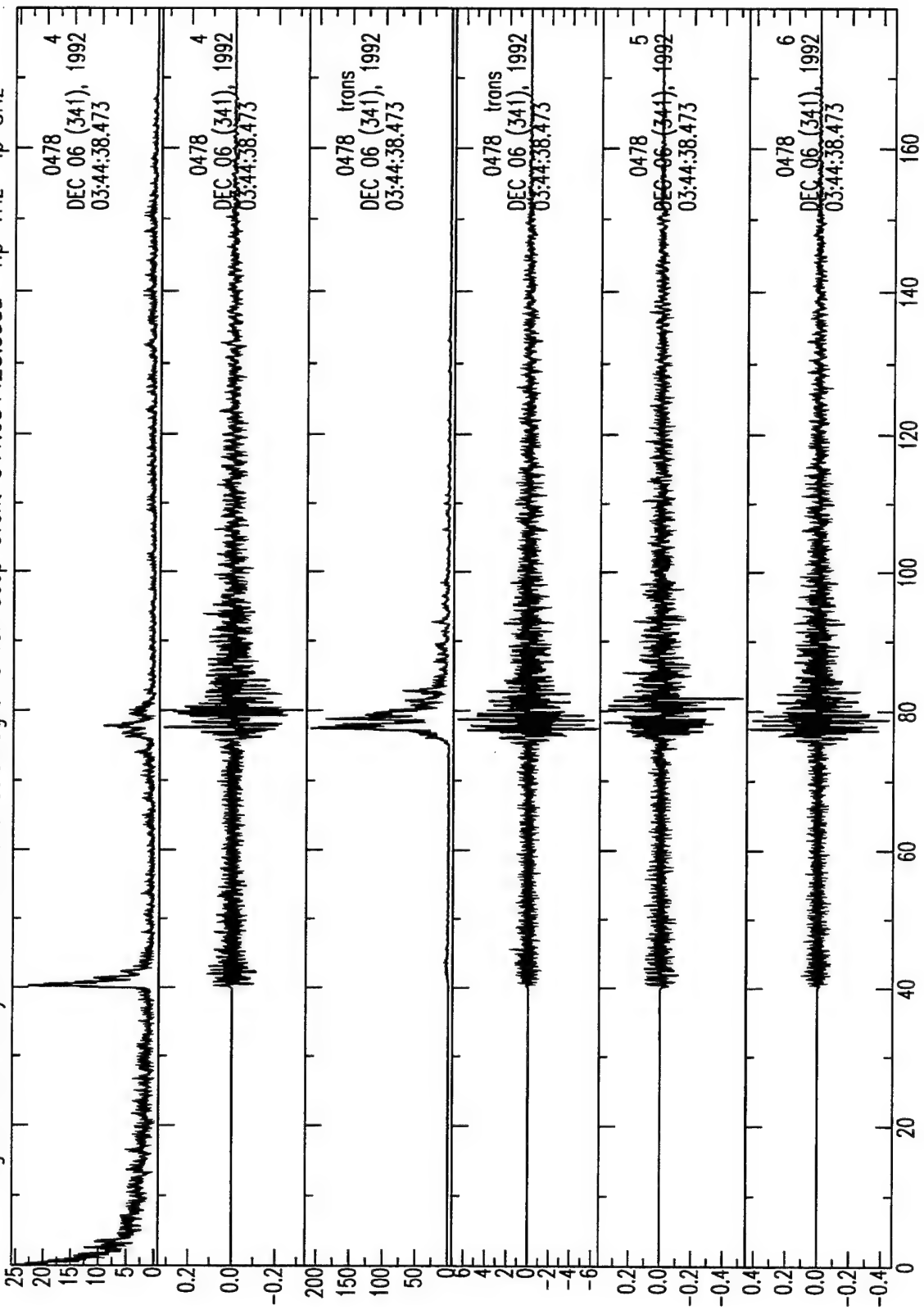


Figure A.81 Analysis of broadband seismograms for deep event 341.034431.dsau

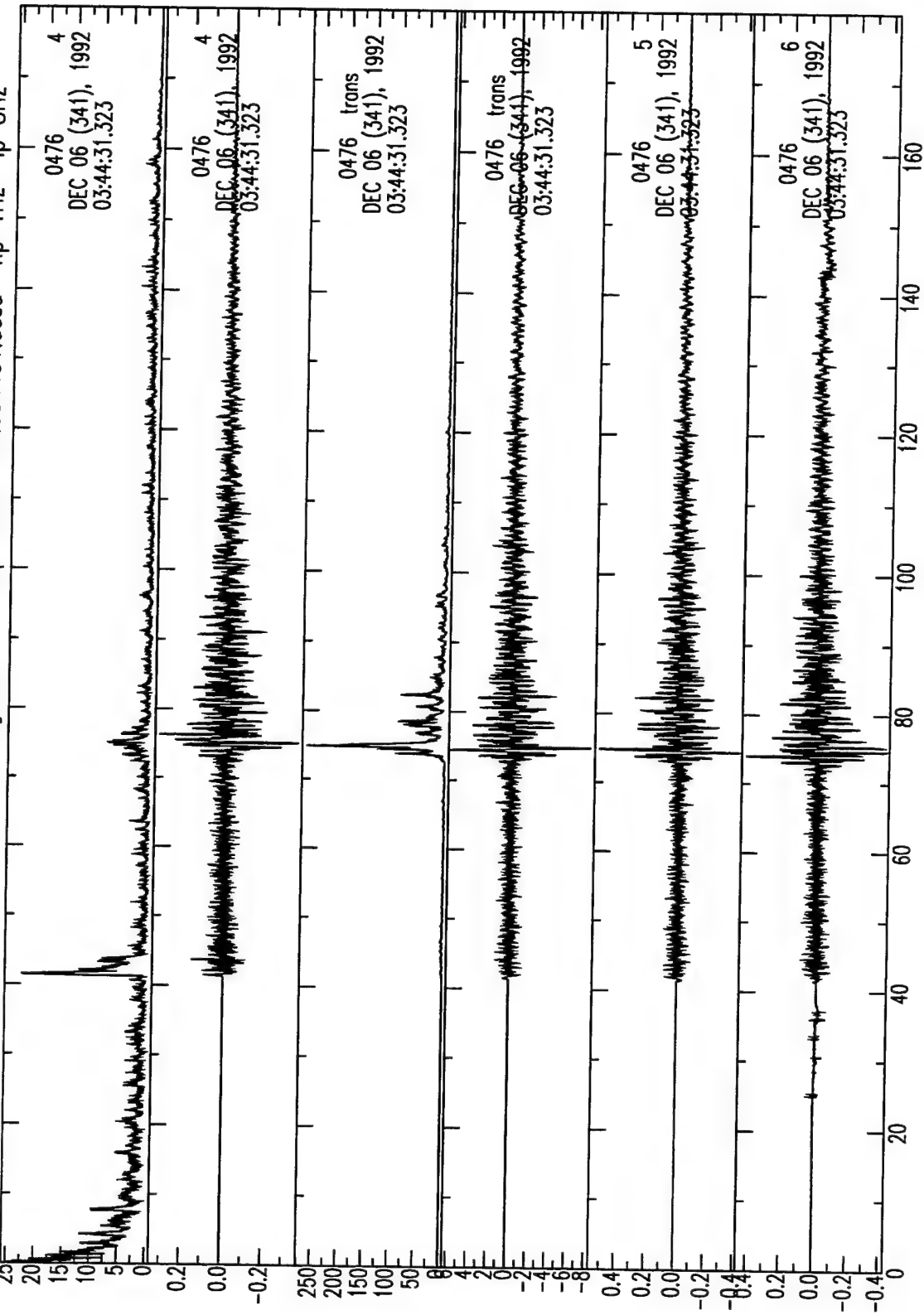


Figure A.82 Analysis of broadband seismograms for deep event 341.034431.patn

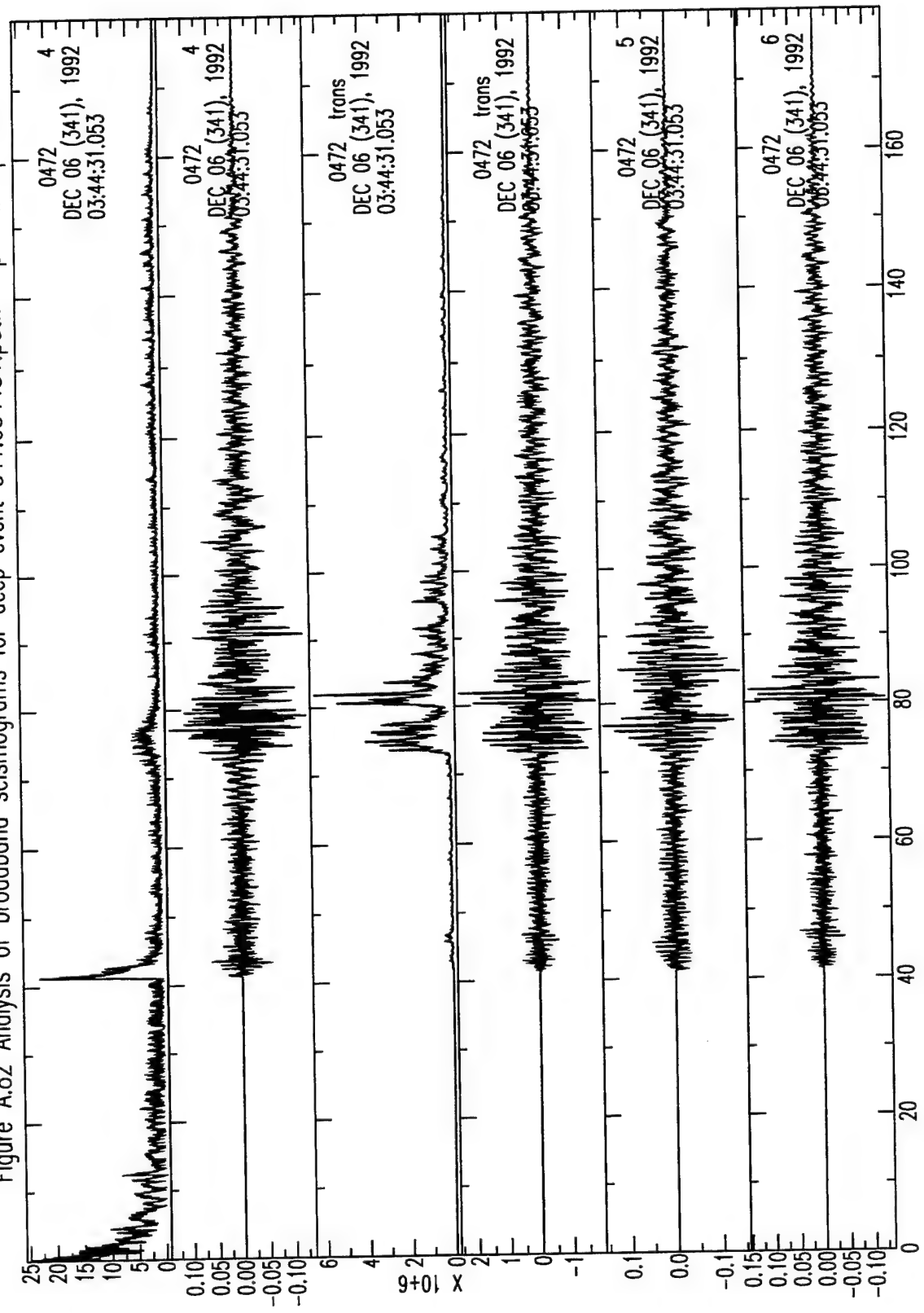
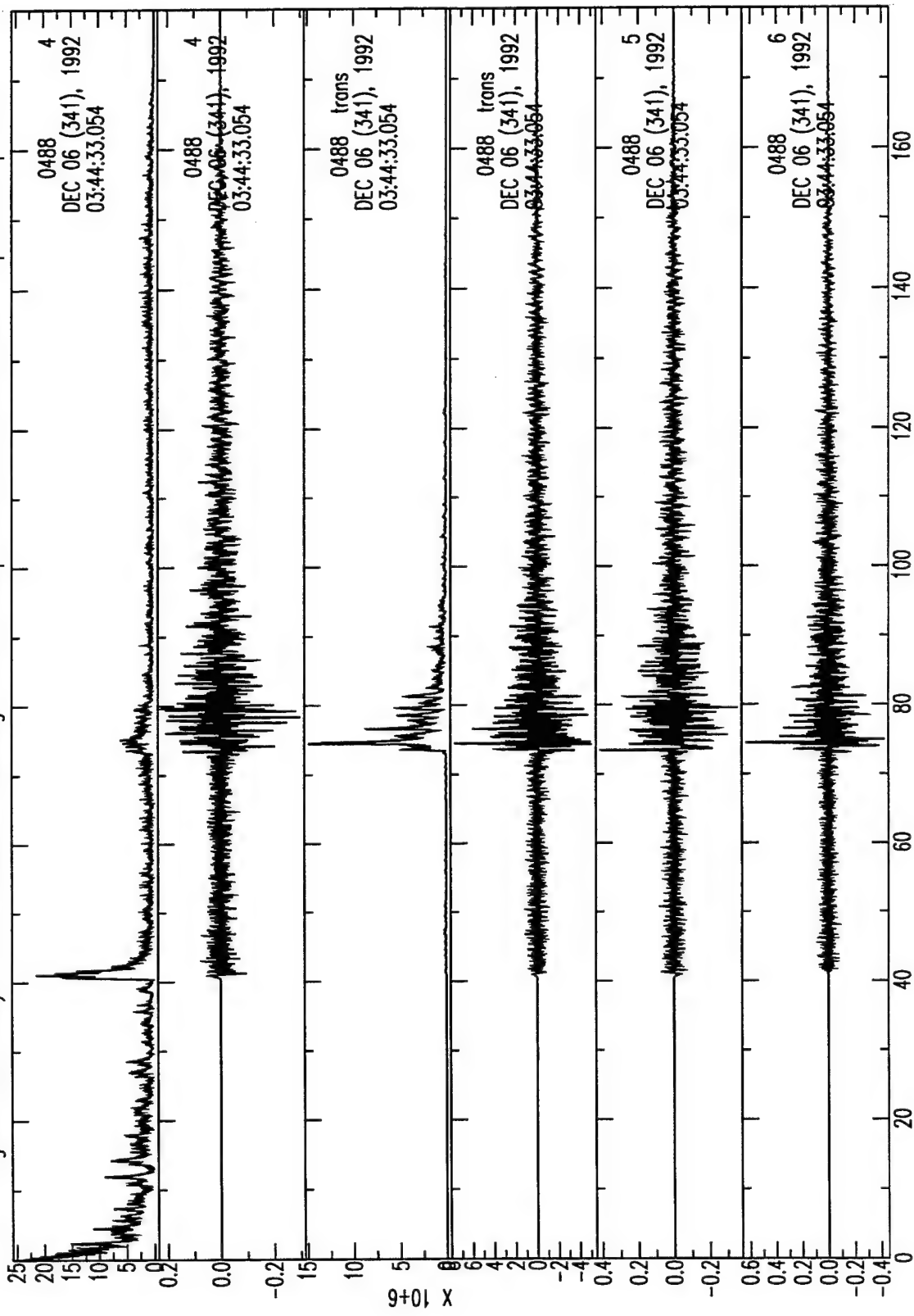


Figure A.83 Analysis of broadband seismograms for deep event 341.034433.shin



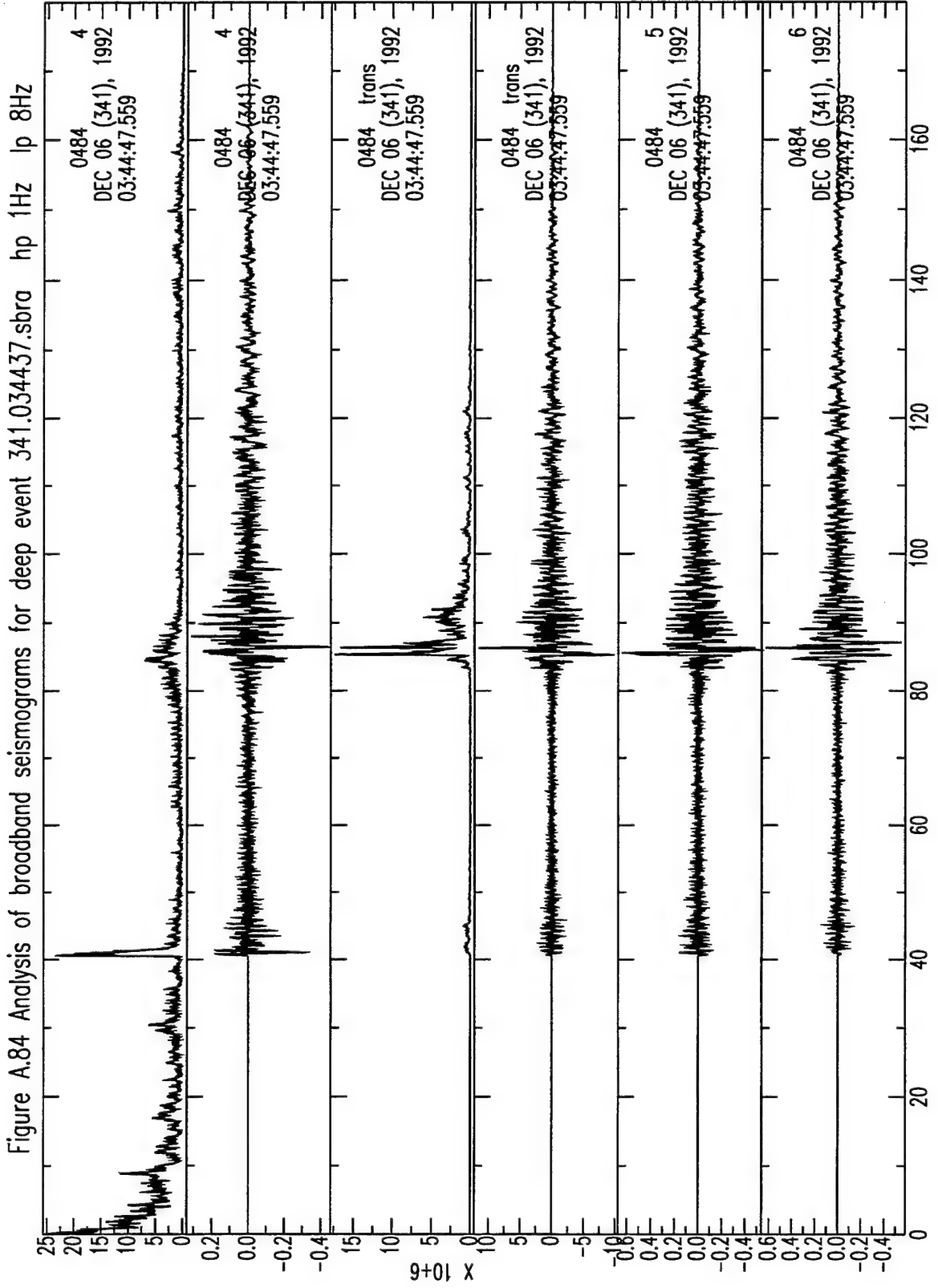
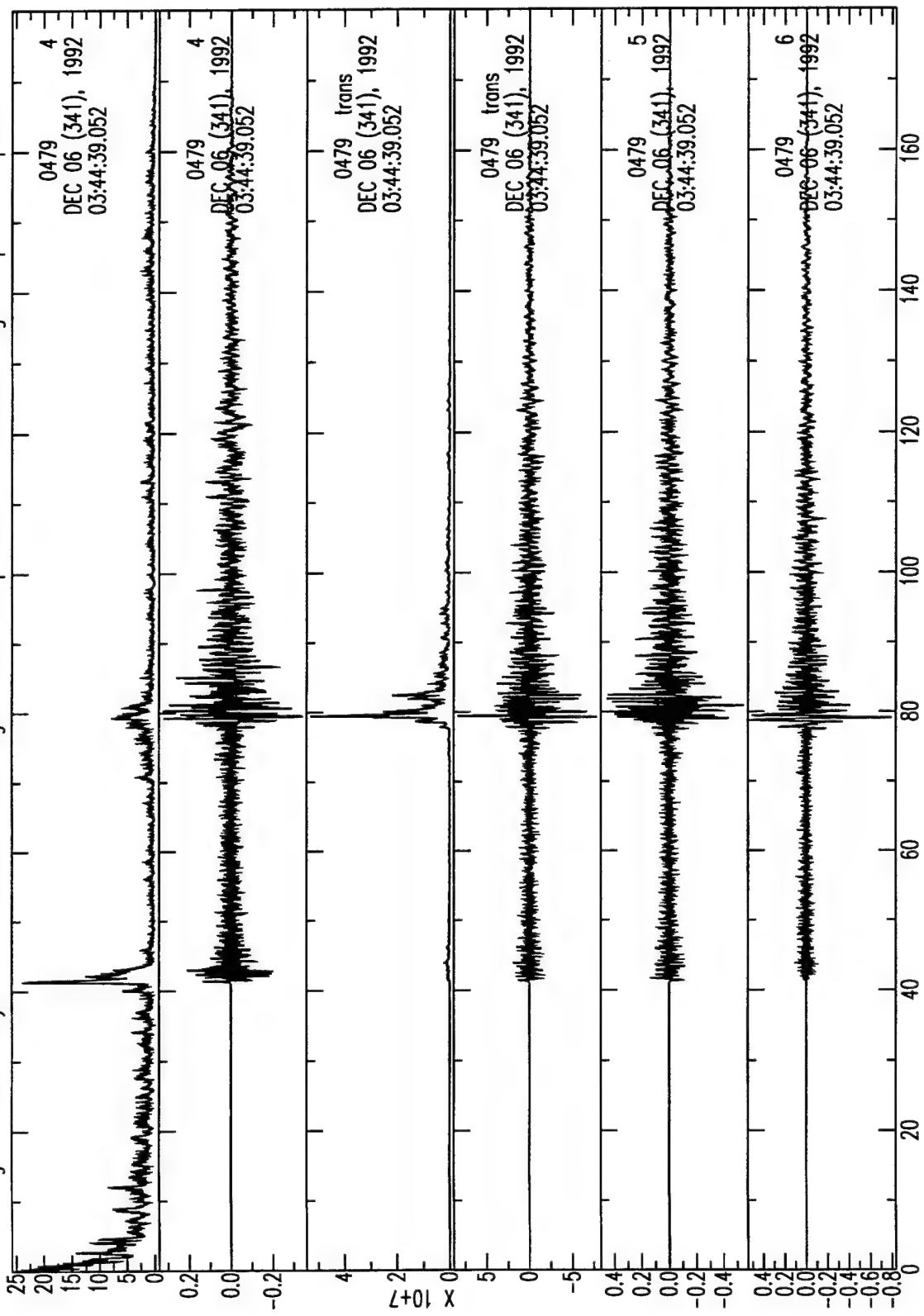


Figure A.85 Analysis of broadband seismograms for deep event 341.034439.btlgm



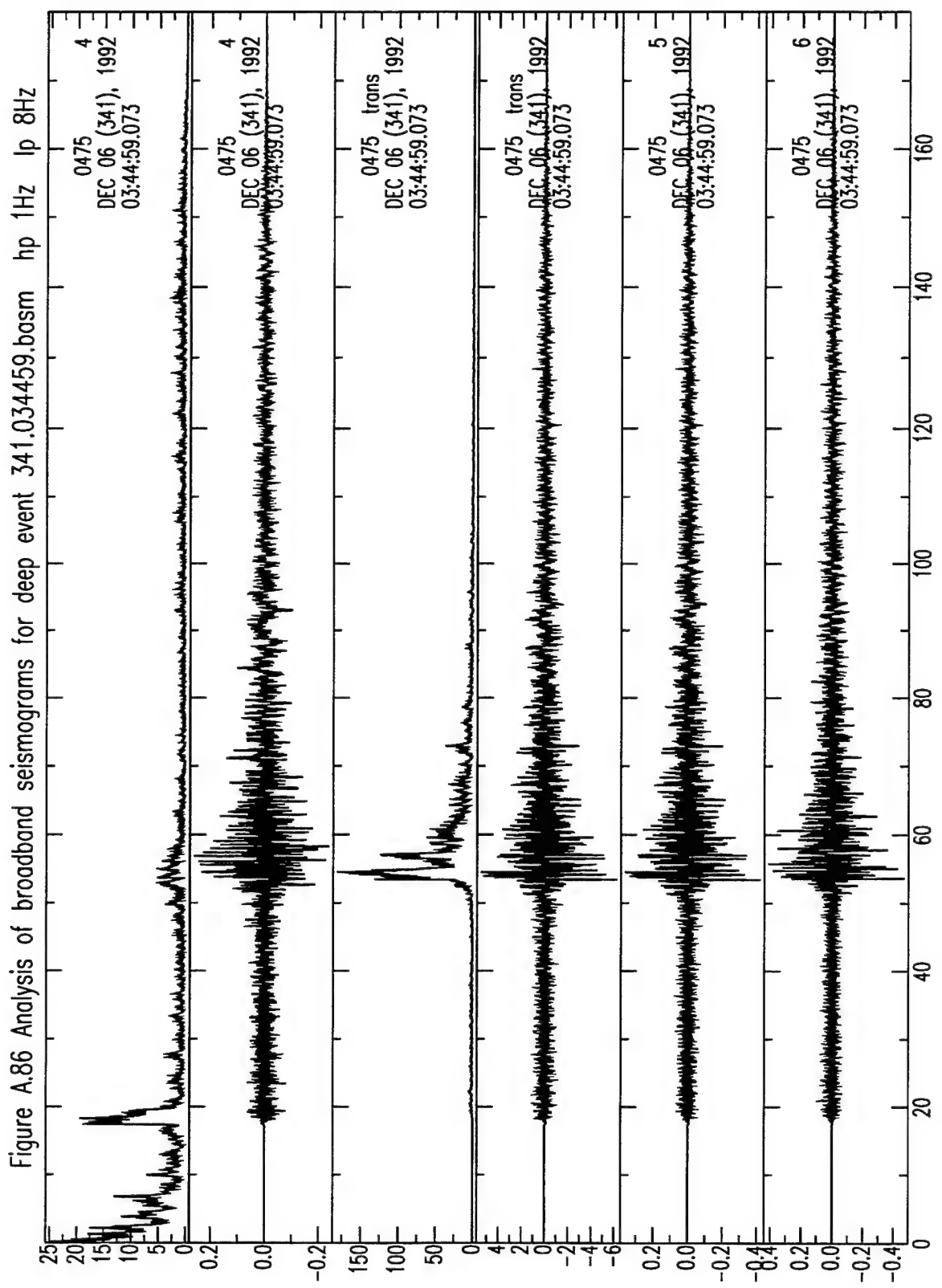
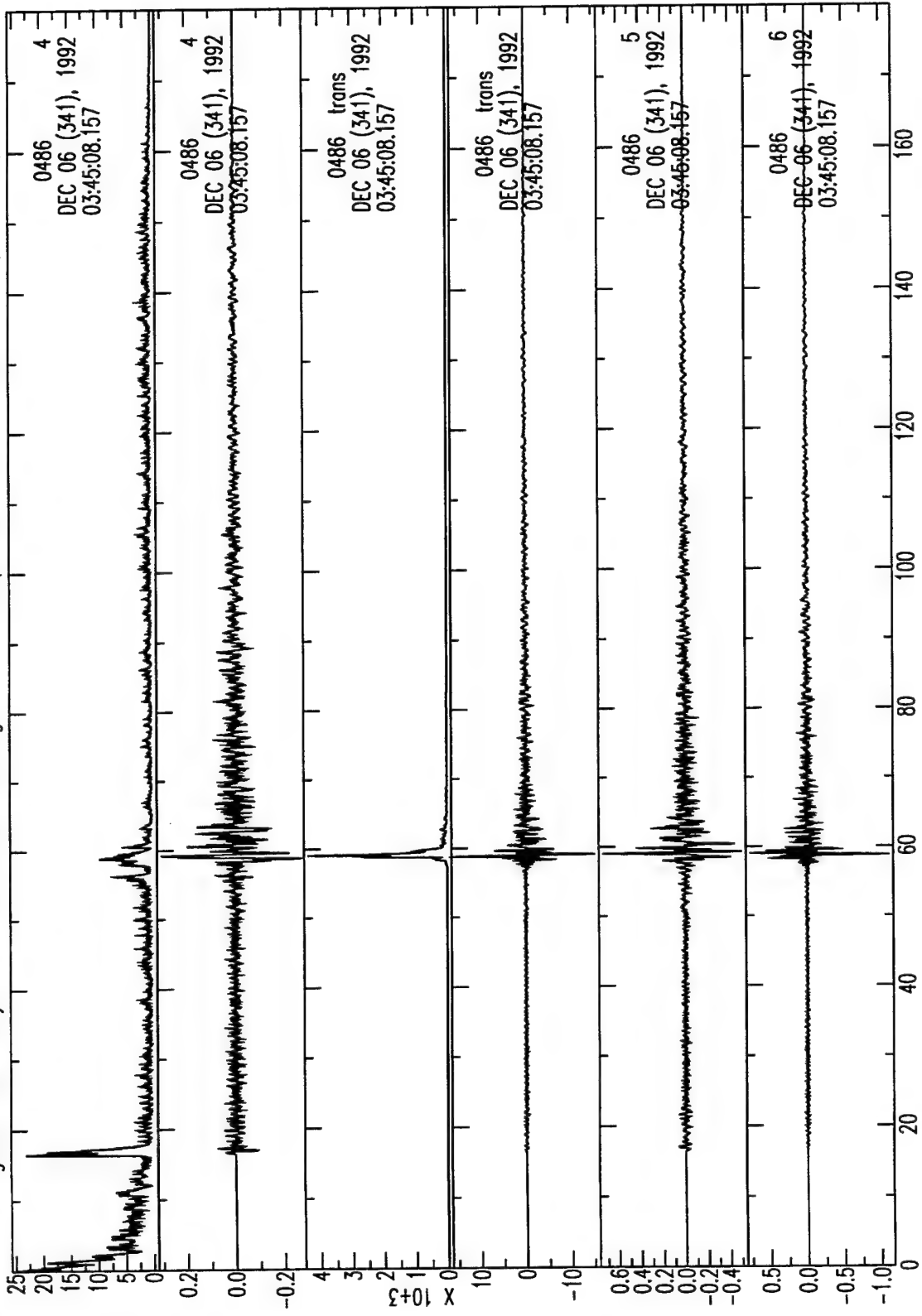


Figure A.87 Analysis of broadband seismograms for deep event 341.034508.shab



THOMAS AHRENS
SEISMOLOGICAL LABORATORY 252-21
CALIFORNIA INSTITUTE OF TECHNOLOGY
PASADENA, CA 91125

RALPH ALEWINE
NTPO
1901 N. MOORE STREET, SUITE 609
ARLINGTON, VA 22209

SHELTON ALEXANDER
PENNSYLVANIA STATE UNIVERSITY
DEPARTMENT OF GEOSCIENCES
537 DEIKE BUILDING
UNIVERSITY PARK, PA 16801

MUAWIA BARAZANGI
INSTITUTE FOR THE STUDY OF THE CONTINENTS
3126 SNEE HALL
CORNELL UNIVERSITY
ITHACA, NY 14853

RICHARD BARDZELL
ACIS
DCI/ACIS
WASHINGTON, DC 20505

T.G. BARKER
MAXWELL TECHNOLOGIES
P.O. BOX 23558
SAN DIEGO, CA 92123

DOUGLAS BAUMGARDT
ENSCO INC.
5400 PORT ROYAL ROAD
SPRINGFIELD, VA 22151

HERON J. BENNETT
MAXWELL TECHNOLOGIES
11800 SUNRISE VALLEY DRIVE SUITE 1212
RESTON, VA 22091

WILLIAM BENSON
NAS/COS
ROOM HA372
2001 WISCONSIN AVE. NW
WASHINGTON, DC 20007

JONATHAN BERGER
UNIVERSITY OF CA, SAN DIEGO
SCRIPPS INSTITUTION OF OCEANOGRAPHY IGPP, 0225
9500 GILMAN DRIVE
LA JOLLA, CA 92093-0225

ROBERT BLANDFORD
AFTAC
1300 N. 17TH STREET
SUITE 1450
ARLINGTON, VA 22209-2308

STEVEN BRATT
NTPO
1901 N. MOORE STREET, SUITE 609
ARLINGTON, VA 22209

RHETT BUTLER
IRIS
1200 NEW YORK AVE., NW
SUITE 800
WASHINGTON, DC 20005

LESLIE A. CASEY
DOE
1000 INDEPENDENCE AVE. SW
NN-20
WASHINGTON, DC 20585-0420

CATHERINE DE GROOT-HEDLIN
UNIVERSITY OF CALIFORNIA, SAN DIEGO
INSTITUTE OF GEOPHYSICS AND PLANETARY PHYSICS
8604 LA JOLLA SHORES DRIVE
SAN DIEGO, CA 92093

STANLEY DICKINSON
AFOSR
110 DUNCAN AVENUE, SUITE B115
BOLLING AFB
WASHINGTON, D.C. 20332-001

SEAN DORAN
ACIS
DCI/ACIS
WASHINGTON, DC 20505

DIANE I. DOSER
DEPARTMENT OF GEOLOGICAL SCIENCES
THE UNIVERSITY OF TEXAS AT EL PASO
EL PASO, TX 79968

RICHARD J. FANTEL
BUREAU OF MINES
DEPT OF INTERIOR, BLDG 20
DENVER FEDERAL CENTER
DENVER, CO 80225

JOHN FILSON
ACIS/TMG/NTT
ROOM 6T11 NHB
WASHINGTON, DC 20505

MARK D. FISK
MISSION RESEARCH CORPORATION
735 STATE STREET
P.O. DRAWER 719
SANTA BARBARA, CA 93102-0719

LORI GRANT
MULTIMAX, INC.
311C FOREST AVE. SUITE 3
PACIFIC GROVE, CA 93950

I. N. GUPTA
MULTIMAX, INC.
1441 MCCORMICK DRIVE
LARGO, MD 20774

JAMES HAYES
NSF
4201 WILSON BLVD., ROOM 785
ARLINGTON, VA 22230

MICHAEL HEDLIN
UNIVERSITY OF CALIFORNIA, SAN DIEGO
SCRIPPS INSTITUTION OF OCEANOGRAPHY IGPP, 0225
9500 GILMAN DRIVE
LA JOLLA, CA 92093-0225

EUGENE HERRIN
SOUTHERN METHODIST UNIVERSITY
DEPARTMENT OF GEOLOGICAL SCIENCES
DALLAS, TX 75275-0395

VINDELL HSU
HQ/AFTAC/TTR
1030 S. HIGHWAY A1A
PATRICK AFB, FL 32925-3002

RONG-SONG JIH
PHILLIPS LABORATORY
EARTH SCIENCES DIVISION
29 RANDOLPH ROAD
HANSCOM AFB, MA 01731-3010

LAWRENCE LIVERMORE NATIONAL LABORATORY
ATTN: TECHNICAL STAFF (PLS ROUTE)
PO BOX 808, MS L-200
LIVERMORE, CA 94551

LAWRENCE LIVERMORE NATIONAL LABORATORY
ATTN: TECHNICAL STAFF (PLS ROUTE)
PO BOX 808, MS L-221
LIVERMORE, CA 94551

ROBERT GEIL
DOE
PALAIS DES NATIONS, RM D615
GENEVA 10, SWITZERLAND

HENRY GRAY
SMU STATISTICS DEPARTMENT
P.O. BOX 750302
DALLAS, TX 75275-0302

DAVID HARKRIDER
PHILLIPS LABORATORY
EARTH SCIENCES DIVISION
29 RANDOLPH ROAD
HANSOM AFB, MA 01731-3010

THOMAS HEARN
NEW MEXICO STATE UNIVERSITY
DEPARTMENT OF PHYSICS
LAS CRUCES, NM 88003

DONALD HELMBERGER
CALIFORNIA INSTITUTE OF TECHNOLOGY
DIVISION OF GEOLOGICAL & PLANETARY SCIENCES
SEISMOLOGICAL LABORATORY
PASADENA, CA 91125

ROBERT HERRMANN
ST. LOUIS UNIVERSITY
DEPARTMENT OF EARTH & ATMOSPHERIC SCIENCES
3507 LACLEDE AVENUE
ST. LOUIS, MO 63103

ANTHONY IANNACCHIONE
BUREAU OF MINES
COCHRANE MILL ROAD
PO BOX 18070
PITTSBURGH, PA 15236-9986

THOMAS JORDAN
MASSACHUSETTS INSTITUTE OF TECHNOLOGY
EARTH, ATMOSPHERIC & PLANETARY SCIENCES
77 MASSACHUSETTS AVENUE, 54-918
CAMBRIDGE, MA 02139

LAWRENCE LIVERMORE NATIONAL LABORATORY
ATTN: TECHNICAL STAFF (PLS ROUTE)
PO BOX 808, MS L-207
LIVERMORE, CA 94551

LAWRENCE LIVERMORE NATIONAL LABORATORY
ATTN: TECHNICAL STAFF (PLS ROUTE)
LLNL
PO BOX 808, MS L-175
LIVERMORE, CA 94551

LAWRENCE LIVERMORE NATIONAL LABORATORY
ATTN: TECHNICAL STAFF (PLS ROUTE)
PO BOX 808, MS L-208
LIVERMORE, CA 94551

LAWRENCE LIVERMORE NATIONAL LABORATORY
ATTN: TECHNICAL STAFF (PLS ROUTE)
PO BOX 808, MS L-195
LIVERMORE, CA 94551

THORNE LAY
UNIVERSITY OF CALIFORNIA, SANTA CRUZ
EARTH SCIENCES DEPARTMENT
EARTH & MARINE SCIENCE BUILDING
SANTA CRUZ, CA 95064

DONALD A. LINGER
DNA
6801 TELEGRAPH ROAD
ALEXANDRIA, VA 22310

LOS ALAMOS NATIONAL LABORATORY
ATTN: TECHNICAL STAFF (PLS ROUTE)
PO BOX 1663, MS F665
LOS ALAMOS, NM 87545

LOS ALAMOS NATIONAL LABORATORY
ATTN: TECHNICAL STAFF (PLS ROUTE)
PO BOX 1663, MS C335
LOS ALAMOS, NM 87545

KEITH MC LAUGHLIN
MAXWELL TECHNOLOGIES
P.O. BOX 23558
SAN DIEGO, CA 92123

RICHARD MORROW
USACDA/IVI
320 21ST STREET, N.W.
WASHINGTON, DC 20451

JAMES NI
NEW MEXICO STATE UNIVERSITY
DEPARTMENT OF PHYSICS
LAS CRUCES, NM 88003

PACIFIC NORTHWEST NATIONAL LABORATORY
ATTN: TECHNICAL STAFF (PLS ROUTE)
PO BOX 999, MS K6-48
RICHLAND, WA 99352

LAWRENCE LIVERMORE NATIONAL LABORATORY
ATTN: TECHNICAL STAFF (PLS ROUTE)
PO BOX 808, MS L-202
LIVERMORE, CA 94551

LAWRENCE LIVERMORE NATIONAL LABORATORY
ATTN: TECHNICAL STAFF (PLS ROUTE)
PO BOX 808, MS L-205
LIVERMORE, CA 94551

ANATOLI L. LEVSHIN
DEPARTMENT OF PHYSICS
UNIVERSITY OF COLORADO
CAMPUS BOX 390
BOULDER, CO 80309-0309

LOS ALAMOS NATIONAL LABORATORY
ATTN: TECHNICAL STAFF (PLS ROUTE)
PO BOX 1663, MS F659
LOS ALAMOS, NM 87545

LOS ALAMOS NATIONAL LABORATORY
ATTN: TECHNICAL STAFF (PLS ROUTE)
PO BOX 1663, MS D460
LOS ALAMOS, NM 87545

GARY MCCARTOR
SOUTHERN METHODIST UNIVERSITY
DEPARTMENT OF PHYSICS
DALLAS, TX 75275-0395

BRIAN MITCHELL
DEPARTMENT OF EARTH & ATMOSPHERIC SCIENCES
ST. LOUIS UNIVERSITY
3507 LACLEDE AVENUE
ST. LOUIS, MO 63103

JOHN MURPHY
MAXWELL TECHNOLOGIES
11800 SUNRISE VALLEY DRIVE SUITE 1212
RESTON, VA 22091

JOHN ORCUTT
INSTITUTE OF GEOPHYSICS AND PLANETARY PHYSICS
UNIVERSITY OF CALIFORNIA, SAN DIEGO
LA JOLLA, CA 92093

PACIFIC NORTHWEST NATIONAL LABORATORY
ATTN: TECHNICAL STAFF (PLS ROUTE)
PO BOX 999, MS K7-34
RICHLAND, WA 99352

PACIFIC NORTHWEST NATIONAL LABORATORY
ATTN: TECHNICAL STAFF (PLS ROUTE)
PO BOX 999, MS K6-40
RICHLAND, WA 99352

PACIFIC NORTHWEST NATIONAL LABORATORY
ATTN: TECHNICAL STAFF (PLS ROUTE)
PO BOX 999, MS K5-12
RICHLAND, WA 99352

KEITH PRIESTLEY
DEPARTMENT OF EARTH SCIENCES
UNIVERSITY OF CAMBRIDGE
MADINGLEY RISE, MADINGLEY ROAD
CAMBRIDGE, CB3 OEZ UK

PAUL RICHARDS
COLUMBIA UNIVERSITY
LAMONT-DOHERTY EARTH OBSERVATORY
PALISADES, NY 10964

CHANDAN SAIKIA
WOODWARD-CLYDE FEDERAL SERVICES
566 EL DORADO ST., SUITE 100
PASADENA, CA 91101-2560

SANDIA NATIONAL LABORATORY
ATTN: TECHNICAL STAFF (PLS ROUTE)
DEPT. 5791
MS 0567, PO BOX 5800
ALBUQUERQUE, NM 87185-0567

SANDIA NATIONAL LABORATORY
ATTN: TECHNICAL STAFF (PLS ROUTE)
DEPT. 5704
MS 0655, PO BOX 5800
ALBUQUERQUE, NM 87185-0655

THOMAS SERENO JR.
SCIENCE APPLICATIONS INTERNATIONAL
CORPORATION
10260 CAMPUS POINT DRIVE
SAN DIEGO, CA 92121

ROBERT SHUMWAY
410 MRAK HALL
DIVISION OF STATISTICS
UNIVERSITY OF CALIFORNIA
DAVIS, CA 95616-8671

DAVID SIMPSON
IRIS
1200 NEW YORK AVE., NW
SUITE 800
WASHINGTON, DC 20005

PACIFIC NORTHWEST NATIONAL LABORATORY
ATTN: TECHNICAL STAFF (PLS ROUTE)
PO BOX 999, MS K6-84
RICHLAND, WA 99352

FRANK PILOTTE
HQ/AFTAC/TT
1030 S. HIGHWAY A1A
PATRICK AFB, FL 32925-3002

JAY PULLI
BBN
1300 NORTH 17TH STREET
ROSSLYN, VA 22209

DAVID RUSSELL
HQ AFTAC/TTR
1030 SOUTH HIGHWAY A1A
PATRICK AFB, FL 32925-3002

SANDIA NATIONAL LABORATORY
ATTN: TECHNICAL STAFF (PLS ROUTE)
DEPT. 5704
MS 0979, PO BOX 5800
ALBUQUERQUE, NM 87185-0979

SANDIA NATIONAL LABORATORY
ATTN: TECHNICAL STAFF (PLS ROUTE)
DEPT. 9311
MS 1159, PO BOX 5800
ALBUQUERQUE, NM 87185-1159

SANDIA NATIONAL LABORATORY
ATTN: TECHNICAL STAFF (PLS ROUTE)
DEPT. 5736
MS 0655, PO BOX 5800
ALBUQUERQUE, NM 87185-0655

AVI SHAPIRA
SEISMOLOGY DIVISION
THE INSTITUTE FOR PETROLEUM RESEARCH AND
GEOPHYSICS
P.O.B. 2286, NOLON 58122 ISRAEL

MATTHEW SIBOL
ENSCO, INC.
445 PINEDA COURT
MELBOURNE, FL 32940

JEFFRY STEVENS
MAXWELL TECHNOLOGIES
P.O. BOX 23558
SAN DIEGO, CA 92123

BRIAN SULLIVAN
BOSTON COLLEGE
INSTITUTE FOR SPACE RESEARCH
140 COMMONWEALTH AVENUE
CHESTNUT HILL, MA 02167

NAFI TOKSOZ
EARTH RESOURCES LABORATORY, M.I.T.
42 CARLTON STREET, E34-440
CAMBRIDGE, MA 02142

GREG VAN DER VINK
IRIS
1200 NEW YORK AVE., NW
SUITE 800
WASHINGTON, DC 20005

TERRY WALLACE
UNIVERSITY OF ARIZONA
DEPARTMENT OF GEOSCIENCES
BUILDING #77
TUCSON, AZ 85721

JAMES WHITCOMB
NSF
NSF/ISC OPERATIONS/EAR-785
4201 WILSON BLVD., ROOM 785
ARLINGTON, VA 22230

JIAKANG XIE
COLUMBIA UNIVERSITY
LAMONT DOHERTY EARTH OBSERVATORY
ROUTE 9W
PALISADES, NY 10964

OFFICE OF THE SECRETARY OF DEFENSE
DDR&E
WASHINGTON, DC 20330

TACTEC
BATTELLE MEMORIAL INSTITUTE
505 KING AVENUE
COLUMBUS, OH 43201 (FINAL REPORT)

PHILLIPS LABORATORY
ATTN: GPE
29 RANDOLPH ROAD
HANSOM AFB, MA 01731-3010

PHILLIPS LABORATORY
ATTN: PL/SUL
3550 ABERDEEN AVE SE
KIRTLAND, NM 87117-5776 (2 COPIES)

DAVID THOMAS
ISEE
29100 AURORA ROAD
CLEVELAND, OH 44139

LAWRENCE TURNBULL
ACIS
DCI/ACIS
WASHINGTON, DC 20505

FRANK VERNON
UNIVERSITY OF CALIFORNIA, SAN DIEGO
SCRIPPS INSTITUTION OF OCEANOGRAPHY IGPP, 0225
9500 GILMAN DRIVE
LA JOLLA, CA 92093-0225

DANIEL WEILL
NSF
EAR-785
4201 WILSON BLVD., ROOM 785
ARLINGTON, VA 22230

RU SHAN WU
UNIVERSITY OF CALIFORNIA SANTA CRUZ
EARTH SCIENCES DEPT.
1156 HIGH STREET
SANTA CRUZ, CA 95064

JAMES E. ZOLLWEG
BOISE STATE UNIVERSITY
GEOSCIENCES DEPT.
1910 UNIVERSITY DRIVE
BOISE, ID 83725

DEFENSE TECHNICAL INFORMATION CENTER
8725 JOHN J. KINGMAN ROAD
FT BELVOIR, VA 22060-6218 (2 COPIES)

PHILLIPS LABORATORY
ATTN: XPG
29 RANDOLPH ROAD
HANSOM AFB, MA 01731-3010

PHILLIPS LABORATORY
ATTN: TSML
5 WRIGHT STREET
HANSOM AFB, MA 01731-3004